Study of Nuclear Structure around N=90

By

ARUNABHA SAHA

PHYS04201204010

Variable Energy Cyclotron Centre, Kolkata

A thesis submitted to the

Board of Studies in Physical Sciences

In partial fulfillment of requirements

for the Degree of

DOCTOR OF PHILOSOPHY

of

HOMI BHABHA NATIONAL INSTITUTE

September, 2018

Homi Bhabha National Institute[1]

Recommendations of the Viva Voce Committee

As members of the Viva Voce Committee, we certify that we have read the dissertation prepared by **Arunabha Saha** entitled **"Study of Nuclear Structure around N=90"** and recommend that it may be accepted as fulfilling the thesis requirement for the award of Degree of Doctor of Philosophy.

Chairman – Prof. Alok Chakrabarti	Alok Chakrabarti	**Date:** 03-09-2018
Guide / Convener – Prof. Sudhee Ranjan Banerjee		**Date:** 03-9-2018
Co-guide - Dr. Tumpa Bhattacharjee	Tumpa Bhattacharjee	**Date:** 03.09.2018
Examiner – Prof. Pragya Das	Pragya Das	**Date:** 3-Sept-2018
Member 1- Dr. Sarmistha Bhattacharyya	S. Bhattacharyya	**Date:** 3-9-18
Member 2- Prof. Asimananda Goswami	Asimananda Goswami	**Date:** 03.09.2018

Final approval and acceptance of this thesis is contingent upon the candidate's submission of the final copies of the thesis to HBNI.

I/We hereby certify that I/we have read this thesis prepared under my/our direction and recommend that it may be accepted as fulfilling the thesis requirement.

Date: 3/9/18

Place: Kolkata

Tumpa Bhattacharjee

Dr. Tumpa Bhattacharjee
Co-guide

Prof. Sudhee Ranjan Banerjee
Guide

[1] This page is to be included only for final submission after successful completion of viva voce.

ACKNOWLEDGEMENTS

I am using this opportunity to express my sincere gratitude to all without whose helps and supports, the present thesis would have never been possible. First of all, I would like to thank my mother and father for making me realize the value of human relationships and emotions in life. The behavior, truthfullness, honesty & sincerity that my parents have blessed me with, is far more than anything else.

I express my warm thanks to Dr. Tumpa Bhattacharjee, my Co-supervisor, who was there with me always standing by my side. Whatever I have known about research in Nuclear Structure, I owe it all to her. On several occassions, I have been invited to her home and offered a home like treatment for which I am thankful to her. I am extremely thankful to Prof. Sudhee Ranjan Banerjee, my Thesis Supervisor, who has always extended a helping hand towards me in times of need. Whenever I have talked to him, I have always felt as if I am talking to my father, who will always guide me in the right direction. I am thankful to him for his physics guidance and suggestions which were extremely helpful for me. I would like to thank Dr. Debasish Banerjee who was more as a friend than a collaborator. I owe a lot to him because without his helps, it would have never been possible for us to prepare the targets for experiments.

I am extremely thankful to all my Foreign Collaborators specially Prof. Jerzy Dudek and Prof. Dominique Curien from IPHC, Strasbourg, France for their extreme guidances in both theoretical and experimental aspects of my work. I am thankful to all my local collaborators specially Prof. M. Saha Sarkar, SINP, Kolkata, Prof. Sukhendusekhar Saha, IIEST, Kolkata and Prof. J. B. Gupta, Delhi University for their helpful guidances.

I am extremely thankful to Prime Minister's Office for their helps in getting NET-JRF fellowship started from University Grants Commission (UGC). I am thankful to all my lovely VECC/non-VECC friends for making my life beautiful with their presence. I sincerely apologize if I have missed someone's name by mistake.

Arunabha Saha

Arunabha Saha

Dedicated to my beloved parents:

My Mother - Smt. Bandana Saha

My Father - Shri Nityananda Saha

13. *"Fast Timing measurement in neutron rich $^{131,132}I$"*

    S.S. Alam, T. Bhattacharjee, D. Banerjee, **A. Saha**, P. Das, S.K. Das.

    Proceedings of the **DAE Symp. Nucl. Phys. 60 (2015) 270.**

14. *"Angular Correlation measurement around Z=64"*

    N. Sensharma, S.S. Alam, D. Banerjee, T. Bhattacharjee, **A. Saha**, S.K. Das.

    Proceedings of the **DAE Symp. Nucl. Phys. 60 (2015) 272.**

15. *"Decay Spectroscopy of ^{134}I"*

    R. Banik, S. Bhattacharyya, Soumik Bhattacharya, D. Banerjee, S. K. Das, G. Mukherjee, T. Bhattacharjee, A. Choudhury, P. Das, R. Guin, **A. Saha**.

    Proceedings of the **DAE Symp. Nucl. Phys. 60 (2015) 244.**

16. *"Clover detector setup at VECC"*

    Soumik Bhattacharya , B. Dey, **A. Saha**, A. Choudhury, S. Bhattacharyya, T. Bhattacharjee, S. R. Banerjee, S. Das Gupta, D. Mondal, G. Mukherjee, P. Mukhopadhyay, S. Mukhopadhyay, D. Pandit, S. Pal, T. Roy, I. Seikh

    Proceedings of the **DAE Symp. Nucl. Phys. 58 (2013) 906.**

Arunabha Saha

(Arunabha Saha)

8. *"Study of nuclear structure in odd-odd $^{122,124}I$"*

   S. S. Alam, **A. Saha**, T. Bhattacharjee , D. Banerjee, Md. A. Asgar, R. Banik, S.Bhattacharyya, Soumik Bhattacharya, A. Dhal, D. Mondal, G. Mukherjee, S. Mukhopadhyay, S. Pal, D. Pandit, T. Roy, and S. R. Banerjee.

   Proceedings of the **DAE Symp. Nucl. Phys. 61 (2016) 316**.

9. *"Decay spectroscopy of fission fragments around ^{132}Sn"*

   S. S. Alam, D. Banerjee, **A. Saha**, T. Bhattacharjee and S. K. Das.

   Proceedings of the **DAE Symp. Nucl. Phys. 61 (2016) 318**.

10. *"Half-life and β-feeding measurements of ^{207}Po by γ-spectroscopy method"*

    A.Dhal, R. Ghosh, A. G. Nair, G. Mukherjee, Md. A. Asgar, T. Roy, T. K. Rana, T. K. Ghosh, K. Banerjee, S. Kundu, R. Pandey, Pratap Roy, S. Manna, A. Sen, A. Dey, J. K. Meena, J. K. Sahoo, A. K. Saha, R. Banik, Soumik Bhattacharya, **A. Saha**, S. S. Alam, D. Mondal, D. Pandit, S. Mukhopadhyay, S. Pal, T. Bhattacharjee, S. Bhattacharyya, C. Bhattacharya, and S. R. Banerjee.

    Proceedings of the **DAE Symp. Nucl. Phys. 61 (2016) 266**.

11. *"Study of multi-quasiparticle band structures in ^{197}Tl using α beam"*

    G. Mukherjee, S. Nandi, H. Pai, T. Roy, Md.A. Asgar, A. Dhal, R. Banik, Soumik Bhattacharya, **A. Saha**, S. S. Alam, S. Bhattacharyya, C. Bhattacharya, Pratap Roy, T.K. Ghosh , S. Kundu, K. Banerjee, T.K. Rana, R. Pandey, S. Manna, A. Sen, S. Pal, S. Mukhopadhyay, D. Pandit, D. Mondal, T. Bhattacharjee, A. Dey, J.K. Meena, A.K. Saha, J.K. Sahoo, R. MandalSaha, A. Choudhury, and S.R. Banerjee.

    Proceedings of the **DAE Symp. Nucl. Phys. 61 (2016) 270**.

12. *"Study of low-spin states of ^{197}Hg from decay spectroscopy"*

    Soumik Bhattacharya, S. Bhattacharyya, R. Banik, S. Dutta, G. Mukherjee, A. Choudhury, T. Bhattacharjee, **A. Saha**, D. Banerjee, R. Guin, P. Das.

    Proceedings of the **DAE Symp. Nucl. Phys. 60 (2015) 260**.

D. Pandit, D. Mondal, T. Bhattacharjee, A. Dey, J.K. Meena, A.K. Saha, J.K. Sahoo, R. Mandal Saha, A. Choudhury, and S.R. Banerjee.

Proceedings of the **DAE Symp. Nucl. Phys. 62 (2017) 420**.

3. *"High spin structure and neutron alignments in* ^{197}Tl*"*

   D. Banerjee, S. S. Alam, Sk Wasim Raja, **A. Saha**, T. Bhattacharjee.

   Proceedings of the **DAE Symp. Nucl. Phys. 62 (2017) 80**.

4. *"Isomers in* $^{117,118}Sn$ *and role of neutron* $1h_{11/2}$ *orbit"*

   Sangeeta Das, Sathi Sharma, S. S. Alam, Arkabrata Gupta, Anik Adhikari, Ananya Das, **A. Saha**, S. K. Dey, Dibyadyuti Pramanik, Abhijit Bisoi, T. Bhattacharjee, C. C. Dey, S. Sarkar, M. Saha Sarkar.

   Proceedings of the **DAE Symp. Nucl. Phys. 62 (2017) 84**.

5. *"Decay spectroscopy of* ^{118m}Sb*"*

   Sathi Sharma, Sangeeta Das, S. S. Alam, Arkabrata Gupta, Anik Adhikari, Ananya Das, **A. Saha**, Dibyadyuti Pramanik, Abhijit Bisoi, Indrani Ray, T. Bhattacharjee, S. Sarkar, M. Saha Sarkar.

   Proceedings of the **DAE Symp. Nucl. Phys. 62 (2017) 200**.

6. *"Deformed structure based on* $\nu i_{13/2}$ *orbital in* ^{199}Hg*"*

   Soumik Bhattacharya, S. Bhattacharyya, R. Banik, S. Das Gupta, A. Dhal, G. Mukherjee, S. S. Alam, Md. A. Asgar, T. Roy, T. Bhattacharjee, **A. Saha**, S. Mukhopadhyay, Debasish Mondal, Deepak Pandit, Surajit Pal and S. R. Banerjee.

   Proceedings of the **DAE Symp. Nucl. Phys. 62 (2017) 118**.

7. *"Oblate band structure based on* $\pi h_{9/2}$ *orbital in* ^{199}Tl*"*

   Soumik Bhattacharya, S. Bhattacharyya, R. Banik, S. Das Gupta, A. Dhal, G. Mukherjee, S. S. Alam, Md. A. Asgar, T. Roy, T. Bhattacharjee, **A. Saha**, S. Mukhopadhyay, Debasish Mondal, Deepak Pandit, Surajit Pal and S. R. Banerjee.

   Proceedings of the **DAE Symp. Nucl. Phys. 61 (2016) 188**.

Bhattacharya, T. Roy, S. Das Gupta, A. Chakraborty, S. Bhattacharyya, D. Mondal, B Dey, D. Pandit, R. Palit, R. P. Singh, S. K. Das, M. Saha Sarkar, A. Goswami,S. K. Basu, S. Saha, S. Biswas, J. Sethi, D. Curien, J. Dudek, G.Duchene and G. de Angelis.

Proceedings of the **DAE Symp. Nucl. Phys. 58 (2013) 178**.

(D) Other Publications (in Peer Reviewed Journals)

1. *"VECC array for Nuclear fast Timing and angUlar corRElation studies (VENTURE)"*

   S.S. Alam, T. Bhattacharjee, D. Banerjee, **A. Saha**, Deepak Pandit, D. Mondal, S. Mukhopadhyay, Surajit Pal, P. Bhaskar, S.K. Das, S.R. Banerjee.

   Nucl. Inst. and Meth. in Phys. Research A 874 (2017) 103.

2. *"Measurement of β-decay end point energy with planar HPGe detector"*

   T. Bhattacharjee, Deepak Pandit, S.K. Das, A. Chowdhury, P. Das, D. Banerjee; **A. Saha**, S. Mukhopadhyay, S. Pal, S.R. Banerjee.

   Nucl. Inst. and Meth. in Phys. Research A 797 (2014) 19.

(E) In Symposia (not related to Thesis)

1. *"Lifetime measurement in neutron rich nuclei around ^{132}Sn"*

   S. S. Alam, D. Banerjee, **A. Saha** and T. Bhattacharjee.

   Proceedings of the **DAE Symp. Nucl. Phys. 62 (2017) 208**.

2. *"Determination of Fission Product Yield for Lifetime and Quadrupole Moment Measurement"*

   S. Nandi, G. Mukherjee, H. Pai, T. Roy, Md. A. Asgar, A. Dhal, R. Banik, Soumik Bhattacharya, **A. Saha**, S. S. Alam, S. Bhattacharyya, C. Bhattacharya, Pratap Roy, T.K. Ghosh, S. Kundu, K. Banerjee, T.K. Rana, R. Pandey, S. Manna, A. Sen, S. Pal, S. Mukhopadhyay,

S. Biswas, A. Chakraborty, S. Das Gupta, B. Dey, A. Goswami, D. Mondal, D. Pandit, T. Roy, R. P. Singh, M. SahaSarkar, S. Saha, and J. Sethi.

Under Review in **Jour. of Phys. G**.

(C) In Symposia

1. *"Angular Correlation and lifetime measurement in ^{150}Sm"*

   A. Saha, S. S. Alam, D. Banerjee, T. Bhattacharjee and S. R. Banerjee.

   Proceedings of the **DAE Symp. Nucl. Phys. 61 (2016) 300**.

2. *"Search for isomeric state in odd-odd ^{150}Pm"*

   A. Saha, D. Banerjee, T. Bhattacharjee, Deepak Pandit, S.S. Alam, P. Das, Soumik Bhattacharya, A. Choudhury, S. Bhattacharyya, A. Mukherjee, R. Guin, S. K. Das, S.R. Banerjee .

   Proceedings of the **DAE Symp. Nucl. Phys. 60 (2015) 98**.

3. *"Evolution of collectivity in ^{160}Yb"*

   A. Saha, T. Bhattacharjee, S. Rajbanshi, A. Bisoi, D. Curien, J. Dudek , P. Petkov, D. Banerjee, S. R. Banerjee, Soumik Bhattacharya, S. Bhattacharyya, S. Biswas, A. Chakraborty, G. de Angelis, S. K. Das, S. Das Gupta, B. Dey, G. Duchene, A. Goswami, D. Mondal, D. Pandit, R. Palit, T. Roy, M. Saha Sarkar, S. Saha, R. P. Singh, J. Sethi.

   Proceedings of the **DAE Symp. Nucl. Phys. 59 (2014) 268**.

4. *"Spectroscopy of low lying states of $N = 88$ ^{150}Sm"*

   A. Saha, D. Banerjee, T. Bhattacharjee, Soumik Bhattacharya, A. Chowdhury, P. Das, S. Bhattacharyya, A. Mukherjee, S. K. Das and S. R. Banerjee.

   Proceedings of the **DAE Symp. Nucl. Phys. 59 (2014) 134**.

5. *"Spectroscopy of $N = 90$ ^{160}Yb"*

   A. Saha, T. Bhattacharjee, D. Banerjee, S. R. Banerjee, S. Rajbanshi, A. Bisoi, Soumik

List of Publications

(A) Published in Peer Reviewed Journal

1. *"Role of p-induced population of medium-mass ($A \sim 150$) neutron-rich nuclei"*

   D. Banerjee, **A. Saha**, T. Bhattacharjee, R. Guin, S. K. Das, P. Das, Deepak Pandit, A. Mukherjee, A. Chowdhury, Soumik Bhattacharya, S. Das Gupta, S. Bhattacharyya, P. Mukhopadhyay, and S. R. Banerjee.

   Phys. Rev. C 93 (2015) 054904.

2. *"Excited negative parity bands in ^{160}Yb"*

   A. Saha, T Bhattacharjee, D Curien, I Dedes, K Mazurek, S R Banerjee, S Rajbanshi, A Bisoi, G de Angelis, Soumik Bhattacharya, S Bhattacharyya, S Biswas, A Chakraborty, S Das Gupta, B Dey, A Goswami, D Mondal, D Pandit, R Palit, T Roy, R P Singh, M Saha Sarkar, S Saha and J Sethi,

   Phys. Scr. 93 (2018) 03400.

3. *"Spectroscopy of low lying states in ^{150}Sm"*

   A. Saha, T. Bhattacharjee, S. S. Alam, D. Banerjee, M. Saha Sarkar, S. Sarkar, J. B. Gupta, P. Das, Soumik Bhattacharya, Deepak Pandit, R. Guin, S. K. Das, S. R. Banerjee.

   Nucl. Phys. A 976 (2018) 1.

(B) Under Review in Peer Reviewed Journal

1. *"Spectroscopy of tetrahedral doubly-magic candidate $^{160}_{70}Yb_{90}$: Search for atypical excitation patterns"*

   A. Saha, T. Bhattacharjee, D. Curien, J. Dudek, I. Dedes, K. Mazurek, A. Gozdz, S. Tagami, Y. R. Shimizu, S. Rajbanshi, A.Bisoi, G. de. Angelis, Soumik Bhattacharya, S. Bhattacharyya,

DECLARATION

I, hereby declare that the investigation presented in the thesis has been carried out by me. The work is original and has not been submitted earlier as a whole or in part for a degree / diploma at this or any other Institution / University.

Arunabha Saha

(Arunabha Saha)

STATEMENT BY AUTHOR

This dissertation has been submitted in partial fulfillment of requirements for an advanced degree at Homi Bhabha National Institute (HBNI) and is deposited in the Library to be made available to borrowers under rules of the HBNI.

Brief quotations from this dissertation are allowable without special permission, provided that accurate acknowledgement of source is made. Requests for permission for extended quotation from or reproduction of this manuscript in whole or in part may be granted by the Competent Authority of HBNI when in his or her judgment the proposed use of the material is in the interests of scholarship. In all other instances, however, permission must be obtained from the author.

Arunabha Saha

(Arunabha Saha)

7 Measurement of β-decay end-point energies ... 159

7.1 Introduction 159

7.2 Experimental details 160

7.3 Data Analysis and Results 161

7.4 Summary 164

8 Summary and outlook 165

8.1 Summary 165

8.2 Future Outlook 167

Bibliography 169

3.10.4 Indian National Gamma Array at TIFR, Mumbai . . . 63
3.10.5 VENUS array at VECC, Kolkata . . . 67
3.10.6 Data Analyzing Techniques . . . 70

4 Spectroscopy of low lying states in ^{150}Sm 85
4.1 Introduction . . . 85
4.2 Experimental Setup and Data Analyzing Techniques . . . 87
4.3 Results . . . 88
4.3.1 Decay scheme of ^{150}Pm: Decay Half Life and $\gamma - \gamma$ coincidence . . . 88
4.3.2 J^{π} assignments for the excited levels of ^{150}Sm . . . 105
4.4 Discussion . . . 111
4.5 Summary . . . 113

5 Spectroscopy of ^{160}Yb 115
5.1 Introduction . . . 115
5.2 Experimental Results . . . 117
5.3 Data Analysis and Results . . . 118
5.3.1 Selective Power of INGA, Reaction used and the limiting intensity branching for unobserved transitions . . . 118
5.3.2 Level Scheme of ^{160}Yb & the Band structures . . . 126
5.4 Discussions . . . 139
5.4.1 Comparision of $B(E2)_{\mathbf{in}}/B(E1)_{\mathbf{out}}$ ratios with neighboring nuclei . . . 141
5.5 Summary and Conclusions . . . 143

6 Excitation Function for ^{150}Nd(p,xn) reaction 145
6.1 Introduction . . . 145
6.2 Experimental Details . . . 146
6.3 Data Analysis and Results . . . 148
6.4 Discussion . . . 154

2.4.2 Historical Identification Criteria for Tetrahedral Deformation 31
2.4.3 Critical Comments Related to the Historical 'Necessary Condition' Criteria: Importance of Dipole Moments 32

3 Experimental Techniques and Data Analysis 35

3.1 Introduction 35
3.2 Production of Nuclear Excited Levels 37
3.2.1 High Spin States : Fusion Evaporation Reaction 37
3.2.2 Low Spin States : Decay Spectroscopy 41
3.3 Selection of Target-Projectile Combination 41
3.4 Calculation of Coulomb Barrier 43
3.5 Target Preparation 44
3.6 Beam selection, Target and Backing Thickness 45
3.7 Experiments related to the present thesis work 46
3.8 Features of γ ray spectroscopy 47
3.8.1 Gamma ray interaction with matter 47
3.8.2 Electromagnetic Transition Probabilities 51
3.8.3 Internal Conversion 52
3.8.4 Gamma detection efficiency 53
3.8.5 Energy Resolution of a detector 54
3.9 Features of β-decay 55
3.9.1 β-decay transition probability 55
3.9.2 Conservation of angular momentum 56
3.9.3 Parity 57
3.10 Experimental Tools employed 58
3.10.1 High-Purity Germanium (HPGe) detectors 58
3.10.2 Clover Detector 60
3.10.3 Low Energy Photon Spectrometer (LEPS) 62

Contents

Synopsis xxiii

List of Figures xxxviii

List of Tables xl

1 Introduction 1

1.1 Preface . . . 1

1.2 Outline . . . 3

2 Theory of Nuclear Structure 5

2.1 Introduction . . . 5

2.2 Microscopic Approach . . . 6

2.2.1 Mean Field Concept . . . 6

2.2.2 Spherical Shell Model . . . 9

2.2.3 Deformed Nuclear Shapes . . . 13

2.2.4 The Nilsson Model or The Deformed Shell Model . . . 15

2.2.5 Cranking (rotating) Model . . . 21

2.3 Macroscopic Approach : Collective Nuclear Models . . . 24

2.3.1 Nuclear Rotation . . . 25

2.3.2 Nuclear Vibration . . . 26

2.4 Exotic Tetrahedral Nuclear Symmetry . . . 27

2.4.1 Specific Nuclear Structure Effects Related to Tetrahedral Symmetry States . 30

parity band is compatible with that of a pear-shape octupole one-phonon vibration band whereas the even-spin band could be its analogue, in that the Y_{30}-vibration is replaced by Y_{32}-vibration. Such bands are said to have the 'pyramid-shape' oscillations.

The Jπ assignment of 3^- to the 1256 keV level has been confirmed from the E1 nature of the 617 keV transition, thereby assigning one more negative parity band in this nucleus. Also, as no connection of this 1256 keV level has been found with the 820 keV, 2_2^+ level in ^{160}Yb, the possibility of this band being the γ vibrational band, as per its earlier assignment, is negated. The higher spin states of one of the earlier known positive parity band are confirmed. However, assignment of spin-parity to this band was not possible with the statistics gathered in the present experiment. Also, the connection of this band to the 1292 keV, 2_3^+ level could not be confirmed, thus, negating the possibility of this band being the β band in ^{160}Yb. The present work suggests future experiment for finding the β and γ bands and to search for stable tetrahedral deformation in this nucleus, which could not be established in the present work.

In conclusion, the decay spectroscopy of N=88 ^{150}Pm and in-beam prompt spectroscopy of N=90 ^{160}Yb have been done using VENUS and INGA array, respectively. The possible candidates for excitation based on γ vibration and $\beta\beta$ bands are identified in ^{150}Sm. Observation of several interconnected positive and negative parity levels indicate the co-existence of octupole and quadrupole shapes in ^{150}Sm nucleus. The β decay end point energies, corresponding to several decay branches of ^{150}Pm ground state, have been measured for the first time. The absolute cross section for the reaction ^{150}Nd(p,xnyp) has been measured for the first time in the present thesis. The level scheme of ^{160}Yb has been significantly modified owing to the observation of doubles and triples-coincidences and measurement of I_γ, R(θ), DCO and IPDCO ratios. Arguments are given towards the possible presence of the tetrahedral component (Y_{32}) vibrations around the ground state equilibrium in this nucleus.

IPDCO (Integrational Polarization Directional Correlation of Oriented States) by using conventional techniques. The DCO, R(θ) and IPDCO ratios have been extracted for the first time in the present work for some of the transitions. Moreover, relative intensities of certain gamma transitions along with their DCO, R(θ) and IPDCO values have been obtained for the first time in this work. Several fragments of the level scheme obtained in the present work differ considerably from the ones obtained in the earlier measurements. Due to a higher target-to-detector distance (i.e. increasing the single-hit probability through smaller aperture solid angle) and a larger number of Clover detectors, the INGA array is much more suitable, compared to the AFRODITE array (used in the most recent experiment) [BAR10] for detecting the triple gamma coincidences in the case of experiments for which the gamma multiplicity is of the order of 20. For these reasons, we were able to collect 6.1 x 10^9 prompt double-coincidence events (three times more compared to the data gathered in recent experiment by Bark et. al.) and 3.5 x 10^8 triple coincidence events, whereas the AFRODITE experiment reported none. These triple-coincidence events have been of utmost importance to us for disentangling many gamma multiplets that were reported in earlier works. Several inter-band transitions based on which band-mixing calculations were earlier done in the latest experiment by Bark et al. could not be confirmed from the present experiment. This observation makes it necessary to revisit those calculations. The intensity limits for the unobserved transitions could be estimated following the comparison of the present data with the known branching ratios for the levels where both the transitions are observed.

The even- and odd-spin negative parity bands in ^{160}Yb have been studied by comparing the reduced transition probability ratios with the similar bands in neighboring even-even rare earth nuclei. B(E2)/B(E1) ratios have been obtained for a pair of odd and even-spin negative-parity sequences which show certain similarities-but also differences- in terms of the Excitation, Alignment and Kinematic and Dynamical moment patterns suggesting their very different structures. The B(E2)/B(E1) ratios for the odd-spin negative-parity band is found to decrease slowly with decreasing angular momentum. The ratios estimated for the even-spin negative-parity band are found to be significantly higher compared to the odd-spin one. This tendency is similar, although not as dramatic as in the results in some of the neighboring nuclei. The behavior of the odd-spin negative-

and logft values have been estimated from the absolute intensities of the γ transitions for all the levels. The J^{π} assignment is done for the various excited levels of ^{150}Sm with the help of logft values and $\gamma - \gamma$ angular correlation measurement. Three γ rays were identified as pure ΔI=0 and two as pure ΔI=1 E1 transitions from the angular correlation measurements. Before assignment of J^{π} values to the unknown levels, the J^{π} value of the ground state of ^{150}Pm is taken as 2^{-} based on the experimental evidences available and a large basis shell model calculation. The β decay end-point energies corresponding to the decay from the ^{150}Pm$\rightarrow$^{150}Sm have been measured by using a $\beta - \gamma$ coincidence setup of two thin window Planar HPGe detectors and four Clover HPGe detectors of the VENUS array. The low lying levels of ^{150}Sm are studied in comparison to the existing experimental and theoretical findings. A variety of shapes and excitations having different degrees of collectivity are found to coexist in N=88 ^{150}Sm nucleus. In the present work, it is proposed that the 1505.2 keV 3_1^+ level is the second excited member for the γ band developed on the 1194.2 keV 2_3^+ level. This is based on the systematics of the 3_1^+ states of the γ band observed in the neighboring nuclei. It is also observed that the band-heads of both the β and γ bands in the N=88 nuclei come down in energy as a function of increasing proton number till Z=66. In this work, the third 0^+ level has been assigned to have a deformed structure compared to the spherical ground state of the nucleus. High E1 strength of few mW.u was found for the decay of 1166.1, 1^- and 1659.1, 2^- keV levels, thereby, characterizing them as developed due to Octupole excitation. A possible admixture of both reflection symmetric and asymmetric shapes and their co-existence is found in this nucleus from various connecting transitions, observed between the levels having octupole excitation and β, γ & $\beta\beta$ character.

In this present work, the spectroscopy of ^{160}Yb has been revisited in order to study the low and moderate spin structure of this N = 90 nucleus around A$\sim$160, by using the conventional gamma ray spectroscopic technique with the Indian National Gamma Array (INGA). The nucleus has been populated using the fusion evaporation reaction ^{148}Sm(^{16}O,4n)^{160}Yb at E_{beam} = 90 MeV. The gamma transitions have been detected using twenty Compton Suppressed Clover HPGe detectors and the level structure has been deduced from the measurements of double, and triple γ-coincidences, relative intensities, DCO (Directional Correlation of Oriented States), R(θ) (asymmetry ratio) and

experiment at VECC was performed using the in-house detector facilities involving Clover HPGe and Planar Ge LEPS detectors to study the low lying states of ^{150}Sm populated from β decay of ^{150}Pm.

During both in-beam and off-beam γ-spectroscopy experiments, a prior knowledge about the excitation function of the various possible reaction channels helps in the proper optimization of the beam energy. It becomes more crucial when the involved reaction channels have very low production cross section and is contaminated with other high yield reaction channels. In the present thesis work, in addition to the $\gamma-\gamma$ spectroscopy experiments as discussed above, the excitation functions of the ^{150}Nd(p,xnyp) reactions have been measured as the reaction of interest was ^{150}Nd(p,n) having very low cross sections compared to other neutron evaporation residues. The experiment was performed by using the stacked foil activation technique with a 97.65% enriched 150Nd target. Measurement was done up to 50% above barrier and down to 18% below the barrier using proton beam energy of 7-15 MeV from the VECC Cyclotron. The yield of suitable gamma rays emitted following the decay of relevant evaporation residues was determined using a 50% high-purity germanium (HPGe) detector. The (p,n) cross section was found to follow the expected trend with a maximum value of 63.7(4.9) mb at Ep$\sim$8.6 MeV. The (p,2n) cross section gradually increased with Ep and had a maximum contribution to the total reaction cross section after $E_p\sim$9.0 MeV. The (p,2n) residues were not found to be produced below 7.9 MeV. The (p,p'n) reaction channel also showed a reasonable yield with a threshold of $E_p\sim$12.0 MeV. The experimental data were corroborated with statistical model calculations using different codes, viz., CASCADE, ALICE/91, and EMPIRE3.1. All the calculations could reproduce the excitation function fairly well in the present energy range.

Using the idea about the excitation function of ^{150}Pm nucleus discussed above, the low lying states of ^{150}Sm have been studied through decay spectroscopy of odd-odd ^{150}Pm populated with ^{150}Nd(p,n)^{150}Pm reaction at E_{beam}=8.0 MeV using 97% enriched ^{150}Nd target. Decay half life is followed for the observed γ transitions and their coincidence relationships are studied with VENUS array comprising of six Compton suppressed Clover HPGe detectors. Twenty new transitions are placed, five tentative γ rays are confirmed and ten transitions are found to have altered placements; resulting in assignment of fourteen new levels to the decay scheme of ^{150}Pm. The β branching

the coexistence of reflection symmetric and asymmetric shapes in this nucleus. In contrast to the nuclear reactions, the β spectroscopy of ^{150}Pm could populate some unique levels in this ^{150}Sm nucleus. It might be worth revisiting such measurements with high efficiency arrays in order to investigate the excited levels in ^{150}Sm which are favorably populated from ^{150}Pm decay.

Most interestingly, the region around N=90, A 160 is also interesting with respect to the asymmetric λ=3 deformation. The N=90 nuclei around Gadolinium (Z=64) and Ytterbium (Z=70) having both proton and neutron numbers close to the tetrahedral magic numbers [DUD02, DUD06] are predicted to be among the most suitable candidate for the observation of the nuclear tetrahedral symmetry. This symmetry corresponds to the λ=3 spherical-harmonic component in the nuclear surface. The corresponding shapes have been predicted to occur in atomic nuclei by several theoretical calculations. Since the nuclear shapes are characterized by Octupole components, it is expected that there will be negative parity rotational sequences involved in the band structures built on top of collective Octupole-type vibrations. Theoretical calculations predict a possible competition between the Octupole Pear shape and Octupole Tetrahedral shape vibrations build on the prolate-deformed ground state configurations in these nuclei. Since tetrahedral symmetry involves the octupole deformation (α_{32}), it will be of importance to study the properties of the negative-parity bands. The negative-parity bands in several nuclei in A$\sim$150-160 mass region show the reduced transition probability ratios of the order of a dozen. This is atleast an order of magnitude more than the same ratio observed in the Actinide nuclei in which an experimental evidence of the stable octupole shapes in the ground-states has been found. In contrast, the same ratios measured in the close lying even-spin negative-parity bands are still at least an order of magnitude larger. The absolute transition probabilities or their ratios measured by using high efficiency γ-detector arrays may help in interpreting the underlying structure of these negative-parity bands.

For the present thesis work, the experiments were carried out at two of the major accelerator facilities in India, i.e., TIFR (Mumbai) and VECC (Kolkata) using different experimental setup based on different experimental objectives. For example, the experiment at TIFR was performed using the Indian National Gamma Array (INGA) comprising of twenty Clover High Purity Germanium (HPGe) detectors, for the population of low and moderately high spin states of ^{160}Yb whereas the

Synopsis

This thesis mainly encompasses the experimental investigations of the low and moderately high spin structure of nuclei around N=90 in the mass (A) $\sim$ 150-160 region using both heavy and light ion beams. The nuclei in the proton rich side of the N-Z plot, thus, the N = 90 nuclei around A$\sim$160, can be accessed using the HI beams. But it is difficult to populate the N = 90 nuclei around A $\sim$ 150 using Heavy Ion (HI) induced reactions and thus the Light Ion (LI) induced reactions and the β decay spectroscopy could be quite useful. In the present work, the N=88 ^{150}Sm (Z=62) and N=90 ^{160}Yb (Z=70) have been studied by using off-beam decay spectroscopy and in-beam prompt spectroscopy, respectively.

In the study of collective nuclear structure of atomic nuclei, the phenomenon of shape-phase transition with the addition of protons or neutrons has been of great interest for a long time. The samarium (Z=62) isotopes near N=90 lie in a region of shape change from spherical vibrator to deformed axial rotor [IAC98, IAC04, CAS98] with increasing neutron number with the presence of X(5) symmetry [IAC01]. This has led to this region of the nuclear chart being the focus of intense experimental and theoretical study. The study of the low lying level structure is an ideal testing ground for the study of the shape-phase transition and phase-coexistence for which the decay measurements could be quite useful [LID04, BHA13]. The existence of octupole correlation has been observed in ^{150}Sm nucleus following the measurement of lifetime and electromagnetic transition rates from the (n,γ) reactions [AND98, JUN93]. The $\gamma - \gamma$ coincidence experiment following the light ion induced fusion evaporation reaction [URB87, BVU13] has extended this observation to

5.4 Table showing the comparison of the reduced transition probability ratios $B(E2)_{in}/B(E1)_{out}$ (in 10^6 fm^2), for the selected lowest negative-parity bands in the Rare Earth nuclei close to the tetrahedral magic numbers Z=64,70 and N=90. Experimental data for nuclei other than ^{160}Yb are taken from Ref. [ENSDF]. The strong disproportions between the $B(E2)_{in}/B(E1)_{out}$ ratios originating from the even-vs.-odd negative-parity states is worth observing. 142

5.5 The B(E2)$_{in}$/B(E1)$_{out}$ ratios for odd- and even-spin negative-parity Band-5 and Band-6 of ^{160}Yb. 142

6.1 The details of the measured reactions and the characteristic γ-rays used for the measurements of CS. 151

6.2 The Reaction CS values obtained in the present work for the reaction ^{150}Nd(p,xnyp). 153

7.1 The β decay end point energies obtained in the present work with relevant details, as described in text. 162

List of Tables

3.1 List of Experiments carried out in the present work. 46

3.2 Classification of β-decay processes 58

4.1 The excited levels of ^{150}Sm, populated from β-decay of ^{150}Pm are listed along with the γ-rays de-exciting from these levels. The γ-rays and the excited levels assigned for the first time in the decay scheme of ^{150}Pm are shown in bold to guide the eye. The γ-rays are marked as: (i)'a' for new transitions observed in the present work; (ii) 'b' for the transitions with altered placement in the level scheme compared to the earlier β-decay work; (iii) 'c' for the tentative transitions known in ENSDF and confirmed in the present work; (iv) 'd' for the transitions confirmed in the present work that could not be placed in the earlier β-decay work and (v)'h' for the transitions with double placement. 91

4.2 Estimates of possible M2 admixure (δ) and B(E1) strength of the E1 transitions observed in the present work 110

5.1 Measured Branching Ratios for some of the observed transitions for which intensity could be measured. The comparison of the deduced ratios to that from the ENSDF database are also shown (see text). 121

5.2 Limiting value of branching ratios for majority of the unseen transitions. An attempt has been made to estimate the limiting value of the branching intensity ratio of transitions for which there exists another transition with known intensity decaying from the same energy level. All the values except the intensities of the unobserved transitions and branching ratio are truncated to first decimal place. 122

5.3 The spectroscopic results for the γ-transitions observed in the present experiment on ^{160}Yb. 126

6.3 The decay plots for the transitions characterising the decay of different evaporation residues formed at a particular beam energy as described in the text. 152

6.4 The extracted efficiency of the 50% HPGe detector used in the experiment. The efficiency of the detector at a distance of 7 cm and 15 cm from the detector has been shown in the bottom panel and top panel respectively with black square and circles. The solid and dotted lines in the two figures represent the fitted curve. 154

6.5 Excitation function for ^{150}Nd(p,xnyp) reaction. Experimental data points for (a)^{150}Pm, (b)^{149}Pm, (c) ^{149}Nd and (d) total CS are shown with filled $\circ$. The calculated values of CS obtained from the work of O. Lebeda *et al.*, are shown with $\star$s. Theoretical CS calculated from Empire3.1, ALICE/91 and CASCADE are shown with dotted, solid and dash dotted lines respectively. 155

6.6 Individual CS for different evaporation residues and total CS are plotted in logarithmic scale. Legends used are same as in Fig. 6.5. 156

7.1 The representative β spectra obtained for some of the decay branches of ^{150g}Pm $\rightarrow$ ^{150}Sm. The experimental data points have been shown with blue circles and the Red line shows the results obtained from Geant3 simulation. The FK plots are shown with the obtained end point energies. 163

7.2 The representative χ^2 plot for two of the β decay branches of ^{150g}Pm. The β decay end point energies obtained from χ^2 and FK analyses are indicated. 163

7.3 The systematics of the isomeric states in neighboring isotones of N=89 ^{150} Pm. The data is taken from ENSDF database [ENSDF]. 164

5.10 The γ-rays observed in the cube gates displayed in (a), (b) and (c) indicate the population of states with energy values ranging from 2365.1 to 4474.9 keV of Band-9. Due to the very weak indication of the 424.5 keV transition between 2789.9 keV and 2365.1 keV levels, as observed from the gate in panel (b), it is shown in bracket in the level scheme (see figure 5.2). Black arrows have been used to mark the in-band transitions. The spins of the Band-9 states could not be determined in this work. . 136

5.11 Population of states with spin value ranging from 12^+ to 18^+ of Band-10 are shown with the added cube gates of [(637 & 763) + (637 & 609)+ (637 & 630)+ (763 & 609)+ (763 & 630)+ (763 & 660)+ (609 & 630) + (609 & 660)+ (630 & 660)+ (587 & 785)+ (587 & 630)+ (785 & 630)+ (785 & 660) in keV]. All the γ-rays related to the de-excitation of this band are marked with their energies and the in-band transitions are marked with black arrows. 137

5.12 The upper panel shows the added cube gate made by all possible combinations (28 in total) of the in-band transitions of Band-5 confirming the presence of this band in the level scheme of ^{160}Yb. The lower panel shows the sum of all possible double gates (6 in total) placed on all the energies reported for Band-12 of Ref. [BAR10], *viz.*, 408 keV, 555 keV, 628 keV and 681 keV. Only background fluctuations are observed at the position of these energies (red arrows). Therefore, it is highly unlikely that these transitions are in coincidences to confirm the existence of Band-12. 138

6.1 The configuration of a typical stack is represented. The number, shape and size of the targets, foils and degraders were different in different stacks as detailed in the text. T1, T2 and T3 are the targets and Cu represents the monitor foil. 147

6.2 The total gamma spectrum taken with the 50% HPGe detector for the irradiated ^{150}Nd target with 15 MeV proton beam. The photopeaks marked with *, **, ***, **** belong to the decay of ^{150}Pm, ^{149}Pm, ^{149}Nd and the Al related or background γ-rays respectively. 150

5.6 The added cube gates show the γ-rays related to the de-excitation of Band-6 as observed in the present work. The top panel (a) shows the presence of three inter-band transitions (790.6, 902.9 and 1056.2 keV) decaying from Band-6 to the yrast band; the middle and bottom panels, (b) and (c) respectively, show all the intra-band transitions (355.9, 477.2 and 481.4 keV) of Band-6 and one inter-band transition (482.7 keV) decaying from Band-6 to Band-5. All the intra-band and inter-band transitions of Band-6 are marked with the symbol #. The transitions marked with asterisks could not be placed in the levels scheme of ^{160}Yb. Blue arrows have been used to mark the weakest and close lying γ-rays. 132

5.7 (a) The added cube gates made by all possible combination (28 in nos.) of the in-band transitions of Band-4. The positions for the unobserved transitions are indicated with red arrows and text. (b) The added cube gate made by all possible combination (28 in nos.) of the in-band transitions of Band-5. The positions for the unobserved transitions are indicated with red arrows and text. A part of the decay of Band-4 and Band-5 are also shown. 133

5.8 (a), (b) and (c) indicate the possible population of the 1256, 1743 and 2274 keV levels of Band-7 in the present experiment. Fig. (c) indicates that the population of the 821 keV, 1^- state could not be confirmed in the present work because of no/very weak indication of 435, 578 and 821 keV transition indicated by red arrows. 134

5.9 The added cube gates of [(243&534) + (243&935) + (461&870) + (243&870) (in keV)] is shown. The γ transitions observed in this added gates confirm the population of the odd-spin positive-parity Band-8 on top of the 1113.2 keV, 3^+ level and are marked with their energy values. Blue arrows have been used to mark close lying peaks. The 255 keV transition is observed in this added gates as this transition connects the positive parity Band-8 to the negative parity Band-3. 135

5.3 The added cube gates showing the transitions from Band-1 (top panel), Band-3 (middle panel) and Band-4 (bottom panel), populated in the present work. For Band-1, the added gates of [(243&395), (395&509), (509&589), (589&637), (637&587), (587&404), (404&484), (484&578), (578&664), (664&736), (736&796)(in keV)] was used. Similarly, the added gates of (216&399), (399&541), (541&654), (654&739), (739&688), (688&712)(in keV)] was used for Band-3 and the added gates of [(283&432), (432&562), (562&671), (671&748), (748&770)(in keV)] was used for Band-4. The observed transitions arising from the de-excitation of these three bands are marked with their energies. Blue arrows have been used to mark the weakest and close lying γ-rays. 124

5.4 The added cube gates showing the inter-band transitions decaying from Band-3 to Band-4. The ones at 213.6 keV and 483.0 keV, marked with asterisks, represent the decay from 12^- and 18^- levels of Band-3. 125

5.5 (top) The spectrum corresponding to the added cube gates of all six possible combinations of the intra-band transitions of Band-2, which are de-exciting the levels above (10^-), is shown. (bottom) The decay of Band-2 is also shown in the partial level scheme. The transitions shown with black arrows in the level scheme are clearly visible in the gated spectrum and are marked with black text. The transitions marked with red arrows in the levels scheme are the ones that were proposed by other authors but could not be confirmed in the present work. The position of these transitions in the gated spectrum are shown with red arrows and red text. The γ-rays shown in the gated spectrum and marked with * could not be placed in the level scheme of ^{160}Yb. The thickness of the transitions given in the decay scheme are not in proportion to their actual intensities. 131

4.10 The partial level scheme for ^{150}Sm, obtained in the present work following the β-decay of ^{150}Pm, is shown in three parts. Some of the levels are shown in more than one part to completely show the decay and feeding of a particular level. The thirteen new levels placed in the decay scheme and nineteen new transitions found in the present work are shown with red. The transitions for which the placement is altered are shown with blue. The tentative transitions that are confirmed in the present work are shown with green. Some of the levels are shown in bold to increase the visibility. 112

4.11 The systematics of the positive parity low lying levels in N = 88 Ce-Er nuclei. The levels those are assigned to the β band in a nucleus are coloured in blue and those to the γ band are coloured in red. The level energies are taken from NNDC. 113

5.1 The first part of the level scheme of ^{160}Yb showing the Yrast band, the positive parity bands and few of the negative parity bands are shown. The level scheme is divided in two parts for clarity. Band-5 is fully displayed on the second part (figure 5.2). The transitions which could be placed in the level scheme by our analysis including double gating on triple coincidence data have been shown in black arrows. Transitions which are proposed by other authors [BAR05, BAR10] using double-coincidence but could not be confirmed from the triple coincidence analysis of the present work are shown as red dotted lines and indicated in brackets; the unobserved levels are shown as red dotted (see text). The newly placed level and transition are shown as green. 119

5.2 The second part of the ^{160}Yb level scheme showing the Yrast band and the negative parity bands (all but Band-6, see figure 5.1). Band-6 and Band-8 are fully displayed in figure 5.1. Transitions reported by other authors [BAR05, BAR10] but unobserved in the present work are shown as red dotted lines and indicated in brackets; the unobserved levels are shown as red dotted (see text). The newly placed transition is shown as green. 120

4.5 Gated spectra for some of the transitions for which the placement has been changed in the level scheme of ^{150}Sm, based on $\gamma - \gamma$ coincidence and (a)1437 keV ($I_\gamma = 0.23$; from 2602.2 keV, 1^- to 1165.5 keV, 1^- level) gate, (b) 1848 keV($I_\gamma = 0.02$; from 2893.1 keV, 2^- level to 1046.0 keV 2^+ level) gate. 100

4.6 Gated spectra for some of the transitions which are doubly placed in the level scheme of ^{150}Sm. (a) 1658 keV transition de-exciting both the 1658.2 keV and 2704.2 keV levels. This is also a new transition observed in the present work. (b) 1940 keV transition de-exciting the 2987.5 keV and 3105.9 keV levels. (c) 1964 keV γ-ray de-exciting both the 1964.8 keV level and 2704.9 keV level. The 1964 keV de-excitation from the 2704.2 keV level is proposed for the first time. (d)The 2680 keV gate shows that this transition also decays from the 3013.6 keV level in addition to the 2679.5 keV level proposed in earlier β-decay work [BAR70]. 101

4.7 Gated spectra for some of the transitions which were placed as dotted in earlier works [BAS13] but confirmed in the present work. (a) 999 keV ($I_\gamma = 0.05$; from 2069.7 keV, 2^- to 1071.3 keV, 3^- level) gate, (b) 2691 keV ($I_\gamma = 0.01$; from 3024.7 keV, 2^+ to 334.1 keV, 2^+ level) gate and (c) 1350 keV ($I_\gamma = 0.08$; from 1684.5 keV, 3^- to 334.1 keV, 2^+ level) gate confirm the transitions which were earlier placed as dotted. 104

4.8 Gated spectra for some of the transitions de-exciting the 2260.7 keV level for which the placement has been confirmed in the present work. 106

4.9 A comparision between theoretical solutions and the experimental data on $\gamma - \gamma$ angular correlation associated with the 334.1 keV ($2_1^+ \rightarrow 0_g^+$) E2 transition. Each measured angular correlation value (A_2, A_4) has been labeled with the energies of the two coincident gamma rays in keV. The ellipses, labeled according to the convention $I_1(L_1,L_2)J(L_3)I_2$, correspond to theoretical solutions of the angular correlations where the first correlated γ is an admixture of two multipoles L_1 and L_2. The single-multipole solutions are indicated by filled squares. The used convention is illustrated in the upper left corner of the figure. 109

3.23 Schematic drawing of a Clover detector showing the parallel and perpendicular scattering of compton scattered γ-rays. 80

3.24 Experimental setup at VECC used for the measurement of β-decay end-point energy. 83

4.1 The singles spectra showing all the transitions observed from the decay measurement. The 286 keV transition, marked with $, is identified to be arising from the decay of ^{149}Pm ($\tau_{1/2}$ = 53.08(5) h). The transitions marked with @ follow longer half lives and have been identified to be coming from background or the contaminations in the Al backing foil. 90

4.2 The decay half lives followed for some of the transitions observed in singles and placed in the level scheme of ^{150}Sm are shown. (a) 439 keV (773 keV, $4^+ \rightarrow$ 334 keV, 2^+), (b) 737 keV (1071 keV, $3^- \rightarrow$ 334 keV, 2^+), (c) 1324 keV (1658 keV, $2^- \rightarrow$ 334 keV, 2^+), (d) 1194 keV (1194 keV, $2^+ \rightarrow$ g.s), (e) 2260 keV (2260 keV, $1^- \rightarrow$ g.s), (f) 2529 keV (2529 keV, $1^- \rightarrow$ g.s), (g) 421 keV (1194 keV, $2^+ \rightarrow$ 773 keV, 4^+), (h) 1658 keV (1658 keV, $2^- \rightarrow$ g.s), (i) 2070 keV (2070 keV, $2^- \rightarrow$ g.s). Among these (a) - (g) are for the transitions which were already known in ^{150}Sm; (h) & (i) for new transitions that are placed in the level scheme of ^{150}Sm. 91

4.3 Gated spectra for some of the transitions which were already known in ^{150}Sm. (a) 876 keV (from 2069.7 keV, 2^- level to 1193.6 keV, 2^+ level) gate , (b) 565 keV (from 2069.7 keV, 2^- level to 1504.6 keV, 3^+ level) gate (c) 1647 keV (from 2812.7 keV, 2^- level to 1165.5 keV, 1^- level) gate and (d) 1214 keV (from 2259.6 keV, 1^- level to 1046 keV, 2^+ level) gate show the known de-excitations in ^{150}Sm. 96

4.4 Gated spectra for some of the new transitions which are placed in the level scheme of ^{150}Sm. (a)1296 keV (I_γ = 0.06; from 2367.2 keV 2^- level to 1071.3 keV, 3^- level) gate and (b) 1557 keV (I_γ = 0.05; from 2298.0 keV 3^- level to 740.6 keV, 0_2^+ level) gate show their placements in the decay scheme of ^{150}Pm. 97

3.8 Conservation of angular momentum in Gamow-Teller decay. 57
3.9 Schematic view of a Clover detector with anti-Compton shield. 61
3.10 Schematic representation showing the position of the Compton-suppressed clover detectors in the Indian National Gamma Array at TIFR [PAL15]. The angle of each of the clover detectors with respect to the beam axis is also shown in the figure. . . 63
3.11 Photograph of INGA at TIFR, Mumbai during June, 2013 64
3.12 Block diagram for the digital DAQ for 24 Compton suppressed clover detectors. It has six Pixie-16 modules; two LVDS level translator modules and one controller arranged in a single Compact PCI/PXI crate [PAL12]. 65
3.13 Photograph of the data acquisition system at TIFR during June, 2013 experiment. . 67
3.14 Photograph of VENUS array coupled with $CeBr_3$ detectors at VECC, Kolkata . . . 68
3.15 Block diagram for the generation of anti-coincidence VETO condition for the CLOVER detectors. 69
3.16 Block diagram of the pulse processing electronics for the offbeam experiment at VECC using VENUS array. 70
3.17 The figure indicates how energy calibration effects on the spectra of the four crystals of a Clover detector. The four panels on the left side shows the 1085 and 1112 keV gamma rays of ^{152}Eu source before calibration for the four crystals whereas the spectra on the right side indicates these spectra after calibration @ 1keV per channel. 74
3.18 Output of the "Effit" subroutine of the RADWARE package indicating the photopeak efficiency of the clover detectors in INGA at TIFR as a function of energy and fitted to the data obtained from the ^{152}Eu and ^{133}Ba radioactive sources. 75
3.19 Schematic drawing of a Clover detector. The four crystals are labelled A, B, C and D to explain the add-back procedure. 76
3.20 Variation of Addback Factor with $\ln(E_\gamma)$ for a Clover Detector for a source-to-detector distance of 25 cm. 77
3.21 Example of a level scheme constructed from the coincidence analysis of γ-rays. . . . 78
3.22 Angular correlation of 1173-1332 keV cascade of ^{60}Co. 80

2.9 Similar to the preceding one but for the protons, c.f. [DUD16]. Observe a big single-particle gap at Z=70, the proton number of the studied here Ytterbium nucleus. . . 30

2.10 Examples of the odd-spin negative-parity bands in two Gadolinium nuclei (proton number Z=64 can be considered as a magic-tetrahedral particle number) with the neutron numbers N=88 and 90 (neutron number N=90 is another magic-tetrahedral particle-number). Note that the E2 intra-band transitions were too weak to be observed below certain spins, and the presence of the rotational bands was deduced via the measured E1 transitions. The corresponding transition energies, $\Delta E_{\gamma-\mathrm{E2}}$, decrease linearly with decreasing spin, whereas the inter-band dipole transition energies, $\Delta E_{\gamma-\mathrm{E1}}$, do not change much with spin. [Experimental results are from http://www.nndc.bnl.gov/ensdf/] At this point it is *not* our intention to refer to the most recent data but rather present the results which have led in the past to the formulation of certain 'historical' necessary but not sufficient criteria of identifying tetrahedral symmetry. 33

3.1 Schematic illustration of heavy-ion collision types. 38

3.2 De-excitation process of a typical compound nucleus, produced in the present work. 40

3.3 Production Cross-section (in mb) of the residual nuclei at varying beam energies (in MeV) populated in the ^{16}O + ^{148}Sm reaction using PACE4 calculations. 42

3.4 Experimental set-up for the electrodeposition process used for preparation of targets. 44

3.5 An illustration of the photoelectric effect. An incident photon interacts with an atom and deposits its energy, causing the ejection of an electron. 48

3.6 An illustration of the process of Compton scattering. An incident photon with energy hν interacts with an electron in the medium and imparts some of its energy to it. The scattered photon, then, propagates away at an angle θ with respect to its original trajectory and with a lower energy hν', while the electron recoils away at some other angle ϕ and energy given by Eq. 3.12 49

3.7 Conservation of angular momentum in Fermi decay. 56

List of Figures

2.1 The evolution of single particle energies from a simple harmonic oscillator potential to a realistic shell model potential modified with addition of l^2 and $\vec{l} \cdot \vec{s}$ term. Blue lines are intruder levels. 12

2.2 Various nuclear shapes in $(\beta - \gamma)$ plane. On the top left is shown the principal axes of the intrinsic frame. Figure taken from Ref. [HIL53]. Lunds conventions [AND76] have been used. 14

2.3 Asymptotic quantum numbers λ, Σ and Ω for the Nilsson model are shown. 17

2.4 Variation of single-particle energies of $i_{\frac{13}{2}}$ orbits with different projections K as a function of deformation 18

2.5 Nilsson diagram for N=82-126 shell. [NIL55] 20

2.6 Nilsson diagram for Z=50-82 shell. [NIL55] 21

2.7 The body-fixed coordinates (x_1, x_2, x_3) and the laboratory coordinates (xyx). 22

2.8 Single-particle neutron energy levels in ^{160}Yb as functions of the tetrahedral deformation α_{32} is shown, c.f. [DUD16]. These energies were calculated with the help of the Woods-Saxon Hamiltonian with the universal parameterization of Ref. [DDC78]. The Nilsson labels are given at the extremities of the horizontal axis. The numbers in the curly brackets represent the percentages with which the corresponding dominating harmonic oscillator basis wave functions are present in the illustrated solution wave-functions. The small values of these coefficients signify the strong mixing of all the basis-states including the parity mixing. Big 'tetrahedral' gaps at N=70 and N=90/94 deserve noticing as well as the presence of the four-fold degenerate levels marked with the full lines and double Nilsson labels. 29

presence of the 'tetrahedral' (Y_{32}) and 'pear-shape' (Y_{30}) vibrational structure is conjectured in this chapter. In Chapter 6, the measurement of the excitation functions of the (p,xnyp) reactions using stacked-foil activation technique have been discussed. In Chapter 7, the measurement of the β-decay end point energies corresponding to the various decay branches of ^{150}Pm$\rightarrow$^{150}Sm have been discussed. Finally, in Chapter 8, conclusion and future perspective of the present thesis has been envisaged.

In the framework of this thesis, spectroscopic investigations of two nuclei, i.e., ^{150}Sm (N=88) and ^{160}Yb (N=90) have been performed. The N=90 nuclei around A∼160 which lie in the proton rich side of the N-Z plot can be accessed using the Heavy Ion (HI) beams. But it is difficult to populate the N=90 nuclei around A∼150 using HI induced reactions for which the light ion induced reactions and/or the β decay could be quite useful. Prior to the study of nuclear structure of ^{150}Sm, an excitation function measurement for the ^{150}Nd(p,xn) reaction has also been performed as a part of this thesis which was of extreme importance in order to understand the relative population cross-sections of different residues. Also, an experiment on β decay end point energy measurement has been carried out in this thesis as a future perspective of studying the structure of the exotic nuclei in A∼150 region where several long-lived beta decaying isomers are known to exist.

1.2 Outline

The present thesis has been structured in the following manner. The general theories of nuclear structure have been discussed in brief in Chapter 2. The microscopic-macroscopic approach together with the exotic Tetrahedral Nuclear Symmetry are the main topic of discussion in this chapter. In Chapter 3, the various experimental techniques and the methods of data analysis have been discussed. This chapter includes discussion on production of nuclear excited states after selection of suitable target-projectile combination, various processes of gamma ray interaction with matter, details about detector efficiency and resolution, various types of detectors and arrays used in course of the present thesis work. Chapter 4 covers the discussion about the spectroscopy of low lying states in ^{150}Sm which includes production of the low lying states of ^{150}Sm from beta decay of ^{150}Pm using proton beam of 8 MeV using ^{150}Nd target. The J^{π} assignment to the various excited levels from *logft* analysis and angular correlation measurements have been discussed in this chapter. In this chapter, the various low lying levels of ^{150}Sm have been discussed in the light of the present experimental observations and informations about the other neighboring nuclei. In Chapter 5, the spectroscopic study of the N=90 ^{160}Yb nucleus, which is predicted theoretically as one of the most suitable candidate for the observation of λ=3 Tetrahedral Symmetry, have been discussed. The possible

topic of contemporary research interest in the field of nuclear structure. One of the central goals of nuclear physics is to come to a basic understanding of the structure and dynamics of the nuclei which can be achieved by studying the structure of the discrete quantum levels in a nucleus below the particle separation threshold. Gamma ray spectroscopy is a powerful technique to carry out such studies in low energy nuclear structure physics.

The present thesis comprises of experimental investigations of the low and moderately high spin structure of nuclei around N=90 in the mass $\sim$ 150-160 region using both heavy and light ion beams. This region around N=90 is interesting with respect to both λ=2 quadrupole and λ=3 octupole deformations. As one goes from N=88 to 90, a sudden increase in quadrupole collectivity is observed to take place in several nuclei (viz., Nd, Sm, Gd, Dy, Eb, Yb etc.) [RAM01]. This shape change of atomic nuclei from the spherical to the axially symmetric deformed was noted during early 1950s by Mottelson and Nilsson [MOT55] but still this phenomenon continues to be of great interest in the study of nuclear structure. At Z=62, While going from ^{148}Sm to ^{154}Sm [PAS86], transition from a vibrational to a rotational character has been observed experimentally. This shape changing phenomena continues upto Z=70 where another interesting observation regarding quadrupole deformation has also been observed. In these nuclei, an increase in Quadrupole collectivity [FEW85, JOH96] with rotational frequency followed by another decrease have been observed for which no theoretical explanation does exist in the literature. Strong evidence of pear shaped λ=3 octupole deformation has also been observed experimentally in nuclei around N=90 namely, ^{151}Pm (Z=61), ^{149,150,151}Sm (Z=62) and ^{153,155}Eu (Z=63) [BUT96, JAI98, URB90, BAS94, PEA94]. There are theoretical predictions which suggest that the N=90 nuclei around Gadolinium (Z=64) and Ytterbium (Z=70), having both proton and neutron numbers close to the tetrahedral magic numbers [DUD02, DUD06], are the most suitable candidates for the observation of the λ=3 nuclear tetrahedral deformation. Thus, it may be concluded that the region around N=90 is of substantial interest for understanding new shapes and excitations in the nucleus. Other than the variety of shapes and excitations, this region is also interesting with respect to the possible presence of long lived isomeric states [JAI98, SOO11, SOO12, KIR63, CAS75].

Chapter 1

Introduction

1.1 Preface

The atomic nucleus is a strongly interacting, many-body quantum mechanical system that exhibits a fascinating variety of shapes and excitation modes, from spherical to super deformed and from excitations of single protons and neutrons to collective vibrations and rotations of the nucleus as a whole. The study of nuclear structure attempts to elucidate the unifying mechanisms by which these rich patterns of behavior emerge from the common underlying strong nuclear interaction between the nucleons (protons and nucleons) that form the nucleus. While the nuclear structure have been well studied close to the 'valley of stability', investigations of exotic nuclei reveals the evolution of the nuclear shell structure as one moves in the isospin degree of freedom. Similarly, several important information about the nuclear structure can also be obtained by exciting the nucleus in the shape degree of freedom. A variety of different nuclear shapes have been observed and/or predicted that depend on the neutron to proton ratio and on the conditions of excitation energy or spin of the nucleus which helps in inducing deformation in the nucleus. Indeed, very few nuclei have a spherical shape in their ground state and a variety of shapes or deformations can be observed, often in the same nucleus. By the term 'nuclear deformation', one generally means λ=2 quadrupole deformation which can be of prolate, oblate and triaxial type. However, there can be other form of nuclear deformations too like λ=3 Octupoles and λ=4 Hexadecapoles which are

proportional to $(\Delta E_{\gamma-\mathrm{E2}})^5$. At the same time the inter-band $\Delta E_{\gamma-\mathrm{E1}}$ energies vary much less with the decreasing spin, or even remain approximately constant, with the possibility that the dipole transitions, whose probabilities are proportional to $(\Delta E_{\gamma-\mathrm{E1}})^3$, win in the competition. Thus at the bottoms of those bands, the only de-excitation mode for the rotational states will involve the E1-transitions to the ground-state bands not so much because of the vanishing quadrupole moments but rather because of the quickly decreasing E2-transition energies as opposed to those of the E1-type. This discussion brings us to an importance of the role of the dipole transitions (and possibly of the collective dipole moments) which seem to determine the de-excitation patterns of certain bands.

the illustrative results presented in Fig. 2.10 show the decreasing tendency only in terms of the ratio in Eq. (2.35).

Moreover, the simple transition-energy considerations disfavor the proposed scenario as a possible

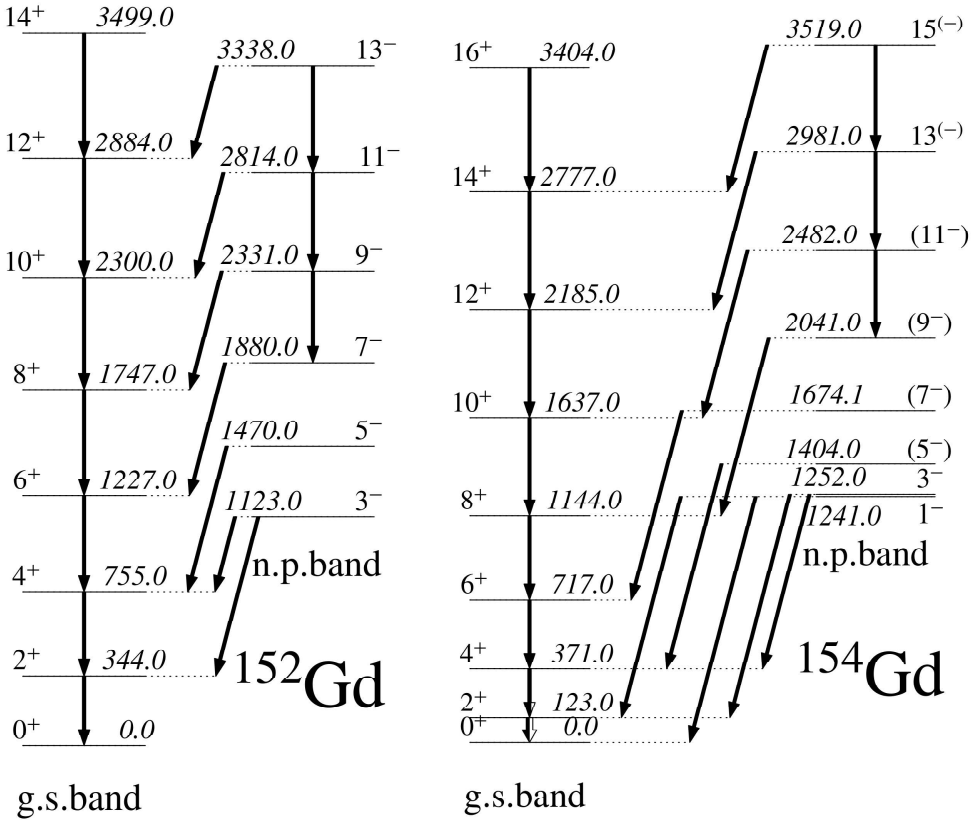

Figure 2.10: Examples of the odd-spin negative-parity bands in two Gadolinium nuclei (proton number Z=64 can be considered as a magic-tetrahedral particle number) with the neutron numbers N=88 and 90 (neutron number N=90 is another magic-tetrahedral particle-number). Note that the E2 intra-band transitions were too weak to be observed below certain spins, and the presence of the rotational bands was deduced via the measured E1 transitions. The corresponding transition energies, $\Delta E_{\gamma-\mathrm{E2}}$, decrease linearly with decreasing spin, whereas the inter-band dipole transition energies, $\Delta E_{\gamma-\mathrm{E1}}$, do not change much with spin. [Experimental results are from http://www.nndc.bnl.gov/ensdf/] At this point it is *not* our intention to refer to the most recent data but rather present the results which have led in the past to the formulation of certain 'historical' necessary but not sufficient criteria of identifying tetrahedral symmetry.

'finger-print' of tetrahedral symmetry in considered nuclei. Indeed, the lower the spin (the lower the energy within the band), the smaller the rotational $\Delta I = 2$ transition *energies*, $\Delta E_{\gamma-\mathrm{E2}}$, the latter decreasing linearly with spin – and the weaker the intra-band E2-transitions, whose probabilities are

According to the proposed scenario, these residual moments result from the presence of the relatively high collective angular momenta, which distinguish a direction in space thus breaking the tetrahedral symmetry. Conversely, with the spin decreasing along the band, the symmetry breaking decreases – so are the residual dipole and quadrupole moments. The results presented in Fig. 2.10 are compatible with the decreasing of the B(E2)/B(E1)-ratio

$$B(E2; I \rightarrow I-2)/B(E1; I \rightarrow I-1) \stackrel{I \rightarrow 0}{\longrightarrow} 0, \tag{2.35}$$

so that towards the bottoms of the bands, no E2 transitions are observed. This evolution could be interpreted as a result of the quadrupole moment approaching zero as should be expected in the case of approaching the exact tetrahedral symmetry limit. Relation (2.35) has, therefore, been in use as a kind of the first-step signal when trying to find the signs of the tetrahedral symmetry in nuclei.

It turns out that the just described scenario is found in several nuclei with the proton and neutron numbers close to the tetrahedral magic numbers both in the Rare Earth and Actinide nuclei. A few examples are shown in Fig. 2.10, in relation to the tetrahedral magic numbers Z=64 and N=90. Similar patterns have been observed in the nuclei with the proton numbers between the Z=64 and Z=70: ${}^{152}_{62}\mathrm{Sm}_{90}$, ${}^{154}_{62}\mathrm{Sm}_{92}$, as well as in ${}^{154}_{66}\mathrm{Dy}_{88}$, ${}^{156}_{66}\mathrm{Dy}_{90}$ and ${}^{160}_{66}\mathrm{Dy}_{94}$ and ${}^{164}_{68}\mathrm{Er}_{96}$.

2.4.3 Critical Comments Related to the Historical 'Necessary Condition' Criteria: Importance of Dipole Moments

It is worth emphasizing at this point that the above scenario is just a necessary but *not* sufficient condition to claim for the observation of the tetrahedral symmetry. For an experimental identification of the tetrahedral symmetry at the band-head configuration, it would be necessary that for a collective band with the energies $E_I \propto I(I+1)$ one finds

$$B(E2; I \rightarrow I-2) \stackrel{I \rightarrow 0}{\longrightarrow} 0, \tag{2.36}$$

tetrahedral symmetric nuclei can rotate collectively with the energy vs spin dependence approximately parabolic, like in majority of known collectively rotating nuclei, thus, $E_I \propto I(I+1)$, provided that the tetrahedral deformation is large enough. Another exotic structural is that at the exact tetrahedral symmetry limit, the nuclear collective dipole and quadrupole moments vanish. As a consequence, despite the presence of the collective-rotation one should not expect any presence of the usual collective E2-transition de-exciting these rotational states. The natural collective transitions de-exciting the tetrahedral symmetry states have an E3-, and might have an E4-character, since the only non-vanishing multipole moments with the multipolarity $\lambda \leq 3$ are the octupole ones in this case, $\lambda=3$, and since the tetrahedral symmetry group is a subgroup of the octahedral one, the latter involving the $Q_{\lambda=4} \neq 0$ moments.

The above observations complicate the experimental posing of the problem of identification of such states considerably, because E3 transitions are by orders of magnitude weaker as compared to the lower multipolarity transitions. Moreover, because of the fact that generally the E3 transitions connect states of opposite parities, one would need to populate and detect simultaneously the parity-doublet bands-and this over two, preferably three or more consecutive E3 transitions. The latter condition would lead to difficulty both in terms of population and detection.

The population via E1- or E2-transitions (which often dominates the feeding of the rotational high-spin levels, e.g., in heavy-ion *xn*-reactions) becomes impossible at the exact symmetry limit since, the dipole and the quadrupole moments vanish (as discussed above). Thus, the remaining modes of population can be either related to the collective octupole transitions, which are orders of mangitude weaker-or to the non-collective, particle-hole type or other radioactive de-excitation modes, which would require specifically designed reactions and experiments.

2.4.2 Historical Identification Criteria for Tetrahedral Deformation

Let us *assume* that a negative-parity rotational band associated with the tetrahedral symmetry minimum has been populated at sufficiently high spins due to the presence of the residual dipole and quadrupole moments.

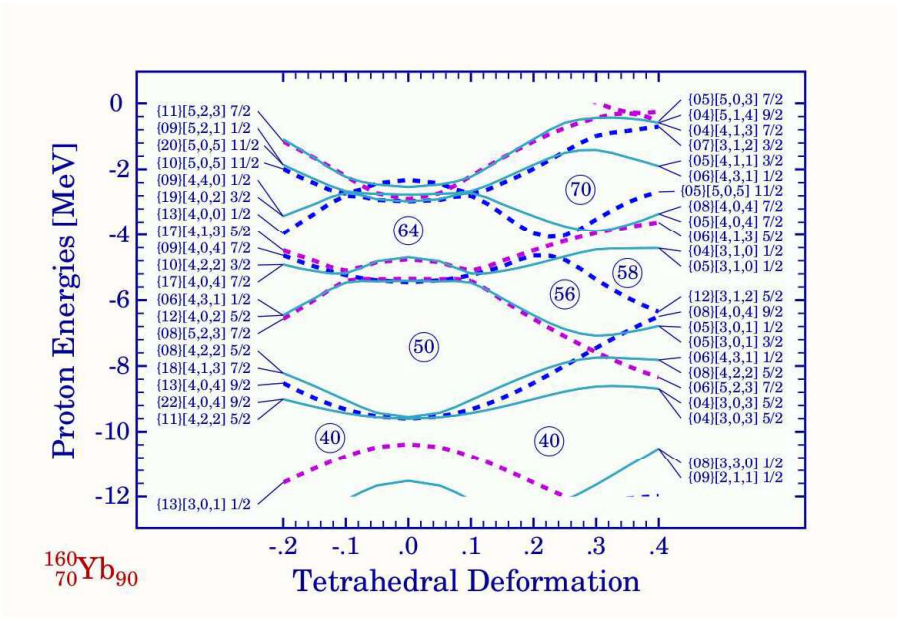

Figure 2.9: Similar to the preceding one but for the protons, c.f. [DUD16]. Observe a big single-particle gap at Z=70, the proton number of the studied here Ytterbium nucleus.

areas of the low nucleon-level densities in the single-nucleon spectra can be related to the mentioned four-fold degeneracies of the single-nucleon levels in the tetrahedral symmetric mean-field potentials, cf. e.g. Ref. [DUD09]. The realistic calculation results of the single nucleon levels show very strong shell effects at the non-zero tetrahedral deformations as illustrated in Figs. 2.8 and 2.9 [DUD16]. As it turns out, the shell-gaps of the order of 2.0-2.5 MeV for Z/N=70 and about 3 MeV for N=90/94 have very strong impact on the calculated new type total energy minima and thus deserve noticing.

2.4.1 Specific Nuclear Structure Effects Related to Tetrahedral Symmetry States

Nuclei with tetrahedral symmetry are non-spherical and therefore, their orientation in space can be defined. Consequently, such nuclei can rotate collectively, in contrast to the spherically symmetric quantum objects. Despite this property, all the three classical moments of inertia of tetrahedral symmetric bodies as well as the effective moment of inertia of the tetrahedral symmetric nuclei are identical. From the possibility of defining the nuclear orientation in space, it follows that the

Calculations of the total energy surfaces using realistic microscopic mean-field theory methods have been focussing on the Rare Earth nuclei since the early days of the extensive studies of the super-deformation at high-spins, from the eighties onwards, and thus, many examples of such calculations can be found in the literature. The results of the calculations obtained previously using the methods similar to those used in the present study can be found in e.g. in the early articles, Refs. [BYR87] and [WER92].

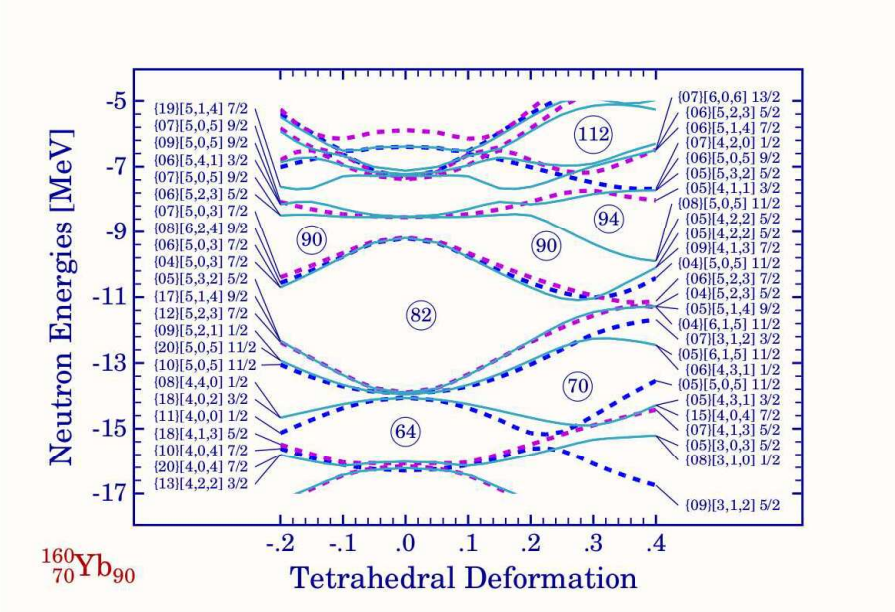

Figure 2.8: Single-particle neutron energy levels in ^{160}Yb as functions of the tetrahedral deformation α_{32} is shown, c.f. [DUD16]. These energies were calculated with the help of the Woods-Saxon Hamiltonian with the universal parameterization of Ref. [DDC78]. The Nilsson labels are given at the extremities of the horizontal axis. The numbers in the curly brackets represent the percentages with which the corresponding dominating harmonic oscillator basis wave functions are present in the illustrated solution wave-functions. The small values of these coefficients signify the strong mixing of all the basis-states including the parity mixing. Big 'tetrahedral' gaps at N=70 and N=90/94 deserve noticing as well as the presence of the four-fold degenerate levels marked with the full lines and double Nilsson labels.

Whereas tetrahedral symmetry has been observed abundantly in molecular physics, its observation in nuclear structure physics remains a challenge. It is known that, to the lowest order, the tetrahedral-symmetry nuclear-surfaces can be represented with the help of the non-zero α_{32} deformation parameters, cf. e.g. Refs. [LI94, DUD02]. The underlying relatively big energy gaps and the

highest mathematically permitted in the case of the deformed mean-field Hamiltonian of Fermions. One of the consequences of the exact T_d^D and/or O_h^D mean field symmetries is the vanishing of the nuclear quadrupole moments. Tetrahedral symmetric nuclei have a well-defined spatial orientation as they are obviously non-spherical. This implies an existence of collective rotational bands. However, these bands differ from those known in the literature since in the exact symmetry limit, the associated nuclear quadrupole moments vanish, implying vanishing of collective E2 transitions. From the mathematical point of view, the point group representing tetrahedral symmetry of geometrical surfaces, T_d, is composed of 24 symmetry elements. In the quantum mechanics of the fermion systems such as atomic nuclei, its so-called double point group partner, T_d^D, composed of 48 symmetry elements is applicable as an indicator of the tetrahedral symmetry of the corresponding Hamiltonian for nucleons. Moreover, tetrahedral group can be seen as a subgroup of the octahedral (O_h^D) point-group, $T_d^D \subset O_h^D$, the latter composed of 96 symmetry elements. The so-called octahedral deformations have been introduced in Ref. [DUD07], where the associated methods of nuclear energy minimization have been discussed as well.

Single-particle levels show strong variation in function of α_{32} and it has been demonstrated using realistic mean-field calculations that huge gaps may appear in the corresponding spectra, comparable to, or larger than the known spherical shell gaps. The predicted [DUD02, DUD03] *tetrahedral-magic numbers* for protons and neutrons are:

$$\begin{aligned} N &= 16, 20, 32, 40, 56, 70, 90, 112, 136. \\ Z &= 16, 20, 32, 40, 56, 70, 90, 112, 126. \end{aligned} \tag{2.34}$$

The corresponding nuclei should, in principle, be the best candidates for the tetrahedral symmetry. The tetrahedral shape correspond to a non-axial octupole shape. Consequently, if rotational bands are built on top of these configurations, they should lead to parity doublets. The bands should be seen at relatively low spins since the angular momentum alignment will tend to break the tetrahedral symmetry, and at relatively high excitation energy. Indeed, tetrahedral minima are predicted at about 1-2 MeV above the ground-states in most of the cases [SCH04].

mechanics, the energy levels of the nucleus can be described as

$$\begin{aligned} E_n - E_{n-1} &= \hbar\omega \\ E_\gamma(I \rightarrow I-2) &= \hbar\omega \end{aligned} \tag{2.33}$$

where, n is the principal quantum number, i.e., the number of vibrational quanta or phonons in the excited state and ω is the energy of the phonon. Each quadrupole phonon carries a spin and parity of 2^+. It should be noted that vibrational nuclei are not just limited to nuclei exhibiting quadrupole surface vibrations, as any mode of oscillation can exist. Octupole vibrations (λ=3 phonons) are generally observed in heavier nuclei [AHM93] and are more difficult to visualize. The first excited state in the doubly closed nucleus ^{208}Pb, is an example of an octupole vibrational state.

2.4 Exotic Tetrahedral Nuclear Symmetry

In the early literature, the term 'nuclear deformation' was associated mainly with the quadrupole axially symmetric elongation (prolate shapes with $\alpha_{20} \geq 0$, $\alpha_{22} = 0$), axially-symmetric flattening (oblate shapes with $\alpha_{20} \leq 0$ and $\alpha_{22} = 0$) and tri-axial deformation (with $\alpha_{20} \neq 0$ and $\alpha_{22} \neq 0$). But there can be another type of deformation which is known as $\lambda = 3$ deformation. The α_{32} term corresponds to the *tetrahedral symmetry* (T_d^D) whereas the α_{30} term relates to the *octahedral symmetry* (O_h^D).

The predictions of tetrahedral and octahedral symmetry are based on a very general analysis of symmetries of the nuclear mean-field and are inspired by the group-theory considerations. The unique 4-fold degeneracies of the single-particle levels characteristic of tetrahedral and octahedral symmetry of the ferimionic mean-field are thought to favor the appearance of large gaps in the shell structure, thus, leading to stable potential minima with the corresponding symmetry. By convention, the tetrahedral and octahedral symmetries are referred to as 'high-rank' symmetries because both lead to the appearance of four-fold degenerate nucleonic levels in the corresponding deformed mean-fields. It is worth emphasizing at this point that the four-fold degeneracies are the

where $\mathscr{J}$ is the moment of intertia of the system and

$$\omega = \frac{I}{\mathscr{J}} \; or \; \omega = \frac{dE}{dI} \tag{2.30}$$

is the rotational angular frequency. Combining Eq. 2.28 and 2.29 and transforming from a classical system to a quantum system, one can obtain a sequence of states with energies:

$$E_I = \frac{\hbar^2}{2\mathscr{J}} I(I+1) \tag{2.31}$$

The classical angular frequency ω defines a quantum of energy $\hbar\omega$:

$$\hbar\omega = \frac{dE(I)}{dI_x} \tag{2.32}$$

The term $I_x = \sqrt{I(I+1) - K^2}$ is the projection of the total angular momentum onto the axis of rotation, where K is the projection of the total angular momentum onto the axis of symmetry.

2.3.2 Nuclear Vibration

The above section introduces the concept that the nucleus can possess permanent deformation. However, another model which is closely associated with this picture is the vibrational model. It describes the observed nuclear excitation spectra in terms of the surface osciallation or vibration about an equillibrium shape. The surface coordinates are considered to be functions of time. In this case, vibrational quanta called *phonons* of multipolarity λ carry the energy. Dipole (λ=1) vibrations correspond to translations of the centre of mass of the nucleus and therefore, can not be produced by internal forces if protons and neutrons move together. Phonons of λ=2 produce low-energy quadrupole vibrations. The basis of vibrational excitation of a spherical nucleus is that the nucleus exists within a quantum harmonic osciallator potential and all equivalent excited states exist in terms of quadrupole phonon excitations of the ground state. Thus, from simple quantum

herently, rather than many independently acting particles. Two such descriptions are especially well-known: the *vibrational model* and *rotational model*. These models are usually discussed for even-even nuclei, which always have 0^+ ground states and usually have 2^+ first excited states. It is also possible to extend the discussion to odd-A and odd-odd nuclei by considering the coupling of one or a few nucleons to an even-even core.

2.3.1 Nuclear Rotation

Far from the closed shells, the large number of residual interactions due to the large number of valence particles, is often sufficient to produce a deformation in the nucleus. A common representation of the shape of such deformed nuclei is that of an ellipsoid of revolution, the surface of which is described by

$$R(\theta, \phi) = R_{av}\Big[1 + \beta Y_{20}(\theta, \phi)\Big] \tag{2.27}$$

β is the quadrupole deformation parameter and when $\beta > 0$, the nucleus has the elongated form of a *prolate* ellipsoid; when $\beta < 0$, the nucleus has the flattened form of an *oblate* ellipsoid. A deformed nucleus can generate angular momentum either by collective motion (rotation) in which all the nucleons rotate coherently about an axis perpendicular to the symmetry axis (called the rotation axis) or by the alignment of the intrinsic angular momenta of individual nucleons with the rotation axis. The total angular momentum of a rotating axially-deformed nucleus, $\vec{I}$, can be written as:

$$\vec{I} = \vec{R} + \vec{J} \tag{2.28}$$

where $\vec{R}$ is the angular momentum generated by the rotation of the core and $\vec{J}$ is the sum of the intrinsic angular momenta of the unpaired valence nucleons. Classically, the kinetic energy of a rotating rigid body is given by

$$E_{rot} = \frac{1}{2}\mathscr{J}\omega^2 \tag{2.29}$$

Hamiltonian is only invariant under space reflection, parity π and under a rotation of 180° about the rotation axis, x. The rotation operator is given by

$$\Re_x = e^{-i\pi j_x} \tag{2.22}$$

with the eigenvalues [BOH75]

$$r = e^{-i\pi\alpha} \tag{2.23}$$

where α is an additive quantum number known as signature [BOH75]. It is related to the total angular momentum by

$$I = \alpha mod\ 2. \tag{2.24}$$

For a system with an even nucleon number

$$\begin{aligned} I = 0, 2, 4, 6, ...\ if\ r &= +1\ (\alpha = 0) \\ = 1, 3, 5, 7, ...\ if\ r &= -1\ (\alpha = 1) \end{aligned} \tag{2.25}$$

while for a system with odd nucleon number

$$\begin{aligned} I = 1/2, 5/2, 9/2, ...\ if\ r &= -i\ (\alpha = +1/2) \\ = 3/2, 7/2, 11/2, ...\ if\ r &= +1\ (\alpha = -1/2) \end{aligned} \tag{2.26}$$

The rotational states are characterized by the parity π and the signature α.

2.3 Macroscopic Approach : Collective Nuclear Models

Beyond the microscopic calculations of the shell model and the Nilsson model, attempts to model nuclei have also been made using a macroscopic geometrical description of the nucleus as a whole. This is mainly useful for those nuclei for which many nucleons are actively determining the properties of the nucleus. Such models are called *collective models* of Bohr and Mottelson [BOH53] because they attempt to describe the nucleus from the standpoint of a collection of nucleons moving co-

coordinate system ($x_1x_2x_3$) is used which has a fixed orientation at all times with respect to the nuclear potential. It rotates with rotational frequency, ω, relative to the laboratory coordinate system (xyz), see Fig. 2.7. If we assume that the intrinsic coordinates rotate around an axis perpendicular to the symmetry axis and the symmetry axis coincides with the intrinsic axis, x_3, and the intrinsic axis, x_1, coincides with the laboratory axis, x, the total cranking Hamiltonian is given by

$$H^w = H^0 - \omega J_x = \sum_\mu [h^0_\mu - \omega j_{x\mu}] \tag{2.18}$$

where H^ω and h^ω_μ=h^0_μ-$\omega j_{x\mu}$ are the total and single particle Hamiltonians in the rotating frame, H^0 and h^0_μ are the total and single-particle Hamiltonians in the laboratory system, and J_x and $j_{x\mu}$ are the total and single particle angular momentum projections onto the rotation axis. The -$\omega j_{x\mu}$ term contains the Coriolis and centrifugal forces [SZY83, VOI83, BEN84]. The Coriolis force acts to align the angular momentum of the nucleons with the rotation axis [STE72, STE75]. The eigenvalues of the Hamiltonian, H^w, are known as Routhians. The total energy in the laboratory system is obtained as

$$E = \sum_\mu e^\omega_\mu + \omega \sum_\mu \langle \mu^\omega | \, j_x \, | \mu^\omega \rangle \tag{2.19}$$

where e^ω_μ denote the eigenvalues in the rotating frame. The projection of the total angular momentum onto the rotation axis can be determined by

$$I_x = \sum_\mu \langle \mu^\omega | \, j_x \, | \mu^\omega \rangle \, . \tag{2.20}$$

The slope of the Routhian is related to the alignment, i_x, i.e., the angular momentum gained by aligning a nucleon along the rotation axis. It is given by

$$i_x = -\frac{de^\omega_\mu}{d\omega}. \tag{2.21}$$

This relation makes it possible to compare the experimental aligned angular momentum with the theoretical Routhians. Because of the -ωj_x term, the time-reversal symmetry is broken. The

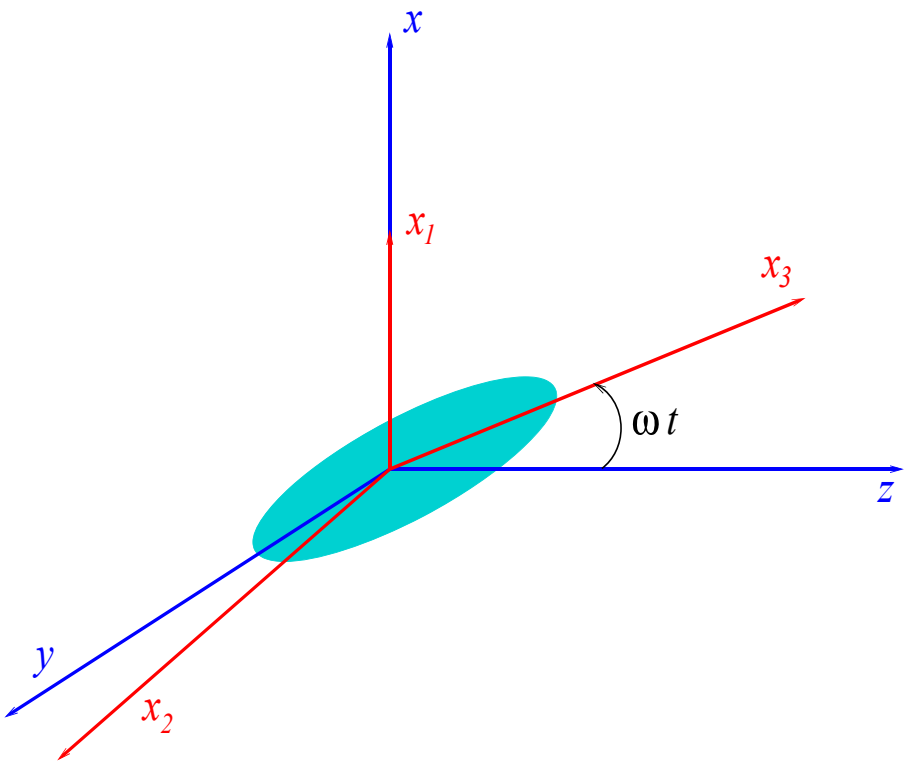

Figure 2.7: The body-fixed coordinates (x_1, x_2, x_3) and the laboratory coordinates (xyx).

nucleus can be treated as a classical rigid body (rotor) [BOH75]. The rotational spectrum of a pure collective rotation is given by [BOH75]

$$E_{rot}(I) = \frac{\hbar^2}{2\mathscr{I}} I(I+1) \tag{2.17}$$

where $\mathscr{I}$ is the moment of inertia and I is the total angular momentum. The effects of rotation on the single-particle states are described within the framework of cranking model. The behavior of the nucleons is studied by cranking (rotating) the nucleus with rotational frequency, ω, hence, the name cranking model. The first mathematical formulation of the model was made by Inglis [ING54, ING55] and has been further developed by Bengtsson and Frauendorf [BEN79B, BEN79A, BEN86]. The model provides a microscopic description of the influence of rotation on single-particle motion. The rotation is treated classically and the nucleons are considered as independent particles moving in an average rotating potential. To simplify the theoretical treatment, the intrinsic (body-fixed)

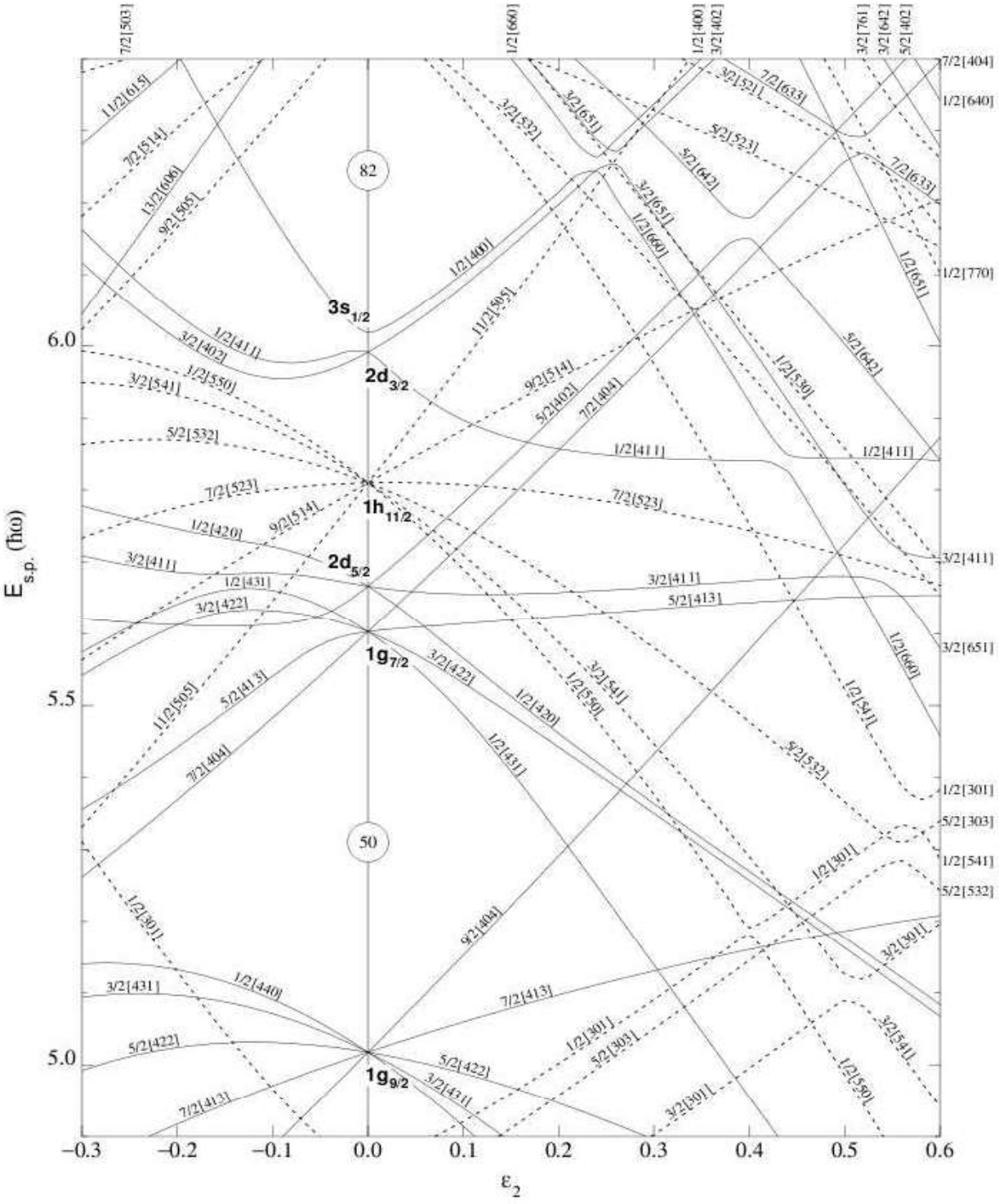

Figure 2.6: Nilsson diagram for Z=50-82 shell. [NIL55]

2.2.5 Cranking (rotating) Model

Within the framework of collective model, the nucleons are assumed to move coherently. They are paired and form the *nuclear core*. Rotation is one degree of freedom of collective motion. The

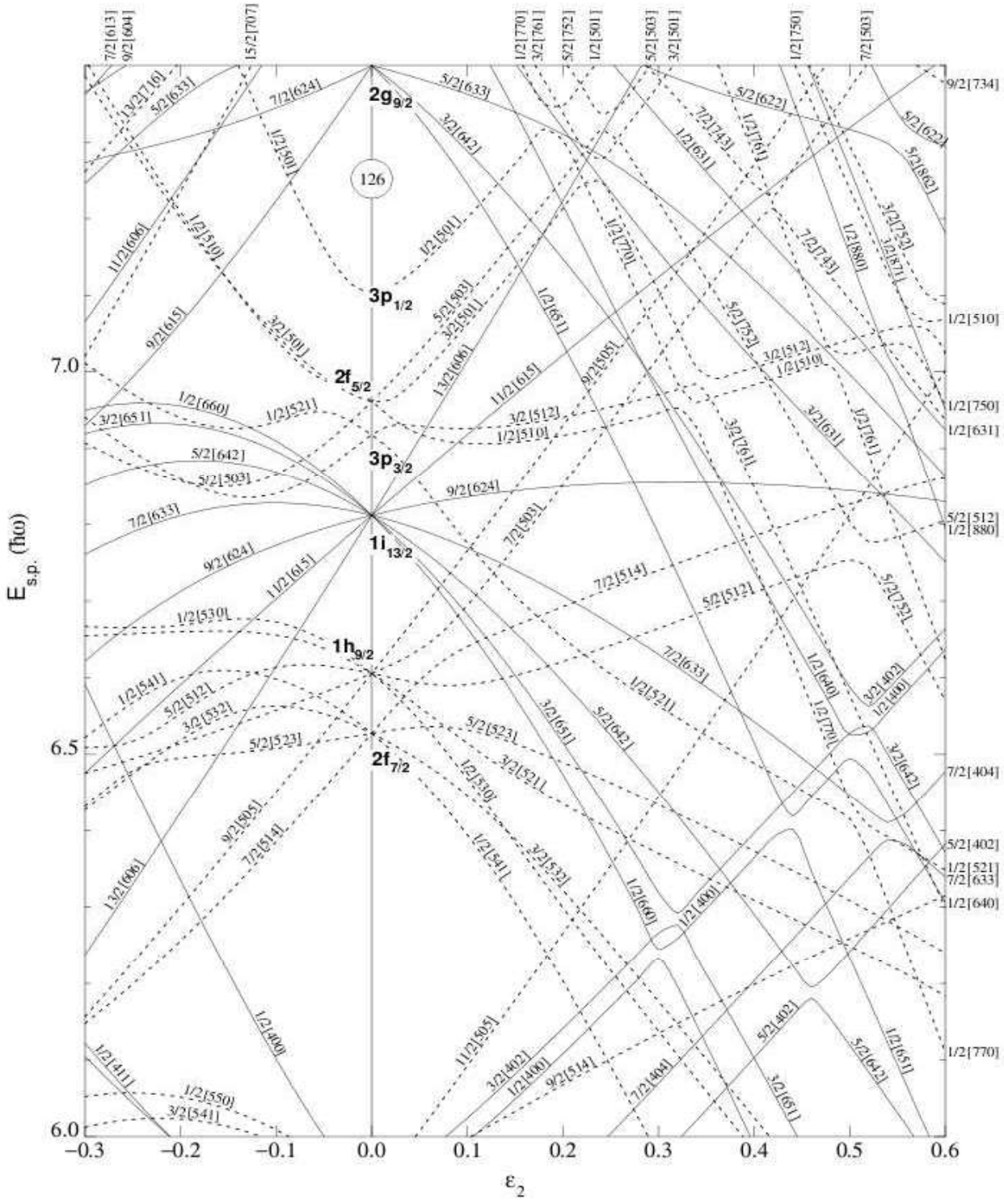

Figure 2.5: Nilsson diagram for N=82-126 shell. [NIL55]

2.6. A number of general features emerge from such a diagram :

(i) The spherical single particle levels of angular momentum j (labelled by n, l, j) split into $(2j+1)/2$ components for prolate ($\delta > 0$) and oblate ($\delta < 0$) deformation with two fold degeneracy of $\pm\Omega$.

(ii) Nilsson states are usually labelled by $[\mathrm{Nn}_z\Lambda\Omega]$ set of quantum numbers, though these quantum numbers are not conserved at small deformation.

(iii) The quadrupole field shifts the lower Ω values downwards for prolate shapes and the same level is shifted upwards for oblate shapes.

(iv) For larger deformation, because of the interaction of two levels with same quantum numbers Ω^{π} coming from different j-shells, the levels change their slope. This is evident from Fig. 2.5 and 2.6, that such levels having same quantum numbers can never cross.

(v) Another point of important consequence is the existence of gaps in the level scheme at larger deformation, i.e., stable configuration even for some deformed shape. This leads to the occurence of shell gaps at higher deformation resulting in superdeformed shape in nuclei at very high spin.

The Nilsson model has been highly successful in describing a large amount of data for nuclei with moderate to large ground state defomation.

$$K = \sum_i \Omega_i. \tag{2.16}$$

The ordering of the Ω-levels depends on the particular shape of the nucleus, since the orbital having lowest energy, has the highest interaction with the core. For prolate nuclei, the states with the lowest Ω values are most tightly bound, whereas for the oblate nuclei, the highest Ω-orbitals occur lowest in energy (see Fig. 2.4). As the nucleons obey the Pauli Exclusion principle, two levels with the same quantum numbers cannot cross. So, if two orbitals with the same Ω and π approach each

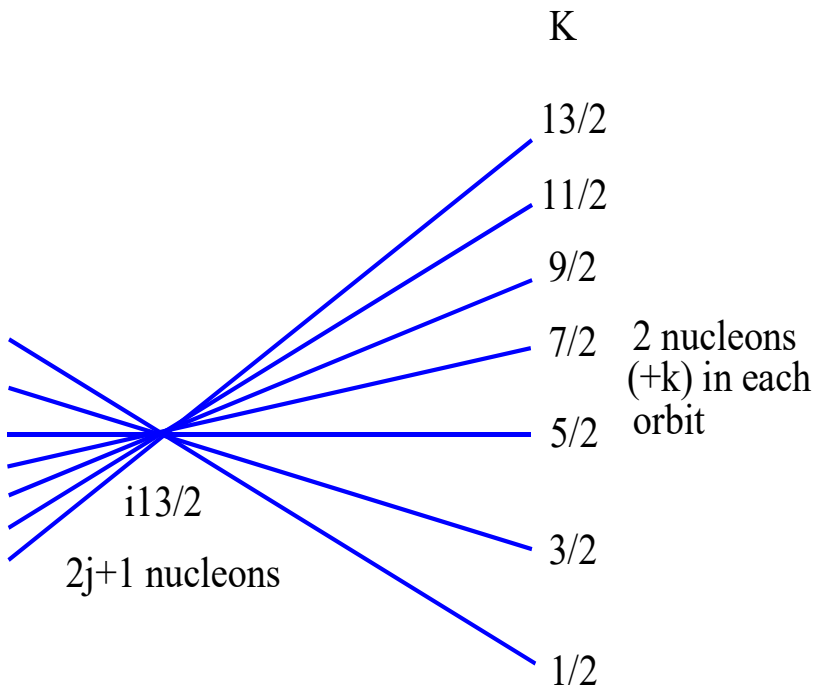

Figure 2.4: Variation of single-particle energies of $i_{\frac{13}{2}}$ orbits with different projections K as a function of deformation

other, they repel. On the other hand, an *intruder orbital* is not affected, as it has the opposite parity as compared to the other orbitals with which it may encounter. High Ω-orbits also remain rather straight, since there are no other orbits of the same Ω nearby. It is observed that the large single-particle gaps occur not only at the spherical shape but also at different deformations. An example of the Nilsson diagram for N = 82 to 126 and Z = 50-82 region are shown in Fig. 2.5 and

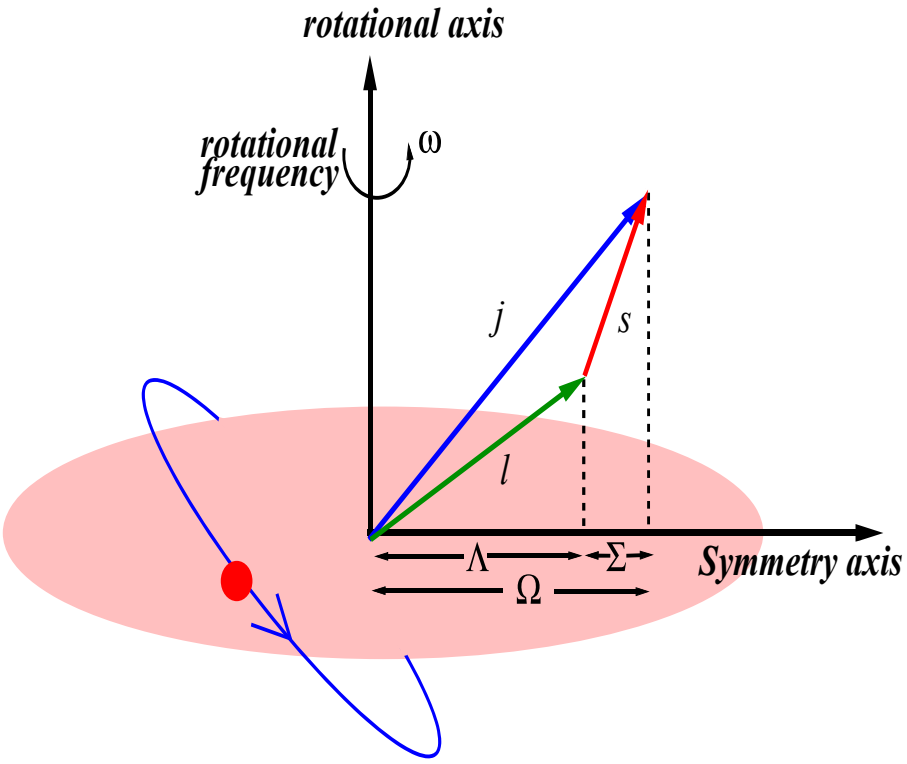

Figure 2.3: Asymptotic quantum numbers λ, Σ and Ω for the Nilsson model are shown.

Each orbital has the following nomenclature:

$$\Omega^{\pi}[Nn_z\Lambda] \tag{2.14}$$

where Ω is the projection of the single-particle angular momentum on the symmetry axis alongwith its parity satisfying

$$\pi = (-1)^N, \tag{2.15}$$

where N is the principal quantum number of the major shell, n_z is the number of oscillator quanta along Z-direction (symmetry axis) and Λ is the projection of the orbital angular momentum along the symmetry axis, such that Ω=$\Lambda \pm \frac{1}{2}$ depending on nucleon spin projection along the symmetry axis (see Fig. 2.3). It should be noted that the total projection of the spin of all the nucleons onto the symmetry axis, K, can be written as:

energy. The Nilsson diagram describes the evolution of the single-particle energies as a function of the deformation parameter.

The Hamiltonian required for a deformed nucleus, is very similar to the spherical shell model Hamiltonian, i.e., it contains a harmonic oscillator term (now allowed to be anisotropic), a spin-orbit term ($\vec{l}\cdot\vec{s}$) and a centripetal term ($\vec{l}\cdot\vec{l}$) as

$$\mathcal{H} = \frac{P^2}{2m} \; + \; \frac{1}{2}m[\omega_\perp^2(x^2+y^2)+\omega_z^2 z^2] \; + \; C\vec{l}\cdot\vec{s} \; + \; D\vec{l}\cdot\vec{l} \tag{2.12}$$

The third term in Eq. 2.12 is the well known $spin-orbit$ term needed to reproduce the magic numbers. The last term is added to produce a more realistic potential that accounts for the fact that for high l-values, the nucleons experience a deeper potential as compared to the harmonic oscillator and consequently, the energy levels of higher l-values are shifted down in energy.

The parameters C and D are parameters containing the oscillator frequency in the spherical potential. The deformation enters the equation through the oscillator frequencies, which are defined as : $\omega_z^2{=}\omega_0^2(\delta)(1\text{-}\frac{2}{3}\delta)$ and $\omega_\perp^2(\delta){=}\omega_0^2(\delta)(1{+}\frac{2}{3}\delta)$, where the parameter δ is named as the *parameter of deformation* by Nilsson and can be considered as the measure of elongation of the potential along the nuclear z-axis and is related to the previously mentioned β_2 parameter to the first-order as $\delta{=}\frac{3}{4}\sqrt{\frac{5}{\pi}}\beta_2$. Moreover, the examples of Nilsson diagrams which can be used to classify the observed single particle energies can be found in [MOT55] where the single particle energies are plotted as a function of a slightly changed deformation parameter, ϵ_2, which is related to δ as:

$$\epsilon_2 \; = \; (\delta \; + \; \frac{1}{6}\delta^2 \; + \; \frac{5}{18}\delta^2 \; + \; ...). \tag{2.13}$$

Negative values of ϵ_2 correspond to a contraction along one of the principal axes and results in an oblate shape. Whereas, a positive ϵ_2 corresponds to a contraction along two of the principal axes and produces a prolate shape. The different non-degenerate orbitals due to deformation can be labelled by a set of asymptotic quantum numbers, resulting from the symmetries of the nucleus.

2.2.4 The Nilsson Model or The Deformed Shell Model

Although the spherical nuclear shell model has been successful in describing nuclei near magic numbers, it fails to describe the structure of nuclei which have many valence nucleons outside the closed shells. There are important consequences of the residual interactions between such nucleons, most notably collective motion and nuclear deformation. One of the important effects of the nuclear deformation on shell model states is that the 2j+1 degeneracy of shell model states no longer persists. Nilsson and Mottelson developed a unified model to account for the effects of deformation on the shell-model states [NIL55]. The idea of an anisotropic oscillator was first introduced by Nilsson to be used as a modified shell-model potential which reproduced well the single-particle states in deformed nuclei. For nuclei far from closed shells, e.g., the rare earth nuclei or the actinides, strongly enhanced B(E2) values indicate the existence of stable quadrupole deformations. Hence, in these regime, a deformed potential is a good assumption.

In case of a spherically symmetric nucleus, it is impossible to allocate a uniquely defined azimuthal axis. Therefore, all possible angular momentum sub-states are degenerate in energy. This means that a nucleon will be attracted to rest of the nucleons by the same force, no matter where the nucleon is placed inside the nucleus. So, for a spherical nucleus, no preferential direction exists and all (2j+1) sub-states for a given j are degenerate in energy. However, such picture changes if the core is deformed axially instead of being spherical. Such an effect breaks the degeneracy in total angular momentum, and therefore, the (2j+1) sub-levels. One can define the symmetry axis and the m-components will be split according to the projection on the symmetry axis, Ω. Hence, the 2j+1 degeneracy is lifted. Only the time-reversed orbits $+\Omega$ and $-\Omega$ are degenerate. In the presence of many valence nucleons outside the closed shells, the residual proton-neutron interaction can drive the nucleus to an energetically favorable deformed state. In the alternative description of the Nilsson model, the nucleons move independently in a non-spherical potential, generating a deformed macroscopic shape. Intuitively, this can be understood as follows : if the matter distribution inside the core is not uniform, the energy of a nucleon orbiting the deformed core will depend on the overlap of the single-particle orbit and the core. States with different Ω will have different

where β_2 represents the magnitude of nuclear quadrupole deformation (which may be either elongation or flattening) and the nonaxiality, γ, represents the deviation of the nuclear shape from axial symmetry.

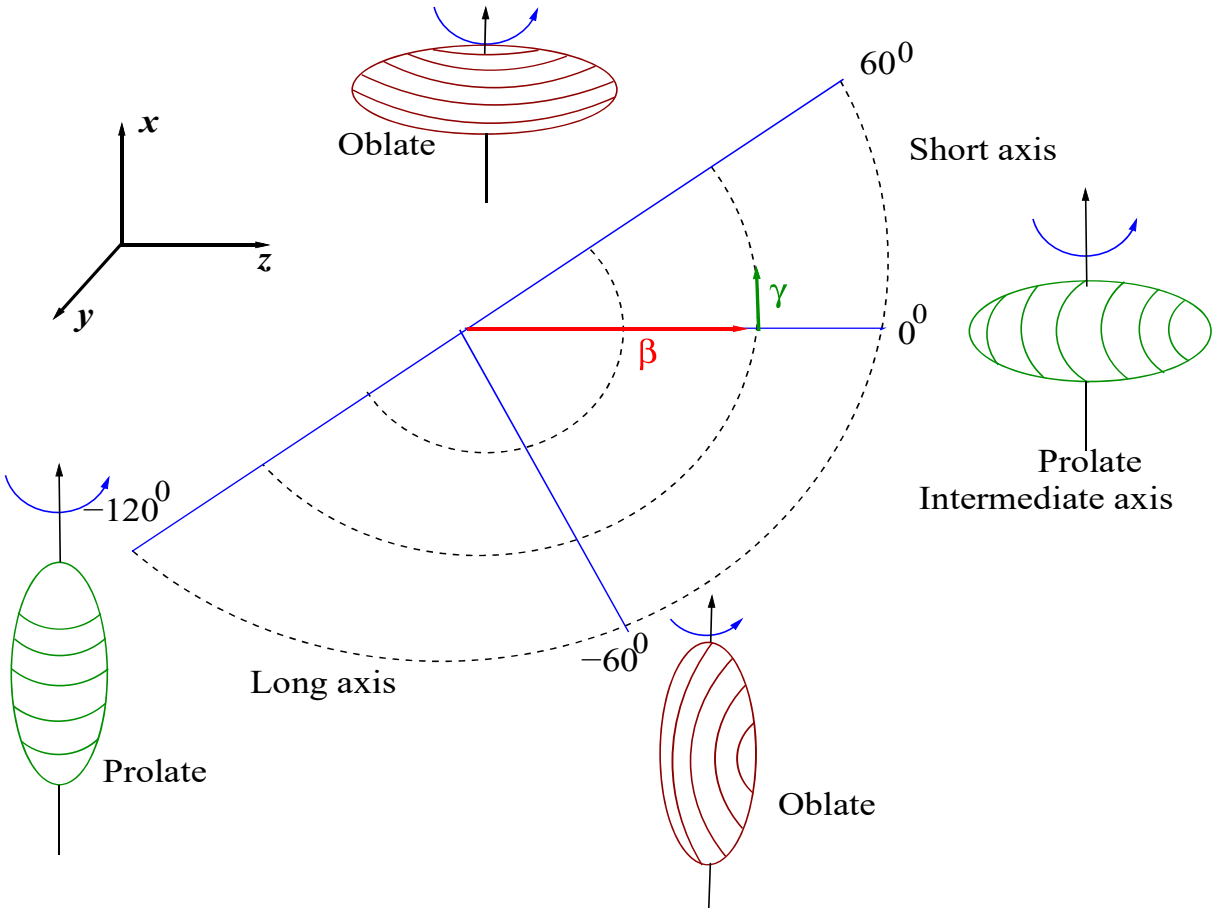

Figure 2.2: Various nuclear shapes in $(\beta - \gamma)$ plane. On the top left is shown the principal axes of the intrinsic frame. Figure taken from Ref. [HIL53]. Lunds conventions [AND76] have been used.

In Fig. 2.2, we have shown nuclear shapes in the $\beta - \gamma$ plane for λ=2. In this figure, Lund conventions [AND76] have been used. γ=0° (-60°) correspond to collective prolate (collective oblate), whereas the γ=60° (-120°) describes the non-collective oblate (non-collective prolate). If the value of λ is not a multiple of 60°, then triaxial shapes occur. Due to discrete symmetries, the interval $0° \leq \gamma \leq 60°$ is sufficient to describe all the quadrupole shapes.

forced down in energy due to the spin orbit interaction, hence it resides amongst levels of the lower major oscillator shell which has opposite parity. For example, $i_{13/2}$ positive parity orbital appears in the 82 to 126 shell along the negative parity orbits $1h_{9/2}$, $2f_{7/2}$, $2f_{5/2}$, $3p_{3/2}$ and $3p_{1/2}$. This unique orbit is important because it does not mix with its opposite parity neighbours in the multiplet. It is also sufficiently far from any of the same parity orbits, so that any possibility of mixing among these orbits is extremely weak. Therefore, configurations arising from these orbits are very pure.

2.2.3 Deformed Nuclear Shapes

The shape of a deformed nucleus can be parametrized by representing the nuclear surface via expansion of the spherical harmonics, $Y_{\mu\lambda}$, as:

$$R(\theta,\phi) = R_0\left[1 + \left\{\sum_{\lambda=0}^{\infty}\sum_{\mu=-\lambda}^{\lambda}\alpha^*_{\lambda\mu}Y_{\lambda}\mu(\theta,\phi)\right\}\right] \tag{2.9}$$

where $R(\theta,\phi)$ describes the radius length as a vector from the center of the nucleus to a point at the surface with polar coordinates (θ,ϕ) and R_0 corresponds to the radius of a spherical nucleus with the same volume. The $\alpha_{\lambda\mu}$ represents amplitude of each spherical harmonic component, λ is the multipolarity of the shape oscillations, μ is the projection of λ. For a shape parametrization, only terms with $\lambda \geq 2$ are considered. The λ=0,1 terms are called as monopole mode and dipole mode respectively. The term λ=1 corresponds to displacement of the center of mass and is eliminated assuming a fixed center of mass. If we consider λ=2 term in the expansion and choose the axes of the coordinate system to coincide with the axes of the body-fixed frame, then a_{21}=a_{2-1}=0 and a_{22}=a_{2-2} and the five coefficients of $\alpha_{2\mu}$ reduces to two real independent deformation parameters a_{20} and a_{22}=a_{2-2}. These two parameters can be expressed, in terms of the Hill-Wheeler [HIL53] coordinates β and γ as:

$$a_{2,0} = \beta_2\cos\gamma,\ \ a_{2,2} = \frac{1}{\sqrt{2}}\beta_2\sin\gamma \tag{2.10}$$

such that,

$$\sum_{\mu} \mid \alpha_{2,\mu} \mid^2 = a^2_{2,0} + 2a^2_{2,2} = \beta^2_2 \tag{2.11}$$

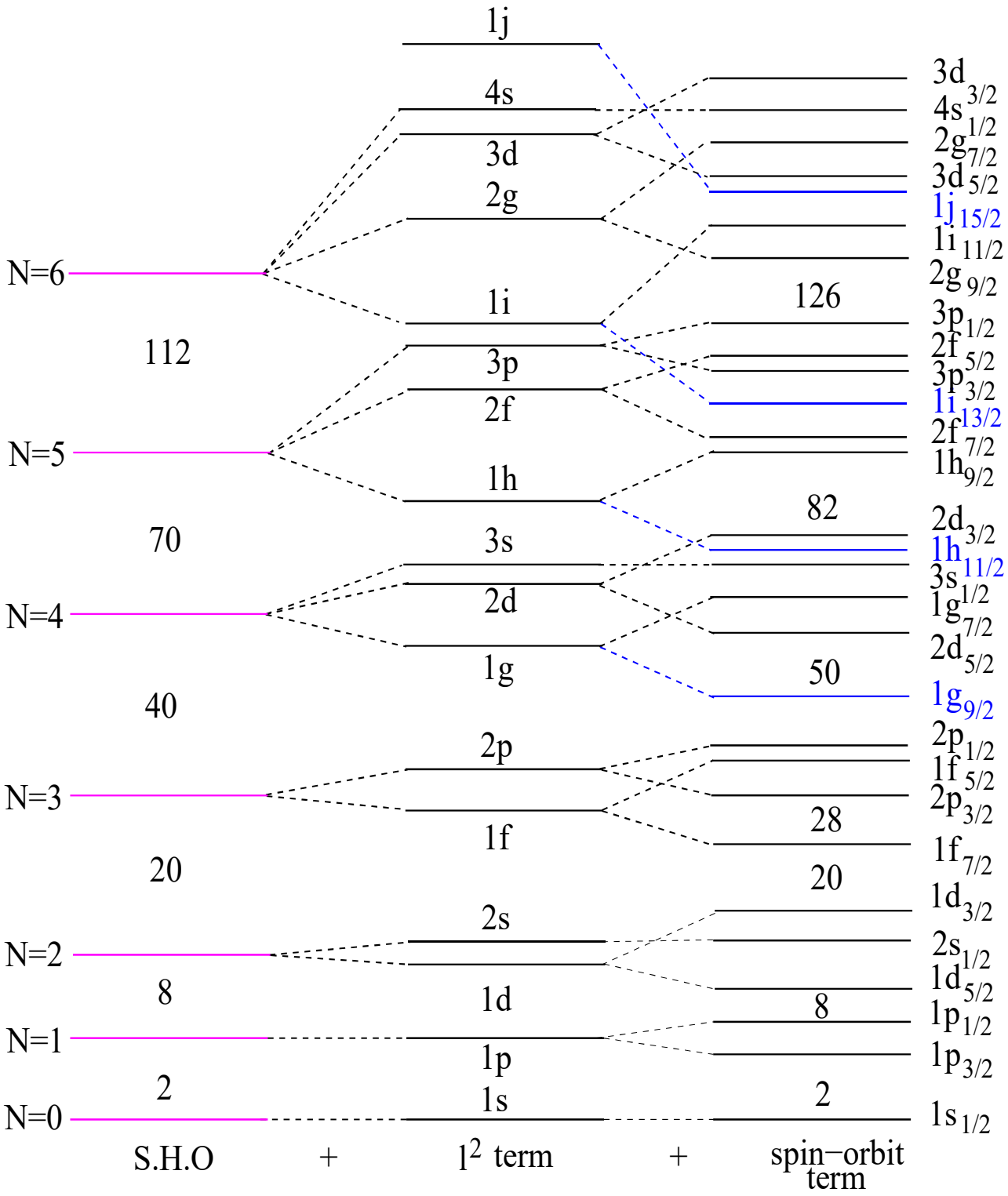

Figure 2.1: The evolution of single particle energies from a simple harmonic oscillator potential to a realistic shell model potential modified with addition of l^2 and $\vec{l} \cdot \vec{s}$ term. Blue lines are intruder levels.

aptly named as the *Spherical Shell Model*.

According to the shell model, the individual nucleons and single-particle excitation can be used to describe the energy levels and the structure of the entire nucleus. In all known nuclei with even number of protons and even number of neutrons, nucleons tend to pair up with opposite spin in such a way that the ground-state has an angular momentum 0, while the ground-state angular momentum of odd and doubly odd nuclei are determined by the orbits occupied by the unpaired nucleons. According to the nuclear shell model, an observed excited energy level in a spherical nucleus with an odd nucleon number can originate from a single particle excitation, i.e, when the valence particle is excited to a different orbit. Another way to create excited energy states in both-odd nuclei and nuclei with an even number of protons and neutrons, is to break an opposite-spin coupled pair. It is, then, possible for these two new valence particles to get excited into different orbits. However, near the magic nucleon numbers, complete filling of the major shells results in greater stability and hence, the energy spacing is relatively large ($\sim$ 1 MeV) which ultimately leads to stable nuclear configuration.

The spherical shell model is best suited for nuclei composed of a closed-shell nucleus plus a few valence nucleons outside, as it implies that nuclei can be described in first approximation as an ensemble of independent particles in a spherical mean field. As the number of nucleons deviates from that of the closed shell configuration, the nuclear shape no longer remains spherical, and as a result, the residual part of the Hamiltonian of Eq. 2.3 starts to play more prominent role in defining the nuclear behavior. So, it needs modification to describe the nuclei with many nucleons outside the closed shells. The residual interactions between these large number of valence nucleons may be more simply described in terms of the deformed potentials. Deformation effects all properties of a nucleus in a major way. The **Nilsson Model** can be used to calculate the total potential energy of a nucleus and thus, predict the existence of stable deformed shapes.

Intruder Orbitals

Simple inspection of the single particle energies shows that for high l-values, the splitting due to the spin-orbit interaction can push the orbit into an entirely different multiplet. The high-j orbital is

coupling, the observed shell gaps with large binding energy for the so called *magic* nucleon numbers are reproduced. The often used *Woods Saxon* potential (Ref. Eqn. 2.4) satisfies the requirements of a realistic nuclear mean-field potential (as described in last section). It is more flat at the bottom and the edge is not as sharp as in the case of a square well. The main effect of this potential is to break the degeneracy of the orbitals with different l in the harmonic oscillator but this potential still does not reproduce the magic numbers after 20. The solution to this puzzle lies in the *spin-orbit coupling*. Spin-orbit coupling ,i.e., the interaction between the orbital angular momentum and spin angular momentum occurs in Atomic Physics where the origin is magnetic field and the effect is a small correction. In case of nuclear binding, this effect is about 20 times larger, and it comes from a term in the nuclear potential itself which is proportional to $\vec{l} \cdot \vec{s}$, i.e.,

$$V(r) \rightarrow V(r) + \phi(r)\vec{l} \cdot \vec{s} \tag{2.7}$$

where

$$\phi(r) = b\frac{1}{r}\left(\frac{\partial f}{\partial r}\right) \tag{2.8}$$

'b' is a constant and ϕ(r) is a function of 'r' depending on f(r) which represents a spherically symmetric function giving the profile of the potential. Similar to the $j - j$ coupling scheme of atomic physics, the orbital and spin angular momenta of the nucleons combine to give a total angular momentum j which can take the values from j=l+$\frac{1}{2}$ to j=l-$\frac{1}{2}$. The spin-orbit coupling term leads to an energy shift proportional to j(j+1) - l(l+1) - s(s+1) where s=1/2. Moreover, an additional feature of this coupling in nuclei is that the energy split is in the opposite sense from its effect in Atomic Physics, i.e., the states with higher j have *lower energy* and vice-versa. When one of these $j = l + \frac{1}{2}$ orbitals appears in a shell lower than it would have been without the spin-orbit term, it is called an *intruder* orbital (see Fig. 2.1). The nucleons fill the neutron and proton levels in sequence, and the highest occupied level represents the *Fermi Surface* for that particle. With the inclusion of $\vec{l} \cdot \vec{s}$ term, the closed shells were fully explained. Mayer [MAY49] and Jensen [HAX49] were awarded the Nobel Prize in physics in the year 1963 for this work. The model introduced was

2. Square Well potential:

$$\begin{aligned} V(r) &= -V_0 \; for \; r \leq R \\ &= \infty \; for \; r > R \end{aligned} \tag{2.6}$$

When harmonic oscillator potential is used, there is a degeneracy between 2s and 1d, 2p and 1f, 3s, 2d & 1g etc which is clearly reflected in Fig. 2.1. Whereas, in case of a square well potential, the l-degeneracy of the oscillator is split up in such a way that 1d subshell falls below 2s, 1g falls below the 2d and so on. In case of the Woods-Saxon potential, the level ordering falls somewhere between the harmonic oscillator and the square well potential.

2.2.2 Spherical Shell Model

In the first half of the 20th century, a model was introduced to explain the observed shell structure in nuclei. This model is similar to the shell structure for the electrons in the atomic shells. Closed shells occur at proton and neutron *magic numbers* of 2, 8, 20, 28, 50, 82 and 126 where there are large gaps between successive nuclear orbitals. At these shell closures, the binding energy of the last nucleon is much larger than the corresponding value in the neighboring nuclei. Historically, it was the observation of the magic numbers that prompted the development of the shell model. After all, a proper model of the nucleus should be able to reproduce the signature of structure that the magic numbers provide. Examples of doubly magic nuclei include ${}^{4}_{2}\mathrm{He}_{2}$, ${}^{16}_{8}\mathrm{O}_{8}$, ${}^{40}_{20}\mathrm{Ca}_{20}$, ${}^{208}_{82}\mathrm{O}_{126}$ etc., where both proton and neutron are magic number and thus, are very stable. Despite the existence of strong interactions between nucleons, each nucleon is treated individually as an independent unperturbed orbiting particle constrained in a central potential which itself arises from the combined effect of all the nucleons. This potential is designed to approximate the average effect of individual interactions between the nucleons. At the same time, each nucleon is expected to retain its individual set of quantum numbers and corresponding single particle wave function. The aim of this potential, therefore, is to allow the construction of a suitable Hamiltonian capable of reproducing the sequence of nuclear shell closures. Using a simple potential which is somewhere in between the isotropic harmonic oscillator and a square well potential, combined with the *spin-orbit*

of the mean potential U is very important in order to predict the nuclear level energies accurately and should be so chosen that $\mathcal{H}_{res}$ is small and can be considered as a perturbation to $\mathcal{H}_{\circ}$. The potential should be such that

1. $\left(\frac{\delta V(r)}{\delta r}\right)_{r=0} = 0$
   which implies that a nucleon close to the centre of the nucleus will feel the nuclear force in a uniform manner.

2. $\left(\frac{\delta V(r)}{\delta r}\right)_{r<R_0} > 0$
   which means that the nuclear force gets stronger as one moves from the surface of the nucleus (at r=R_0) to the interior.

3. V(r)≈0 for r>R_0
   which means that the nuclear force weakens as one moves outward from the surface of the nucleus (at r=R_0).

A model potential which satisfies the above mentioned conditions is the *Wood-Saxon potential*, the analytic form of which is given by

$$V^{W.S}(r) = -\frac{V_0}{\left[1 + \frac{exp(r-R_0)}{a}\right]} \tag{2.4}$$

where R_0=$r_0A^{1/3}$, V_0 ≈50 MeV; a=0.5 fm and r_0 ≈1.2 fm. The *disadvantage* of using a Wood-Saxon potential is that the Schrödinger equation can not be solved analytically using this potential and hence, the following two approximations are often used for qualitative considerations and for sake of simplicity in calculations:

1. Harmonic Oscillator (HO) potential:

$$V^{H.O}(r) = -V_0\left[1 - \left(\frac{r}{R_0}\right)^2\right] = \frac{m}{2}\omega_0^2(r^2 - R_0^2) \tag{2.5}$$

where, the Hamiltonian $\mathcal{H}$ is of the form :

$$\mathcal{H} \;=\; \sum_{i=1}^{A} T_i \;+\; \sum_{i<j}^{A} V_{i,j} \tag{2.2}$$

with A = N + Z is the total number of nucleons, T_i is the kinetic energy of the i-th nucleon and $V_{i,j}$ is the short range two-body nucleon-nucleon interaction potential. Except for the lightest nuclei, Eq. 2.2 cannot be solved exactly. A drastic simplification is offered by the following basic properties of the nucleon-nucleon interaction :

∗ The attractive strong force is a short-range force.

∗ The saturation of the binding energy per nucleon around a value 8 MeV indicates that the nucleons can interact only with their nearest neighbors.

∗ Nuclear density is almost constant inside and is independent of the number of the nucleons inside.

∗ Plenty of evidences show that nuclei with a certain number of protons or neutrons are more stable than others. These number of nucleons, known as *magic numbers* provide an insight into the fact that the nucleus has a shell structure, similar to that of the electrons surrounding the atom in the *Bohr Model*.

Combined with the *Pauli Exclusion Principle*, these properties validate the idea that all the nucleons move as independent particles within an average potential U (also known as *mean field*) generated by the nucleons themselves such that $U \;=\; \sum_{i=1}^{A} U_i$. The Hamiltonian eqn3.2 can, then, be rewritten as:

$$\mathcal{H} \;=\; \sum_{i=1}^{A}[T_i \;+\; U_i] \;+\; [\sum_{i<j}^{A} V_{i,j} \;-\; U_i] = \mathcal{H}_\circ \;+\; \mathcal{H}_{res} \tag{2.3}$$

where $\mathcal{H}_\circ$ reflects the independent movement of the nucleons and the residual interaction $\mathcal{H}_{res}$ corrects for the fact that the nucleons do not move completely independent of each other. Unfortunately, while various properties of the nuclear force are known, the exact form of the nuclear potential U is not known. For this reason, a great deal of effort has gone and continues to go into discovering ways to model the nucleus despite not knowing the nuclear potential. The exact form

approach and they study phenomena that involve the nucleus as a whole.

Apart from such an approach, there exist a class of *independent particle models* or *microscopic approach* that assume that the Pauli principle restricts the collisions of the nucleons inside the nuclear matter, leading to a larger mean free path. The several forms of shell models belong to this class. Today we have a clear notion that the nucleus can exhibit both collective and independent particle phenomena and that each model finds its usefulness in the explanation of a specific group of nuclear properties.

2.2 Microscopic Approach

The ultimate goal of nuclear physics is to describe any nuclear structure from the basic interactions between the nucleons. This is called the microscopic or $ab-initio$ approach of nuclear physics. Such a model is able to explain nuclear microscopic properties like spin-parity and energy of the single particle states etc., as it is based on the constituent nucleons forming the nucleus. In the following sub-sections, we will take a closer look at some of the relevant topics on microscopic models, with the introduction of some ingredients for building up the average single-particle potential and the residual interaction.

2.2.1 Mean Field Concept

The atomic nucleus consists of two types of fermions : protons and neutrons, confined within a very small spatial volume (the nucleus measures 10^{-14} to 10^{-15} m in diameter) to form a stable system in the presence of a strong attractive nucleon-nucleon interaction. There are two major problems in the description of nuclei. Firstly, one has to tackle a complex many body quantum problem. Secondly, our knowledge on the extrapolation of two-body interaction into the many-body problem is incomplete. A fully analytic microscopic calculation of nuclear properties requires a solution of the many-body non-relativistic Schrödinger equation given by,

$$\mathcal{H}\Psi(1,2,...,A) \;=\; E\Psi(1,2,...,A) \tag{2.1}$$

Chapter 2

Theory of Nuclear Structure

2.1 Introduction

The atomic nucleus is a many-body quantum system, consisting of A particles (i.e., Z protons and N neutrons) bound by the strong nucleon-nucleon interactions. The Coulomb repulsion between the charged protons along with the weak interaction that governs the β-decay process, also play a significant role for the proton and neutron distributions inside the nucleus. An important characteristic of a nucleus is the ordering and energy separation of its excited states. A nucleus can be excited in energy and angular momentum in two different ways, either by few-nucleon excitation or by a coherent movement of many of its constituent nucleons. For the explanation of new nuclear phenomenon, the development of new theoretical models has always been necessary. In this chapter, the theoretical descriptions relevant to the physics discussion related to the various experimental observations made during the present thesis related work will be reviewed.

It is almost impossible to obtain the properties of a system of A nucleons starting from its constituents and their underlying interactions, and hence there is always a need to use models that represent some aspects of the real problem. Theoretical models are essentially of two classes. The first class of models assume that the nucleons interact strongly in the interior of the nucleus and that their mean free path is small. This is a situation identical to that of molecules of a liquid, and the liquid drop model belongs to this first class. These are called as *collective models* or *macroscopic*

plots have been fitted with a linear function y=a.x+b in order to determine the respective end point energies. The relation E_p = b/a + d has been used for this purpose, where E_p is the β-decay end point energy and 'd' is the correction factor for the degradation at the Be window of the planer detector. The correction factor was calculated by using the built-in routine 'Elec-Stop' included in the spectrometer code LISE [TAR03, KAN95]. The pulse processing for the above two coincidence measurements was performed by using sixteen channel Mesytec high resolution Shaper and Amplifier module and VME DAQ system LAMPS [LAMPS] with the 32 bit Mesytec ADC (MADC-32).

3.10.6.8 The Chi-Square Distribution

The Chi-square distribution is particularly useful for testing the *goodness-of-fit* of theoretical formulae to experimental data. Mathematically, the Chi-square fit is defined in the following manner. Suppose, we have a set of n independent random variables, x_i, distributed as Gaussian densities with theoretical means μ_i and standard deviations σ_i, respectively. The sum

$$u = \sum_{i=1}^{n} \left(\frac{x_i - \mu_i}{\sigma_i}\right)^2 \tag{3.35}$$

is then known as the chi-square. This is more often designated by the Greek letter χ^2. By forming the chi-square between measured data and an assumed theoretical mean, a measure of the reasonableness of the fluctuations in the measured data about this hypothetical mean can be obtained. If an improbable chi-square value is obtained, one must then begin questioning the theoretical parameters used.

Figure 3.24: Experimental setup at VECC used for the measurement of β-decay end-point energy.

detector obtained by gating any particular γ ray in Clover HPGe detector will contain all possible coincident β-decay branches and all possible coincident γ-rays (photopeak and Compton) when data is taken using setup-1. Hence, a separate $\gamma - \gamma$ coincidence measurement was performed with the same setup by putting 10 mm thick Al block in front of the LEPS detector. Another coincidence spectrum ('spec-gg') was generated from this measurement by putting the gate in the Clover HPGe detector at the same γ energy used in the previous $\beta - \gamma$ coincidence measurement. The 'spec-gg' was subtracted from the 'spec-bg', after appropriate normalization at the most intense photopeak in coincidence, in order to obtain the pure β spectrum. The contribution from the unwanted low energy β-decay branches, feeding the higher lying levels, was then removed by appropriately subtracting the two different γ gates. While generating the β spectra, the original spectra were compressed in order to increase the statistical accuracy. Compression of 10, 20 and 40 keV/channel for the generation of β-decay spectrum was employed as and when required with appropriate γ energy gates from the Clover events.

The Fermi-Kurie plots were generated from the experimentally obtained β spectrum by using the built-in routine 'FK-Energy' included in the spectrometer code LISE [TAR03, KAN95]. These

3.10.6.6 Measurement of Decay Half lives

A useful concept in nuclear structure is the time taken by a nucleus to decay by half of its original number. This time is known as the decay half life. The decay half life depends on the decay rate constant λ so that the larger the decay rate, the smaller is the half-life ($T_{1/2}$). It is mathematically defined as follows :-

$$T_{1/2} = \frac{0.693}{\lambda} \tag{3.34}$$

The measurement of decay half lives is very useful in the identification of a long lived beta decaying isomers. Whenever a parent nucleus beta decays to the excited states of a daughter nucleus, the γ-rays decaying from those excited states follows the half life of the beta decaying state of the parent nucleus. Therefore, following the half life of the de-exciting γ-rays gives us information regarding the half life of the β-decaying state in an indirect way. Similar measurements have also been performed in the present thesis work.

3.10.6.7 Measurement of β-decay End-point Energy

During the present thesis work, the measurement of β-decay endpoint energies were carried out by using two Low Energy Photon Spectrometer (LEPS), made up of planer High Purity Germanium crystals and having 300 μm Be window (which completely attenuates the β particles with energy up to $\sim$ 250 keV), in conjunction with four Clover detectors of the VENUS array (as shown in Fig. 3.24), by following the $\beta - \gamma$ coincidence technique [BHA14]. During this measurement, only the bare target has been used by placing it in such a way that the irradiated target material faces the LEPS detectors in order to ensure the efficient emission of β particles from the target material. The LEPS detector used in the setup is sensitive to both β and γ radiations. Hence, the present experimental setup is able to detect both the $\beta - \gamma$ and $\gamma - \gamma$ coincidence events. During the experiment, data is taken using two configurations. In one configuration, the front faces of only the Clover HPGe detectors were covered with 10 mm thick Al block (setup-1) whereas in another set-up (setup-2), the front faces of the all the detectors were covered. The use of the Al block is to ensure that no β particle is entering into the detector. The coincidence spectrum ('spec-bg') in the LEPS

From DCO analysis, one can determine the multipolarity of the transition but no information about the electric or magnetic nature of the radiation could be directly obtained. To resolve such ambiguities, it is useful to investigate the Linear Polarisation of a γ-ray which may be experimentally measured by the use of the Clover detectors as Compton polarimeters, where each of the 4 crystals functions as a scatterer and the 2-adjacent crystals act as the absorbers (see Fig. 3.23). This method utilizes the direction of the scattered radiation to determine the electric or magnetic nature of the transition. The Electric multipole transitions prefer perpendicular Compton scattering whereas the Magnetic transitions prefer parallel Compton scattering. The asymmetry of Compton scattered polarized photons are defined as:

$$IPDCO = \frac{a(E_\gamma)N_\perp - N_\parallel}{a(E_\gamma)N_\perp + N_\parallel} \tag{3.32}$$

where $N_\perp$ and $N_\parallel$ is the number of γ-rays of a particular energy, scattered into the perpendicular and parallel segments of the Clover w.r.t the beam axis, a is the asymmetry factor which arises due to the geometrical asymmetry of the Clover crystals in the set-up and is defined as:

$$a(E_\gamma) = \frac{N_\parallel}{N_\perp} \tag{3.33}$$

where $N_\perp$ and $N_\parallel$ is taken from the Compton scattered data of ^{152}Eu and ^{133}Ba sources. Two $\gamma - \gamma$ matrices can, therefore, be constructed of which one axis of both the matrices corresponds to the event recorded in any detector while the other axis contains the coincident scattered events in a direction perpendicular or parallel to the emission plane. In this way, spectra can be produced by gating on the selected transition to remove contamination. From the projected spectra, the number of perpendicular ($N_\perp$) and parallel ($N_\parallel$) scattered events for the desired γ-ray could be obtained. Since, the angular momentum vector of a pure electric transition is polarized perpendicular to the beam axis, and that of a pure magnetic transition is polarized parallel, a positive value of IPDCO will show the transition multipole to be predominantly electric in nature whereas a negative value corresponds to a magnetic transition and a value close to zero indicates a mixed transition.

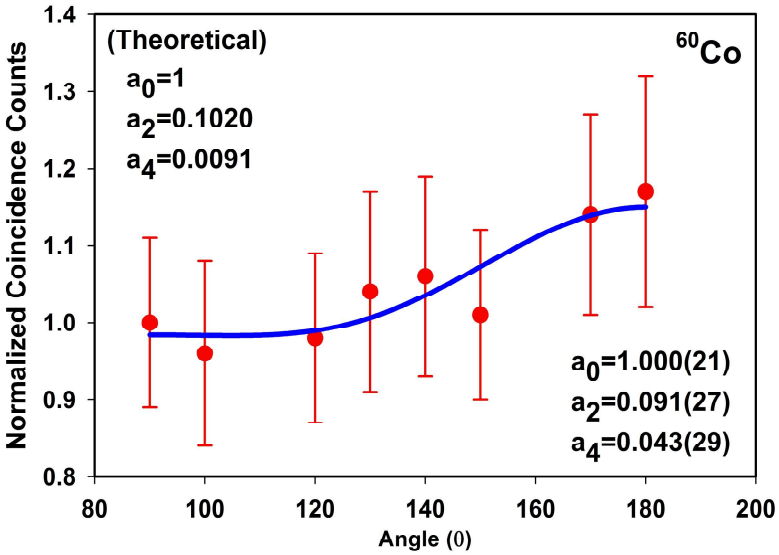

Figure 3.22: Angular correlation of 1173-1332 keV cascade of ^{60}Co.

(D5), 130° (D6), 150° (D2), 180° (D4)) were obtained w.r.t the reference detector at 0° (D1) and the rest three equivalent angles (120° (D2),140° (D6),170° (D5)) were obtained by considering the 90° (D3) detector as the reference detector. At first, the angular correlation coefficients for the well known 1173-1332 keV (Q-Q) cascade of ^{60}Co was reproduced (as shown in Fig. 3.22) and then, the geometrical correction factor required for this purpose was used for the subsequent measurements (see Section-4.3.2.2).

3.10.6.5 Determination of Parity

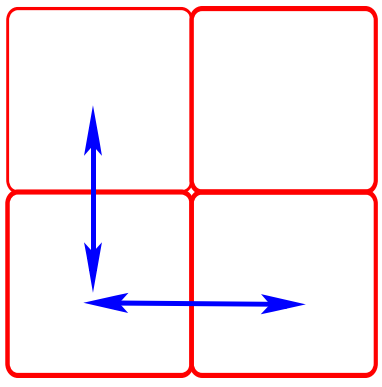

Figure 3.23: Schematic drawing of a Clover detector showing the parallel and perpendicular scattering of compton scattered γ-rays.

3.10.6.4.2 ADO ratio of the γ-ray transitions It is mathematically defined as:

$$R_\theta = \frac{I_{\gamma 1}(at\ \theta_1,\ gated\ by\ \gamma 2\ at\ \theta_3)}{I_{\gamma 1}(at\ \theta_2,\ gated\ by\ \gamma 2\ at\ \theta_3)} \tag{3.30}$$

During the present thesis work, θ_1=157° and θ_2=90° has been used while θ_3 has been considered as the sum over all the available angles. Because of this, all the angular correlation effects are almost completely washed out and the measured γ-ray intensities at both the angles of 157° and 90° follow the ordinary angular distribution features. In the present work, the typical values of this ratio falls within the range of 0.8-1.2 for the known dipole, and 2.18-2.57 for the known quadrupole transitions, respectively.

3.10.6.4.3 $\gamma-\gamma$ angular correlation The observation of directional correlation of two successively emitted nuclear radiations, especially during the decay spectroscopy experiments, gives direct information of the angular momenta of the nuclear states involved and of the multipole nature of the emiited radiation. The angular correlation method is very useful for the determination of the relative amount of different angular momentum components in mixed multipole transitions.
The probability of detecting γ_2 at an angle θ w.r.t γ_1 is given by the angular correlation function which is written as a sum of lengendre polynomials, P_k, by

$$W(\theta) = 1 + a_2 P_2(cos\theta) + a_4 P_4(cos\theta) \tag{3.31}$$

a_2, a_4 depends on the spin of the levels and the multipolarity of the transitions and can be calculated theoretically or can be determined as free parameters in a fit of experimental data. Comparision of the experimental (a_2, a_4) values with the theoretical results gives the mixing ratio (δ) of the corresponding transitions. W(θ) for stretched 'dipole' transitions have maxima at θ=90° and minima at 0° or 180°. The reverse is true for stretched 'quadrupole' transitions.

The data taken using VENUS array were used for the measurement of $\gamma-\gamma$ angular correlation at eight different angles (see Section-3.10.5 for details). Five equivalent angles (90° (D3), 100°

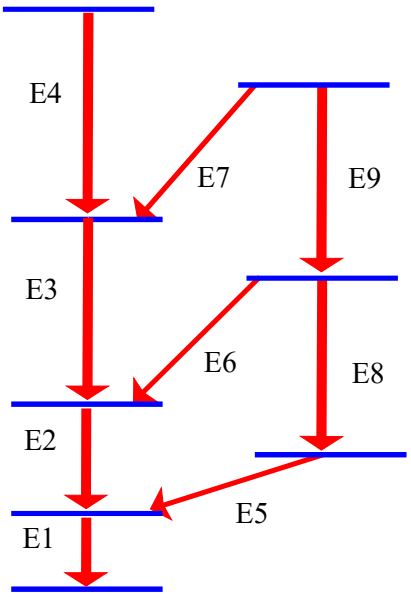

Figure 3.21: Example of a level scheme constructed from the coincidence analysis of γ-rays.

an asymmetric $\gamma - \gamma$ coincidence matrix (where the axes correspond to detector at different angles relative to the beam axis), it is possible to distinguish between the transition multipolarities by comparing and taking ratio of the intensities of the projected transitions for given angles.

The experimental DCO ratio for a γ transition ($\gamma 1$) at an angle θ_1 w.r.t another γ transition ($\gamma 2$) at an angle θ_2 is defined as [KRA89, KAB93],

$$R_{DCO} = \frac{I_{\gamma 1}(\theta_1)(Measured\ at\ \theta_1;\ Gated\ by\ \gamma 2\ at\ \theta_2)}{I_{\gamma 1}(\theta_2)(Measured\ at\ \theta_2;\ Gated\ by\ \gamma 2\ at\ \theta_1)} \tag{3.29}$$

where $I_{\gamma 1}(\theta_1)$ $[\theta_2]$ is the intensity of $\gamma 1$ at an angle θ_1 $[\theta_2]$.

To get the highest sensitivity, one of the angles between θ_1 and θ_2 is choosen nearly 0° or 180° while the other angle to be nearly 90°. During the present thesis related work, experimental data was sorted into a $4k \times 4k$ asymmetric, angle-dependent, $\gamma - \gamma$ matrix by taking energy signals from Clovers of the 90° ring on one axis and Clovers at angles 157° on the other axis. The DCO ratios were obtained for the known dipole and quadrupole transitions which showed the values of 0.442(44) and 1.041(26) respectively in a pure quadrupole gate. In a pure dipole gate, the ratio was found to be 2.000(78) for the pure quadrupole Ground State transition.

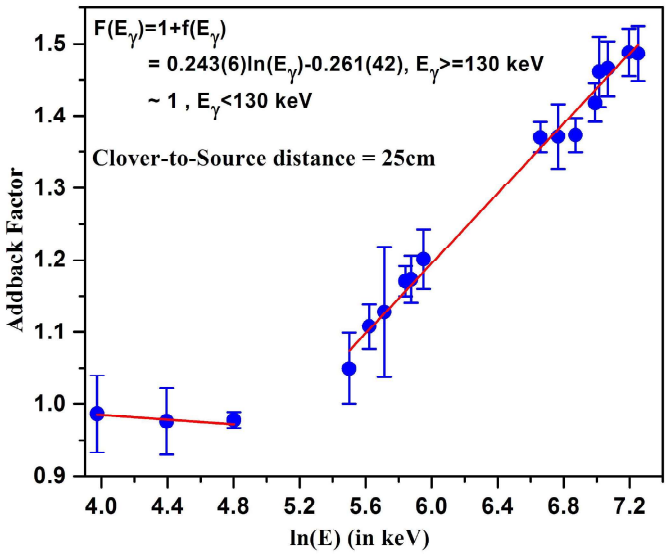

Figure 3.20: Variation of Addback Factor with ln(E_γ) for a Clover Detector for a source-to-detector distance of 25 cm.

to make spin assignments for nuclear excited states.

3.10.6.4.1 DCO ratio analysis In a typical heavy-ion induced nuclear reaction, a large number of residual nuclei are populated with competing cross-sections. This results in a complex γ-ray spectra in the singles mode. These spectra usually have large continuum background and overlapping γ-peaks originating from different nuclei. As a result, it is very difficult to extract reliable angular distribution of γ-rays from singles spectrum. The Doppler broadening of γ-rays complicate the spectra further.

Measurement of $\gamma - \gamma$ angular correlation is advantageous in this case because it reduces the background significantly and eliminates contaminated peaks from neighboring channels as a result of which the coincidence spectrum gets considerably simplified. The weak γ-peak, that is completely hidden in the singles spectrum, may be identifiable in coincidence with another transition. Large angular correlations observed in the coincidence measurements allow reliable extraction of multipolarities of the transitions. One of the procedures for determining these multipolarities is the DCO ratio method using pairs of coincident γ-transitions, emitted at angles $\theta 1$ and $\theta 2$ w.r.t beam axis. By setting a software gate on a specific energy of known multipolarity on both the axes in

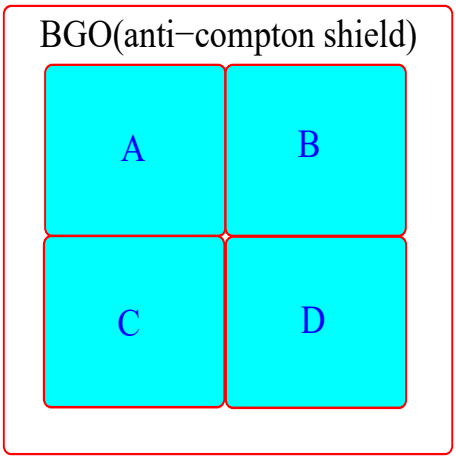

Figure 3.19: Schematic drawing of a Clover detector. The four crystals are labelled A, B, C and D to explain the add-back procedure.

E2, then energies E3, E4, E6, E7 and E9 appear in the coincidence spectrum. Whereas, if we set a doubles gate on E2 and E6, only E1 and E9 appear in the coincidence spectrum.

3.10.6.4 Determination of Spin

A fusion evaporation reaction produces nuclei in excited states with its angular momentum vector perpendicular to the axis defined by the direction of the beam. Inspite of the subsequent evaporation of particles leading to some alteration of the orientation of the recoil nuclei, most of the nucleus are strongly oriented. When a nucleus in such a state emits γ-radiation, the relative intensities at different angles w.r.t the beam-axis depend on the multipolarity of the transition. Therefore, the information about the γ-ray multipolarity can be obtained by observing the intensity of the emitted radiation at different angles w.r.t the beam axis. By determining the DCO (Directional Correlation of Oriented states) ratio of γ-rays de-exciting the oriented states, the spin of the state and the γ-ray multipolarity can also be deduced. The multipolarities of the γ-rays can also be determined from the ADO (Angular Distribution from Oriented nuclei) ratios [PII96]. This procedure is mostly useful for those transitions in which the DCO ratios could not be determined because of their poor statistics or due to unavailability of pure gating transitions.

Also, in case of off-beam experiments, i.e., decay spectroscopy studies, where there is no specific spin alignment of the compound nucleus, angular correlation measurement is an effective method

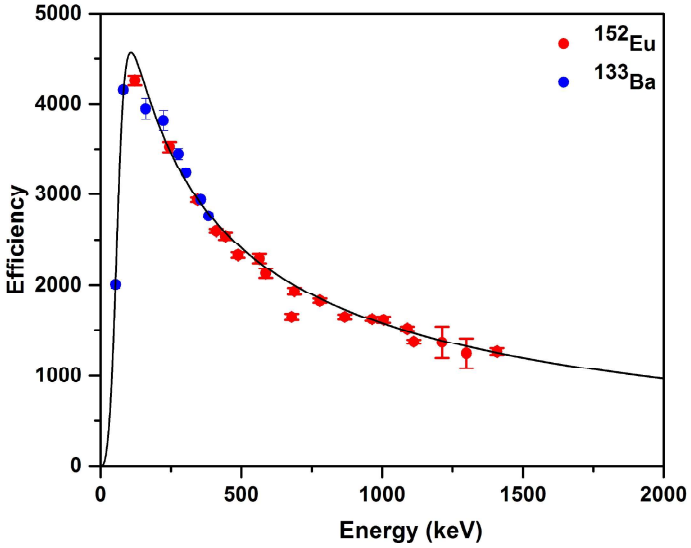

Figure 3.18: Output of the "Effit" subroutine of the RADWARE package indicating the photopeak efficiency of the clover detectors in INGA at TIFR as a function of energy and fitted to the data obtained from the ^{152}Eu and ^{133}Ba radioactive sources.

to make them fall on each other. This procedure is known as Gain matching. Once the spectra are gain matched, the data of individual crystals for each clover detector can be added to generate the addback spectrum. While doing the addback, the time correlated signals from two neighboring segments (horizontal or vertical) are added. The ratio of addback photopeak efficiency and the added photopeak efficiency is known as the *Addback Factor*. Fig. 3.20 indicates the variation of addback factor with energy observed while characterizing a Clover detector for a source-to-detector distance of 25 cm. It is clear from this figure that the addback factor for a clover detector remains close to 1.0 at lower energies (<130 keV) and increases with increasing energy at higher energy ($\geq$130 keV).

3.10.6.3 Coincidence relationships among γ-rays

The pictorial representation of the excited state of a nucleus is known as the level scheme. For building up the level scheme, the γ ray gating has been done on the γ ray de-exciting from the first excited state and thereafter, the γ transitions associated with this nucleus have been identified. The placement of γ-ray transitions in sequence gives rise to the band-like structure. Fig. 3.21 explains the concept of coincidence method. For example, if we apply a singles gate on transition with energy

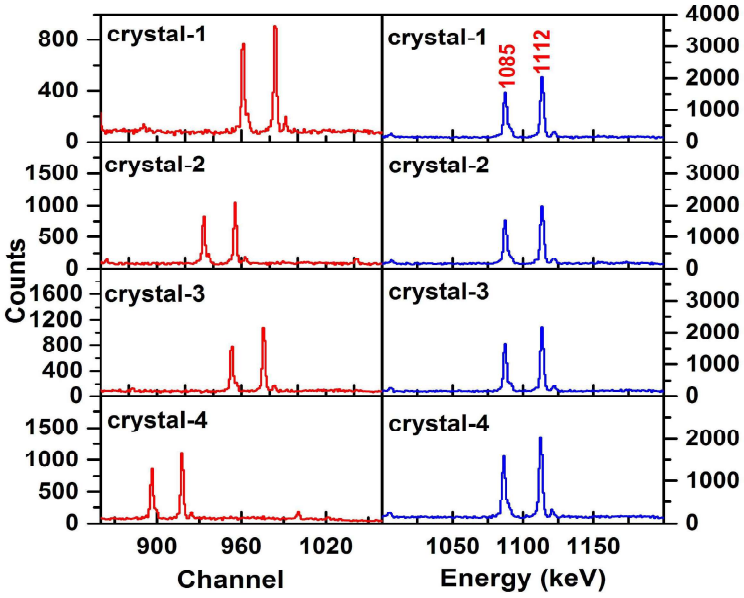

Figure 3.17: The figure indicates how energy calibration effects on the spectra of the four crystals of a Clover detector. The four panels on the left side shows the 1085 and 1112 keV gamma rays of ^{152}Eu source before calibration for the four crystals whereas the spectra on the right side indicates these spectra after calibration @ 1keV per channel.

and low-energy efficiency curves. To achieve a good efficiency calibration, the calibration source is mounted at the position of the target, and the same set-up configuration is used as that during the experiment. Fig. 3.18 shows the output of the "effit" subroutine of RADWARE indicating the photopeak efficiency of the Clover detectors in INGA at TIFR, during one of the thesis related experiments, as a function of energy along with the curve fitted to the data obtained from the ^{152}Eu and ^{133}Ba radioactive sources. The fitted parameters are A=9.43(7), B=2.76(12), C=0.0(0), D=7.363(3), E=-0.656(6), F=-0.064(6) and G=15.0(0).

3.10.6.2 Add-back effect in a Clover Detector

A great advantage of the composite detectors is the enhancement of the peak-to-total ratio P/T by applying an add-back procedure. If a γ ray is scattered from one crystal into a neighbouring one, the two registered energies can be added to obtain the full energy. In order to generate the addback spectrum of a clover detector, the energy calibrated spectrum from each crystal (i.e., A, B, C and D) (see Fig. 3.19) has to be gain matched. During addback, the spectra from each crystal are shifted

3.10.6.1 Energy and Efficiency Calibration

The very first step of analyzing data in γ-spectroscopy is the energy calibration of detectors. The height of the output pulse produced as a result of the interaction of γ-rays with the HPGe crystals of a clover detector, are generally different. This is generally refered to as the gain of that particular channel.

Different detectors have different gains and many a times, it happens that the gain of the detector does not remain stable and fluctuate during the measurements. In order to accurately determine the energies of the detected γ-rays, the detectors must be energy calibrated using the standard γ-ray sources, viz., ^{152}Eu and ^{133}Ba placing them at the target position of the detector array. To calibrate the detector, the peak positions (in channel number) of known energy peaks of the radioactive sources are determined. The energies are plotted against channel numbers and fitted using a polynomial

$$E = \sum_{n=0}^{n} a_n x^n = a_0 + a_1 x + a_2 x^2 + a_3 x^3 \tag{3.27}$$

where E is the γ-ray energy in keV and x is the channel number. The term x^3 results in a better fit for the high energies (above 1.5 MeV) whereas to get correct energy below 200 keV, we must add a term $\sqrt{x}$ to the polynomial. Fig. 3.17 represents pictorially the effect of energy calibration and gain matching on the spectra of the four crystals of a clover detector for ^{152}Eu source.

To measure the relative intensities of the observed γ-rays, it is necessary to determine the efficiency of the detectors as a function of energy. This can be achieved by using the radioactive sources where the relative intensity and/or disintegration per second (dps) are well known and by fitting the data points using the following parameterization [RAD95]

$$ln(\epsilon) = [(A + Bx + cx^2)^{-G} + (D + Ey + Fy^2)^{-G}]^{-1/G} \tag{3.28}$$

where ϵ is the efficiency, x= ln(E$_\gamma$/100) and y= ln(E$_\gamma$/1000). The γ-ray energy E_γ is in keV. A, B and C are the fit parameters for the low-energy region and D,E and F are the fit parameters for the high-energy region. The parameter G determines the shape of the turn-over region between the high-

finally extract the information about the γ-ray energies, intensities, coincidence relationships, spins, parities and lifetimes of the energy levels of the nucleus of interest from recorded list mode data. In a typical in-beam experiment, spectroscopic measurements are performed to determine the energies and relative intensities of the γ transitions followed by $\gamma - \gamma$ and/or $\gamma - \gamma - \gamma$ analysis to establish the coincidence relationship to construct the level scheme of a particular nucleus. The idea about the spin of the nuclear states is obtained from the distribution and angular correlation data while polarization measurements give us the idea of parity.

The time-stamped digitized signal coming from the preamplifiers connected to the crystals of the clover detectors and the corresponding ACS used during the experiments were recorded in binary data files in List modes. In this mode, the data are stored in an event-by-event description, where the event is defined as the satisfaction of certain preset condition. These data sets were, then, used for offline analysis to extract different entities which characterize the excited states of the nucleus of interest. The method of extracting information from these data sets is discussed in the following sections.

The coincidence information is necessary for the construction of level schemes. The high-fold events can be decomposed into lower-fold sub-events where the fold of the sub-event depends on the dimension of the considered histogram. A two-dimensional histogram is generated from two-fold coincidence data and is referred to as $\gamma - \gamma$ matrix. To create a two-dimensional matrix, each event is unfolded into pairs of two energies (E_x,E_y) and the bins corresponding to E_x and E_y are incremented on the x- and y- axis, respectively. Using the matrix, only a single gate can be set on one of the energy axes, and the gated spectrum is projected on the other axis. Three-dimensional histogram (cube) is produced from triple coincidence (γ^3). For this purpose, four axes are required. Out of these four axes, x, y, and z axis are meant for the γ-ray energies whereas fourth axis records the time of the γ-ray event. In this case, one can apply single gates or double gates to obtain one dimensional coincidence spectra. The different dimensional energy vs. count histogram (matrix, cube and spectrum) has been constructed with the help of the analysis software packages INGASORT [BHO17] and RADWARE [RAD95, RAD95A].

of a nucleus, first we need to do the calibration of energy and efficiency of the detectors. After that, we have to sort the raw data into symmetric and asymmetric $\gamma - \gamma$ matrices. The symmetric $\gamma - \gamma$ matrix helps us to get the relative intensities (which is measurable from the singles data as well) and coincidence relations of the γ-ray transitions. From asymmetric $\gamma - \gamma$ matrix, we perform the angular correlation studies and linear polarization measurements to get the spin and parity of the nuclear levels respectively. Alongwith these informations, lifetime of the nuclear states is also important to get the complete picture of the nuclear structure. Based on the order of the lifetime, different techniques are employed. If the lifetime of the state is of the same order of the slowing down time in a backing or target ($\sim 10^{-12}$s) and if the experimentalist has a knowledge of the slowing down process of the recoil in the target and target backing, one can use the lineshape of the transition of interest as a function of detector angle to determine the nuclear level lifetime. This method is known as the Dopler Shift Attenuation Method (DSAM). Similarly, lifetimes of the order of 10^{-8} to 10^{-12}s are measureable using the Recoil Distance Method (RDM) where nuclei are formed in a thin target ($\sim 500 \mu \mathrm{cm}^{-2}$) usually by fusion evaporation reaction. The recoils then fly out of the thin target towards a thick stopper where they are stopped. This leads to a shifted and an unshifted peak from which information about the lifetime can be extracted. If the lifetime is >min, then slope method is useful. To know the multipolarity of the electromagnetic transition, angular correlation measurement can be very useful. The anisotropic angular distribution of the intensity of gamma rays is observed when a preferred nuclear orientation is established prior to the emission of the photon. The pattern depend on the order of the multipole : dipole, quadrupole etc. but they are the same for electric and magnetic transitions with the same order. In order to assign the excitation energy of the isomeric level, the measurement of β-decay end-point energies is very important specially when there is no isomeric transition decaying to the ground state of the parent. Also, the measurement of intensities of the β-feeding gives the information on the *logft* values which, in turn, can be used to guess the spin of the isomeric level and the spin of the excited states of the daughter. The data have been analyzed by software packages like LAMPS, INGASORT and RADWARE.

In this section, variety of analyzing techniques will be discussed with the help of which one can

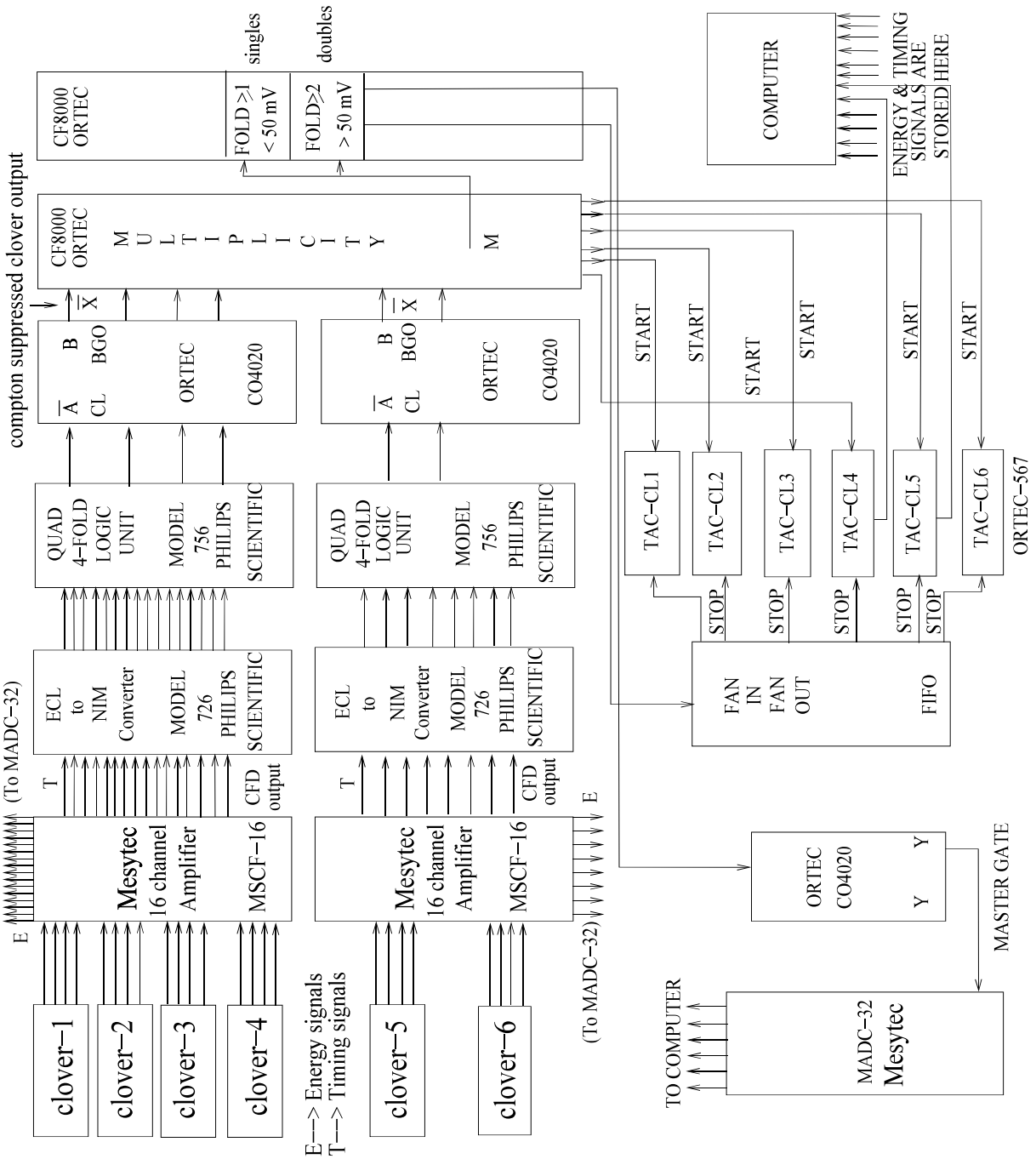

Figure 3.16: Block diagram of the pulse processing electronics for the offbeam experiment at VECC using VENUS array.

3.10.6 Data Analyzing Techniques

One of the main purpose of this present work is to construct complete and consistent level schemes of the nuclei to be investigated by using the γ spectroscopic techniques. To get the level scheme

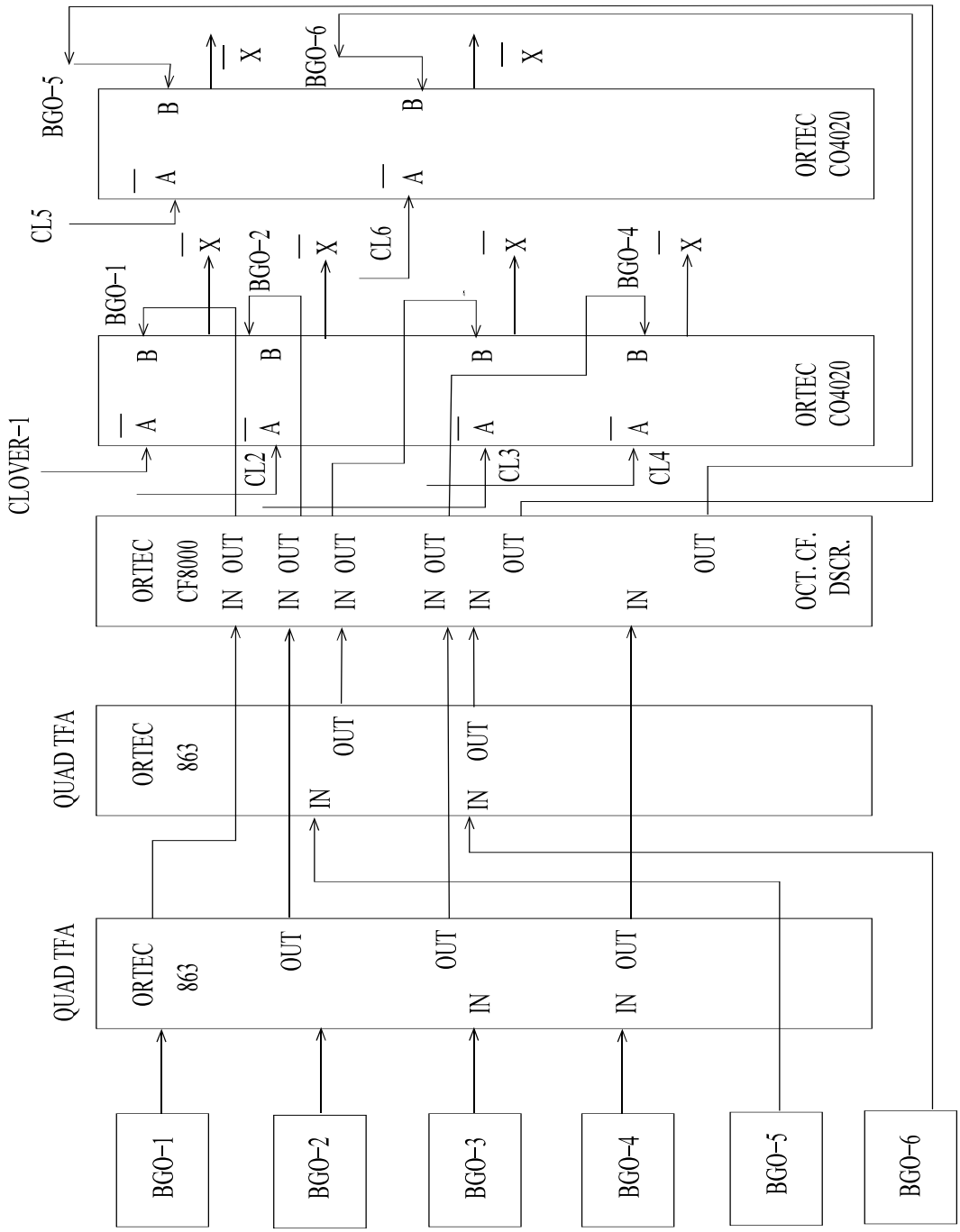

Figure 3.15: Block diagram for the generation of anti-coincidence VETO condition for the CLOVER detectors.

identification etc.

Figure 3.14: Photograph of VENUS array coupled with $CeBr_3$ detectors at VECC, Kolkata

3.10.5.1 Electronics and Data Acquisition system related to VENUS array

The block diagram of the pulse processing electronics is shown in Fig. 3.15 and Fig. 3.16. During the experiment related to the present thesis, the preamplifier signals from the 24 crystals for the six Clover detectors of the VENUS array, were processed by 16-channel high resolution Mesytec Amplifiers, which give analog energy signals as well as ECL standard logic signals.

The energy signals were taken out with 4 μs shaping time and processed through high resolution 14-bit Mesytec VME ADCs. The logic ECL outputs of 16-channel amplifiers were converted to NIM standard and used to make OR of the signals of four crystals of each Clover detector. To process the BGO signals, NIM standard TFA and CFDs are used and the anticoincidence 'VETO' condition for the corresponding Clover detectors were applied using the quad logic unit ORTEC-CO4020 to get $CLOVER.\overline{ACS}$ signal that corresponds to a valid event in the Clover. The master gate for data acquisition system is generated from the (A_{coin}) signals from individual detectors satisfying the desired gamma-multiplicity of the Compton-suppressed events within the stipulated coincidence time window (Δ= 50 ns). VME data acquisition system was used in LAMPS platform to collect the data in LIST mode which contains all the informations regarding energy, time sequence, detector

A photograph of the TIFR data acquisition system is shown in Fig. 3.13.

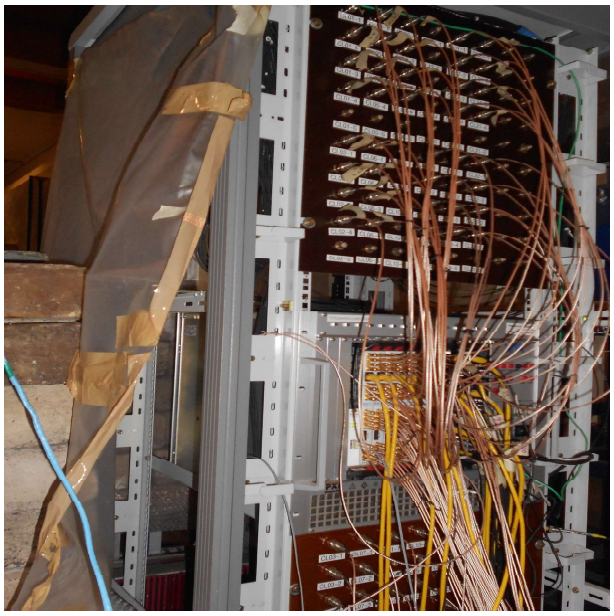

Figure 3.13: Photograph of the data acquisition system at TIFR during June, 2013 experiment.

3.10.5 VENUS array at VECC, Kolkata

VENUS stands for VECC array for NUclear Spectroscopy (VENUS), which consists of six BGO shielded Clover HPGe detectors. The VENUS array was used in one of the experiment related to this thesis (see Section-7.2) where ^{150}Sm was studied from the decay spectroscopy. In this off-beam experiment, the Clover detectors of the VENUS array were placed at a distance of 18 cm from the target and at the angles of 30° (D2), 90° (D3), 180° (D4), 260° (D5) & 310° (D6) w.r.t one of the detectors taken as a reference of 0° (D1) as shown in Fig. 3.14. During the experiment, the Clover detectors were coupled to eight $CeBr_3$ detectors for off-beam data collection. But it is worth mentioning here that the data gathered by the Clover detectors alone have been analysed for the present thesis related work. Hence, in the following sub-section, the pulse processing electronics is discussed in relation to the Clover detectors only.

The crate is connected to the Windows PC via a MXI-4 PXI-PCI optical controller. Each Pixie-16 card having 16 channels, serves four clover detectors. The preamplifier signals of the clover are digitized with a 100 MHz 12-bit flash analog-to-digital converter. One copy of the data stream generates a trigger by a fast filter once the output crosses the threshold. The fast trigger pulse is stretched to 100 ns and is used for multiplicity computation in the on-board FPGA. The fast triggers from the 16 channels of a Pixie-16 module are distributed to its adjacent modules through the PXI back-plane for generating global trigger after multiplicity computation. This trigger stretch length is kept as 10 μs to enable one to carry out prompt-delayed coincidence in the off-line analysis. The time-stamp will be latched and the event header information will be written for a channel if its fast trigger gets validated by the external trigger and not vetoed by channel veto signal.

After gathering the data, a data sorting routine developed at TIFR known as 'Multiparameter time-stamp-based coincidence search program (MARCOS)', was used to sort the time-stamped data to generate one-dimensional histograms, E_γ-E_γ matrices and E_γ-E_γ-E_γ cubes. The RADWARE software package [RAD95] was used for the analysis of matrices and cubes. A large number of isotopes were produced at high spins in one of the present thesis works which were identified using E_γ-E_γ-E_γ cubes.

The target to detector distance in INGA is 25 cm and the overall photopeak efficiency is around 5% at $E_\gamma \sim 1$ MeV. A PCI-PXI based digital data acquisition (DDAQ) system with 96 channels has been implemented for the Compton suppressed clover array. Each crystal is connected to a low temparature FET coupled with the resistive charge sensitive preamplifier. The preamplifier has a gain of 200 mV/MeV and the decay time constant of the output is 50 μs. The compton suppressed BGO shield has 16 photomultiplier and operates at 950 V. The sum of the 16 photomultipliers is given to a timing module which generates a NIM logic signal. This goes as an input to the digital data acquisition system for the veto of the clover signals. The requirements of the TIFR digital DAQ is to provide the energy and timing information for all the 96 channels of 24 clovers vetoed with the respective Compton suppressed BGO shields. The system should be able to handle high count rate (20 kHz) for each crystal without deteriorating the energy resolution over the full dynamic range of the clovers. The details of the basic configuration of the DDAQ is given in Ref. [PAL12].

3.10.4.1 Electronics and Data Acquisitions related to the experiment at INGA, TIFR

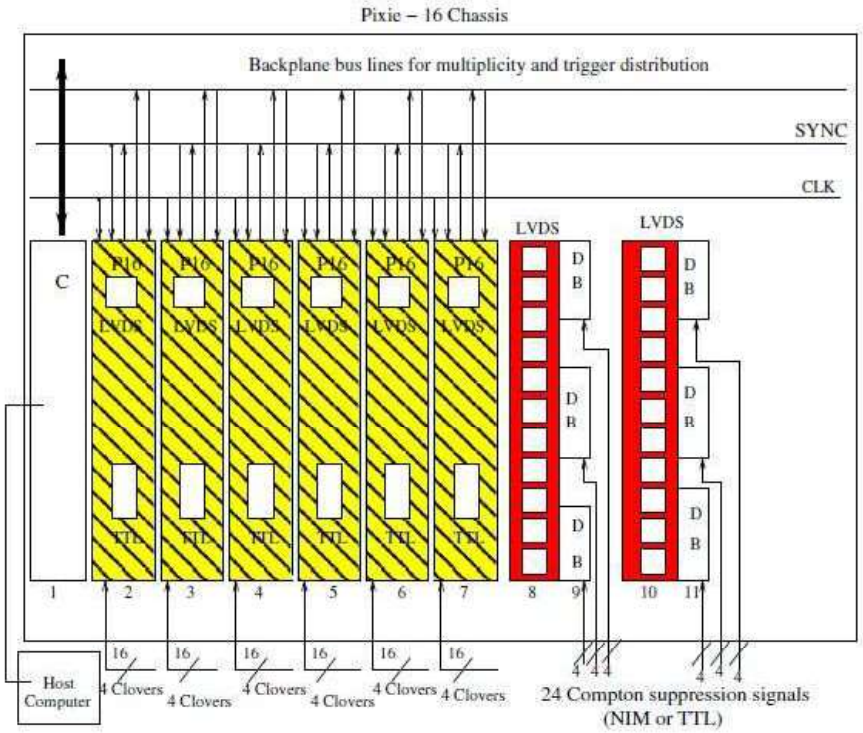

Figure 3.12: Block diagram for the digital DAQ for 24 Compton suppressed clover detectors. It has six Pixie-16 modules; two LVDS level translator modules and one controller arranged in a single Compact PCI/PXI crate [PAL12].

The basic requirements for the data acquisition is to provide the digitized energy and the timing information for all the channels. During the experiment, a fast digital acquisition system (DDAQ) based on Pixie-16 modules of XIA LLC [PAL12] was used to record two- and higher-fold coincidence events in the list mode form along with the time-stamp. In addition to the Compton suppression due to vetoing of Compton scattered events by the BGO detector, the four Ge crystals packed in each clover detector help in generating the addback spectrum leading to a further reduction in the Compton background. For energy calibration and determination of relative photopeak efficiency of the array, a mixed source of ^{133}Ba and ^{152}Eu was used. In the present DDAQ, a single Compact PCI/PXI crate contains six Pixie-16 modules, two LVDS level translator modules and one controller. A block diagram of the DDAQ for 24 Compton suppressed clover detectors is shown in Fig. 3.12.

The Indian National Gamma Array (INGA) (see Fig. 3.10 and 3.11) is a multi-detector array at India, set up in collaboration with Tata Institute of Fundamental Research (TIFR), Inter University Accelerator Centre (IUAC), Bhaba Atomic Research Centre (BARC), Saha Institute of Nuclear Physics (SINP), Variable Energy Cyclotron Centre (VECC), UGC DAE Consortium for Scientific Research and many Universities in India.

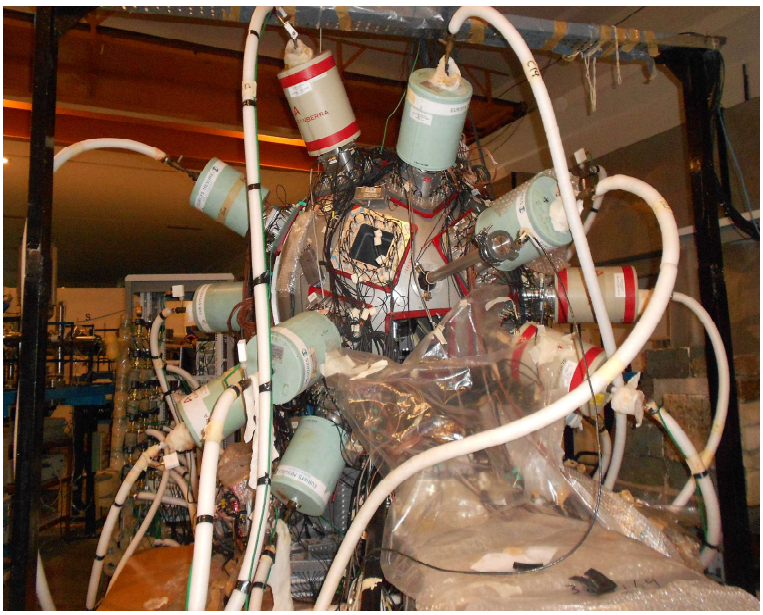

Figure 3.11: Photograph of INGA at TIFR, Mumbai during June, 2013

This array, consisting of Compton suppressed clover detectors, also facilitates measurement of polarization for the excited states due to the segmented structure of clovers and its higher efficiency. The INGA is setup with different accelerators in the country and was installed at TIFR during one of the experiment related to this thesis work. This array can accommodate 24 Compton suppressed Clover detectors arranged in six different azimuthal angles with six detectors at 90° and three detectors each at 23°, 40°, 65°, 115°, 140° and 157° with respect to the beam direction. Fig. 3.11 represents INGA stationed at TIFR during the experiment mentioned above where out of 24 detectors, 20 Clover HPGe detectors were present during the experiment. There were one detector at 23°, four detectors at 90° and three detectors on each of the rest of the angles, during the experiment.

have been widely used for the detection of β particles providing a reasonable energy resolution and detection efficiency. However, their use is not suitable in case of very high energy β particles which become more abundant as one moves away from the line of stability. Instead, the planar HPGe detectors, having low Z window materials have been found to be quite efficient for this purpose. Morever, these detectors can be calibrated for β detection over a wide energy range using appropriate γ ray sources. The high atomic number of Ge gives rise to a distortion of the Fermi Kurie plot at the low energy end due to the production of high backscattering and bremsstrahlung. Inspite of that, the planar HPGe detectors are being used in many important fields of high precision nuclear β-decay because of their high energy resolution and increased efficiency compared to the silicon detectors [BHA14].

3.10.4 Indian National Gamma Array at TIFR, Mumbai

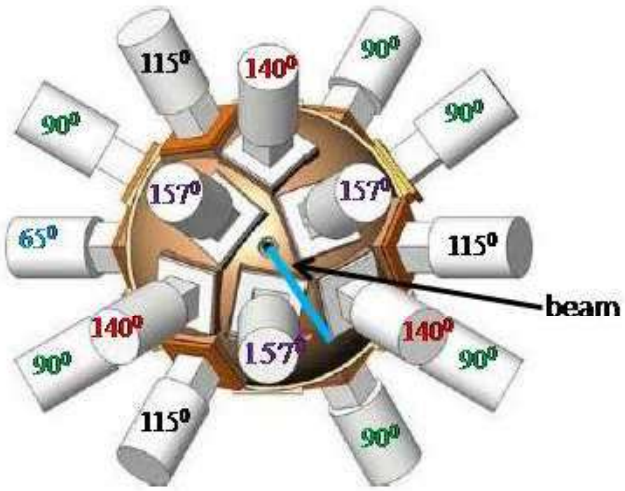

Figure 3.10: Schematic representation showing the position of the Compton-suppressed clover detectors in the Indian National Gamma Array at TIFR [PAL15]. The angle of each of the clover detectors with respect to the beam axis is also shown in the figure.

The advent of large detector arrays in γ-ray spectroscopy has started a new era in nuclear structure research. The high efficiency of these arrays allow us to observe very weak γ-ray cascades.

3.10.3 Low Energy Photon Spectrometer (LEPS)

Gamma detector arrays consisting of Clover HPGe detectors usually have very low detection efficiency for photons with energies less than 50 keV due to the absence of suitable detectors which are efficient at these low energies. However, this energy range has special importance for detection of (i) X-rays for identification of the nucleus of interest, (ii) highly converted low energy gammas emitted from isomers in medium and heavy nuclei, (iii) gamma transitions connecting the lowest stages in heavy nuclei, etc. The low energy photon spectrometers (LEPS) having reasonable resolution at this energy range have very low efficiency. So, it may be beneficial to use a composite detector which includes more than one planar LEPS having good resolution to get higher efficiency. Electrically segmented planar LEPS has been used in some of the arrays as a solution to this problem. The crystal in this planer detector is of p-type. It has a thin Be window of thickness$\sim$300 μm, to maximize the low energy efficiency of the detector which completely attenuates the beta particles with energy upto 250 keV. The effective area of a LEPS detector is 4 $\times$ 80 mm^2. The necessary reverse bias for this composite LEPS for operation is very low, only -300 V. Bias always depends on the material, crystal quality and design. This low bias for optimum performance indicates that the crystal quality is good. The Composite detector use a single bias supply. The detector assembly is designed such that the supply provides reverse voltage to four segments.

3.10.3.1 Use of LEPS detectors in detection of β-decay

During the present thesis work, electrically segmented LEPS detector have been used for measurement of β-decay end-point energies (see Section-3.10.6.7 for details). The detection of β particles has been explored for many years using a variety of active ionization detectors having a wide range of efficiency and resolution, viz., magnetic spectrometer [JOH73], plastic scintillators [GRO92], silicon [HOR96] and germanium solid state detectors [TEN88][VOM83]. Inspite of a high energy resolution of the magnetic spectrometer, its use is limited by the poor efficiency and the requirement of an elaborate experimental setup. The use of plastic scintillator, in order to enhance the efficiency for the detection of β particles, is again limited by its poor energy resolution. The silicon detectors

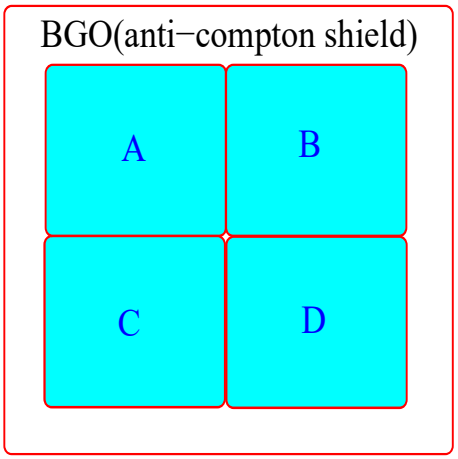

Figure 3.9: Schematic view of a Clover detector with anti-Compton shield.

Whenever γ-ray fall on a single Clover detector, the corresponding electronic pulses are detected in the coincident mode of detection and recorded in the data acquisition system sequentially in real time. This mode of data acquisition is popularly known as $event - by - event$ mode or *list* mode. If the γ-ray detected in a particular event, undergoes Compton scattering from one crystal to the next, then the coincident pulses generated in the event are added back together which is commonly known as *addback*. This increases the overall peak-to-total ratio of the clover detector. Also, as a consequence of this addback effect, the clover detectors have a great advantage of measuring the high energy γ-ray.

A Clover detector due to its typical 4-leaf arrangement, and placement in appropriate orientation, can distinguish between events which are Compton scattered parallel or perpendicular to the reaction plane. This feature can be used to measure the *linear polarization* of γ-rays.
Moreover, the Clover detectors are, in fact, less vulnerable to neutron damages. To enable the close packing of the Ge crystals the outer surfaces of the crystals are at ground whereas the high voltage (common for the 4 crystals) is applied on the inner contacts. Energy and timing signals are obtained for each crystal through AC-coupling.

Ge(Li) or Si(Li) detectors, these detectors need not always be kept at liquid nitrogen temparature, when not in use. However, time resolution of HPGe detector (∼10 ns) is poor in comparision to the scintillator detectors.

3.10.2 Clover Detector

The Clover detector consists of four coaxial N-type Ge-detectors, arranged like a four-leaf clover. Each crystal has a square front face with round edges obtained by tapering it on two adjacent faces with an angle of 7.1° starting at around the half of the length and by cutting the two remaining faces parallel to the crystal axis and along its whole length. This enables a close packing of the crystals (Ge-Ge distance of about 0.2mm). The individual Ge crystals are 50 mm in diameter and 70 mm in length for the CLOVERS used in the experiments of the present thesis. The four tapered crystals have a total volume of ∼470 cm^3 which is about 89 % of the total volume. Fig. 3.9 shows the schematic diagram of a clover detector encapsulated in an Anti-Compton shield and attached to a liquid nitrogen Dewar. The Anti-Compton shields, consists of a scintillating material known as Bismuth Germanate ($Bi_4Ge_3O_{12}$) (BGO). It is used to detect the Compton scattered γ-rays escaped from the Ge crystals. These surrounding BGO detectors functions as a veto for gammas which scatter out of the Clover volume and therefore, BGO helps in suppressing the Compton background. Each of the four crystals of the clover detector behaves as an individual detector and has two separate outputs for the energy and the timing signals. The effective solid angle is reduced for individual crystals of clover, which improves the energy resolution. Since, the crystals are smaller in size, the timing characteristics are much better than that of a single large HPGe crystal of equivalent volume. There are a number of advantages of using the Clover detectors than the more conventional single crystal detectors. The individual smaller Ge crystal presents a reduced opening angle in comparision to a large volume Ge detector, thus, significantly reducing the effects of Doppler broadening on the resulting spectra.

high resistivity compared to the n- and p-type materials on either side of the junction. Electron-hole pairs that are created within the depletion region by the passage of radiation will be swept out of the depletion region by the electric field, and their motion constitutes a basic electrical signal. An unbiased junction will function as a detector, but only with very poor performance. The contact potential (of about 1 V) that is formed spontaneously across the junction is inadequate to generate a large enough electric field to make the charge carriers move very rapidly. Therefore, charges can be readily lost as a result of trapping and recombination, and incomplete charge collection often results. For these reasons, unbiased junctions are not used as a pulse mode radiation detector, but instead, an external voltage is applied in the direction to cause the semiconductor diode to be reverse biased. A reverse biased p-n junction diode makes an attractive radiation detector because charge carriers created within the depletion region can be quickly and efficiently collected. For a semiconductor detector, the depletion depth is given by

$$d = \left(\frac{2\epsilon V}{eN}\right)^{1/2} \tag{3.26}$$

where, V is the reverse bias voltage, N represents the net impurity concentration in the initial semiconductor material, ϵ is the dielectric constant and e is the electronic charge. If germanium of normal semiconductor impurity is employed, the maximum achievable depletion depth is only a few mm even at bias voltage close to the breakdown level. Thus, the impurity concentration should be much reduced down to 10^{10} atoms/cm^3 in order to realize intended depletion depths of the order of a few cm. At this impurity concentration, a reverse bias voltage of 1 kV can produce a depletion depth of 1 cm. Since, impurity concentration is much lower, such detectors are known as a High-Purity Germanium detector. HPGe detector has an excellent energy resolution ($\sim$2 keV at 1 MeV) compared to gas detectors or scintillators. To create one ion pair $\sim$35 eV energy is required for a gas detector, on the other hand, $\sim$100 eV or more energy is required to create photoelectrons in scintillator detector. Energy resolution is better in germanium detector because only $\sim$3 eV is required to create one electron-hole pair. HPGe detector must be operated at liquid nitrogen temparature (77K) to reduce the leakage current due to its smaller band gap ($\sim$0.7 eV). Unlike

observed to correspond to different values of ft.

Table 3.2: Classification of β-decay processes

Type	log(ft)	L	$\Delta\pi$	$\Delta\vec{J}$	
				$\vec{S}$=$\vec{0}$ Fermi	$\vec{S}$=$\vec{1}$ Gamow-Teller
super-allowed	2.9-3.7	0	+	0	0
allowed	4.4-6.0	0	+	0	0,1
first forbidden	6-10	1	-	0,1	0,1,2
second forbidden	10-13	2	+	1,2	1,2,3
third forbidden	>15	3	-	2,3	2,3,4

3.10 Experimental Tools employed

For the detection of γ-rays, it is necessary to use a detector made up of a material with high Z so that the photoelectric cross-section is maximized. Moreover, for high resolution γ-ray spectroscopy, the detectors should have the good energy resolution and reasonable efficiency. Semiconductor detectors made of High-Purity Germanium (HPGe) crystals are preferably used for the detection of γ-ray photons and β particles in γ spectroscopy and β-decay experiments, respectively.

3.10.1 High-Purity Germanium (HPGe) detectors

These detectors are semiconductor type detectors. The important parameter which is of consideration is the active volume of the detector determined by the thickness 'd' of the depletion region. The depletion region exhibits some very attractive properties as a medium for the detection of radiation. The electric field that exists causes any electrons created in or near the junction to be swept back towards the n-type material, and any holes are similarly swept toward the p-type side. The concentration of holes and electrons is greatly suppressed in that region. The only significant charges remaining in the depletion region are the immobile ionized donor sites and filled acceptor sites. Because these later charges do not contribute to conductivity, the depletion region exhibits a very

3.9.2.2 Gamow-Teller β-decay

In the Gamow-Teller decay mode, the conservation of angular momentum requires that the spin of the baryons should point in the opposite direction before and after the decay. This decay mode is sometimes called as the spin-flip mode.

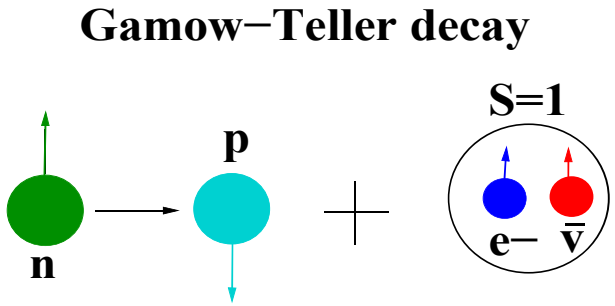

Figure 3.8: Conservation of angular momentum in Gamow-Teller decay.

The leptons (electron and neutrino) are light. The lepton orbital angular momentum L can be different than zero if leptons are emitted at high energy. However, the energy available to the leptons can not exceed Q which imposes limit on the angular momentum. As a consequence, the largest β-decay rates are for the processes with L=0 and the processes with L=1, 2 and 3 are possible but have rapidly decreasing probabilities or increasing lifetimes.

3.9.3 Parity

The conservation of angular momentum in the β-decay

$$\vec{J}_p = \vec{J}_d + \vec{L} + \vec{S} \implies \Delta\vec{J} = \vec{J}_p - \vec{J}_d = \vec{L} + \vec{S} \tag{3.24}$$

imposes the following condition on the parity of the initial and final state

$$\pi_p = \pi_d(-1)^L \implies \pi_p\pi_d = (-1)^L \tag{3.25}$$

with L being the magnitude of the lepton angular momentum $\vec{L}$. Based on these conservation laws, the observed β-decay process are classified into several groups. Various observed groups are

value, the more probable is the occurance of the transition. Transitions in which the value of M_{if} is near unity produce the lowest values of *ft* are called *superallowed*. Forbidden transitions can have *ft* values several orders of magnitude larger than the allowed ones. The use of log *ft* values allows separation of the several transitions by their degree of forbiddenness, since each degree has a certain range of log *ft* values. However, this separation is not perfect since, the bands intercept themselves.

3.9.2 Conservation of angular momentum

The conservation of angular momentum in the β-decay requires that

$$\vec{J}_p = \vec{J}_d + \vec{L} + \vec{S} \tag{3.23}$$

with $\vec{J}_p$ and $\vec{J}_d$ being the spin of the parent and the daughter and $\vec{L}=\vec{L_e}+\vec{J_\nu}$ being the orbital angular momentum of the leptons and $\vec{S}=\vec{S_e}+\vec{S_\nu}$ being the spin angular momentum of the leptons. There are two types of β-decay, the Fermi decay with $\vec{S}=\vec{0}$ (see Fig. 3.7) and the Gammow-Teller decay with $\vec{S}=\vec{1}$ (see Fig. 3.8).

3.9.2.1 Fermi β-decay

In the Fermi decay mode, the conservation of angular momentum requires that the spin of the baryons should point in the same direction before and after the decay.

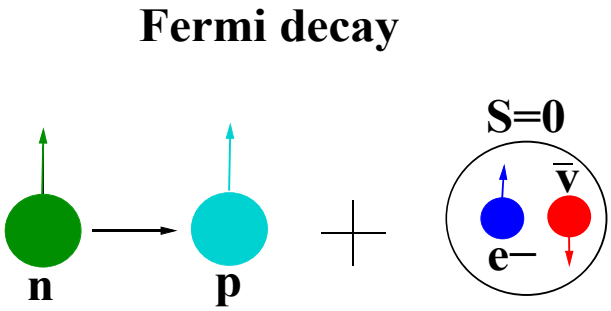

Figure 3.7: Conservation of angular momentum in Fermi decay.

leads to excellent *signal to noise ratio* and, therefore, a better energy resolution of the detector. So, energy resolution depends on the detector material and on the statistics of charge carrier. For example, a Sodium Iodide (NaI) detector may have a resolution of 7.5 % at 122 keV whereas a germanium detector may give resolution of 0.46 % at the same energy.

3.9 Features of β-decay

One of the most common form of radioactive disintegration is β-decay, detected in isotopes of practically all elements, with the exception, up to now, of the very heavy ones at the extreme of the chart of nuclides. It consists in the emission of an electron and an antineutrino (β^--decay) or in the emission of a positron and a neutrino (β^+-decay), keeping the nucleus, in both cases, with the same number of nucleons. In case of β-decay, the electron (positron) is forbidden to exist inside the nucleus and is created at the instant of the emission by means of the so-called *weak interaction*, one of the four fundamental particle interaction, along with the nuclear, electromagnetic, and gravitational ones. It is responsible for the transmutation of a neutron into a proton with the emission of an electron and an antineutrino or the change of a proton into a neutron with the emission of a positron and a neutrino. In case of β-decay, as more than one particle is emitted, there is a continuous spectrum for the kinetic energy of the emitted particles. As the mass of a proton is less than that of the neutron, the positron decay of a free proton is impossible. However, for a proton bound in a nucleus, such a transformation is possible since the missing energy is supplied by the nucleus.

3.9.1 β-decay transition probability

According to Fermi's theory of β-decay,

$$ft_{\frac{1}{2}} = \frac{1.386\pi^3\hbar^7}{g^2m^5c^4 \mid M_{if} \mid^2} \tag{3.22}$$

where $\mid M_{ij} \mid^2$ is a nuclear matrix element representing the overlap between the initial and final *nuclear* states. The product $ft_{1/2}$ or, simply, ft, depends only on M_{ij}: the larger the matrix element

It depends not only on detector properties but also on distance from source to detector.

ϵ_{int}=intrinsic efficiency, $\epsilon_{geom.}$=geometric efficiency

$$\textbf{Intrinsic efficiency} : \epsilon_{int} = \frac{events\ registered}{events\ impinging\ on\ detector} \tag{3.19}$$

It depends on the detector material, the radiation energy and the thickness of the detector in the direction of the incident radiation. Geometric efficiency, in contrast, is that fraction of the source radiation which is geometrically intercepted by the detector. It depends entirely on the solid angle subtended by the detector on the source position.

$$\textbf{Geometric efficiency} : \epsilon_{geom.} = \frac{events\ impinging\ on\ detector}{events\ emitted\ by\ the\ source} = \Omega/4\pi \tag{3.20}$$

The above definition assumes isotropic emission of γ-rays from the source.

3.8.5 Energy Resolution of a detector

The energy resolution of a detector is conventionally defined as the full-width at half-maximum (FWHM) of the full energy peak divided by the value of the energy of this peak. The width of the peak originates from the random statistical fluctuations that occur in the charge creation and collection process and from various noise sources. This results in a Poisson distribution of the number of charge carriers (n) produced by the interaction of γ-ray photon with the detector material. The noise includes contributions from both the detector and its associated electronics. Total FWHM can be expressed as

$$(FWHM)^2_{total} = (FWHM)^2_{statistical} + (FWHM)^2_{noise} \tag{3.21}$$

For large 'n', the Poisson distribution leads to a Gaussian distribution and the corresponding FWHM is related to the standard deviation σ by FWHM=2.36σ. When the energy required to produce a unit charge carrier in a detector is small, the number of charge carriers generated per unit energy of incident radiation in the detector is large, resulting in less statistical fluctuation. It eventually

process of internal conversion is caused by the direct interaction of the nucleus with its surrounding electrons. In any case, the nuclear charge does not change in internal conversion, so that this process is not a form of β-decay. Internal conversion is a nucleus de-excitation mode which often competes with γ emission. It is also called as *electronic conversion*. The internal conversion probability is the largest for electrons belonging to the innermost K layer and decreases rapidly with the outermost layers. When the electron is emitted from an inner shell, the vacancy is rapidly filled up by an higher shell electron, leading to the emission of characteristic X-rays. The competition between internal conversion and γ decay is quantified in the form of the *internal conversion coefficient* which is defined as $\alpha = e/\gamma$ where e is the rate of electron conversion and γ is the rate of γ-ray emission observed from a decaying nucleus. For increasing *atomic number* (Z) and decreasing γ-ray energy, internal conversion coefficients are observed to increase.

Internal conversion is favored over the γ-ray emission whenever the energy available for a gamma transition is small ($\leq$200 keV), and it is also the primary mode of de-excitation, e.g., in case of $0^+ \rightarrow 0^+$ transitions, only conversion electrons are emitted since emission of γ-ray photons are forbidden by angular momentum conservations.

3.8.4 Gamma detection efficiency

All radiation detectors, will give rise to an output pulse for each quantum of radiation. For charged particle radiation such as α or β-particles, interaction in the form of ionization will take place immediately. After travelling a small fraction of its range, a particle will form enough ion pairs along its path to ensure that the resulting pulse is large enough to be recorded. Thus, a detector will see every α or β-particle that enters its active volume. Under this condition, the detector is said to have a counting efficiency of 100 %. But, uncharged radiation like γ-rays or neutrons must first undergo a significant interaction in the detector before detection is possible. Because these radiation can travel large distance between interactions, detectors are often less than 100 % efficient.

$$\textbf{Total efficiency} : \epsilon_{tot} = \frac{events\ registered}{events\ emitted\ by\ the\ source} \tag{3.18}$$

between the initial and final state (i.e., $\mid J_f - J_i \mid$)=L). The lowest possible multipole transition is favored, since the total transition probability ratio decreases with increasing L according to the relation:

$$T_{fi}(\sigma L) = \frac{8\pi(L+1)}{\hbar L[(2L+1)!!]^2}(\frac{E_\gamma}{\hbar c})^{2L+1}B(\sigma L \ : \ J_i \ \rightarrow \ J_f), \tag{3.16}$$

where σ is either E or M signifying Electric or Magnetic transition, L is the multipolarity, E is energy of the emitted photon, and $B(\sigma L \ : \ J_i \ \rightarrow \ J_f)$ is the reduced transition probability. Often, multipolarity of a transition is not and pure, rather, there is an admixture of different multipolarities. The transition probability for a mixed multipolarity transition (generally restricted to $M1/E2$ decays) can be calculated using multipole mixing ratio, δ, it is related to transition probability T by the expression:

$$\delta^2_{E2/M1} \ = \ \frac{T(E2 : J \ \rightarrow \ J-1 \ )}{T(M1 : J \ \rightarrow \ J-1)} \tag{3.17}$$

The above transition probabilties assume that the transition is due to a jump of single nucleon from one shell model state to another.

3.8.3 Internal Conversion

A nucleus in an excited state can pass spontaneously to a state of the same nucleus, but of lower energy, either by emitting a γ ray with an energy hν equal to the difference between the energies of the two nuclear states, or by giving the energy to an electron in the K-, L-, ..., shell of the same atom. The electron is ejected with kinetic energy hν-E_K, hν-E_L,..., where E_K, E_L,... are the binding energies of the electron in the K-, L-,..., shells, respectively. This process is called *internal conversion.* It was thought earlier that the energy of the nuclear transition was first emitted as γ radiation, the γ ray then ejecting a photoelectron just as it would have emitted from any atom through which it might pass. It has been shown later that this explanation is incorrect and that the

corresponds to the full energy of the γ ray. Larger the volume of the detector, the more reduced will be this effect.

3.8.2 Electromagnetic Transition Probabilities

In a nuclear reaction, the nuclei produced in the exit channel are raised to a certain level of excitation depending on the bombarding energy as well as the target-projectile combination involved. The nuclei even after evaporation of light charged particles, neutrons and continuum γ-rays, remain in excited states for a short period of time. When a nucleus produced in an excited state, decays from an initial state (E_i, J_i^π) to a final state (E_f, J_f^π), it usually emits a γ-ray photon with a discrete energy ($E_\gamma = E_i - E_f$). The γ-ray, being the result of decay of a multipolar electromagnetic excitation of the nucleus involved, will have a definite multipolarity, and will follow a certain set of selection rules depending on the angular momenta and the parity of the initial and final state. If the nature of the electomagnetic excitation follows that of the dynamics of a purely charged system, the corresponding transition is called Electric (E) type. Whereas, if it involves dynamics of a purely magnetic system, the corresponding transition is called Magnetic (M) type. The multipolarity of a γ-transition means, how much angular momentum is carried away from the nuclues by the detected γ-ray.

$$\textbf{Multipole Selection Rule} \ : \ \mid J_i - J_f \mid \ \leq \ L \ \leq \ \mid J_i + J_f \mid \tag{3.14}$$

As the intrinsic spin of photon is 1 $\hbar$, γ-ray transition from 0^+ to 0^+ (i.e., L=0) is forbidden.

$$\textbf{Parity Selection Rule} \ : \ \pi(EL) = (-1)^L, \ \pi(ML) = (-1)^{L+1} \tag{3.15}$$

Thus, if there is no parity change (π_i=π_f), then, the transition is either an even Electric or an odd Magnetic and if there is a parity change (π_i=-π_f), then it is an odd Electric and even Magnetic transition. A *stretched* transition is one in which the photon carries the algebric spin difference

by,

$$E_e^{max} = \frac{2E_\gamma^2}{m_0c^2 \ + \ 2E_\gamma} \tag{3.13}$$

This is known as the *Compton Edge*. Thus, the Compton Scattered electrons are manifested in the γ-energy spectrum as a continuum distribution upto E_e^{max} below the corresponding full energy photopeak. So, at all angles, less than 100% of the total γ-ray energy is absorbed by the detector leading to an undesirable continuous Compton background. Solution to this undesirable background will be discussed in the subsequent section. Compton Scattering cross-section is dependent on the number of available electrons for the photons to scatter from, and hence, increases with increasing Z.

3.8.1.3 Pair Production

This process occurs at relatively higher energies when a γ-ray, exceeding twice the rest mass energy of an electron ($m_0c^2 \ = \ 0.511 \ MeV$), is converted into an electron-positron pair ($e^+ - e^-$), and the excess energy is shared as the kinetic energy of these two particles. The $e^+ - e^-$ pair can, then, be absorbed in the medium. The positron will, subsequently, annihilate with an electron from the surrounding material to produce two back to back 511 keV photons (for conserving momentum). When both the annihilation photons are reabsorbed in the detector volume, a full energy peak at E_γ is detected. If one of the photons escapes the detector, then only a γ-ray of E_γ-0.511 MeV energy is observed in the energy spectra, which is known as *single escape peak*. If both the photons escape from the detector, the corresponding peak is observed at an energy E_γ-1.022 MeV, and this peak is known as the *double escape peak*.

Out of the three processes of γ ray interaction with matter, photoelectric effect is the important one for γ-ray spectroscopy experiment because γ-ray deposits its full energy in this process. Full energy deposition is also possible when a series of these interaction mechanisms take place within the detector volume. When a γ ray undergoes a Compton interaction or pair production, and a portion of the energy escapes from the detector volume without being absorbed, the backgroud in the spectrum is increased by one count. This count will appear in a channel below the channel that

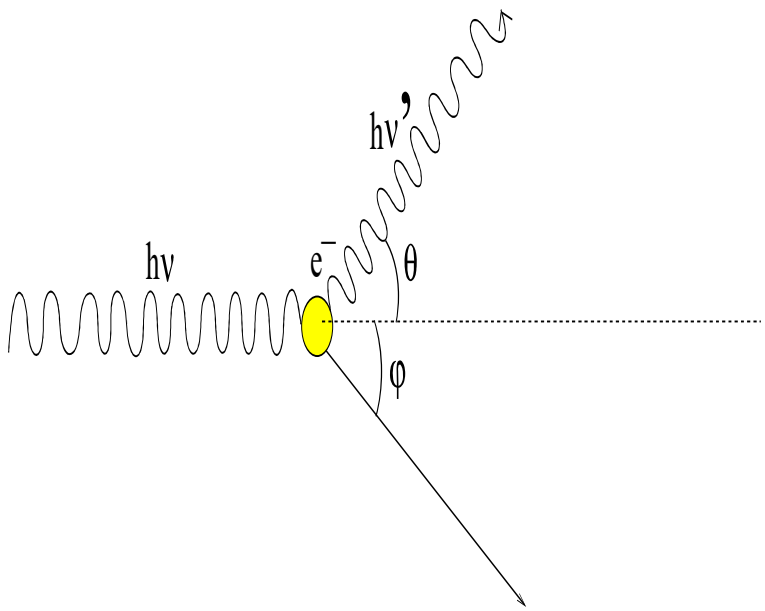

Figure 3.6: An illustration of the process of Compton scattering. An incident photon with energy hν interacts with an electron in the medium and imparts some of its energy to it. The scattered photon, then, propagates away at an angle θ with respect to its original trajectory and with a lower energy hν', while the electron recoils away at some other angle ϕ and energy given by Eq. 3.12

3.8.1.2 Compton Scattering

This is the most probable interaction in the intermediate energy range (100 keV $\leq E_\gamma \leq$ 1500 keV). During this process, an incident γ-ray is elastically scattered from a loosely bound electron in the absorbing material (see Fig. 3.6). The result is the creation of a recoil electron and scattered γ-ray photon, with the division of energy between the two depending on the scattering angle. According to the law of conservation of energy, the K.E of recoil electron can be written as:

$$E_e = h\nu - h\nu\prime = \frac{E_\gamma^2(1-\cos\theta)}{m_0c^2 \ + \ E_\gamma(1-\cos\theta)} \tag{3.12}$$

where, $E_\gamma = h\nu$ and $h\nu\prime$ are the incident and scattered γ energies respectively, θ is the angle at which the γ-ray is scattered relative to its original direction, and m_0c^2 is the rest mass of the electron. Generally, Compton Scattering produces a continuous distribution of electron energies (E_e), known as Compton Continuum, ranging from the $E_e = 0$ for θ=0° to its maximum value (at θ=180°) given

are three major interaction processes by which γ-radiation deposits energy in the detector medium, namely, *photoelectric absorption*, *Compton scattering* and *pair production*.

3.8.1.1 Photoelectric Absorption

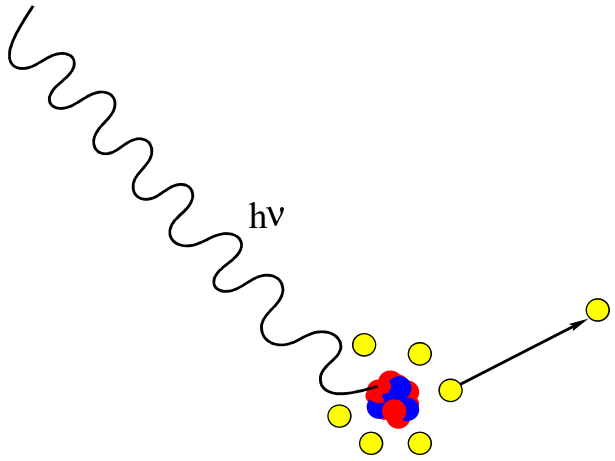

Figure 3.5: An illustration of the photoelectric effect. An incident photon interacts with an atom and deposits its energy, causing the ejection of an electron.

It is the most desirable process for γ-spectroscopy which is dominant mainly at relatively low energies ($\leq$ 200 keV). In this process, photon interact with an absorber atom (see Fig. 3.5) in which photon disappears completely and one of the bound atomic electrons is ejected. The interaction can't take place with a free electron. For γ-rays of sufficient energy, the most probable origin of the photoelectron is the K-shell of the atom. The energy of this ejected electron E_e is given by, E_e=E_γ-E_b, where E_b is the binding energy of the atomic electron. The vacancy left by the ejected electron in the atomic orbital may be filled by an electron from the outer shell resulting in emission of characteristic X-ray. These X-rays are usually absorbed in the detector itself. So, photoelectric effect results in a sharp peak corresponding to the full energy of the incident photon. The probability for photoelectric absorption per atom varies as: $Z^n/E_\gamma^{3.5}$, where Z is the atomic number of the detector material and n varies from 4 to 5.

3.1. The $\gamma-\gamma$ and $\gamma-\gamma-\gamma$ coincidence measurements following the reaction ^{148}Sm(^{16}O,4n)^{160}Yb were carried out at TIFR, Mumbai. This experiment was performed to populate the low and moderate spin states of ^{160}Yb by using conventional gamma ray spectroscopic technique with the Indian National Gamma Array (INGA). This was followed by two other experiments - one of them was performed to measure the excitation functions for the ^{150}Nd(p,xpyn) reaction by stacked-foil activation technique at VECC, Kolkata and the another experiment was done to search for the presence of Isomeric states in ^{150}Pm by decay spectroscopy using the reaction ^{150}Nd(p,n)^{150}Pm. For the study of isomeric state in the later nucleus, the half lives of the observed γ transitions were followed and the $\gamma-\gamma$ coincidences were observed. The β-decay end-point energies corresponding to the decay from the ^{150g}Pm and ^{150m}Pm have also been measured. The following sections would deal with a brief discussion on the experimental techniques, data processing and analyzing techniques used in the present investigations.

3.8 Features of γ ray spectroscopy

The basics of γ-ray spectroscopy can be divided into two major aspects which are highlighted in the following sub-sections. These are the mechanism of conversion of γ-rays into electrical signals, and extraction of spectroscopically relevant information from the detected γ-rays.

The γ-rays are said to be detected by the detector, when they deposit energy into the detector medium resulting in electrical pulses, which carry a lot of information regarding the characteristics of the electromagnetic radiation. Let us now look at how the energy deposited in the detector medium gets converted to the electrical pulses. In order to do that, a close look at the process of energy deposition into the detector medium is required.

3.8.1 Gamma ray interaction with matter

A significant fraction of the deposited energy produce electron-hole pairs which are then drifted away by the large electric field applied externally to the medium. The moving charge carriers induce electric signals at the electrodes, which are processed and analyzed by the electronics. There

Eq. 3.9. The Kinetic Energies of the compound nucleus and the residual nucleus are calculated using Eqs. 3.10 and 3.11 respectively. The energy loss of the recoiling nuclei inside backing is, then, calculated using the simulation code SRIM [ZIE]. Thus, the minimum thickness of the backing material has been chosen in a way so as to stop all residual nuclei inside the backing which are produced at the last layer of the target.

3.7 Experiments related to the present thesis work

Table 3.1: List of Experiments carried out in the present work.

Accelerator & Laboratory	Reaction used	Projectile Energy	Measurements done	Nucleus studied
K=130 AVF Cyclotron VECC Kolkata	^{150}Nd(p,n)	7-15 MeV	Excitation Function	^{150}Pm
K=130 AVF Cyclotron VECC Kolkata	^{150}Nd(p,n)	8 MeV	decay spectroscopy $\gamma-\gamma$ coincidence, β-endpoint energy & half-life of γ-rays	^{150}Pm
14 UD Pelletron TIFR, Mumbai	^{148}Sm(^{16}O,4n)	90 MeV	$\gamma-\gamma$ coincidence & $\gamma-\gamma-\gamma$ coincidence	^{160}Yb

In the present work, different in-beam and off-beam γ spectroscopic techniques have been employed as per the requirements, using the experimental facilities availabe at TIFR (Tata Insitute of Fundamental Research) and VECC (Variable Energy Cyclotron Centre), as indicated earlier in table-

The targets, thus, prepared were dried under IR lamp and then kept in a vaccum descicator. The precursor for each type of target was either in nitrate or chloride form and isopropyl alcohol was used as the organic medium for the electrodeposition.

For the heavy ion experiment done at the BARC-TIFR Pelletron Accelerator, we have used 97% enriched 900 μg/cm^2 Sm_2O_3 target prepared by electro-deposition technique on a 3 mg/cm^2 Pb backing foil.

In course of the experiment done using proton beam at VECC, the ^{150}Nd target was prepared from commercially available 97.65 % enriched powdered oxide sample (Nd_2O_3), on a 0.3 mil thick Aluminium (Al) foil. The thickness of the targets used in the experiment was $\approx$ 900 μg/cm^2.

3.6 Beam selection, Target and Backing Thickness

A higher beam energy combined with a thicker target may produce a larger number of nuclei of interest but at the cost of an enhanced production of other strong reaction channels potentially affecting the quality of the γ-ray energy spectra of interest. When the main objective is to study the low-lying states of the weak evaporation channel, the energy of the beam should be estimated in such a way that it is only slightly higher than the Coulomb barrier to reduce other unwanted reaction channels as much as possible. By considering different beams and targets and comparing the estimated relative yield of the nucleus of interest to the total fusion evaporation yield, the beam target selection should be optimized in such cases. Targets often have a thicker gold or lead backing to stop the recoiling nuclei. The choice of these high-Z stoppers is due to their higher Coulomb barrier which reduces the likelihood of beam-induced fusion events in the backing. Also, higher Z stoppers cause the nucleus to slow down faster. For this purpose, we have to calculate the rate of loss of energy, dE/dx (in MeV/(mg/cm^2)) of the recoiling nucleus inside the target and backing materials so as to make an estimate of the thickness of the backing required. The simulation code SRIM [ZIE], based on the Monte Carlo tenchiques is used to calculate the energy loss of the projectile and residual nucleus inside the target and the backing. For the chosen target-projectile combination and the beam-energy, the recoil velocity of the compound nucleus is calculated using

3.5 Target Preparation

For the nuclear physics experiments, the preparation of targets is of considerable importance [UET97]. The parameters such as thickness, uniformity, backing, chemical form, etc., of the target are important inputs for any light or heavy ion induced experiment. The target must be strong enough to withstand stress related to mechanical and thermal shock and should not break under vacuum. For the preparation of targets related to the present thesis, *Electrodeposition* process in a

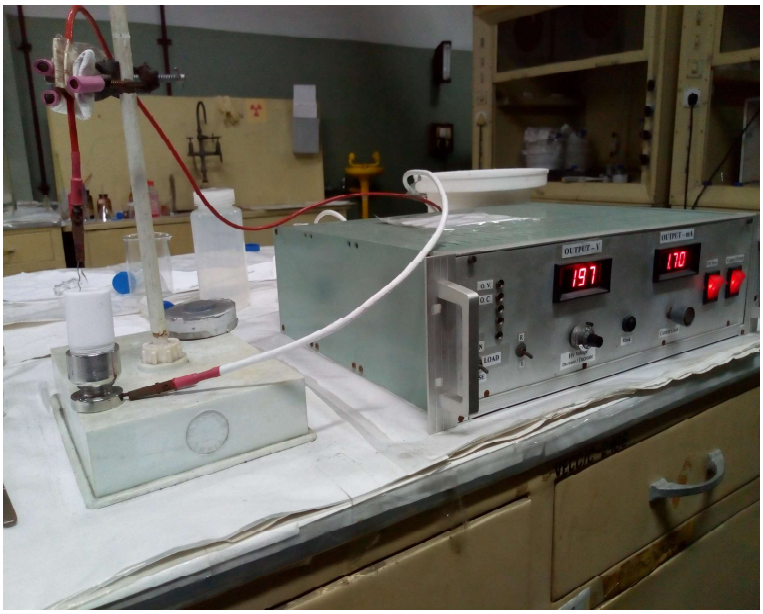

Figure 3.4: Experimental set-up for the electrodeposition process used for preparation of targets.

non-aqueous medium has been employed. The experimental set-up used for this purpose has been shown in Fig. 3.4. Electodeposition is the conventional process of coating a thin layer of one metal on top of a different metal. It is a process, based on the principle of electrolysis, that uses electrical current to reduce the cations of a desired material from an electrolyte and coat those materials as a thin film onto a conductive substrate surface. For the electrodeposition process, a voltage of 500 V and current of 1 - 3 mA were used. The target was deposited on Al-foil and the *weight difference method* was used to weigh the target. The deposited targes were made with a diameter of 10 mm and weight of 900 μgcm^{-2}. Duration of the electrodeposition process was $\sim$1 hr for each target.

A∼150 region which is described in details in chapter 6.

3.4 Calculation of Coulomb Barrier

The basic principle of the fusion process is that when two nuclei come close to each other, they fuse together to form a compound nucleus. Classically, the formation of compound nucleus is possible only when the kinetic enery of the system is greater than the coulomb barrier of the system. The coulomb barrier in the lab frame can be expressed as,

$$V_{B(lab)}(MeV) = V_{B(cm)}\frac{A_T + A_P}{A_T} \tag{3.8}$$

where A_P and A_T are the mass numbers of the projectile and target, respectively.

It is also necessary to calculate the velocity (β) of the residual nucleus of interest. The $\beta(= v/c)$ value of the compound nucleus is given by,

$$\beta = 0.046\frac{\sqrt{(A_P E_{lab})}}{A_T + A_P} \tag{3.9}$$

The kinetic energy of the compound nucleus and the residual nucleus are

$$K.E_C(MeV) = \frac{931.5}{2}A_C\beta^2 \tag{3.10}$$

and

$$K.E_R(MeV) = \frac{931.5}{2}A_R\beta^2 \tag{3.11}$$

respectively. This energy of the residual nucleus is crucial for the estimation of the target and the backing thickness. Because the knowledge of the energy together with the rate of energy loss of the residual nucleus through the target and backing material act as the guiding factors for deciding their thickness to be used.

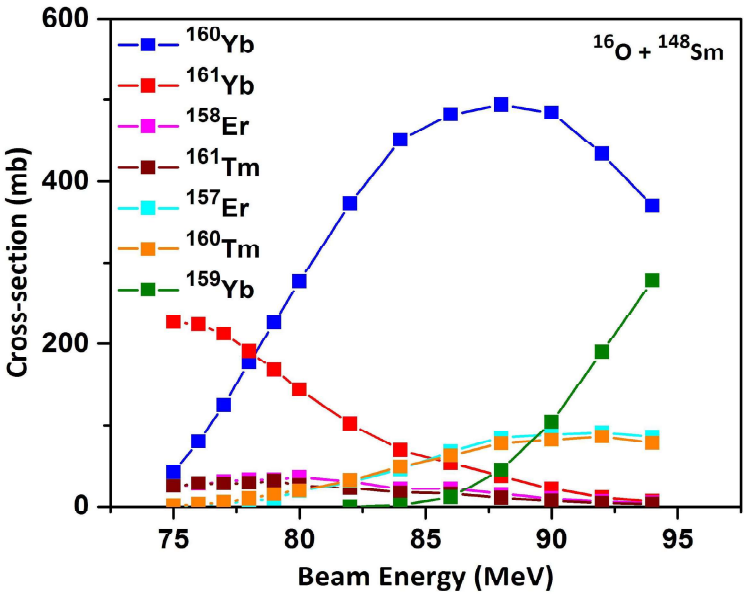

Figure 3.3: Production Cross-section (in mb) of the residual nuclei at varying beam energies (in MeV) populated in the ^{16}O + ^{148}Sm reaction using PACE4 calculations.

approach [WON73]. The calculation with CASCADE [PUH77] code assumes the formation of a compound nucleus in statistical equillibrium, and the intensities of different evaporation residues are calculated applying the Hauser-Feshback formula in combination with the statistical nuclear model whereas ALICE/91 [BLA85] is a precompound and evaporation model code system for calculating the excitation functions and angular distribution of emitted particles in nuclear reactions.

For the ^{150}Nd(p,n)^{150}Pm and ^{148}Sm(^{16}O,4n)^{160}Yb reactions related to the present thesis, PACE4 has been used for selecting the beam energy for the appropriate Target-Projectile Combination. The selection of energy of the projectile is done using this model by looking at that energy value for which the production cross-section of the nuclei of interest is maximum. For example, Fig. 3.3 depicts the results of variation of the production cross-section with beam energy, of the various recoiling nuclei populated in the ^{16}O + ^{148}Sm reaction, obtained using PACE4 calculations. It is clear from this figure that the production cross-section of ^{160}Yb (one of the nuclei of interest) is maximum at a beam energy of around 90 MeV. Moreover, sometimes it is very important to estimate the low cross-section of the residues produced from the particle evaporation channels and the present thesis work also encompasses such estimatation regarding the various isotopes of Pm nucleus around mass

are emitted parallel to the yrast line are either dipole or quadrupole type with electric or magnetic character, although a large fraction are either E2 or M1 type. Within about 10^{-9} s, the total decay process is completed. The stages of the de-excitation process for the compound nucleus are shown schematically in Fig. 3.2.

3.2.2 Low Spin States : Decay Spectroscopy

Only few alternative probes are available for investigating non-yrast states in nuclei. The careful investigation of the β-decay from a parent nucleus is one of the useful ways to study the unique non-yrast states in nuclei which may not be resolved with the use of fusion evaporation reaction. Also, many of the nuclear excited levels in the region of interest for this thesis can not be populated with the HI fusion evaporation and the available stable target and projectile combination. In those cases, the LI induced reactions become important which is able to produce nuclei on the neutron rich side of the beta stability line by using neutron rich target. Such an investigation has been done as a part of this thesis work in order to understand the population of n-rich nuclei in A $\sim$ 150 region by using LI induced reaction. Decay spectroscopy is very much useful for studying some of the unique phenomena in nuclei with the study of low lying states.

3.3 Selection of Target-Projectile Combination

In order to populate the excited states of the nucleus of interest, a proper selection of the ion beam and the target is essential. Before the experiment, the production cross section of the reaction channel of interest and the most competing neighboring reaction channels are estimated by running statistical simulation codes such as CASCADE [PUH77], ALICE [BLA85], PACE4 [TAR08, GAV80] etc. PACE4 (**P**rojection **A**ngular-momentum **C**oupled **E**vaporation) is a Monte-Carlo fusion-evaporation code coupling angular momentum. This code enables us to have an idea about the cross-section of the various nuclei produced as a result of particle evaporation after compound nucleus formation for a particular beam energy and a target-projectile combination. Moreover, it can be used to calculate a fusion cross section below the Coulomb barrier using the quantum-mechanical

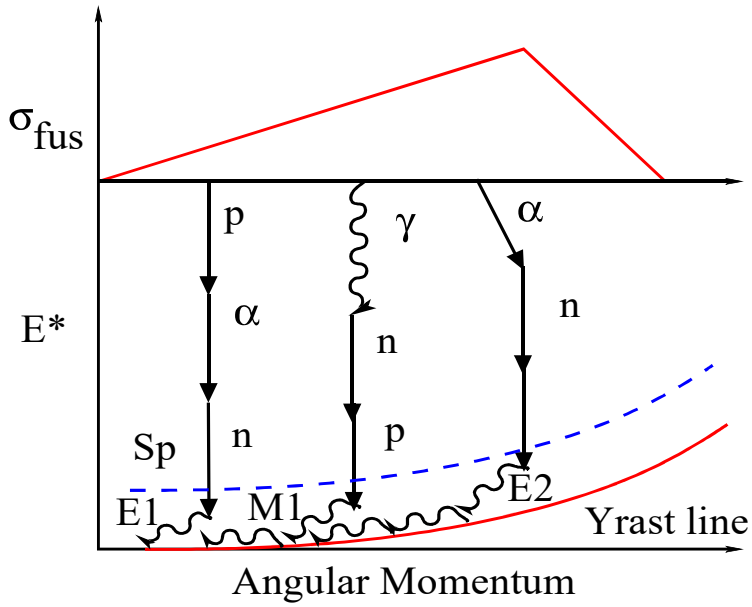

Figure 3.2: De-excitation process of a typical compound nucleus, produced in the present work.

hand, protons and alphas being charged particles, their evaporation are hindered by the Coulomb Barrier. Particle evaporation is no longer possible when the excitation energy becomes less than the particle emission threshold and the residual nucleus enters the *'entry-line'* which is roughly one neutron binding energy above the 'Yrast line'. When no more energy is left for particle emission, then the residual nucleus de-excites through emission of stretched γ-rays to reach the ground state. Now, for reaching to the ground state, two types of γ-rays are emitted : those that cool down the nucleus to or toward the yrast line, called *"statistical"* γ-rays and those that are more or less parallel to the yrast line and remove the angular momentum, called *"yrast-like"* γ-rays. At each point, there is a competition between these two types of γ-rays. From the entry-line, residual nucleus decay by emitting statistical γ-rays which are predominantly E1-transitions. They take away only a few units of angular momentum, but much of the energy. Since the nuclear level density is very high around the entry line, statistical γ-ray transitions are not resolvable and hence, called quasi-continuum transitons. When the yrast line is reached, the γ-rays cascade from one yrast level to the another carrying a major fraction of the angular momentum of the excited residual nucleus. These non-statistical γ-rays will have resolvable energies and are discrete in nature. The yrast-like γ-rays which

where μ, E_p and V are the reduced mass of the beam & target system, energy of the projectile in (centre of mass) c.m frame and Coulomb barrier respectively. Therefore, the maximum angular momentum transfer is given by

$$L_{max} = 2R\mu(E_p - V)^{1/2} \tag{3.4}$$

The grazing radius, reduced mass and energy of the projectile in the c.m frame are given by

$$R = R_0(A_p^{1/3} + A_t^{1/3}) \tag{3.5}$$

$$\mu = \frac{A_p * A_t}{A_p + A_t} \tag{3.6}$$

$$E_{CM} = \frac{E_{lab} * A_t}{A_p + A_t} \tag{3.7}$$

The main advantage of the heavy ion induced fusion evaporation reaction is that a very high angular momentum can be brought into the system. It allows us to populate states which we would otherwise be unable to study using other reactions (e.g., Coulomb excitation or transfer reactions.) In a fusion-evaporation reaction, the kinetic energy of collision in the centre of mass frame is converted into excitation energy of the compound system. The higher the energy and mass of the beam particles, the more will be the angular momentum transferred into the compound system. Fusion reactions only occur for small values of impact parameter, while other nuclear reactions occur at increased target-beam distances. The projectile and the target fuse together within 10^{-22} to 10^{-20} secs.

The compound nucleus formed, which is a very hot system can cool down by emission of protons, neutrons, alpha particles and with a much lower probability by emission of γ-rays, giving rise to various residual nuclei in the exit channel. The compound nucleus loses considerable amount of the excitation energy of about 8 MeV (one neutron separation energy) and only a few units of angular momentum (about 1-2 $\hbar$) per neutron or proton evaporation. Probability of evaporation of neutrons are more than protons, or alphas because neutrons do not face a Coulomb barrier. On the other

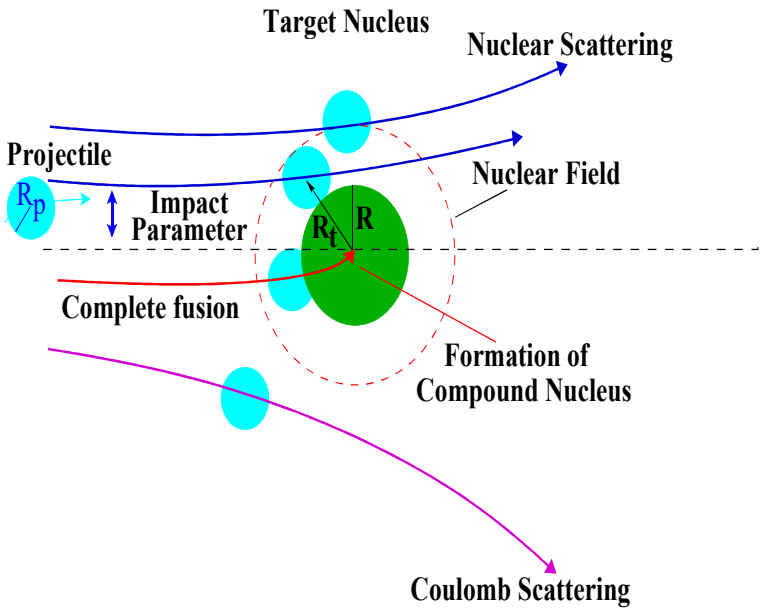

Figure 3.1: Schematic illustration of heavy-ion collision types.

the compound nucleus formation is that the beam energy must be large enough to overcome the coulomb barrier and angular momentum transfer should not be too high to cause fission. For a given projectile and target combination, the coulomb barrier is given by the following equation

$$V_{CB}(MeV) = \frac{1}{4\pi\epsilon_0}\frac{Z_p Z_t e^2}{R_0(A_p^{1/3} + A_t^{1/3})} \tag{3.1}$$

where Z_p and A_p are the *atomic number* and the *mass number* of projectile and Z_t and A_t are the *atomic number* and the *mass number* for target.

The maximum angular momentum transfer ,i.e., $\vec{L} = \vec{R} \times \vec{P}$ can be estimated from grazing radius

$$R = R_{target} + R_{projectile} \tag{3.2}$$

and momentum of the projectile when it hits the target nuclei, i.e.,

$$P = 2R\mu(E_p - V)^{1/2} \tag{3.3}$$

3.2 Production of Nuclear Excited Levels

The development of both HI and light ion accelerators together with high resolution detection systems has made it possible to populate and study the properties of the residual nuclei starting from very high excitation energy and angular momentum of the yrast cascade and down to very low-spin non-yrast states. By a proper choice of reaction and target-projectile combination, one is also able to produce nuclei which are substantially away from the line of β stability. Different types of nuclear reactions have been explored to produce nuclei on both sides of the stability line, having enough angular momentum and excitation energy in order to study the residual nuclei of interest. Similarly, it is also possible to populate a nucleus selectively at low spin which often helps in the study of non-yrast structures and isomers in nuclei. For producing moderate to high spin states, heavy ion fusion evaporation reaction is the suitable method whereas for low spin states, light ion induced reactions or decay spectroscopy are the best known methods. A brief description of the production and decay mechanism of nuclei at high spin is given in the following section.

3.2.1 High Spin States : Fusion Evaporation Reaction

Fusion evaporation reaction is a standard tool for the population of high spin states in nuclei. Different types of nuclear reactions occur when the target is bombarded with a projectile depending on the energy of the incoming beam and the impact parameter. Figure 3.1 gives a schematic representation of the various kinds of nuclear reactions possible with heavy ion beams based on the impact parameter. If the projectile energy is lower than the Coulomb barrier and the impact parameter is large so that their is no overlap between the nuclear matter distribution of the projectile and the target nuclei, *Coulomb excitation* is the most predominant one which refers to pure electromagnetic excitation of the nuclear states. If the energy of the projectile is slightly above the barrier energy with partial overlap of the nuclear matter of the target and the projectile, transfer of nucleons is favorable. When the matter distributions overlap and the energy of the projectile is above the coulomb barrier, then the compound nucleus formation takes place. The condition necessary for

the investigations reported in this thesis, will be presented. The experiments related to the present thesis were carried out at TIFR (Mumbai) and VECC (Kolkata) using different experimental setups based on different experimental objectives which have been summarised in Table-3.1. Before performing an experiment, statistical model calculations using standard computer codes like PACE IV provide a good guideline for the estimation of production cross-sections of various exit channels. Prior to an experiment for studying a particular nucleus of interest, it is usual to find the excitation function so as to decide the optimum beam energy to maximise the production cross-section and angular momentum input for the channel of interest because increasing the beam energy will increase the maximum input angular momentum but will also increase the excitation energy of the compound system, resulting in more particles being evaporated.

Detection of γ radiation is one of the most important research tools in nuclear physics. *Gamma Spectroscopy* is a powerful technique that deals with the study of nuclear structure by detection of γ radiation emitted from the de-exciting nucleus yielding information on various properties like excitation energies, angular momentum, decay properties etc. of states in nuclei. The present thesis work encompasses both in-beam prompt spectroscopy as well as off-beam decay spectroscopic studies. Now, during both in-beam and off-beam experiments, the de-exciting γ-rays from the excited states of the nucleus are detected using suitable detectors from which the level scheme is constructed on the basis of $\gamma-\gamma$ and/or $\gamma-\gamma-\gamma$ coincidence relationships. The multipolarity of the observed transitions emitted during the in-beam experiment related to the present thesis have been determined from the conventional method of DCO ratios (Directional Correlation of de-exciting γ-rays from Oriented states). For the determination of the electromagnetic nature (i.e., Electric or Magnetic) of the emitted transitions, IPDCO ratios (Integrated Polarizational Directional Correlation of gamma rays from Oriented nuclei) were calculated which is based on the asymmetry between the perpendicular and the parallel scattering w.r.t the reaction plane of the Electric and Magnetic transitions. In case of the off-beam experiment, the decay half-life of nuclear excited states have been measured by the conventional slope method. β end-point energy corresponding to several excited states have been measured using the conventional $\beta-\gamma$ coincidence technique.

Chapter 3

Experimental Techniques and Data Analysis

3.1 Introduction

Studies in low and medium energy nuclear physics have been dominated by Heavy-Ion (HI) induced reactions for last few decades. HI induced nuclear reactions have enriched our knowledge about the evolution of nuclear structure at the extremes of angular momentum and excitation energy. On the contrary, the Light-Ion (LI) beams can help in performing the horizontal spectroscopy in a nucleus and gives access to study nuclear structure phenomena observed in the non-yrast states populated in parallel to the yrast ground state bands. Using HI beams, we can populate nuclei in the proton rich side of the $N - Z$ plot because of the decreasing proton to neutron ratio for heavy stable nuclei. Though nuclear fission is the *'ideal'* process to produce neutron rich nuclei but LI induced reactions can produce those nuclei which are little away from the stability line of the N-Z plot towards the neutron rich side but are difficult to be produced via HI induced fusion evaporation reactions. During the present thesis work, experiments with both Heavy-Ion and Light-Ion (LI) beams have been carried out.

In this chapter, a brief description of the experimental facilities, variation mechanisms of radiation interaction with matter, radiation detectors, and the data analyzing techniques used for

of β and γ vibration bands respectively, in agreement with the evidence in Ref. [GUP81, GUP10]. These levels also follow the systematics in the Ce-Dy isotones (c.f Fig. 4.11). The observation of the 371.5 keV E2 transition decaying from the 1417.4 keV, 2_4^+ level; which is based on the 1255.4 keV, 0_3^+ level; to 2_β level identified in the present work supports the $\beta\beta$ character of the 1417.4 keV state.

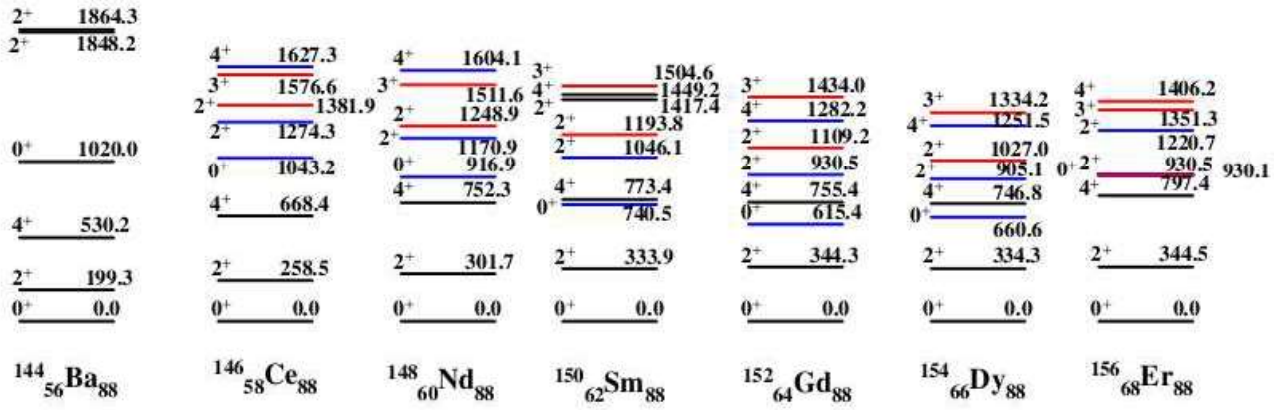

Figure 4.11: The systematics of the positive parity low lying levels in N = 88 Ce-Er nuclei. The levels those are assigned to the β band in a nucleus are coloured in blue and those to the γ band are coloured in red. The level energies are taken from NNDC.

4.5 Summary

The decay spectroscopy of ^{150}Pm has been performed by populating the nucleus with ^{150}Nd(p,nγ)^{150}Pm reaction at E_p = 8.0 MeV. The observed γ-rays were detected both in singles and coincidence mode with VENUS array having six Compton suppressed Clover HPGe detectors. The decay half lives have been followed for the observed transitions and their $\gamma - \gamma$ coincidences were studied. The outcome of the present experimental work has been the observation of nineteen new γ transitions and altered placements of eight earlier known transitions resulting in the addition of thirteen new levels of ^{150}Sm, as shown in Fig. 4.10, which could be populated from β-decay of ^{150}Pm. The *logft* analyses were performed using the intensities of different γ transitions to determine the J^π assignment for the levels in ^{150}Sm, populated from β-decay. From the *logft* analysis, J^π assignment was made to twenty eight levels for which the assignment was not known or was uncertain. Some of these assignments were also corroborated with the angular correlation measurement which could also confirm the pure E1 nature of five transitions in ^{150}Sm. The indirectly derived B(E1) values support the octupole character of the 1165.5 and 1658.4 keV levels. The intra- and inter-band E2 transitions from 2_2^+ and 2_3^+ levels, observed in the present work, suggest that these levels in ^{150}Sm are the candidates

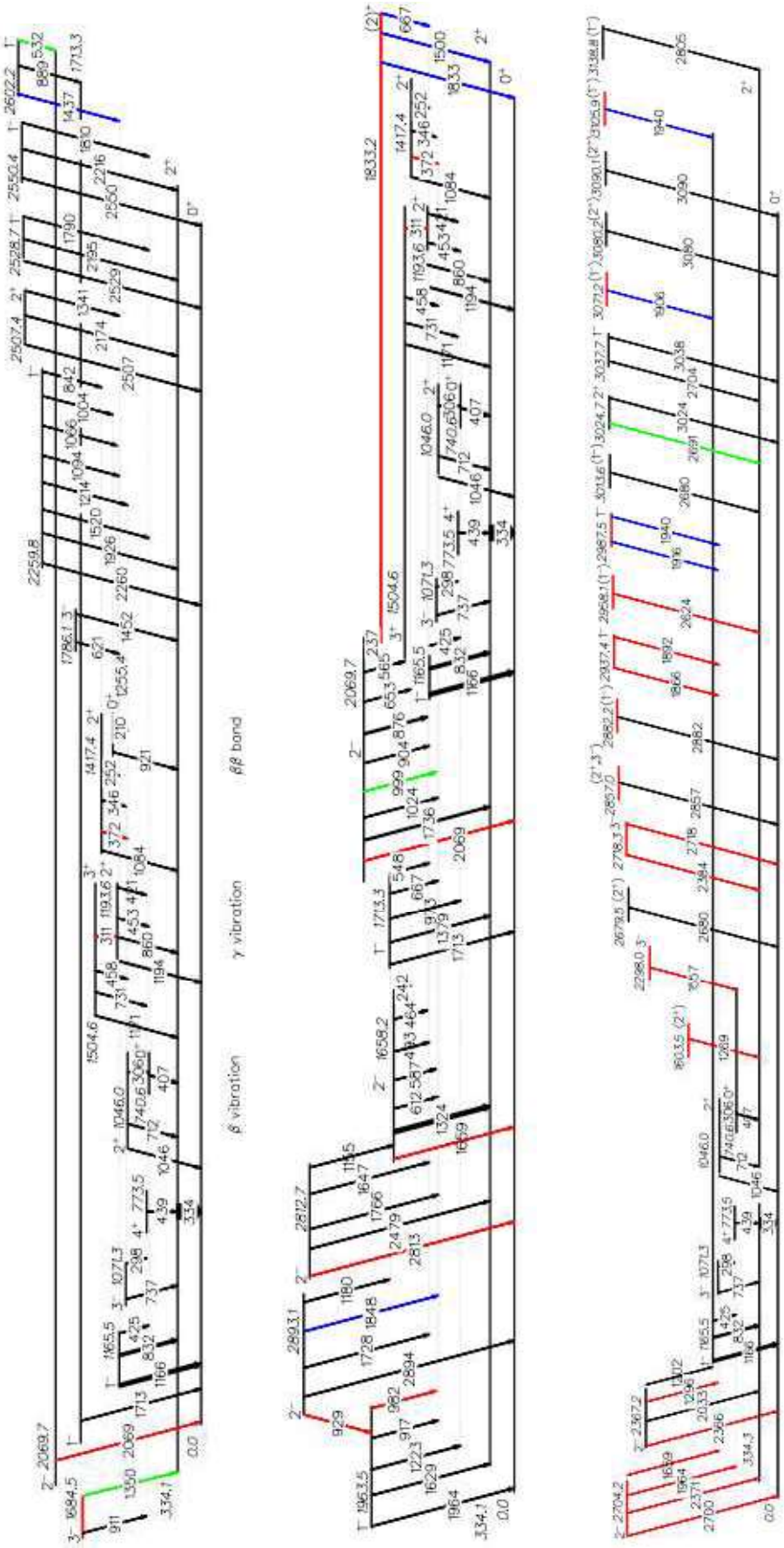

Figure 4.10: The partial level scheme for ^{150}Sm, obtained in the present work following the β-decay of ^{150}Pm, is shown in three parts. Some of the levels are shown in more than one part to completely show the decay and feeding of a particular level. The thirteen new levels placed in the decay scheme and nineteen new transitions found in the present work are shown with red. The transitions for which the placement is altered are shown with blue. The tentative transitions that are confirmed in the present work are shown with green. Some of the levels are shown in bold to increase the visibility.

the $B(E1)_{\gamma}/B(E1)_{832}$ ratios obtained from the measured intensity of the respective γ-ray. These estimations might be important for the interpretation on the possible structure of these levels as discussed in the following section.

4.4 Discussion

A number of low lying positive and negative parity excited levels of ^{150}Sm, as shown in Table 4.1 and Fig. 4.10, are populated from the β-decay of ^{150}Pm. The following two paragraphs are devoted to discuss the systematic observations made and experimental information derived in the present work on few specific positive and negative parity levels in ^{150}Sm.

The systematics of the β and γ bands observed in the neighboring nuclei has been shown in Fig. 4.11 including the 2_3^+ and 3_1^+ states of ^{150}Sm. Both of the latter two levels of ^{150}Sm follow this systematics for the K=2 γ phonon structure in the neighboring nuclei and their character is also understood from their similar decay pattern as suggested by Gupta *et al.* [GUP10].

In the present work, the connection of the 1417.4 keV, 2_4^+ level to the 2_2^+ level of the β band has been established with the placement of the 371.5 keV transition in the level scheme. This finding strongly supports the $\beta\beta$ character of the 1417.4 keV, 2_4^+ level. The 1417.4 keV level also decays to the 1165.5 keV, 1^- level which has a possible octupole structure based on pure E1 nature of the 831.5 keV transition decaying from this level to the 334.1 keV, 2_1^+ level.

The pure E1 transitions decaying from some of the negative parity levels have B(E1) strengths ranging from 0.02 mW.u to 2.9 mW.u, as observed from Table 4.2. Out of these, high values of the B(E1) strength of 2.9 mW.u and 1.1 mW.u for the 831.5 keV (ΔI = 1, E1) and 1324.1 keV (ΔI = 0, E1) transitions, respectively, indicate a possible octupole vibration involved in the structure of the 1165.5 keV, 1^- and the 1658.4 keV, 2^- levels, when compared to that observed in the neighboring ^{151}Pm [URB90].

the earlier β-decay spectroscopy [BAR70].

The most important observation of the present angular correlation analysis has been the possible assignment of pure $\Delta I = 0$ (1324, 1736 and 2033 keV) and $\Delta I = 1$ (832 and 1379 keV) E1 character to five transitions decaying from the five negative parity levels, viz., 1165.5, 1658.2, 1713.3, 2069.7 and 2367.2 keV respectively, to the ground state band. This assignment could be based on the fact that the experimental A_2 and A_4 coefficients for these cascades were close to the single-multipole solutions that are indicated by filled squares in Fig. 4.9. The negligible M2 admixtures(δ), that might be associated with these transitions are shown Table 4.2 and it was found to have an upper limit of $\sim$5%. The results on these five transitions were also compared with the earlier angular correlation measurements [SMI66, KAL75, RED69] which have several contradictions among themselves. It is observed that the present results are in line with the work of Kalfas *et al.* [KAL75], except the high values of M2 admixtures proposed for 1736 and 2033 keV transitions and the (3^+) assignment of the 2367.2 keV level. The pure $\Delta I = 1$, E1 nature of the 831.5 keV and 1379.2 keV transitions support the spin assignment of the 1165.5 keV and 1713.3 keV levels as 1^-. The J^π assignment of 1165.5 keV level was known from the earlier measurements and that of 1713.3 keV level is assigned in the present work. The E1 nature of the 1324.1, 1735.7 and 2033.1 keV transitions also support the spin assignment of the 1658.2 keV, 2069.7 keV and 2367.2 keV levels, respectively, as 2^-.

Table 4.2: Estimates of possible M2 admixure (δ) and B(E1) strength of the E1 transitions observed in the present work

E_γ (keV)	Cascade	Sequence (proposed)	A_2	A_4	δ	$\frac{B(E1)_\gamma}{B(E1)_{832}=2.9(12)}$ (Expt.) (mW.u)	$B(E1)_\gamma$ (approx.) (mW.u)
832	334-832	1→2→0	-0.270(27)	0.006(30)	-0.018(25)		
1324	334-1324	2→2→0	0.216(42)	0.003(46)	-0.046(35)	0.36(9)	1.1(5)
1379	334-1379	1→2→0	-0.276(28)	0.000(31)	-0.024(25)	0.06(2)	0.16(8)
1736	334-1736	2→2→0	0.270(72)	0.003(78)	0.028(108)	0.06(2)	0.16(8)
2033	334-2033	2→2→0	0.231(51)	0.012(55)	-0.026(19)	0.006(1)	0.018(8)

With the consideration of E1 nature of the five transitions, viz.,832, 1324,1379, 1736 and 2033 keV, their B(E1) values can be estimated in comparison to the known B(E1) of the 831.5 keV (2.9^{+14}_{-10} mW.u (10^{-3} W.u) [BAS13] γ-ray. The values are shown in Table 4.2 that have been calculated with

admixtures of two multipoles. When only one multipole is considered for both the gamma rays in the cascade, the mathematical solutions for A_2 and A_4 are unique and the ellipse converges to a point that indicates the single-multipole solution. The spin assignments to the various levels made

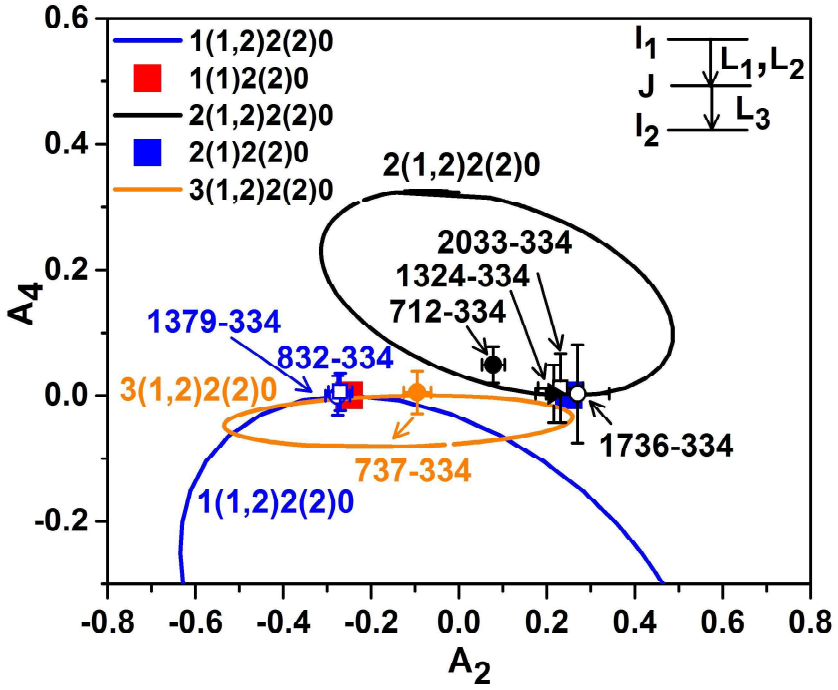

Figure 4.9: A comparision between theoretical solutions and the experimental data on $\gamma - \gamma$ angular correlation associated with the 334.1 keV ($2_1^+ \rightarrow 0_g^+$) E2 transition. Each measured angular correlation value (A_2, A_4) has been labeled with the energies of the two coincident gamma rays in keV. The ellipses, labeled according to the convention $I_1(L_1,L_2)J(L_3)I_2$, correspond to theoretical solutions of the angular correlations where the first correlated γ is an admixture of two multipoles L_1 and L_2. The single-multipole solutions are indicated by filled squares. The used convention is illustrated in the upper left corner of the figure.

from the *logft* analysis, discussed in Section 4.3.2.1, have been found also to be corroborating well with the angular-correlation results obtained in the present experiment. For instance, the angular correlation results for the 737-334 keV cascade agrees pretty well with the assigned 3→2→0 spin sequence. Similar is the case for the 1379-334 keV and 1736-334 keV cascades for which 3→2→0 and 2→2→0 spin sequences have, respectively, been proposed in the existing literature. Using the angular correlation results and the *logft* values, J^π assignment of the 2367.2 keV level has been changed from (3^+) to 2^-. This is also supported by the *logft* analysis and the prediction made in

ground state will be either M2 or E3 in nature. The M2 assignments to any of these transitions would, however, imply the level lifetimes $\sim$ few picoseconds (ps) to hundred ps, as was also discussed for the 2812.7 keV, 2^- level, in the earlier β-decay work [BAR70].

The $J^\pi = 2^+$ assignment has also been made for five of the levels in ^{150}Sm, by comparing their *logft* values with that of 1046 keV, 2^+ level. For some of these 2^+ levels, viz. 2507.4, 2679.5, 3080.2 and 3090.1 keV, their direct decay to the 0^+ ground state was also taken into consideration and the corresponding γ-rays were assigned to have E2 multipolarity. The J^π assignment of 2^+ for the 2679.5 keV level is based on the estimated *logft* value by considering the decay of this level through a single 2679.5 keV γ-ray. The 2^+ assignment to the 2679.5 keV level was also suggested in the earlier β-decay spectroscopy, based on the connection of this level to the 773.5 keV, 4^+ level in ^{150}Sm. However, in the present work, none of the transitions other than the direct ground state decay by 2679.5 keV could be confirmed from the $\gamma - \gamma$ coincidence measurement. Hence, the J^π value corresponding to this level has been shown in bracket. Similar treatment was adopted for all those levels which are based on the decay of a single γ-ray as the present work could not rule out the possibility of further modification of the decay of these levels.

In the present work, the $J^\pi = 3^-$ assignment was made to only one excited level, viz., 1786.1 keV level for which the spin was known as ≤ 3 and no parity was assigned. The present assignment is made by comparing the *logft* value obtained for this level to those of the 1684.5 and 2298.0 keV 3^- levels. Also it is considered that the 3^- assignment to the 1786.1 keV levels allows the 620.6 keV and 1452.4 keV γ decays from this level to the 1165.5 keV, 1^- and 2_1^+ levels, respectively, and these transitions could be E2 and E1 in nature. The 2857 keV level was also assigned a $J^\pi = (2^+, 3^-)$ from the derived *logft* value.

4.3.2.2 $\gamma - \gamma$ angular correlation measurements

In Fig. 4.9, the experimental values of angular correlation coefficients (A_2, A_4) are shown together with some of the theoretical solutions as a function of mixing ratio (δ) in order to determine the appropriate spin value for a particular level in the cascade. The theoretical solutions correspond to the ellipses shown in the figure when one of the correlated γ-ray is considered to have the

the present work, the 1684.5, 2298.0 and 2718.3 keV levels of ^{150}Sm are observed to be populated from β-decay of ^{150}Pm and the J^{π} assignments of 3^- to these three levels are confirmed from earlier works [BAS13]. The 1^- assignment to the ground state of ^{150}Pm does not corroborate with the 3^- spin-parity of these levels of ^{150}Sm, considering the *logft* values obtained for these levels (8.6(2), 9.2(1) and 9.6(2) respectively) and the corresponding range (10.6 - 14.2 for the $\Delta J = 2$, $\Delta\pi$ = 'no' decays) given for that in β-decay *logft* table [SIN98]. The *logft* values obtained for all these three levels and their known 3^- assignment supports, however, the $J^{\pi} = 2^-$ for the ground state of ^{150}Pm. Hence, the spin-parity of 2^- is considered for the ground state of ^{150}Pm while assigning the J^{π} values to the excited levels of ^{150}Sm based on the *logft* values.

The β-decay *logft* table [SIN98] has been used for this assignment and the J^{π} of the excited levels of ^{150}Sm are given in Table 4.1. The *logft* values for the levels with known spin-parity have also been taken as a guiding factor. For instance, the *logft* value for the 1165.5 keV level, for which the J^{π} value is already known as 1^-, comes out to be 7.7(1). Taking this as a guiding factor, the J^{π} value for the 1963.5 keV level has been assigned as 1^- which was shown as $1^{(-)}$ in the adopted level scheme. Similar is the case for the other levels with different spin-parity. References have also been taken from the considerations made in earlier experiments. It is worth mentioning that the *logft* values obtained for most of the levels, with already known J^{π}, lie on the higher side of the range of values provided in Ref. [SIN98]. Also, for many of the levels, the obtained *logft* values indicate the presence of Gamow-Teller (GT) type of β-decay of ^{150}Pm $\rightarrow$ ^{150}Sm.

Fifteen excited levels, observed in the present work, were found to have *logft* values close to 7.7(1), the *logft* value that has been obtained for the 1165.5 keV level. These levels were assigned to have $J^{\pi} = 1^-$ based on the known 1^- assignment of the 1165.5 keV level. Among these, the J^{π} assignment to the 2528.7 and 2550.4 keV levels as 1^- from the *logft* analyses also supports the proposition made by Barrette *et al.* [BAR70].

For six of the excited levels, $J^{\pi} = 2^-$ assignments were made from the present work. Out of these, the 2^- assignment of three levels, viz., 1658.2, 2069.7 and 2367.2 keV, are also supported by the angular correlation analysis. In the present work, the direct decay of all these six 2^- levels to the 0^+ ground state are observed. The γ transitions which are connecting these 2^- levels to the 0^+

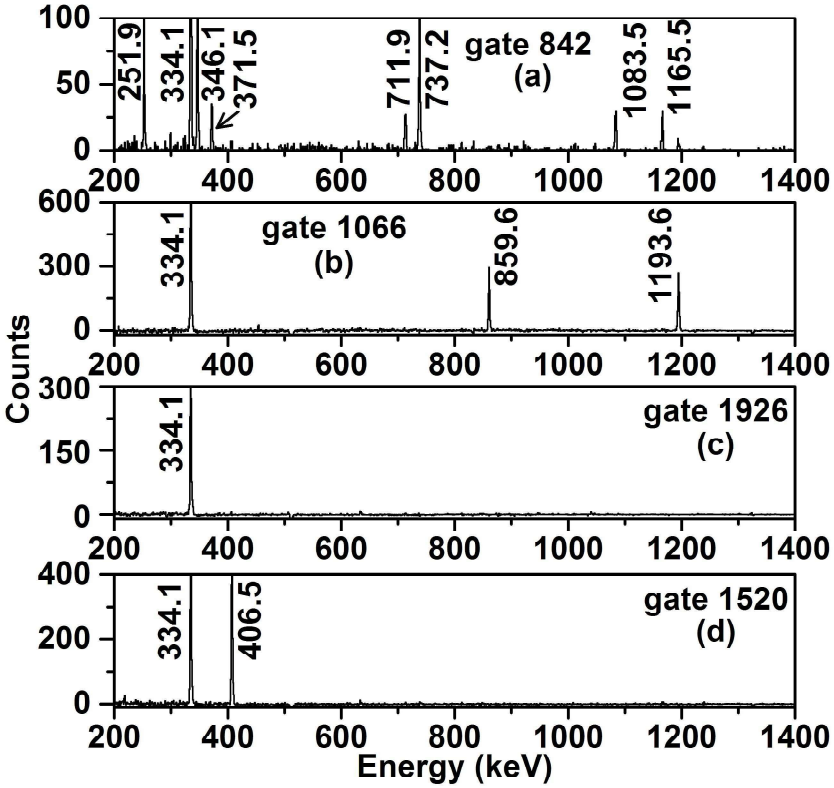

Figure 4.8: Gated spectra for some of the transitions de-exciting the 2260.7 keV level for which the placement has been confirmed in the present work.

4.3.2.1 *Logft* analysis

The modification in level scheme obtained in the present work calls for re-determination of β-decay branching intensities associated to different known and the new excited levels in ^{150}Sm. For this purpose, the relative intensities of the γ transitions have been estimated with respect to the 334.1 keV ($2^+ \rightarrow 0^+$) transition after correcting for the 10% β-decay branching of ^{150}Pm to the ground state of ^{150}Sm [BAS13]. The γ-ray intensities derived in the present work have been used to estimate the β-decay branching to different levels and the same has been compared with the earlier work (c.f Table 4.1). The β branching intensities so obtained have been used to estimate the *logft* values by using the *logft* calculator available in NNDC [LOGFT].

The ground state of ^{150}Pm has been evaluated as 1^- in ENSDF [BAS13]; suggested as 2^- in the work of D. Bucurescu *et al.* [BUC12] and as 1^- or 2^- in the work of Barrette *et al.* [BAR70]. In

confirms its placement in the level scheme of ^{150}Sm. Similarly, the 2690.6 keV transition, which had a tentative placement in the level scheme, is found to be in coincidence with the 334.1 keV γ-ray and, thus, confirming the placement of this transition from the 3024.7 keV level to the 334.1 keV, 2_g level. Similarly, the tentative placement of the 532.3 keV transition could be confirmed to be de-exciting from the 2602.2 keV level using $\gamma - \gamma$ coincidence data. However, the second placement of this 532.3 keV γ-ray, de-exciting the 3212.5 keV level, could not be confirmed and the present work suggests that 532.3 keV has only a single placement in the level scheme.

4.3.1.4 Level structure around 2260 keV level

All the eight transitions reported to be de-exciting the 2259.8 keV level, by Barrette *et al.* [BAR70], have been observed in the present work in contrast to the recent observation made by Humby *et al.* [HUM16] who observed only one out of the eight transitions, viz., 1926.1 keV. From the $\gamma - \gamma$ coincidence measurement, performed in the present work, the placement of all these eight transitions could be confirmed as de-exciting the 2259.8 keV level. These spectra are shown in Fig. 4.3(d) and Fig. 4.8. Hence, the present work does not support the propositions made in Ref. [HUM16] in which the possibility of the existence of multiple discrete states near 2260 keV was suggested.

4.3.2 J^π assignments for the excited levels of ^{150}Sm

The spin-parity assignment to the observed levels in ^{150}Sm have been done based on the *logft* and $\gamma - \gamma$ angular correlation analysis as described in the following subsections 4.3.2.1 and 4.3.2.2. The J^π assignments that are made from the present work are shown in Table 4.1 in comparison to the spin-parity known from ENSDF data base. In the present work, J^π value is assigned/confirmed for twenty eight levels in ^{150}Sm for which the spin-parity was either not known or uncertain. The following sections describe the methods of analysis and the salient observations made in the present work.

4.3.1.3 Modification based on confirmation of tentative transitions

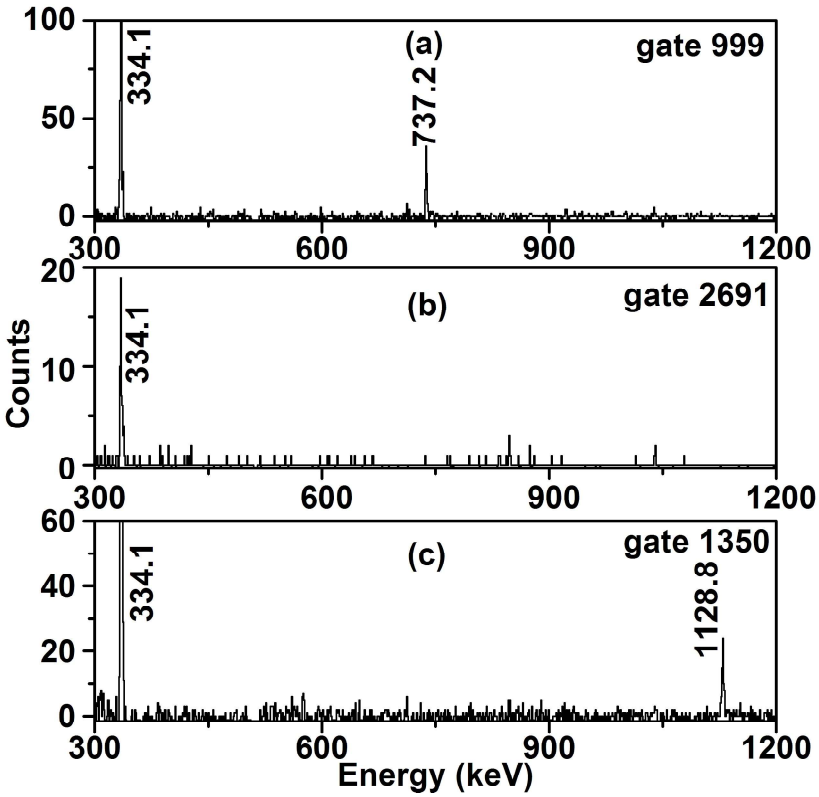

Figure 4.7: Gated spectra for some of the transitions which were placed as dotted in earlier works [BAS13] but confirmed in the present work. (a) 999 keV (I_γ = 0.05; from 2069.7 keV, 2^- to 1071.3 keV, 3^- level) gate, (b) 2691 keV (I_γ = 0.01; from 3024.7 keV, 2^+ to 334.1 keV, 2^+ level) gate and (c) 1350 keV (I_γ = 0.08; from 1684.5 keV, 3^- to 334.1 keV, 2^+ level) gate confirm the transitions which were earlier placed as dotted.

Fig. 4.7 shows the gated projections for some of the tentative γ lines which are confirmed in the present work. The placement of the 1350.4 keV transition, which was tentatively placed as de-exciting the 1684.5 keV, 3^- level to the 334.1 keV, 2^+ level in the earlier β-decay work [BAR70], is confirmed from the coincidence measurement (c.f. Fig. 4.7(c)) and by following its decay half-life. It is also observed that the 1350.4 keV γ-ray has a single placement in the level scheme of ^{150}Sm as the coincidence data could not confirm the second placement of the 1350.4 keV γ-ray decaying from the 3138.8 keV level to the 1786.1 keV level. The 999.1 keV transition which was tentatively placed as decaying from the 2069.7 keV, 2^- level to the 1071.3 keV, 3^- level is also observed in the present work (Fig. 4.1(b)). This γ-ray follows half-life comparable to that of ^{150}Pm and its coincidence gate

Similarly, the 1963.6 (Fig. 4.6(c)) γ-ray is in coincidence with 334.1 and 406.5 keV lines and this confirms the de-excitation of 2704.2 keV level also by 1963.6 keV γ-ray to the 740.6 keV, 0^+ level. The 2704.2 keV level, which is de-excited by the 2370.9 keV transition, might be same as the 2701.3(5) keV level that was earlier observed in the (γ, γ') experiment [BAS13]. A 2700.4 keV transition is observed as doublet with another 2704.2 keV γ-ray. The latter transition is found in 334.1 keV gate and is, thus, assigned to be decaying from the 3037.7 keV, 1^- level. The 2700.4 keV transition, however, is not present in the coincidence data and might indicate the population of a 2701 keV level in β-decay of ^{150}Pm. The energy of this transition shows a difference of nearly 3 keV compared to the 2704.2 keV level under discussion and this conjectures the existence of more than one discrete energy levels around 2702 keV. However, in the present work, this γ-ray is listed as decaying from the 2704.2 keV level only.

The 1916.2 keV transition, following similar half-life as ^{150}Pm, is found to be in coincidence with only 334.1 and 737.2 keV γ-rays. This transition has no coincidence with the 1165.5 and 831.5 keV transitions and, thus, can not de-excite the 3080.2 keV level, as placed earlier. Hence, this transition is placed on top of the 1071.3 keV, 3^- level and, thus, de-excites the 2987.5 keV level. This level is proposed for the first time in the present work.

The gated projection of the 667.1 keV transition, known to be de-exciting the 1833.2 keV level to the 1165.5 keV, 1^- level (as per ENSDF), shows that it has a double placement in the level scheme. In addition to its placement above 1046.0 keV level, this transition is in coincidence with the 1165.5 keV and 831.5 keV γ-rays. Hence, this suggests the population of the 1833.2 keV,$(2)^+$ level from the β-decay of ^{150}Pm as well. The population of this level is also supported by the observation of the 1499.5 keV transition (Fig. 4.1(b)) which is known as de-exciting from the 1833.2 keV level to the 334.1 keV level, as per the ENSDF data [BAS13]. The 1499.5 keV transition shows coincidence only with the 334.1 keV γ-ray but no other low lying transitions in ^{150}Sm level scheme. In the earlier β-decay work also, a 1499 keV transition was observed but that was placed on top of the 1713.3 keV level. The 1833.2 keV transition is observed in the singles data which also confirms the population of 1833.2 keV level from β-decay of ^{150}Pm which was earlier known from the ϵ decay of ^{150}Eu.

other gated projections. Hence, the 1848 keV transition is placed on the top of 1046.0 keV, 2^+ level and, thus, de-excites the 2893.1 keV level instead of 3012.3 keV. The gated spectrum of 1940.4 keV γ-ray also shows that this transition is in coincidence with 334.1 and 711.9 keV but not with 737.5 keV. Hence, the 1940.4 keV transition is placed on top of the 1046.0 keV, 2^+ level, thus, populating the 2987.5 keV level. The 1940.4 keV γ-ray is also found to have double placement in the level scheme and this transition is de-exciting from both the 2987.5 keV, 1^- and 3105.9 keV, 1^- levels to 1046.0 keV, 2^+ and 1165.5 keV, 1^- levels, respectively. The latter level of 3105.9 keV, 1^- was not known earlier in the level scheme of ^{150}Sm and is proposed for the first time. Also, as the presence of 1507.1 keV transition could not be confirmed from the coincidence analysis, the existence of the 3012.3 keV level in the decay scheme of ^{150}Pm could not be established. However, the 3013.6 keV level was observed in the present work which is de-excited with the emission of a 2679.5 keV γ-ray to the 334.1 keV level. This is confirmed from the coincidence analysis. Also, in the earlier β-decay work [BAR70], one dotted 2679.5 keV transition was shown to be de-exciting the 2679.5 keV level which could not also be negated from the present experiment.

With a similar analysis of the 1906 keV gate, it was found that this transition is to be placed on top of the 1165.5 keV, 1^- level and not 1193.6 keV, 2^+ level, as it is neither in coincidence with 1193.6 nor 859.6 keV γ; but in coincidence with the 334.1, 831.5 and 1165.5 keV transitions. This transition was earlier known to be de-exciting the 2679.5 keV level but the present work shows that the transition is decaying from 3071.2 keV, 1^- level to the 1165.5 keV, 1^- level. The 3071.2 keV level is proposed for the first time in the level scheme of ^{150}Sm.

A 1658.5 keV transition has been observed in singles which follows half-life of ^{150}Pm ground state (see Fig. 4.2(h)). Hence, this γ-ray has been placed on the ground state as there is a 1658.2 keV level already known in the level scheme of ^{150}Sm. However, the gated projection of 1658 keV (Fig. 4.6(a)) shows that this transition is in coincidence with 334.1 and 711.9 keV γ-rays. This indicates that 1658 keV has a double placement, de-exiting both the 1658.5 and 2704.2 keV levels to the 0.0 keV, 0_g and the 1046.0 keV, 2_β levels respectively. The intensity of this transition is found to be $\sim$ 0.5% compared to 334.1 keV transition which may be contributed by the summed intensity of two γ-rays present in the decay of ^{150}Pm.

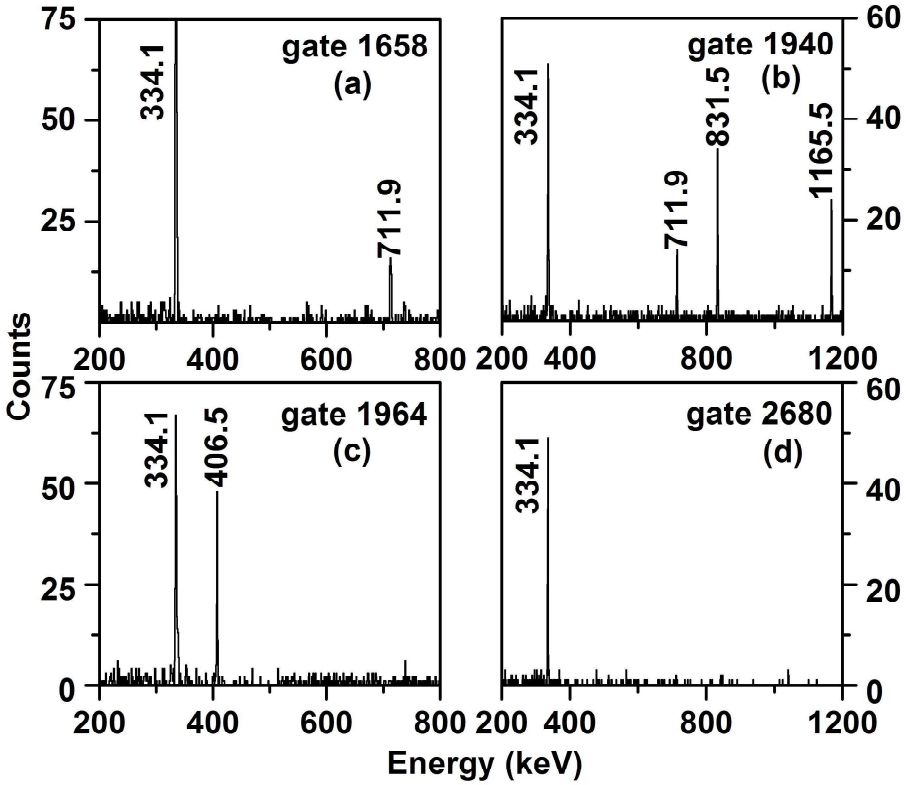

Figure 4.6: Gated spectra for some of the transitions which are doubly placed in the level scheme of ^{150}Sm. (a) 1658 keV transition de-exciting both the 1658.2 keV and 2704.2 keV levels. This is also a new transition observed in the present work. (b) 1940 keV transition de-exciting the 2987.5 keV and 3105.9 keV levels. (c) 1964 keV γ-ray de-exciting both the 1964.8 keV level and 2704.9 keV level. The 1964 keV de-excitation from the 2704.2 keV level is proposed for the first time. (d)The 2680 keV gate shows that this transition also decays from the 3013.6 keV level in addition to the 2679.5 keV level proposed in earlier β-decay work [BAR70].

coincidence data.

Similarly, from the 1848 keV gate, the altered placement of this transition is understood. The 1507.1, 1848.0 and 1940.6 keV transitions were earlier known to be de-exciting a 3012.3 keV level to 1504.6 keV, 3_1^+; 1165.5 keV, 1^- and 1071.3 keV, 3^- levels respectively, as per the β-decay spectroscopy of ^{150}Pm [BAR70]. Out of these γ-rays, the 1848 and 1941 keV γ-rays are observed to have different placements in the level scheme from the $\gamma - \gamma$ coincidence data of the present work (see Fig. 4.5 and Fig. 4.6). The gated projection of the 1848 keV transition (see Fig. 4.5(b)) has 334.1 and 711.9 keV γ-rays in coincidence. The non-observation of 1046 keV transition in this gated spectrum could be justified from its intensity ratio compared to the 711.9 keV γ-ray in singles and

4.3.1.2 Modification in the level scheme based on altered and double placements of γ-rays

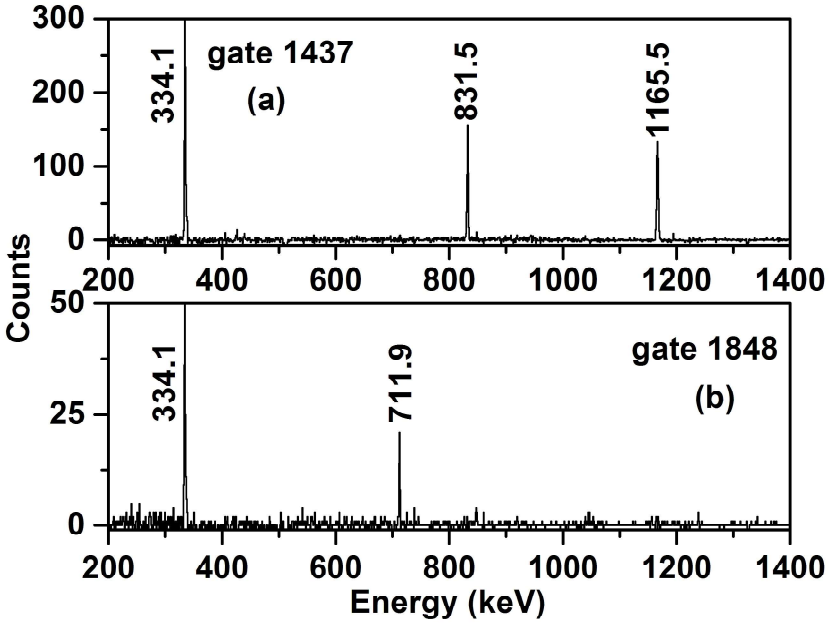

Figure 4.5: Gated spectra for some of the transitions for which the placement has been changed in the level scheme of ^{150}Sm, based on $\gamma-\gamma$ coincidence and (a)1437 keV ($I_\gamma = 0.23$; from 2602.2 keV, 1^- to 1165.5 keV, 1^- level) gate, (b) 1848 keV($I_\gamma = 0.02$; from 2893.1 keV, 2^- level to 1046.0 keV 2^+ level) gate.

Similar to the case for placements of new γ-rays, Fig. 4.5 and Fig. 4.6 show the coincidence for the transitions which are found to have altered and double placements, respectively. The presence of 831.5 and 1165.5 keV transitions in the gated projection of 1436.7 keV ($I_\gamma = 0.23$) suggests the altered placement of this transition. This, along with 1766.4 keV γ-ray, decaying out of the 2507.6 keV, 2^+ level as per ENSDF, is found to have different placement according to the present $\gamma-\gamma$ analysis. The doubles gate of 1436.7 keV transition shows that this γ-ray sits over 1165.5 keV, 1^- level instead of 1071.3 keV, 1^- (see Fig. 4.5(a)). Hence, the placement of this transition is changed and is found to be de-exciting from the 2602.2 keV, 1^- level. The 1766.4 keV transition is found to have a single placement in the level scheme which is on top of the 1046.0 keV, 2^- level. Also, the 848 keV transition, earlier known to be decaying from this 2507.4 keV level, is found to follow a much longer half-life and is confirmed to be originated from contamination in Al backing foil from

Ref. [BAS13]. However, a 2715.5 keV level is proposed in the recent (p,t) experiment [HUM16] that decays through a 1522 keV transition to the 1193.6 keV, 2_3^+ level. In the present work, no 1522 keV transition is observed that satisfies the population of 2715.5 keV level proposed in Ref. [HUM16]. Instead, a 1519.6 keV transition is observed in singles (Fig. 4.1(b)) which follow the half-life of ^{150}Pm but shows coincidence with 334.1 and 406.5 keV transitions (Fig. 4.8). Hence, this γ-ray has been placed on top of the 740.6 keV, 0_2^+ level and is, thus, decaying from the 2259.8 keV, 1^- level (c.f Table 4.1).

Two γ transitions of energy 2857.0 and 2882.2 keV are observed in the singles data out of which the 2882.2 keV γ is found to follow the half-life similar to ^{150}Pm. The half-life followed by the other transition could not be determined due to low statistics. One 2861(7) keV level is proposed in ENSDF which were observed in (n,γ) and (d,p) reaction. The 2880.9(5) keV level proposed in ENSDF were observed in (γ, γ') data. The observation of 2857.0 keV and 2882.2 keV transitions in singles data might indicate the population of the above two excited levels from the β-decay of ^{150}Sm.

In the earlier β-decay work, transitions of energy 1865.2(10) and 1893.2(10) keV were observed but were not placed in the level scheme. Two transitions of energy 1866.1 and 1892.1 keV, are found also in the present work from both singles and coincidence data. Their coincidence relationships show that they may de-excite from 2937.4 keV level to the 1071.3 keV, 3^- and 1046.0 keV, 2^+ levels respectively. It is worth mentioning here that a 2937(20) keV level is already known in the adopted level scheme of ^{150}Sm which was suggested in three different experiments with (p,t), (d,p) and (n,γ) reactions.

The 2624 keV transition, observed in the present and earlier β-decay work, is found to follow half-life close to the half-life of ^{150}Pm. This transition is in coincidence with 334.1 keV and, thus, belongs to the level scheme of ^{150}Sm. This suggests that there could be a 2958.1 keV state in the level scheme of ^{150}Sm which is proposed for the first time.

The 310.9 keV transition, decaying from 1504.6 keV, 3^+ level to the 1193.6 keV, 2_3^+ level, was not observed in the earlier work on β-decay of ^{150}Pm. This important transition is observed to be in coincidence with the 565.4 keV transition decaying from the 2069.7 keV, 2^- level to this 1504.6 keV level (see Fig. 4.3(b)).

From $\gamma - \gamma$ coincidence analysis, the 892 keV γ-ray is found to be in coincidence with 334.1 ($2_g \rightarrow 0_g$) and 737.2 ($3^- \rightarrow 2_g$) keV transitions. Hence, this new γ-ray is placed in the level scheme of ^{150}Sm and it de-excites the 1963.5 keV level to the 1071.3 keV, 3^- level.

A new 929.3 keV transition is found from the present experiment which is in coincidence with 334.1, 406.5, 1222.9, 1629.1 and 1963.6 keV transitions, as per the 1223 and 1964 keV gated projections. This indicates that the 929.3 keV γ-ray is de-exciting from the 2893.1 keV level to the 1963.5 keV, 1^- level.

Two new γ-rays, viz., 2069.4 keV and 2812.8 keV, have been observed in singles data which follow the half-life of ^{150}Pm (see Fig. 4.2) but have no coincidence with the γ-rays of ^{150}Sm. These transitions are proposed to be feeding directly to the ground state as the 2069.7 keV and 2812.7 keV levels are already known in the level scheme. A 237 keV transition is also observed for the first time in the decay of ^{150}Pm and this could be placed as de-exciting the 2069.7 keV level and placed on top of the 1833.2 keV, $(2)^+$ level, as per 667 and 1499 keV gated projections.

The 1269.3(10) keV transition was observed in the earlier β-decay work [BAR70] but could not be placed in the level scheme. A 1269.4 keV transition is found in the present work as well (Fig. 4.1(b)) following ^{150}Pm decay half-life. This γ-ray is found to be in coincidence with the 334.3 keV γ, thus, possibly de-exciting the 1603.5 keV level to the 334.1 keV, 2^+ level. A 1603(4) keV level was also observed in (p,t) reaction [BAS13, HUM16].

A 2384.2 keV transition, observed for the first time, could be placed on top of the 334.1 keV, 2_1^+ level based on decay half-life and coincidence measurements and is, thus, decaying from a 2718.3 keV, 3^- excited level. The population of this level is also indicated by the observation of a 2718 keV transition following half-life similar to that of ^{150}Pm. One 2715(4) keV, 3^- level is known in ^{150}Sm from the (p,p$'$) and (d,d$'$) reactions [BAS13]. However, no γ transition was known to be decaying from this level. The newly observed 2718.3 keV level could be same as this 2715(4) keV level of

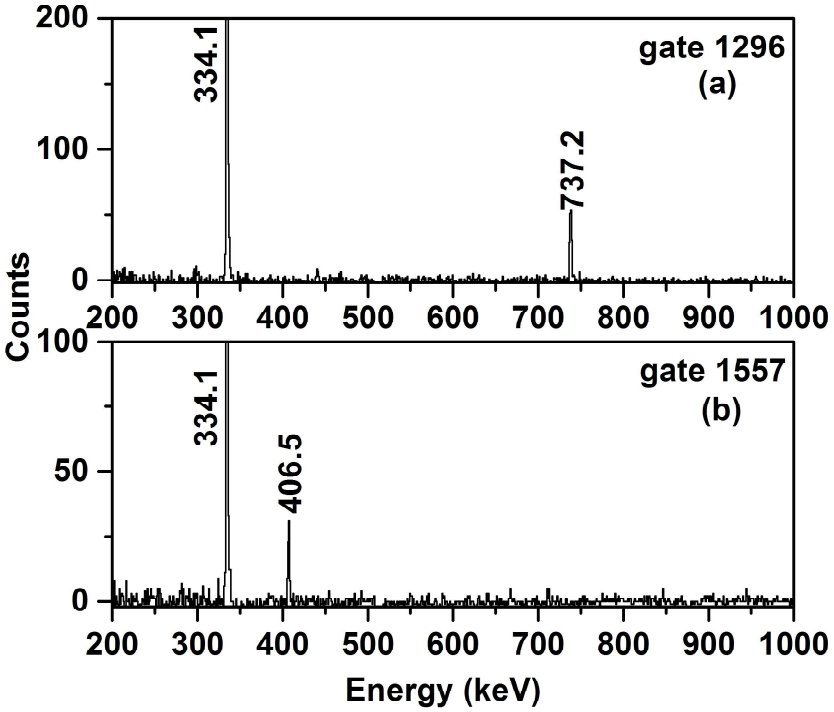

Figure 4.4: Gated spectra for some of the new transitions which are placed in the level scheme of ^{150}Sm. (a)1296 keV ($I_\gamma = 0.06$; from 2367.2 keV 2^- level to 1071.3 keV, 3^- level) gate and (b) 1557 keV ($I_\gamma = 0.05$; from 2298.0 keV 3^- level to 740.6 keV, 0_2^+ level) gate show their placements in the decay scheme of ^{150}Pm.

known in the level scheme of ^{150}Sm from (p,p′), (d,d′) reactions which could possibly be the 2298.0 keV level proposed in the present work. The 1296.3 keV γ-ray was observed in the earlier β-decay work but could not be placed in the decay scheme of ^{150}Pm. In the present work, the 334.1 and 737.2 keV transitions are found to be in coincidence with the 1296.3 keV γ-ray (c.f. Fig. 4.4(a)) and, thus, this transition is placed to be de-exciting from the already known 2367.2 keV level to the 1071.3 keV, 3_1^- level.

Similarly, few more new transitions were observed in the present work which were confirmed from the coincidence data as well as half-life measurement. For example, a 371.5 keV transition is found in the singles data and the 712 keV gated projection shows that it can be placed on top of the 1046.0 keV level. This confirms the connection of the 1417.4 keV, 2_3^+ level to the 2_β level of ^{150}Sm. It is important to mention that, although this transition was also observed in some earlier works of Ref. [KAL75, RED69], it is not mentioned in ENSDF [BAS13].

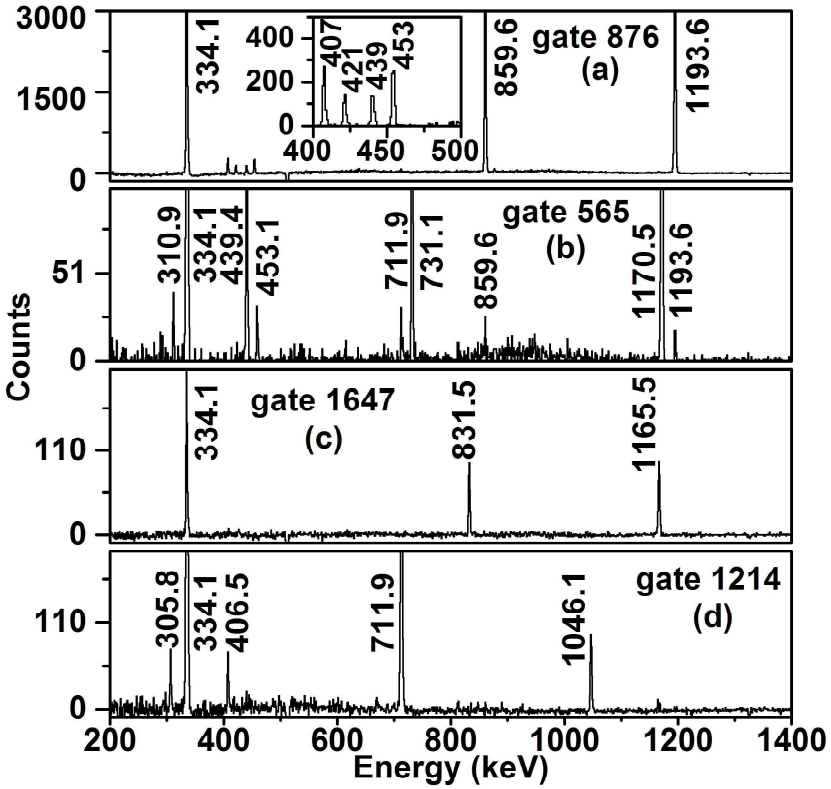

Figure 4.3: Gated spectra for some of the transitions which were already known in ^{150}Sm. (a) 876 keV (from 2069.7 keV, 2^- level to 1193.6 keV, 2^+ level) gate , (b) 565 keV (from 2069.7 keV, 2^- level to 1504.6 keV, 3^+ level) gate (c) 1647 keV (from 2812.7 keV, 2^- level to 1165.5 keV, 1^- level) gate and (d) 1214 keV (from 2259.6 keV, 1^- level to 1046 keV, 2^+ level) gate show the known de-excitations in ^{150}Sm.

probable ones (c.f Sec. 4.3.2). The following subsections describe the modification made in the level scheme of ^{150}Sm in the present work, based on the new information obtained with different γ-rays.

4.3.1.1 Modification in the level scheme based on the new transitions

Fig. 4.4 shows the coincidence relationships of two of the nineteen new γ-rays found in the present work, viz., 1557.4 keV (I_γ = 0.05) and 1296.3 keV (I_γ = 0.06) transitions de-exciting the 2298.0 keV and 2367.2 keV levels, respectively. Both these transitions are observed in singles data (see Fig. 4.1(b)) and follow half-life of ^{150}Pm. The 1557.4 keV γ-ray, being in coincidence with the 334.1 keV and 406.5 keV transitions (c.f. Fig. 4.4(b)), is placed on top of the 740.6 keV, 0_2^+ level, thus, forming the 2298.0 keV level populated from β-decay of ^{150}Pm. One 2294(5) keV, 3^- level is already

TABLE I: continued...

E_x (keV)	J^π		E_γ (keV)	I_γ	$I_{\beta-}$		*logft*
Pres. work	Lit. [BAS13]	Pres. work	Pres. work	Pres. work	Lit. [BAS13]	Pres. work	Pres work
3037.7	$1,2^+$	1^-	2704.2	0.03(1)	0.10(3)	0.05(2)	7.7(2)
			3037.7	0.02(1)			
3071.2	-	(1^-)	1905.7[b]	0.04(1)	-	0.04(1)	7.6(1)
3080.2	$1^{(+)}$	(2^+)	3080.2	0.01(1)	0.102(16)	0.01(1)	8.2(5)
3090.1	$1,2^+$	(2^+)	3090.1	0.01(1)	0.29(4)	0.01(1)	8.2(5)
3105.9	-	(1^-)	1940.4[b,h]	0.05(1)	-	0.05(1)	7.4(1)
3138.8	(1,2)	(1^-)	2804.7	0.04(1)	0.14(3)	0.04(1)	7.4(2)

The $\gamma - \gamma$ coincidence analyses were performed with the γ-rays listed in Table 4.1. The coincidence information related to the well known transitions and levels were verified from the data before placing the new and weak γ-rays in the level scheme. Fig. 4.3 shows few gated projections on those γ transitions, which are well known in the decay scheme of ^{150}Pm. The transitions are chosen to have a wide range of intensity values to determine the quality of the data obtained in the present coincidence measurement. The 876.1 keV ($I_\gamma = 6.52$) and 565.4 keV ($I_\gamma = 1.16$) gates show the strong and weak decay branches from the 2069.7 keV level. The 1213.8 keV ($I_\gamma = 0.89$) gate shows the decay of the 2259.6 keV level and the 1647.4 keV ($I_\gamma = 0.23$) gate shows the same for the 2812.7 keV level.

From the present analysis of decay half-life and $\gamma - \gamma$ coincidence, in total, thirteen new levels were placed in the decay scheme of ^{150}Pm. Out of these new levels, six levels (viz., 1684.5, 1833.2, 2704.2, 2718.3, 2937.4 and 2987.5 keV) are based on multiple γ decays, most of which are observed for the first time and few have altered placements. The spin-parity of these levels could also be confirmed from *logft* analysis (c.f Sec. 4.3.2). Rest of the new levels, assigned to the decay scheme of ^{150}Pm, are based only on a single transition and again four of these levels (viz. 1603.5, 2298.0, 2857.0 and 2882.2 keV) were also known from other reactions but not from β-decay [BAS13]. However, no de-exciting γ-ray were known earlier from these four levels. The assigned spin-parity, for the levels which are based only on single transition, are kept in bracket and may be considered as the most

TABLE I: continued...

E_x (keV)	J^π		E_γ (keV)	I_γ	$I_{\beta-}$		*logft*
Pres. work	Lit. [BAS13]	Pres. work	Pres. work	Pres. work	Lit. [BAS13]	Pres. work	Pres work
			2195.4	0.09(2)			
			2528.7	0.36(8)			
2550.4	$1^{(-)}$	1^-	1810.3	0.05(1)	0.39(5)	0.44(9)	7.9(1)
			2216.3	0.23(5)			
			2550.4	0.15(3)			
2602.2	$(1^+,2,3)$	1^-	532.3[c]	0.03(1)	0.20(3)	0.36(8)	7.9(1)
			889.0	0.10(2)			
			1436.7[b]	0.23(5)			
2679.5	3	(2^+)	2679.5[h]	0.05(1)	0.11(3)	0.05(1)	8.6(1)
2704.2	-	2^-	**1658.5**[a,h]	0.51(10)	-	2.14(44)	6.9(1)
			1963.6[a,h]	1.50(31)			
			2370.9[d]	0.07(2)			
			2700.4[a]	0.06(1)			
2718.3	3^-		**2384.2**[a]	0.03(1)	-	0.04(2)	8.6(2)
			2718.0[a]	0.01(1)	-		
2812.7	$(1^-,2)$	2^-	1128.8	0.05(2)	1.42(10)	1.17(28)	6.9(1)
			1154.5	0.33(8)			
			1647.4	0.23(5)			
			1766.4	0.19(4)			
			2478.7	0.34(7)			
			2812.8[a]	0.01(1)			
2857.0		$(2^+, 3^-)$	2857.0	0.01(1)	-	0.01(1)	8.9(5)
2882.2	$1^{(-)}$	(1^-)	2882.2	0.03(1)	-	0.03(1)	8.3(2)
2893.1	$(1^-,2)$	2^-	633.1	0.06(1)	0.61(6)	0.60(14)	7.0(1)
			929.3[a]	0.04(1)			
			1179.9	0.05(1)			
			1727.6	0.22(5)			
			1848.0[b]	0.02(1)			
			2893.8	0.21(5)			
2937.4	-	1^-	**1866.1**[d]	0.08(2)	-	0.12(3)	7.6(1)
			1892.1[d]	0.04(1)			
2958.1	-	(1^-)	**2624.0**[d]	0.04(1)	-	0.04(1)	8.0(1)
2987.5	-	1−	1916.2[b]	0.07(2)	-	0.12(3)	7.4(1)
			1940.4[b,h]	0.05(1)			
3013.6	-	(1^-)	2679.5[h]	0.05(1)	0.19(3)	0.05(1)	7.7(1)
3024.7	2^+		2690.6[c]	0.01(1)	0.163(24)	0.04(1)	7.8(1)
			3024.1	0.03(1)			

TABLE I: continued...

E_x (keV)	J^π		E_γ (keV)	I_γ	$I_{\beta-}$		*logft*
Pres. work	Lit. [BAS13]	Pres. work	Pres. work	Pres. work	Lit. [BAS13]	Pres. work	Pres work
			1713.4	0.40(8)			
1786.1	(≤3)	3^-	620.6	0.11(2)	0.16(4)	0.18(5)	9.3(1)
			1452.4	0.07(2)			
1833.2	$(2)^+$		667.1[b,h]	0.20(4)	-	0.24(5)	9.1(1)
			1499.5[b]	0.04(1)			
			1833.2	0.02(1)			
1963.5	$1^{(-)}$	1^-	**892**[a]	<0.01	5.5(3)	5.11(1.55)	7.6(1)
			917.2	0.47(9)			
			1222.9	2.35(46)			
			1629.1	0.84(17)			
			1963.6[h]	1.50(31)			
2069.7	$2^{(-)}$	2^-	**237**[a]	<0.01	17.5(8)	15.25(5.63)	7.0(2)
			565.4	1.16(20)			
			652.6	0.28(5)			
			876.1	6.52(1.22)			
			904.2	0.78(15)			
			999.1[c]	0.05(1)			
			1024.0	0.67(13)			
			1735.7	5.55(1.34)			
			2069.4[a]	0.26(6)			
2259.8	(1^-)	1^-	842.1	0.38(9)	3.26(17)	3.15(89)	7.5(1)
			1004.0	0.78(15)			
			1065.9	0.41(8)			
			1093.8	0.03(1)			
			1213.8	0.89(18)			
			1519.6	0.29(6)			
			1926.1	0.33(7)			
			2259.6	0.09(2)			
2298.0	3^-		**1557.4**[a]	0.05(1)	-	0.05(1)	9.2(1)
2367.2	(3^+)	2^-	1201.7	0.03(1)	1.04(9)	1.12(24)	7.8(1)
			1296.3[d]	0.06(1)			
			2033.1	1.00(21)			
			2366.4[a]	0.03(1)			
2507.4	$(1^-,2^+)$	2^+	1340.8	0.03(1)	0.58(7)	0.15(4)	8.4(1)
			2173.7	0.06(1)			
			2507.4	0.06(1)			
2528.7	$1,2^+$	1^-	1789.6	0.03(1)	0.44(5)	0.48(10)	7.9(1)

TABLE I: continued...

E_x (keV)	J^π		E_γ (keV)	I_γ	$I_{\beta-}$		*logft*
Pres. work	Lit. [BAS13]	Pres. work	Pres. work	Pres. work	Lit. [BAS13]	Pres. work	Pres work
1046.0	2^+		305.8	0.10(2)	1.3(4)	0.19(5)	9.9(1)
			711.9	3.63(66)			
			1046.1	0.46(9)			
1071.3	3^-		298.2	0.11(2)			
			737.2	1.93(37)			
1165.5	1^-		425.3	0.44(7)	25.9(14)	24.12(6.73)	7.7(1)
			831.5	11.03(2.05)			
			1165.5	15.18(2.95)			
1193.6	2^+		420.5	0.06(1)	0.6(7)	0.50(14)	9.3(1)
			453.1	0.11(2)			
			859.6	2.97(55)			
			1193.6	4.35(85)			
1255.4	0^+		209.5	0.09(1)			
			921.3	0.71(13)			
1417.4	2^+		251.9	0.18(3)			
			346.1	0.31(6)			
			371.5[a]	0.07(1)			
			1083.5	0.16(3)			
			1417.9	-			
1504.6	3^+		310.9	-			
			458.4	0.03(1)			
			731.1	0.20(8)			
			1170.5	0.98(20)			
1603.5	-	(2^+)	**1269.4**[d]	0.04(1)	-	0.04(1)	10.1(1)
1658.2	$2^{(-)}$	2^-	241.6	<0.01	19.4(12)	18.74(6.07)	7.4(1)
			464.4	0.05(1)			
			492.5	0.34(6)			
			586.7	1.16(20)			
			611.9	0.78(15)			
			1324.1	16.24(3.23)			
			1658.5[a,h]	0.51(10)			
1684.5	3^-		910.6	0.15(3)	0.089(25)	0.18(7)	9.4(2)
			1350.4[c]	0.08(2)			
1713.3	1	1^-	548.3	0.04(2)	3.5(3)	3.45(1.08)	8.0(1)
			667.1[h]	0.20(4)			
			972.5	0.07(1)			
			1379.2	2.89(58)			

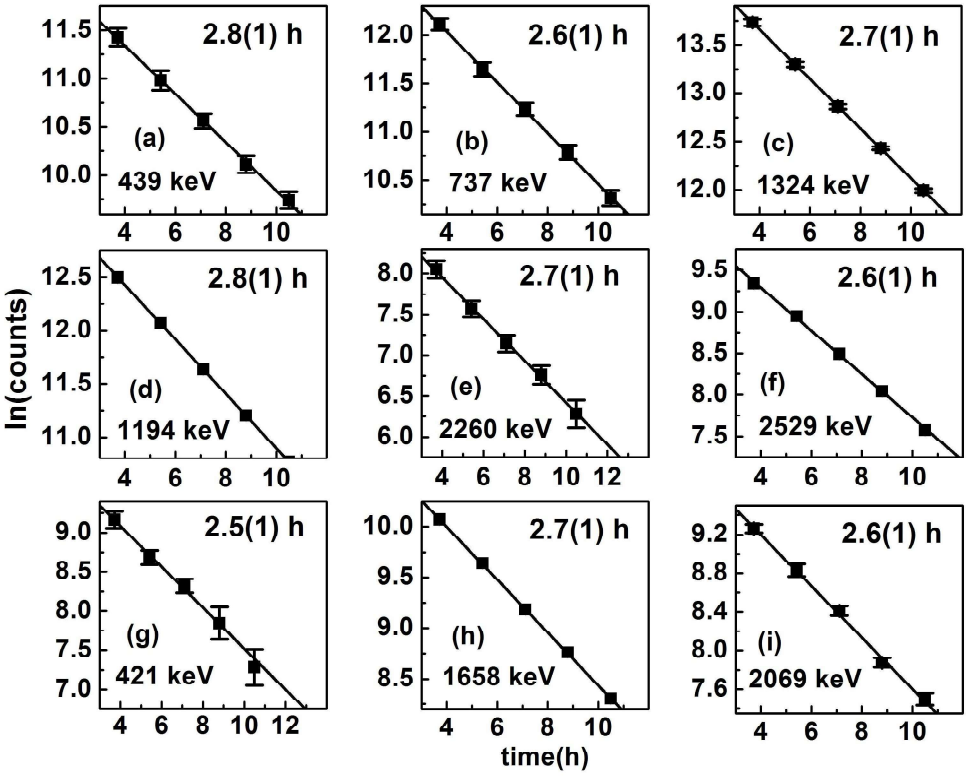

Figure 4.2: The decay half lives followed for some of the transitions observed in singles and placed in the level scheme of ^{150}Sm are shown. (a) 439 keV (773 keV, $4^+ \rightarrow$ 334 keV, 2^+), (b) 737 keV (1071 keV, $3^- \rightarrow$ 334 keV, 2^+), (c) 1324 keV (1658 keV, $2^- \rightarrow$ 334 keV, 2^+), (d) 1194 keV (1194 keV, $2^+ \rightarrow$ g.s), (e) 2260 keV (2260 keV, $1^- \rightarrow$ g.s), (f) 2529 keV (2529 keV, $1^- \rightarrow$ g.s), (g) 421 keV (1194 keV, $2^+ \rightarrow$ 773 keV, 4^+), (h) 1658 keV (1658 keV, $2^- \rightarrow$ g.s), (i) 2070 keV (2070 keV, $2^- \rightarrow$ g.s). Among these (a) - (g) are for the transitions which were already known in ^{150}Sm; (h) & (i) for new transitions that are placed in the level scheme of ^{150}Sm.

Table 4.1: The excited levels of ^{150}Sm, populated from β-decay of ^{150}Pm are listed along with the γ-rays de-exciting from these levels. The γ-rays and the excited levels assigned for the first time in the decay scheme of ^{150}Pm are shown in bold to guide the eye. The γ-rays are marked as: (i)'a' for new transitions observed in the present work; (ii) 'b' for the transitions with altered placement in the level scheme compared to the earlier β-decay work; (iii) 'c' for the tentative transitions known in ENSDF and confirmed in the present work; (iv) 'd' for the transitions confirmed in the present work that could not be placed in the earlier β-decay work and (v)'h' for the transitions with double placement.

E_x (keV)	J^π		E_γ (keV)	I_γ	I_{β^-}		*logft*
Pres. work	Lit. [BAS13]	Pres. work	Pres. work	Pres. work	Lit. [BAS13]	Pres. work	Pres work
334.1	2^+		334.1	66.40(10.82)	9.4(18)	10.97(2.80)	8.6(1)
740.6	0^+		406.5	5.30(88)	1.5(6)	0.33(9)	9.8(1)
773.5	4^+		439.4	0.63(12)			

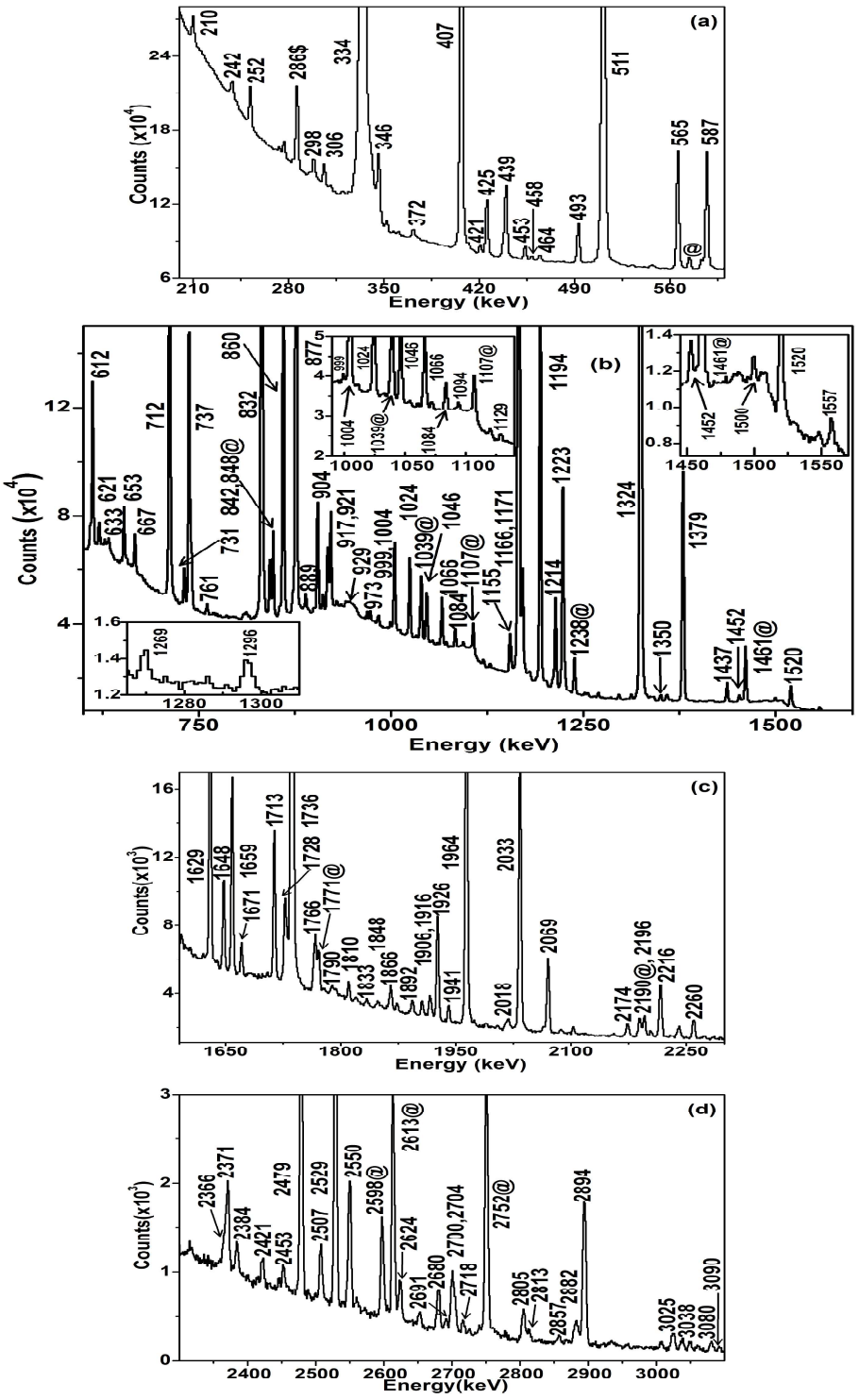

Figure 4.1: The singles spectra showing all the transitions observed from the decay measurement. The 286 keV transition, marked with \$, is identified to be arising from the decay of ^{149}Pm ($\tau_{1/2}$ = 53.08(5) h). The transitions marked with @ follow longer half lives and have been identified to be coming from background or the contaminations in the Al backing foil.

by few representative transitions are shown in Fig. 4.2. The decay half lives followed by the γ-rays were used for confirming their placement in the level scheme of ^{150}Sm. The coincidence relationships among the γ-rays were also taken into consideration for their final placement in the level scheme. All the transitions identified as belonging to the decay scheme of ^{150}Pm are tabulated in Table 4.1 along with the energy of the corresponding excited level of ^{150}Sm, from which these transitions are decaying. The energies of the γ-rays and excited levels, measured in the present work, are in agreement with the values obtained in ENSDF [BAS13] considering the error involved in the measurement.

the prompt gate were subtracted by placing gates on the left and right background of the prompt $\gamma-\gamma$ time peak. This significantly reduced the random coincidence events that may be present in the $\gamma-\gamma$ coincidence data.

This data were also used for the measurement of $\gamma-\gamma$ angular correlation at eight different angles (see Section-3.10.6.4.3 for details). The angular correlation coefficients were obtained from the $\gamma-\gamma$ coincidence data by fitting the coincidence count (W(θ)), corresponding to a particular $\gamma-\gamma$ cascade, at different angles between the two γ-rays with the equation 3.31. The theoretical solutions to the A_2 and A_4 coefficients have been obtained, by using the F_k coefficients [MOR76] corresponding to both the γ decays in a particular cascade, for different values of multipole mixing in one of the transitions.

The pulse processing for the $\gamma-\gamma$ coincidence measurement was performed by using standard NIM electronics and 32 bit VME ADC. For the singles measurement with the isolated Clover detector, standard NIM electronics and CAMAC ADC were used. All the measurements have been carried out after a cooling time of ~2 h or more after the irradiation in order to ensure that all the short lived activities produced during irradiation have decayed out. All the data were gathered in zero suppressed LIST mode using LAMPS [LAMPS] and the offline analyses were performed using the LAMPS and RADWARE [RAD95] analysis packages.

4.3 Results

The experimental data were analysed in order to (i) develop the decay scheme of ^{150}Pm from the analysis of decay half lives and $\gamma-\gamma$ coincidence data and (ii) assign the spin-parity (J^{π}) to the excited levels of ^{150}Sm from the analysis of *logft* values and $\gamma-\gamma$ angular correlation. The following subsections gives details on the new findings obtained from the present work.

4.3.1 Decay scheme of ^{150}Pm: Decay Half Life and $\gamma-\gamma$ coincidence

The γ transitions obtained in singles data are shown in Fig. 4.1. The decay curves exhibited by all the γ-rays were studied in order to identify the origin of each transition. The half lives followed

4.2 Experimental Setup and Data Analyzing Techniques

The excited states of ^{150}Pm were populated by the ^{150}Nd (p, n)^{150}Pm reaction using 8.0 MeV proton beams provided by K = 130 AVF cyclotron at Variable Energy Cyclotron Centre (VECC), Kolkata, India. The beam energy was chosen from the measured excitation function for the p + ^{150}Nd reaction [BAN15] so as to have maximum cross section for the (p,n) channel. The ^{150}Nd target was prepared by electro-deposition technique, starting from commercially available 97.65% enriched powdered oxide sample (Nd_2O_3), on a 0.3 mil thick aluminium (Al) foil. The isotopic impurities in the target material consisted of 0.50% ^{142}Nd, 0.31% ^{143}Nd, 0.68% ^{144}Nd, 0.23% ^{145}Nd, 0.47% ^{146}Nd and 0.26% ^{148}Nd, as per the data sheet provided by the supplier. The thickness of the targets used in the experiment was ∼900 μg/cm^2. Several targets were irradiated following the stacked foil technique [BAN15]. The irradiated targets were subsequently counted with different configurations of Ge detectors as per the requirement of the decay spectroscopy measurements as discussed below.

In order to measure the decay half lives, the γ decay was followed in singles mode over a period of ∼10h where each counting was continued for a duration of 10 minutes. Decay half-life measurement was performed with an isolated Clover HPGe (High Purity Ge) detector and it was also ensured that the detector dead time is kept below 5% during counting. The measurement was performed by using the standard techniques where the background subtracted areas of a particular full energy peak were studied as a function of time. The statistics were increased by adding data files generated during time differentiated counting. The data obtained from this measurement was also used for the measurement of absolute intensities for most of the γ-rays as the absolute efficiency of the detector could be measured with the ^{152}Eu and ^{133}Ba sources of known disintegration per second (dps).

In the present work, the decay γ transitions have been detected using the VENUS (see Section-3.10.5 for details). In the $\gamma - \gamma$ coincidence measurement, conventional two fold coincidence logic was used. The $\gamma - \gamma$ coincidence data obtained from this setup were used to establish the level scheme. For this purpose, the data were sorted to generate RADWARE compatible 4k × 4k matrix using prompt gating of ∼ 50ns from the total $\gamma - \gamma$ time events. The random events present within

of the 2_2^+ and 2_3^+ states in the complex spectral features of ^{150}Sm. Although, the lowest few levels of ^{150}Sm correspond roughly to those of the vibrational model (VM), the large number of currently known positive parity levels can be grouped into the ground, β, γ, and $\beta\beta$ rotational bands [BAS13, NDS18]. The 0_2^+ and 4_1^+ levels lie at about twice the 2_1^+ state energy, but the 2_2^+ state lies at more than 3E(2_1^+). The B(E2, 0 $\rightarrow$ 2) value drops from 3.4 e^{2}b^2 in ^{152}Sm to only 1.2 e$^2b^2$ in ^{150}Sm, but the latter still has a large quadrupole moment Q(2_1^+) $\sim$ -1.25 e-barn. More recently, Gupta *et al.* [GUP10] also explained the structure of ^{150}Sm and resolved the anomaly of the shape co-existence. They reproduced the absolute B(E2) values and the inter-band B(E2) ratios fairly well by a careful balance of the quadrupole forces and pairing interaction, and predicted the slightly deformed status of ^{150}Sm, reproducing the quadrupole moment Q(2_1^+) [GRO73].

The study of the low lying states populated through decay spectroscopy may reveal important information on the structure of a nucleus [YXU94, FOG92, LIN99, NÁC04, DIL03]. Firstly, the excitation energies and the spins of these states are limited by β-decay Q-value (Q$_\beta$) and the selection rules. As a result, many unique levels can be excited from decay which are otherwise not possible from the nuclear reactions that are suitable to populate the band structures. Secondly, detailed information on these low lying levels and precise measurement of β-decay intensity provides a wealth of information regarding the underlying nuclear structure.

In the present work, decay spectroscopy of ^{150}Pm has been carried out to study the low lying levels in ^{150}Sm. The decay half lives followed by the observed transitions along with their $\gamma - \gamma$ coincidence information have been used for the development of level scheme. New levels have been assigned to the decay scheme of ^{150}Pm with the placement of new transitions, confirming uncertain transitions and also by changing the earlier placements of few transitions. The *logft* analysis and angular correlation measurement has been utilized to assign/confirm the spin-parity to the excited levels of ^{150}Sm.

Chapter 4

Spectroscopy of low lying states in ^{150}Sm

4.1 Introduction

The $N = 88$ Sm lies at the transition path of the vibrational to the axially symmetric deformed rotor region and could be associated with the competition between the long-range quadrupole polarizing effects of the nucleon-nucleon force and its short-range part favouring the spherical shapes [MOT55]. Its complex nature is apparent from the varied structures interpreted in this nucleus [GUP13] which also provides a challenge for nuclear theory. Hence, over the time, several experimental and theoretical works have been carried out to enrich the understanding of this nucleus. The experiments include the measurement of singles and coincidence decay spectroscopy [BAR70, TAY77]; angular correlation and directional distribution measurements [SMI66, KAL75, RED69]; determination of absolute B(E2) values [HOS77] and quadrupole moments [GRO73, YAM78] of 2^+ states using Coulomb excitation and the measurement of lifetime and electromagnetic transition rates using (n,γ) reaction [BOR06, JUN93, AND98]. The results from the lifetime measurements suggested the existence of octupole correlation in this nucleus. The transitions from 0_2^+ band to the octupole band was observed [BVU13] and that suggested the co-existence of reflection symmetric and asymmetric octupole shapes in ^{150}Sm. In theory, Kumar [KUM74] reproduced the shape transition at $N = 88 - 90$ in Sm, Scholten *et al.* [SCH78] reproduced the variation in the nuclear structure of Sm isotopes with $N = 86 - 92$ and Gupta and Kumar [GUP81] resolved the overlapping character

be associated with the Y_{30} pear-shape vibration. The present work suggests future experiment for finding the β and γ bands to search for *stable tetrahedral deformation* in this nucleus, which could not be established in the present work.

Thus, the results concerning the structure of the two bands obtained in this work indicate that the bands in question cannot be interpreted as signature partners, and that their properties are compatible with the interpretation in terms of the *'pear-shape'* and *'tetrahedral-shape'* oscillations for the odd-spin and even spin bands, respectively.

Moreover, the absence of the interconnecting transitions suggested in this work suggests at the same time that the interpretation in terms of the band-mixing model cannot be applied, unless a new, even more sensitive experiment can present the new data.

5.5 Summary and Conclusions

Excited negative parity states in ^{160}Yb nucleus have been populated using ^{148}Sm(^{16}O, 4n)^{160}Yb reaction at E_{beam} = 90 MeV. In the present work, in total 6.1 $\times$ 10^9 prompt $\gamma-\gamma$ events and 3.5 $\times$ 10^8 prompt $\gamma-\gamma-\gamma$ events were collected by using the INGA array consisting of twenty Compton suppressed Clover detectors. The level scheme of ^{160}Yb has been significantly modified owing to the observation of doubles and triples-coincidences and measurement of I_γ, R(θ), DCO and IPDCO ratios. It is important to mention that the aim of the present experiment was not to look for new gamma rays or bands that may be populated in ^{160}Yb in addition to the data existing in literature. As discussed in the beginning of this chapter, the main goal was to verify the multiplet gamma rays that were proposed only in a single experiment peformed with AFRODITE array but not in any of the other experiments that have been carried out so far using mainly the GAMMASPHERE array. According to the present analysis, 97 gamma rays have been found which are in confirmation with the the ealier work. The number of gamma rays which could not be confirmed/observed in the present experiment but were claimed to have been seen ealier is 82. There are two gamma rays of energies 606 keV & 483 keV and an energy level of 4474.9 keV which are newly placed in the level scheme of ^{160}Yb. The two non-yrast negative parity structures have been studied which show strong E1 decay to the yrast band. From the comparison of the reduced transition probability ratios with the neighbouring rare earth nuclei, it is conjectured that the even-spin negative parity Band-6 might have a "tetrahedral" (Y_{32} vibrational) structure, whereas the odd-spin negative-parity Band-5 can

Table 5.4: Table showing the comparison of the reduced transition probability ratios $B(E2)_{in}/B(E1)_{out}$ (in 10^6 fm^2), for the selected lowest negative-parity bands in the Rare Earth nuclei close to the tetrahedral magic numbers Z=64,70 and N=90. Experimental data for nuclei other than ^{160}Yb are taken from Ref. [ENSDF]. The strong disproportions between the $B(E2)_{in}/B(E1)_{out}$ ratios originating from the even-vs.-odd negative-parity states is worth observing.

Spin	$^{156}_{64}$Gd$_{92}$	$^{160}_{68}$Er$_{92}$	$^{164}_{70}$Yb$_{94}$	$^{160}_{70}$Yb$_{90}$
19^-	50(10)	-	-	-
18^-	-	-	-	-
17^-	16(3)	-	-	-
16^-	-	-	-	-
15^-	6(2)	61(?)	-	-
14^-	-	74(28)	-	-
13^-	7(4)	18(8)	17(9)	-
12^-	-	148(?)	-	-
11^-	15(8)	10(?)	11(6)	19(8)
10^-	-	813(95)	279(48)	-
9^-	-	-	10(4)	9(3)
8^-	312(45)	181(?)	558(92)	18(6)
7^-	-	-	-	5(2)
6^-	161(50)	1349(?)	908(220)	56(22)
5^-	-	-	-	-
4^-	123(15)	-	-	-

Table 5.5: The B(E2)$_{in}$/B(E1)$_{out}$ ratios for odd- and even-spin negative-parity Band-5 and Band-6 of ^{160}Yb.

Structure	I_i^π	E_i	E$_\gamma$(E2) (keV)	E$_\gamma$(E1) (keV)	I_γ(E2)	I_γ(E1)	I_γ(E2)/I_γ(E1)	B(E2)$_{in}$/B(E1)$_{out}$ 10^6·fm^2
Band-5	7^-	1928.0	359.5	779.7	0.4(0.1)	8.9(2.4)	0.04(0.02)	5(2)
	9^-	2373.6	445.6	635.8	2.9(0.7)	5.9(1.5)	0.49(0.17)	9(3)
	11^-	2879.0	505.4	503.7	5.3(1.3)	1.4(0.5)	3.79(1.64)	19(8)
Band-6	$6^{(-)}$	2051.2	355.9	902.9	0.6(0.2)	1.8(0.4)	0.33(0.13)	56(22)
	(8^-)	2528.4	477.2	790.6	1.5(0.4)	2.2(0.5)	0.68(0.24)	18(6)

'contamination' from the previous one. Consequently, $B(E2)_{\rm in}/B(E1)_{\rm out}$ values are expected to be smaller for the pear-shape and relatively higher for the tetrahedral shapes.

5.4.1 Comparision of $B(E2)_{in}/B(E1)_{out}$ ratios with neighboring nuclei

The $B(E2)_{in}/B(E1)_{out}$ ratios have been obtained for the negative parity sequences Band-5 (odd-spin) and Band-6 (even-spin) with the following relation [MOR76], by using the values of transition energies and relative intensities:

$$\frac{B(E2)_{in}}{B(E1)_{out}} = 1.3 \times 10^6 \times \frac{E_\gamma^3(E1)}{E_\gamma^5(E2)} \times \frac{I_\gamma(E2)}{I_\gamma(E1)}\,\mathrm{fm}^2, \tag{5.1}$$

where E_γ and I_γ are the transition energies and intensities for the E1 and E2 transitions as indicated. These ratios are shown in table 5.4 along with the similar ratios deduced in some of the neighbouring even-even rare earth nuclei.

It is apparent that at comparable spin values the $B(E2)_{in}/B(E1)_{out}$ ratios estimated for the even-spin Band-6 are markedly higher, compared to the odd-spin Band-5. Moreover, it is visible from the results in table 5.4 that the tendency of the evolution of the two ratios obtained for Band-6 is in line with the systematic observed in case of ^{164}Yb and ^{160}Er, however it is opposite to that shown in Ref. [BAR10]. This difference can possibly be attributed to not taking into account the multiplets in the decay spectrum in that reference.

One can summarise by saying that the reduced-probability ratios $B(E2)_{in}/B(E1)_{out}$ are higher for the even-spin bands than those of the odd-spin ones by the order of a dozen or a couple of dozens in the neighbouring Rare Earth nuclei around ^{160}Yb. This can hardly be in agreement with the signature-partnership of the two bands in question.

Assuming that the bands in question are associated with the ground-state minimum with a given quadrupole deformation it will be natural to consider that the $B(E2)_{in}$-values in the two bands are close and to conclude that the differences in $B(E2)_{in}/B(E1)_{out}$ ratios originate from the differences in the B(E1)-values. The 'pear-shape oscillations' carry a relatively big dipole-moment and could be associated with the $K^\pi = 1^-$ band characterised by the odd-spin structures whereas the 'pyramid-type', can be associated with the $K^\pi = 2^-$ even-spin structures which, as related to the Y_{32} component can carry only a second order (induced) dipole moments originating from the

might be ruled out.

The positive parity Band-9 is confirmed from 2365.1 keV to 4474.9 keV. However, assignment of spin parity to this band was not possible with the statistics gathered in the present experiment and the population of this band has been the weakest among all the observed bands. Connection of this band to the 1292 keV, 2_3^+ level, that was observed only in β decay work of Ref. [BAR05], could not be confirmed as well. Hence, the possibility of this band being the β band in ^{160}Yb could not be investigated in the present work.

The non-observation of β and γ bands (as once interpreted by another authors [BAR05]) may be related to the fact that with the HI reaction it is difficult to populate the low spin candidates of such weak non-yrast band structures as nearly all of the band feeding comes from the top of the band with almost no side feeding for the low spin states of the corresponding band. Moreover, in case of a β or γ band, that has similar B(E2) rates for both in-band & out-of-band transitions and the latter are almost double in energy value in comparison to that of the in-band transitions, the intensity of the in-band transitions would be only a few % compared to the out of band transitions. Hence, even if Band-9 could have a connection with the (0_2^+), 1086.1 keV or 2_3^+, 1292 keV level in ^{160}Yb, the in-band decay of this band below the 2789.9 keV level is very difficult to be traced from triples statistics gathered in the present experiment. On the other hand, the doubles data were not useful because of the presence of multiplets for most of the γ energies, proposed at the bottom of this band. This observation is calling for a new experiment of high statistics feeding preferentially the low and medium spin states with high efficiency. However, this could be difficult to achieve since no light particle reactions are available to feed ^{160}Yb at these spins, hence, the feeding is from top of the band with a large loss of flux at each level because of the significative branching ratio of the in-band and the out-of-band transitions.

The structures of Band-5 and Band-6 are compatible with those of the 'pear-shape' *octupole* and 'pyramid-shape' *tetrahedral* oscillations, respectively (as discussed in the following section), the octupole shapes being superposed with the quadrupole shape of the ground-state.

where this level is identified at 1112.0 keV, and from the E1-character of the 255.0 keV transition, assigned in the present work.

The Band-9 was populated up to 4474.9 keV excitation, however, its spins and parities could not be determined in the present experiment. This band was observed also in Ref. [BAR05], where it was assigned even-spins and positive parity, and interpreted as β-vibration band. However, in the present work, the levels below 2365.1 keV could not be established and these levels are shown with dotted lines. Consequently, no connection to the band is found with the 1086.1 keV, (0_2^+) or 1292.8 keV, 2_3^+ level of ^{160}Yb [REI05]. A new level at 4474.9 keV has, however, been observed in this band, which was not known prior to the present work.

The presence of Band-10 has been confirmed (c.f. Fig. 5.11). It has been observed in the previous work [RIE80-B]. The spin-parity identification is based on the R(θ) value of the 763 keV transition, connecting this band to the 10^+ level of Band-1. The latter was measured in the present work and was confirmed I^π=12^+ identification of the lowest level of Band-10.

5.4 Discussions

The level structure of ^{160}Yb, observed in the present work, consist of several band structures with the observation of maximum $J^\pi = 30\hbar$. The weakest transition that could be confirmed from the cube data is the 483 keV transition, connecting Band-3 and Band-4, for which the intensity is even lower than 0.1% compared to the $2_1^+ \rightarrow 0_1^+$ transition (the lowest intensity that could be measured in the present work). However, many of the transitions observed in some of the recent experimental works [BAR10, BAR05] could not be confirmed even with the given selective power of the INGA array. The limiting values for their intensities and the corresponding branching ratios have been estimated from the available data.

The J^π assignment of 3^- to the 1256 keV level has been confirmed from the E1 nature of the 617 keV transition, thereby confirming the Band-7 as a negative parity band. Also, as no connection of this 1256 keV level has been found with the 820 keV, 2_2^+ level, that was observed only in β decay in ^{160}Yb prior to Ref. [BAR05], the possibility of this band being the γ vibrational band [BAR05]

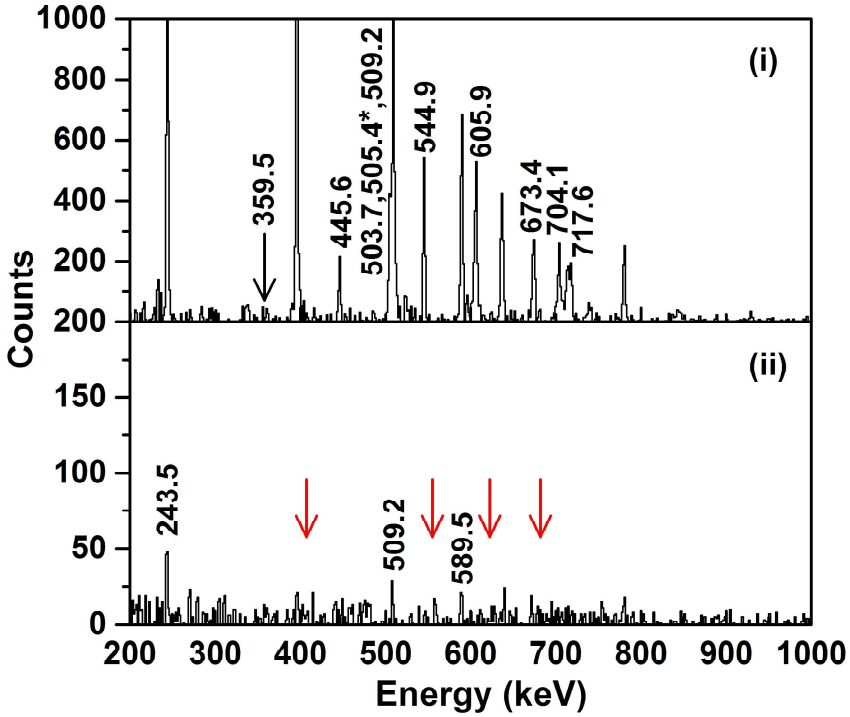

Figure 5.12: The upper panel shows the added cube gate made by all possible combinations (28 in total) of the in-band transitions of Band-5 confirming the presence of this band in the level scheme of ^{160}Yb. The lower panel shows the sum of all possible double gates (6 in total) placed on all the energies reported for Band-12 of Ref. [BAR10], *viz.*, 408 keV, 555 keV, 628 keV and 681 keV. Only background fluctuations are observed at the position of these energies (red arrows). Therefore, it is highly unlikely that these transitions are in coincidences to confirm the existence of Band-12.

1256 keV level as 3^+ and connecting the 1256 keV level to the 820 keV level by a 435 keV transition. In our cube data, we could not observe this connection of the 1256 keV level to the 820 keV, 2_2^+ level, as the presence of 435 keV transition could not be confirmed.

5.3.2.2 Positive Parity Bands: Band-8, Band-9 and Band-10

The positive-parity side bands were observed up to spins 11 $\hbar$ for Band-8, and 18 $\hbar$ for Band-10, respectively and no spin-parity assignment has been possible for Band-9. The population of Band-8, Band-9 and Band-10 are shown in Fig. 5.9, Fig. 5.10 and Fig. 5.11 respectively.

The odd-spin positive-parity sequence of Band-8 has been developed on 1113.2 keV level as observed from the above gated spectra. The assigned spin-parity combination for Band-8 comes from the confirmed spin-parity of 1113.2 keV level as 3^+ from the earlier works, Ref. [REI05, AUE84],

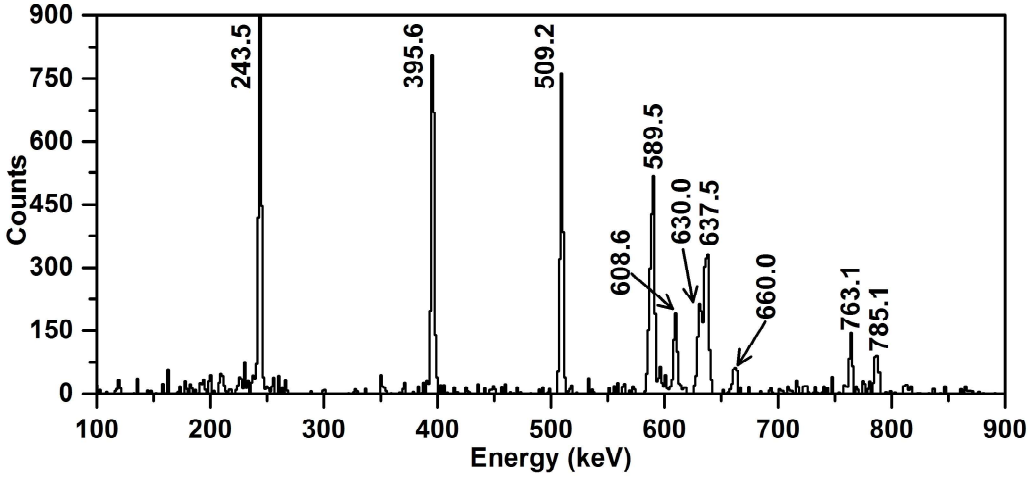

Figure 5.11: Population of states with spin value ranging from 12^+ to 18^+ of Band-10 are shown with the added cube gates of [(637 & 763) + (637 & 609)+ (637 & 630)+ (763 & 609)+ (763 & 630)+ (763 & 660)+ (609 & 630) + (609 & 660)+ (630 & 660)+ (587 & 785)+ (587 & 630)+ (785 & 630)+ (785 & 660) in keV]. All the γ-rays related to the de-excitation of this band are marked with their energies and the in-band transitions are marked with black arrows.

The 359.5 keV transition has also been shown as dotted in the level scheme, given in Fig. 5.2.

It was observed that there is no connection between Band-4 and Band-5 beyond spin $11\hbar$, as evident from Fig. 5.7. The 833 keV transition has been found to be a contaminant transition in coincidence with all the transitions belonging to Band-4 and Band-5. Similarly, the 659 keV transition is observed in coincidence with 283.4 keV of Band-4 and all the transitions of Band-2 from the analysis of the $\gamma - \gamma$ matrix and γ^3 cube. The present work confirms that there is a single 659.0 keV transition in the level scheme of ^{160}Yb and it belongs to Band-2; even from the cube gate, no sign for the presence of the 659 keV transition, connecting the 13^- level of Band-5 and 11^- level of Band-4, could be obtained.

The odd-spin negative-parity Band 7 is built on the 1256 keV and development of the band has been shown in Fig. 5.8. The spin-parity $I^\pi = 3^-$ identification of the 1256 keV level was adopted in Ref. [REI05] after the experimental work on the decay of ^{160}Lu [AUE84]. In the present work also we have measured for the first time the E1 character of the 616.9 keV line by gamma-ray spectroscopic techniques confirming the $I^\pi = 3^-$ assignment of ENSDF. The Band-7 was, however, proposed as the positive parity gamma band [BAR05] with 820 keV, 2_2^+ level as the band head, by making the

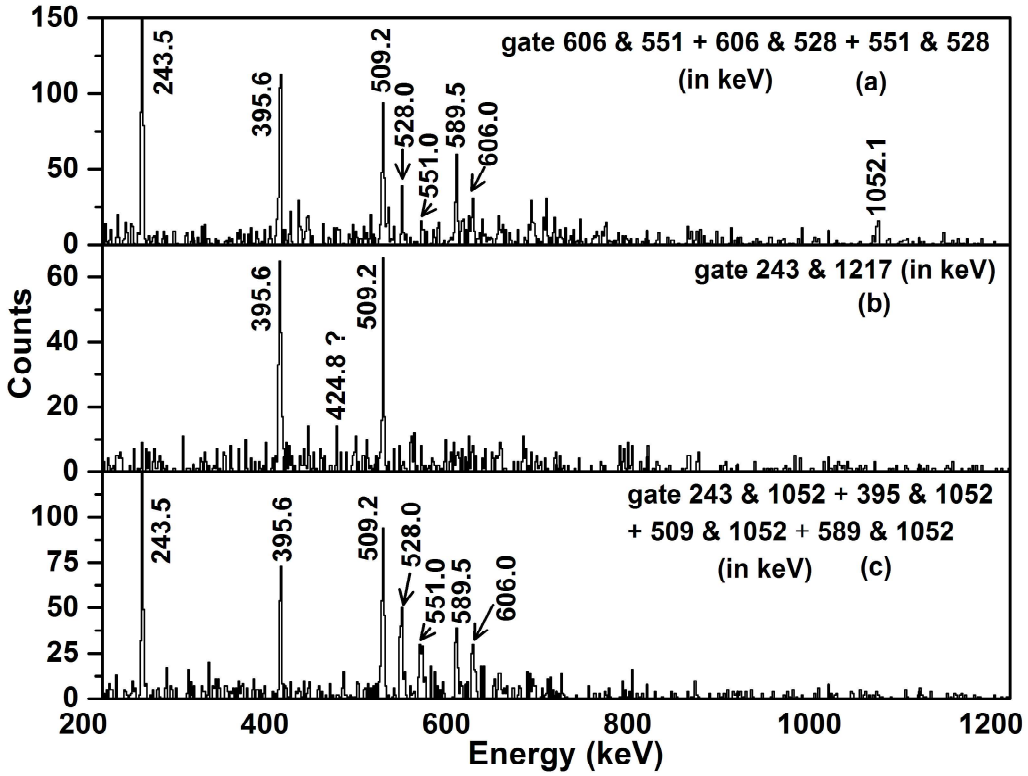

Figure 5.10: The γ-rays observed in the cube gates displayed in (a), (b) and (c) indicate the population of states with energy values ranging from 2365.1 to 4474.9 keV of Band-9. Due to the very weak indication of the 424.5 keV transition between 2789.9 keV and 2365.1 keV levels, as observed from the gate in panel (b), it is shown in bracket in the level scheme (see figure 5.2). Black arrows have been used to mark the in-band transitions. The spins of the Band-9 states could not be determined in this work.

but in no other HI data [REI05]. In the present work, the existence of this level could not be confirmed either, possibly because of lack of direct feeding from the reaction at low spin. The 1568.5 keV (5^-) level, decaying through 929.4 keV transition, has been confirmed from the cube data. This level is fed by the 482.7 keV transition decaying from the $6^{(-)}$ level of Band-6 and 359.5 keV transition from the 7^- level of Band-5. However, the added gate from γ^3 cube with all possible combinations of the intra-band transitions of Band-5, shows very weak signatures of the presence of the 359.5 and 929.4 keV γ-rays. We believe that this is due to the fact that almost full intensity of the 1928.0 keV 7^- level of Band-5 decays through the 779.7 keV E1-transition and compared to that, the intensity decaying through the intra-band E2-transition of 359.5 keV is almost negligible. This is also apparent from the relative intensity values of these two transitions, as given in Table 5.3.

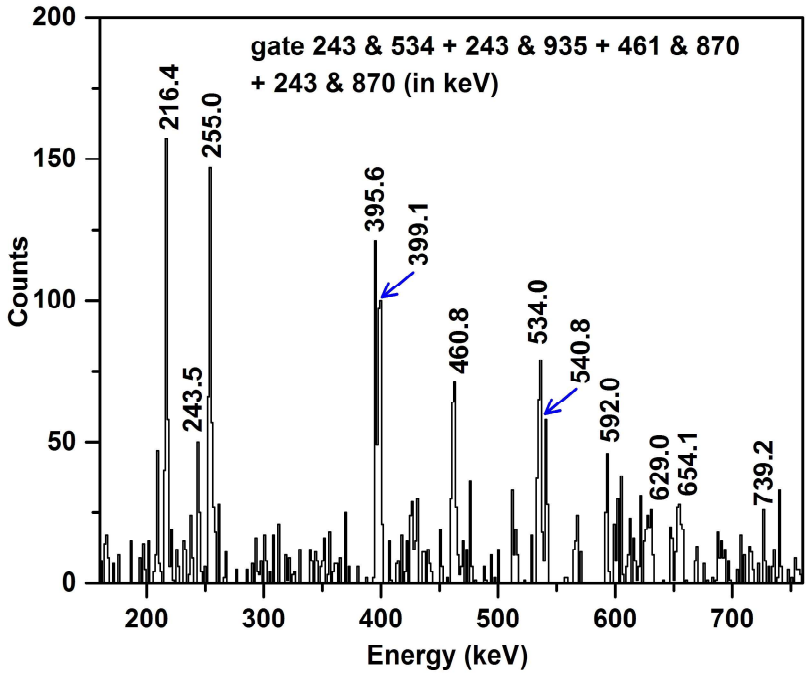

Figure 5.9: The added cube gates of [(243&534) + (243&935) + (461&870) + (243&870) (in keV)] is shown. The γ transitions observed in this added gates confirm the population of the odd-spin positive-parity Band-8 on top of the 1113.2 keV, 3^+ level and are marked with their energy values. Blue arrows have been used to mark close lying peaks. The 255 keV transition is observed in this added gates as this transition connects the positive parity Band-8 to the negative parity Band-3.

triple-coincidence data. This can be considered as the result of using an array with bigger number of detectors, resulting in a higher detection efficiency.

However, figure 5.12 also shows that in the case of Band-12, when adding all the possible combinations of double gates (6 in total) arising out of the in-band transitions of Band-2 (i.e., 408, 555, 628 & 681 keV) reported in Ref. [BAR10], only background fluctuations are found at the positions of the in-band energies (black arrows). This suggests being highly unlikely that these transitions are in coincidences and for this reason, the four transitions in question should not be considered a part of a single rotational band. Hence, the presence of Band-12 in the spectrum of ^{160}Yb is not confirmed by our triple-gate analysis.

All the in band transitions of Band-6 are observed except the top most one, viz., 536 keV, reported in Ref. [BAR10]. The development of Band-6 have been illustrated using Fig. 5.6. The 1358 keV 3^- level of Band-5, reported in Ref. [BAR10], was observed in the decay of ^{160}Lu [AUE84]

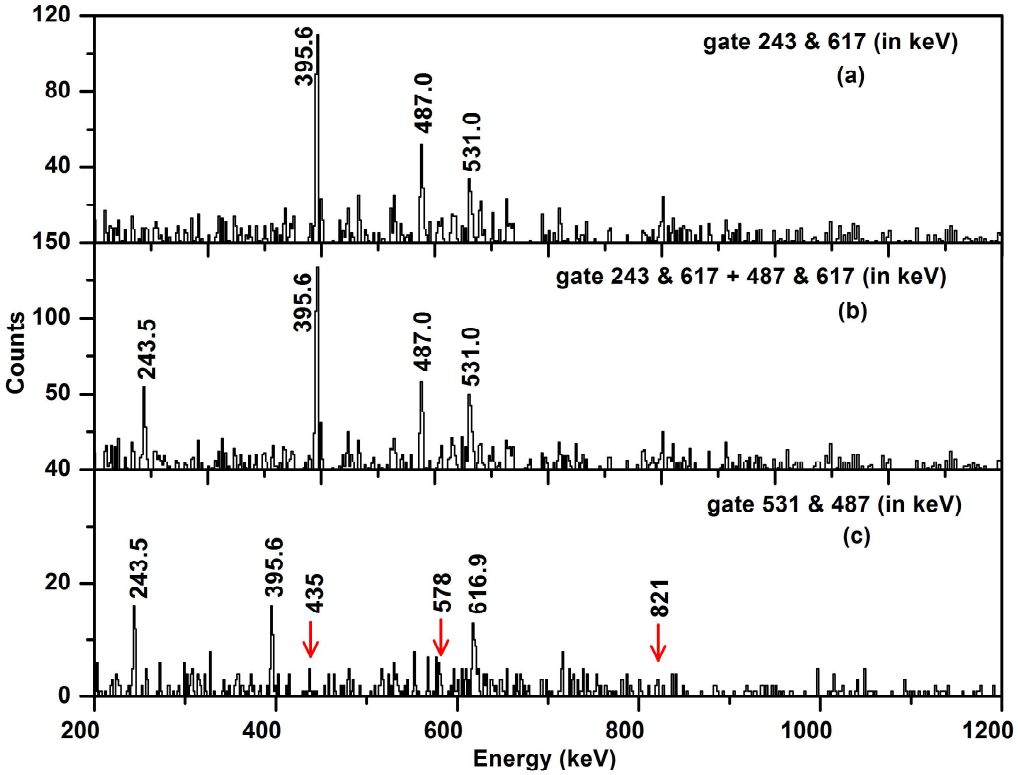

Figure 5.8: (a), (b) and (c) indicate the possible population of the 1256, 1743 and 2274 keV levels of Band-7 in the present experiment. Fig. (c) indicates that the population of the 821 keV, 1^- state could not be confirmed in the present work because of no/very weak indication of 435, 578 and 821 keV transition indicated by red arrows.

5.3.2.1 Negative Parity Bands: Band-2, Band-4, Band-5, Band-6 and Band-7

The population of the states of Band-2 is shown in Fig. 5.5 and all the in-band transitions of this band could be confirmed except some of the inter connecting transitions to the other negative parity bands.

The odd-spin Band-5 and the even-spin Band-6 are connected mainly to the yrast band (Band-1) by several $\Delta I = 1$ and $\Delta I = 0$ E1-transitions, respectively which is shown in Fig. 5.1 and 5.2. Fig. 5.12 illustrates the importance of this analysis in the construction of Band-5 and Band-12, c.f. Ref. [BAR10], by double gating on the in-band transitions. This clearly shows that the existence of Band-5 can be nicely confirmed in the level scheme. The 717 keV transition was observed at the top of Band-5, in addition to the other transitions of this band reported in Ref. [BAR10], even in

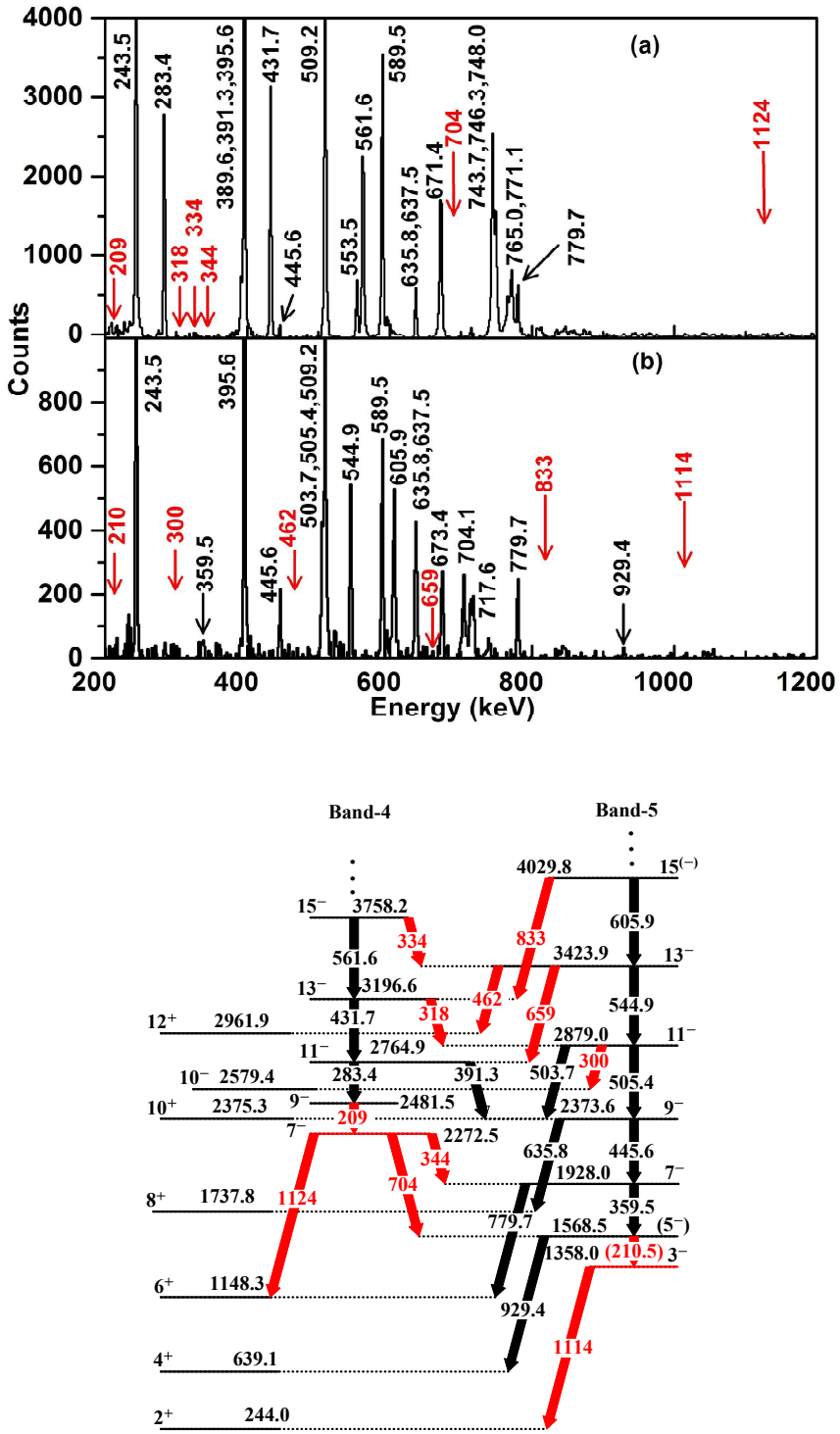

Figure 5.7: (a) The added cube gates made by all possible combination (28 in nos.) of the in-band transitions of Band-4. The positions for the unobserved transitions are indicated with red arrows and text. (b) The added cube gate made by all possible combination (28 in nos.) of the in-band transitions of Band-5. The positions for the unobserved transitions are indicated with red arrows and text. A part of the decay of Band-4 and Band-5 are also shown.

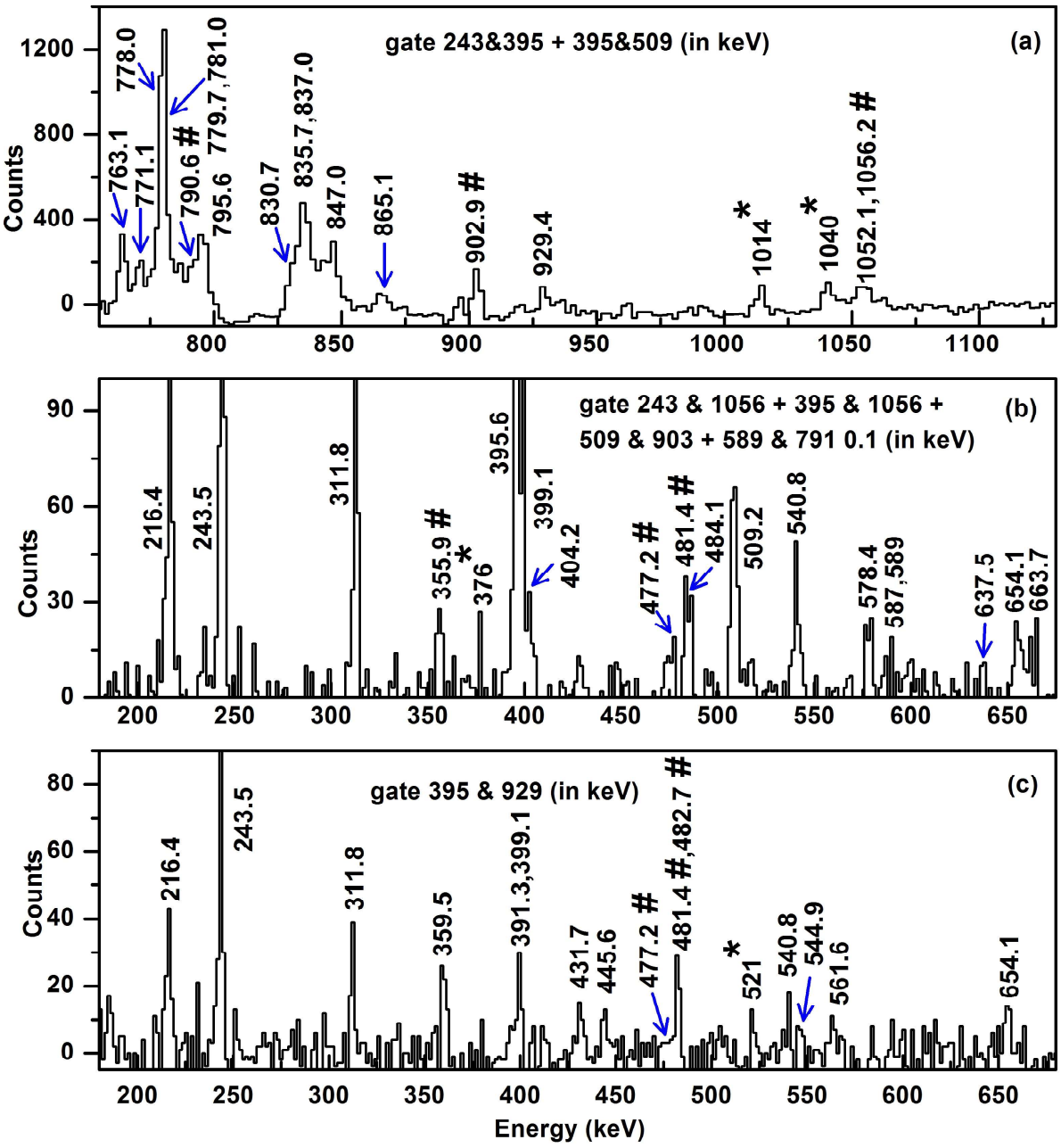

Figure 5.6: The added cube gates show the γ-rays related to the de-excitation of Band-6 as observed in the present work. The top panel (a) shows the presence of three inter-band transitions (790.6, 902.9 and 1056.2 keV) decaying from Band-6 to the yrast band; the middle and bottom panels, (b) and (c) respectively, show all the intra-band transitions (355.9, 477.2 and 481.4 keV) of Band-6 and one inter-band transition (482.7 keV) decaying from Band-6 to Band-5. All the intra-band and inter-band transitions of Band-6 are marked with the symbol #. The transitions marked with asterisks could not be placed in the levels scheme of ^{160}Yb. Blue arrows have been used to mark the weakest and close lying γ-rays.

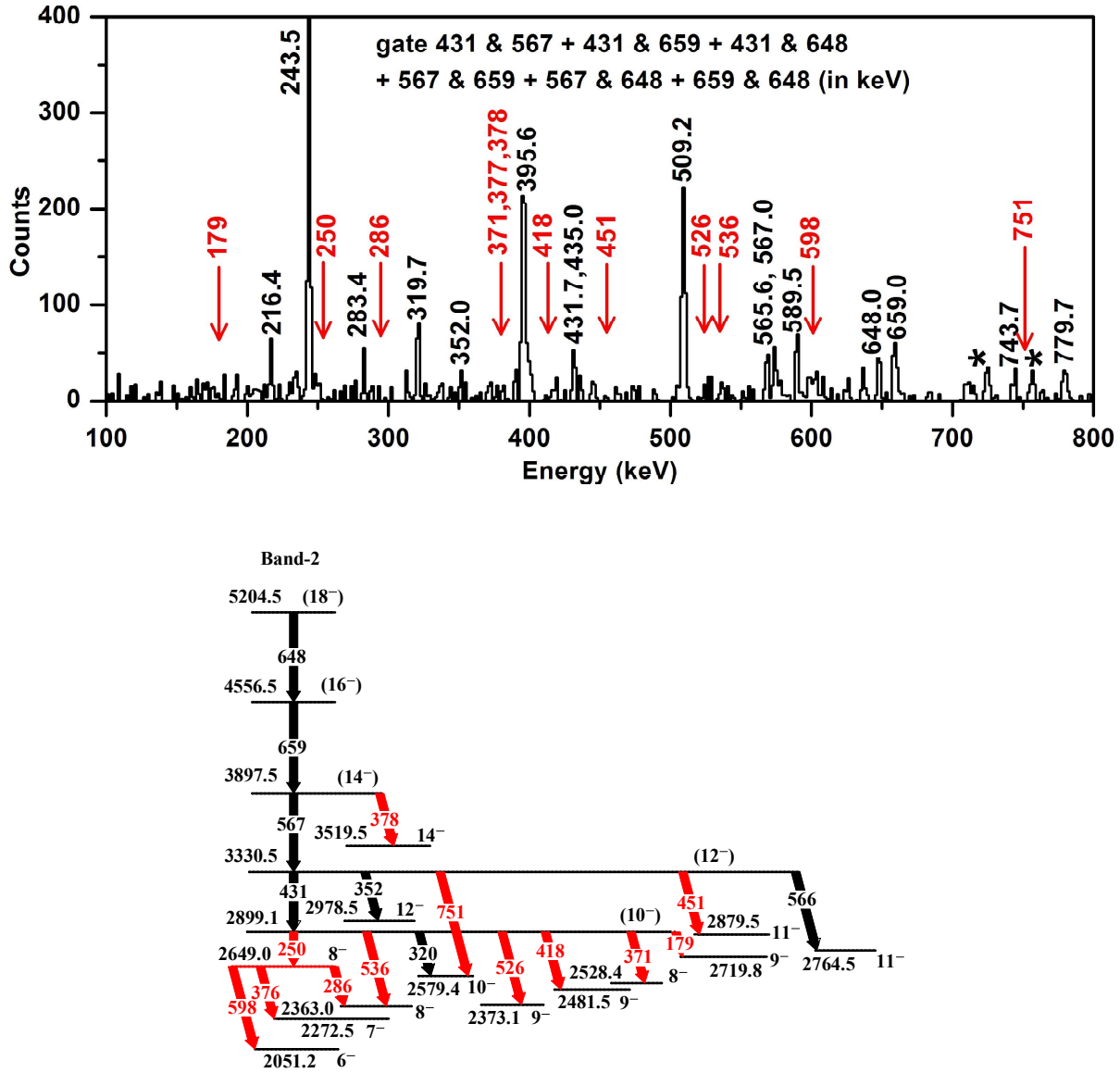

Figure 5.5: (top) The spectrum corresponding to the added cube gates of all six possible combinations of the intra-band transitions of Band-2, which are de-exciting the levels above (10^-), is shown. (bottom) The decay of Band-2 is also shown in the partial level scheme. The transitions shown with black arrows in the level scheme are clearly visible in the gated spectrum and are marked with black text. The transitions marked with red arrows in the levels scheme are the ones that were proposed by other authors but could not be confirmed in the present work. The position of these transitions in the gated spectrum are shown with red arrows and red text. The γ-rays shown in the gated spectrum and marked with * could not be placed in the level scheme of ^{160}Yb. The thickness of the transitions given in the decay scheme are not in proportion to their actual intensities.

TABLE III: continued...

E_i (keV)	J_i^π	→	J_f^π	E_γ[1] (keV)	I_γ[2]	DCO[3] (err)(gate)	IPDCO (err)	R(θ) (err)	Mult.
1113.2	3^+	→	2^+	869.7	0.6				E1
2051.2	$6^{(-)}$	→	6^+	902.9	1.8	0.76(14)(Q)		2.35(35)	E1
1568.5	(5^-)	→	4^+	929.4	1.1			0.98(27)	E1
1574.0	(5^+)	→	4^+	934.9	0.9				(E1)
2789.9	(8^+)	→	8^+	1052.1	0.3				(E2)
1695.3	(4^-)	→	4^+	1056.2	0.7				(E1)
4985.7	(17^+)	→	16^+	1135.5	0.4				(M1)
2365.1	(6^+)	→	6^+	1216.8	0.2				(E2)

The development of the respective band structures are shown by adding the double gates in all possible combinations among the in-band transitions, wherever possible. These added gates are shown in the following figures, viz., Fig. 5.5 to Fig. 5.11, where all the unobserved transitions have been marked in red.

[1]The uncertainties in the deduced energy values are, typically, of ±(0.1-0.2) keV.

[2]The uncertainty in the intensity values, originated due to peak fitting, come out to be on average less to ∼3%. For some cases, weak transitions and/or multiplets, these uncertainties could range up to ∼30% or even up to ∼50% for the weakest ones.

[3]The nature of the gated transition has been indicated using letters, Q for quadrupole and D for dipole.

TABLE III: continued...

E_i (keV)	J_i^π	→	J_f^π	E_γ[1] (keV)	I_γ[2]	DCO[3] (err)(gate)	IPDCO (err)	R(θ) (err)	Mult.
4429.6	17^-	→	15^-	671.4	3.4	0.73(11)(Q)	+0.11(7)	2.64(22)	(E2)
4703.2	$(17)^-$	→	$(15)^-$	673.4	1.5			2.03(17)	(E2)
6381.6	$(22)^-$	→	$(20)^-$	688.0	1.0				(E2)
5407.3	$(19)^-$	→	$17^{(-)}$	704.1	0.7				(E2)
7093.3	$(24)^-$	→	$(22)^-$	711.7	0.4				E2
6124.9	$(21)^-$	→	$(19)^-$	717.6	0.4				(E2)
5828.7	(22^+)	→	20^+	736.4	5.8	1.39(18)(Q)	+0.15(11)	2.52(15)	(E2)
4912.6	$18^{(-)}$	→	16^-	739.2	2.9	1.87(23)(D)	+0.18(8)	2.31(36)	E2
2481.5	9^-	→	8^+	743.7	12.6	0.43(6)(Q)	+0.24(17)	1.46(10)	E1
6695.0	$(23)^-$	→	$(21)^-$	746.3	0.5				(E2)
5177.6	$19^{(-)}$	→	17^-	748.0	2.0	0.51(17)(Q)		2.01(23)	(E2)
3138.4	12^+	→	10^+	763.1	12.9			1.97(22)	E2
7460.0	$(25)^-$	→	$(23)^-$	765.0	0.4				(E2)
5948.7	$(21)^-$	→	$19^{(-)}$	771.1	0.6			2.49(25)	(E2)
7871.3	$(26)^-$	→	$(24)^-$	778.0	0.3				(E2)
1928.0	7^-	→	6^+	779.7	8.9	0.44(5)(Q)	+0.11(11)	1.11(5)	E1
5693.6	$(20)^-$	→	$18^{(-)}$	781.0	1.0				(E2)
3747.0	14^+	→	12^+	785.1	6.8				E2
2528.4	(8^-)	→	8^+	790.6	2.2				(E1)
6624.3	(24^+)	→	(22^+)	795.6	4.1	0.74(10)(Q)	+0.05(8)	2.57(8)	E2
8290.7	(28^+)	→	(26^+)	830.7	1.6				(E2)
7460.0	(26^+)	→	(24^+)	835.7	2.6				(E2)
9127.7	(30^+)	→	(28^+)	837.0	1.6				(E2)
8709.3	$(28)^-$	→	$(26)^-$	838.0	0.2				(E2)
9556.3	$(30)^-$	→	$(28)^-$	847.0	0.1				(E2)
4715.3	(18^+)	→	16^+	865.1	0.5				M1

TABLE III: continued...

E_i (keV)	J_i^π	→	J_f^π	E_γ[1] (keV)	I_γ[2]	DCO[3] (err)(gate)	IPDCO (err)	R(θ) (err)	Mult.
2108.0	7^+	→	(5^+)	534.0	0.8				(E2)
3519.3	14^-	→	12^-	540.8	8.2	1.06(19)(Q)	+0.16(7)	2.32(11)	E2
3423.9	13^-	→	11^-	544.9	3.4	0.85(16)(Q)	+0.18(17)	1.97(11)	E2
3868.9				551.0	0.5				
2481.5	9^-	→	7^-	553.5	2.2	0.94(17)(Q)		2.11(15)	E2
3758.2	15^-	→	13^-	561.6	11.0	1.97(25)(D)	+0.17(8)	2.11(14)	E2
3330.5	(12^-)	→	11^-	565.6	1.3				(M1)
3897.5	(14^-)	→	(12^-)	567.0	2.1				(E2)
4428.6	18^+	→	16^+	578.4	18.0			2.45(12)	E2
2961.9	12^+	→	10^+	586.6	33.9	0.87(4)(Q)	+0.12(1)	2.23(5)	E2
1737.8	8^+	→	6^+	589.5	73.0	1.04(9)(Q)	+0.10(1)	2.34(4)	E2
2700.0	(9^+)	→	7^+	592.0	0.1				(E2)
4029.8	$(15)^-$	→	13^-	605.9	2.1			2.26(18)	(E2)
4474.9				606.0	0.4				
3747.0	14^+	→	12^+	608.6	14.1				E2
1256.0	3^-	→	4^+	616.9	2.7	0.56(15)(Q)	+0.25(18)	1.21(13)	E1
2363.0	8^-	→	8^+	625.2	4.7	1.34(27)(Q)	-0.07(10)	2.86(16)	(E1+M2)
3329.0	(11^+)	→	(9^+)	629.0	0.1				(E2)
4377.0	16^+	→	14^+	630.0	10.3			2.54(58)	E2
2373.6	9^-	→	8^+	635.8	5.9	0.59(11)(Q)			E1
2375.3	10^+	→	8^+	637.5	49.8	0.82(9)(Q)	+0.13(5)		E2
5204.5	(18^-)	→	(16^-)	648.0	1.2				(E2)
4173.4	16^-	→	14^-	654.1	4.9	1.06(16)(Q)	+0.13(8)	2.18(24)	E2
4556.5	(16^-)	→	(14^-)	659.0	2.1				(E2)
5037.0	18^+	→	16^+	660.0	1.5				(E2)
5092.3	20^+	→	18^+	663.7	12.7	0.72(5)(Q)	+0.18(7)	2.21(14)	E2

TABLE III: continued...

E_i (keV)	J_i^π	→	J_f^π	E_γ[1] (keV)	I_γ[2]	DCO[3] (err)(gate)	IPDCO (err)	R(θ) (err)	Mult.
3330.5	(12^-)	→	12^-	352.0	0.3				(M1)
2051.2	$6^{(-)}$	→	(4^-)	355.9	0.6				(E2)
1928.0	7^-	→	(5^-)	359.5	0.4				(E2)
2764.9	11^-	→	10^+	389.6	2.2				(E1)
2764.9	11^-	→	9^-	391.3	4.4				(E2)
639.1	4^+	→	2^+	395.6	91.7	1.04(3)(Q)	+0.10(3)	2.45(6)	E2
2978.5	12^-	→	10^-	399.1	12.7	0.93(7)(Q)	+0.06(7)	2.46(11)	E2
3366.1	14^+	→	12^+	404.2	33.3	1.04(3)(Q)	+0.08(4)	2.51(12)	E2
4173.4	16^-	→	15^-	415.2	0.1				(M1)
2789.9				(424.8)					
3330.5	(12^-)	→	(10^-)	431.4	0.2				(E2)
3196.6	13^-	→	11^-	431.7	10.6	1.00(7)(Q)	+0.09(6)	2.24(13)	E2
2363.0	8^-	→	7^-	435.0	3.0	0.49(7)(Q)	+0.11(9)	1.20(5)	E2+M1
2373.6	9^-	→	7^-	445.6	2.9	1.03(16)(Q)	+0.19(20)	2.74(21)	E2
1574.0	(5^+)	→	3^+	460.8	0.8				(E2)
2528.4	(8^-)	→	$6^{(-)}$	477.2	1.5				(E2)
3009.8	(10^-)	→	(8^-)	481.4	2.5				(M1)
2051.2	$6^{(-)}$	→	(5^-)	482.7	0.7				(M1)
4912.6	$18^{(-)}$	→	17^-	483.0*	<0.1				M1
3850.2	16^+	→	14^+	484.1	21.9	0.94(5)(Q)	+0.20(7)	2.14(5)	E2
1743.0	(5^-)	→	3^-	487.0	1.9				(E2)
2879.0	11^-	→	10^+	503.7	1.4				(E1)
2879.0	11^-	→	9^-	505.4	5.3	1.33(38)(D)			E2
1148.3	6^+	→	4^+	509.2	87.6	0.89(6)(Q)	+0.09(3)		E2
3317.9				528.0	0.5				
2274.0	(7^-)	→	(5^-)	531.0	0.5				(E2)

plets of the confirmed transitions. These multiplets were observed as a part of genuine coincidence events possibly because of the lower granularity of the AFRODITE array. The intensity of these unobserved transitions, even if existing, are very low as shown with the branching ratios listed in Table 5.2. For these unobserved transitions, the limiting value of the possible intensity branching ratios are shown in Table 5.2, by considering the maximum possible intensities for these transitions as the lowest value of intensity (i.e., 0.1% w.r.t 243 keV) that could be measured in the present work and by considering the error as 50% (maximum error obtained). It is worth mentioning that most of these unobserved transitions tabulated in table 5.2 are part of multiplets and were observed only in Ref. [BAR10, BAR05].

5.3.2 Level Scheme of ^{160}Yb & the Band structures

The energies, relative intensities, DCO ratios, R_θ and IPDCO ratios for the transitions observed in the present experiment have been tabulated in Table 5.3 along with other relevant details.

Table 5.3: The spectroscopic results for the γ-transitions observed in the present experiment on ^{160}Yb.

E_i (keV)	J_i^π	→	J_f^π	E_γ[1] (keV)	I_γ[2]	DCO[3] (err)(gate)	IPDCO (err)	R(θ) (err)	Mult.
2579.4	10^-	→	9^-	97.9	0.4				(M1)
2481.5	9^-	→	10^+	106.2	0.2				(E1)
2764.9	11^-	→	10^-	185.5	0.2				(M1)
2579.4	10^-	→	9^-	205.8	1.2				(M1)
2978.5	12^-	→	11^-	213.6	0.6				(M1)
2579.4	10^-	→	8^-	216.4	9.2	1.09(8)(Q)	+0.19(17)	2.31(8)	E2
243.5	2^+	→	0^+	243.5	100	2.00(8)(D)	+0.19(4)	2.51(6)	E2
2363.0	8^-	→	7^+	255.0	0.8	0.53(8)(Q)		1.23(18)	E1
2764.9	11^-	→	9^-	283.4	11.8	1.03(5)(Q)	+0.22(8)	2.42(9)	E2
2363.0	8^-	→	$6^{(-)}$	311.8	2.7	0.84(10)(Q)	+0.05(9)	2.65(12)	E2
2899.1	(10^-)	→	10^-	319.7	0.5				(M1)
3519.3	14^-	→	13^-	322.7	0.5				(M1)

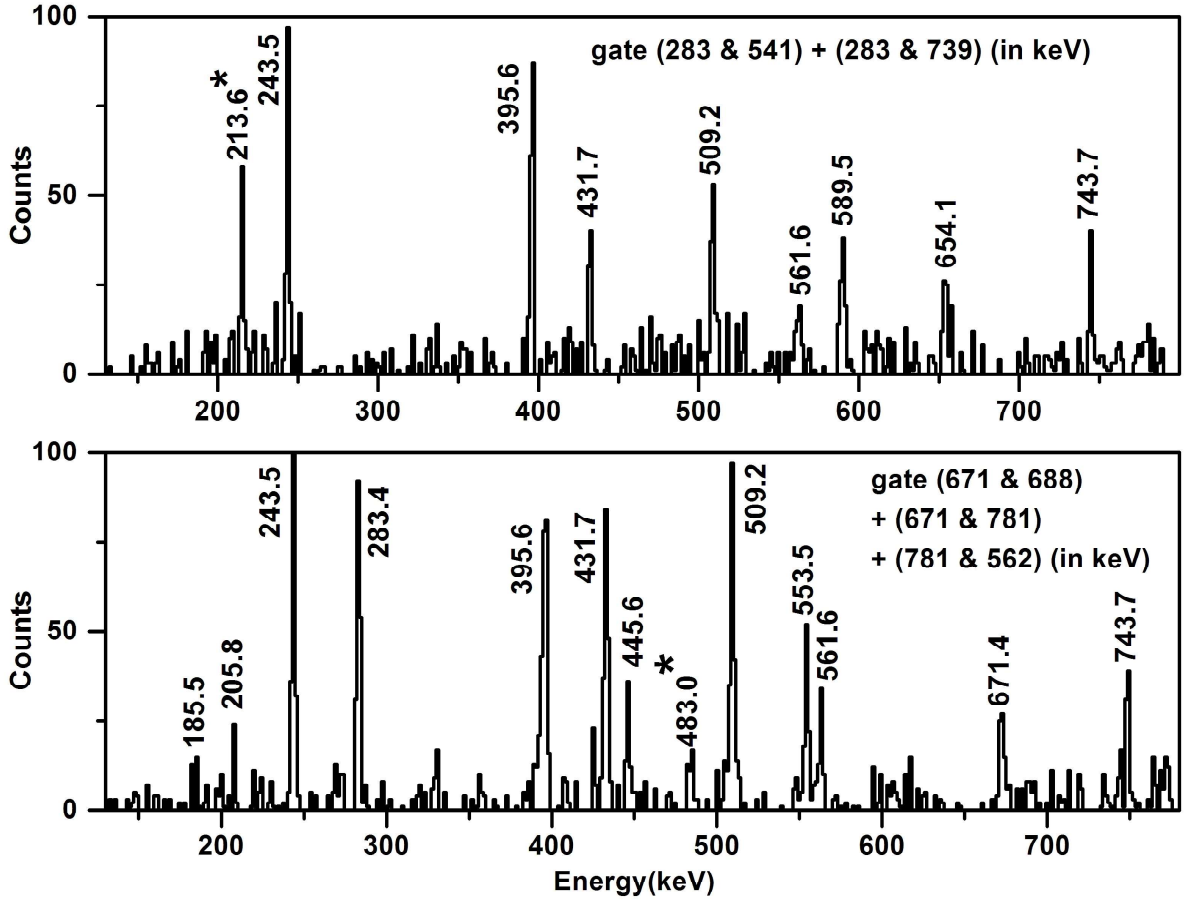

Figure 5.4: The added cube gates showing the inter-band transitions decaying from Band-3 to Band-4. The ones at 213.6 keV and 483.0 keV, marked with asterisks, represent the decay from 12^- and 18^- levels of Band-3.

clear that the intensity branching ratios for the observed transitions are much in agreement with the branching ratios published in ENSDF. This is expected because branching ratio for a particular level is an observable which is independent of the reactions used for its population.

However, in the present experiment, some of the in-band and interband transitions, reported earlier [BAR10, BAR05] using similar HI reaction, could not be confirmed even with the high selective power of the INGA array. Owing to the comparision of the INGA array w.r.t the AFRODITE array, 3 times more statistics gathered in the experiment compared to that in the AFRODITE experiment, use of cube analysis in the present experiment compared to the doubles analysis of the AFRODITE experiment and the study of branching ratio as shown in Table 5.1 and Table 5.2, it may be concluded that the mentioned unobserved gamma transitions are the part of the multi-

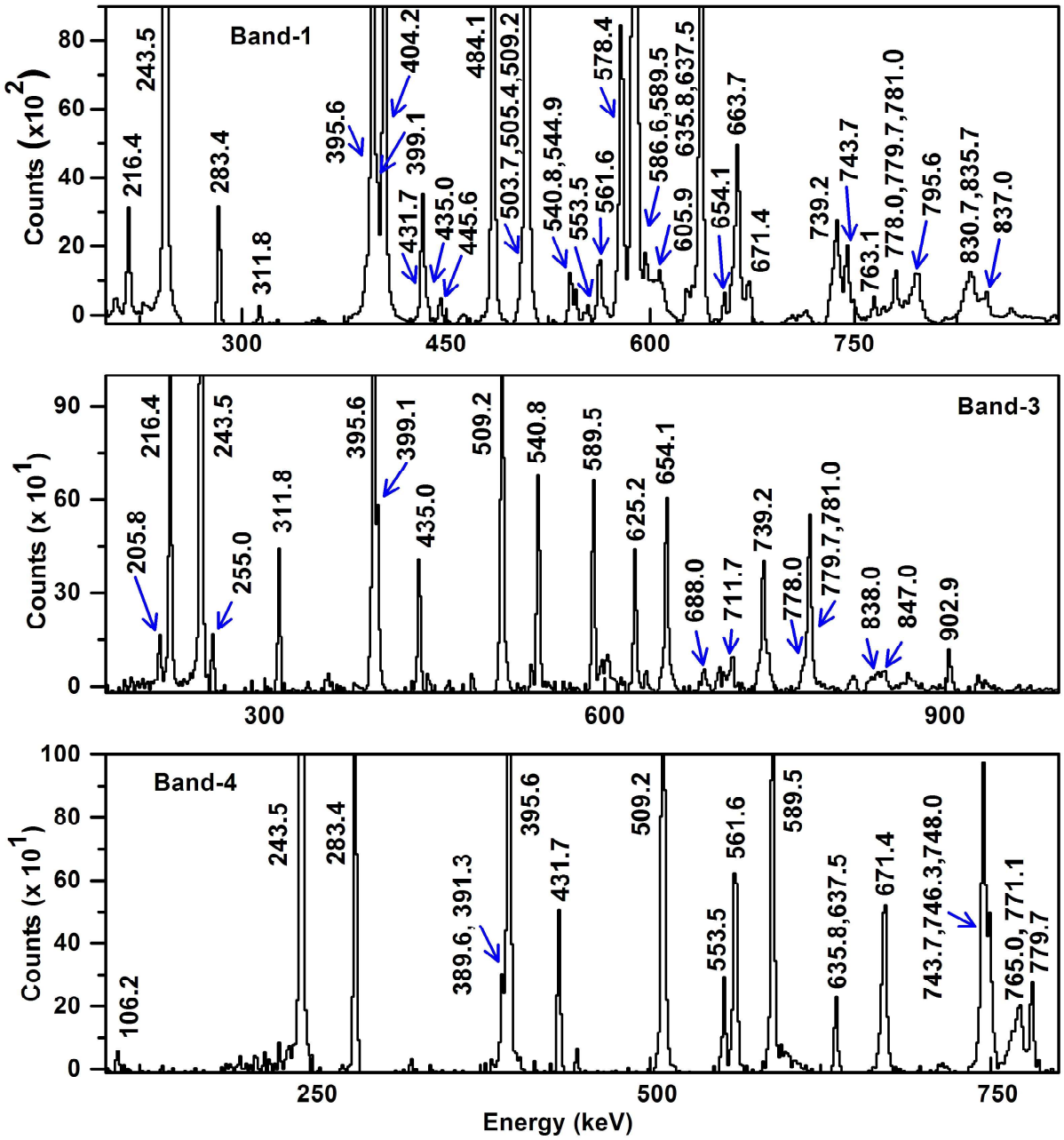

Figure 5.3: The added cube gates showing the transitions from Band-1 (top panel), Band-3 (middle panel) and Band-4 (bottom panel), populated in the present work. For Band-1, the added gates of [(243&395), (395&509), (509&589), (589&637), (637&587), (587&404), (404&484), (484&578), (578&664), (664&736), (736&796)(in keV)] was used. Similarly, the added gates of (216&399), (399&541), (541&654), (654&739), (739&688), (688&712)(in keV)] was used for Band-3 and the added gates of [(283&432), (432&562), (562&671), (671&748), (748&770)(in keV)] was used for Band-4. The observed transitions arising from the de-excitation of these three bands are marked with their energies. Blue arrows have been used to mark the weakest and close lying γ-rays.

earlier measurements mainly differs because of the efficiency and granularity of the array used in the present work. In the present experiment, we were able to collect 6.1×10^9 and 3.5×10^8 prompt double-coincidence and triple-coincidence events respectively. The intensity of 0.1% with respect to the 243.5 keV γ-transition (the most intense ground state feeding transition), has been estimated for the topmost transition of 847.0 keV of Band-3. This is the lowest intensity that could be measured in the present experiment with an acceptable accuracy. The observation of some of the weakest [i.e. $\sim$ 0.1% compared to 243.5 keV (ground-state transition)] γ-rays known in the level scheme of ^{160}Yb quantify the observational limit that was achievable in the present experiment. The triple-coincidence events has been of extreme importance for disentangling gamma multiplets and to confirm the presence of the very weak transitions in a band. This comes clearly out of the observations detailed below.

In the present work, the Band-1 and Band-3 of ^{160}Yb were observed up to the maximum spin of 30 $\hbar$ and Band-4, up to 25 $\hbar$. The population features of Band-1, Band-3 and Band-4 have been represented in Fig. 5.3 by adding the cube gates corresponding to all possible combinations of the intra-band transitions of the corresponding bands. The observed transitions which are reported in the ENSDF database [REI05] but are not observed in Ref. [BAR10] have been marked with asterisk in the Figure. Moreover, all the weak inter-band transitions from Band-3 to Band-4, reported by D. B. Campbell [CAMXX], have been observed in the present work as confirmed from the added double gates from the γ^3 cube, shown in Fig. 5.4. The intensities of these transitions, as estimated in the present work, are smaller than 0.6% of 243.5 keV transition. Although, the presence of the 483.0 keV transition (not observed in Ref. [BAR10]) connecting the 18^- level of Band-3 to the 17^- level of Band-4 was confirmed in the present work, its intensity could not be established as this weak transition was the part of a multiplet of the strong 484 keV transition of the yrast band.

The Table 5.1 gives an idea on the extent of population of a particular level in ^{160}Yb and the detection of the transitions decaying from that particular level, that could be attained in the present experiment, from the measurement of their branching ratios from the present data. The said ratios for some of the levels were compared with the available data in ENSDF [REI05] for which at least two decaying transitions were known in ENSDF with their intensity values. From the table it is

Table 5.2: Limiting value of branching ratios for majority of the unseen transitions. An attempt has been made to estimate the limiting value of the branching intensity ratio of transitions for which there exists another transition with known intensity decaying from the same energy level. All the values except the intensities of the unobserved transitions and branching ratio are truncated to first decimal place.

E_x(keV)	γ_1 & γ_2 (keV)	$I_{\gamma 1}$ (max.)	$I_{\gamma 2}$ Pres. work	Ratio (max.)
1113.2	I(292)/I(869.7)	0.10(5)	0.60(12)	0.17(9)
	I(474)/I(869.7)	0.10(5)	0.60(12)	0.17(9)
1256.0	I(435)/I(616.9)	0.10(5)	2.7(7)	0.04(2)
1568.5	I(210)/I(929.4)	0.10(5)	1.1(3)	0.09(5)
1574.0	I(318)/I(460.8)	0.10(5)	0.8(2)	0.13(7)
	I(426)/I(460.8)	0.10(5)	0.8(2)	0.13(7)
1695.3	I(337)/I(1056.2)	0.10(5)	0.70(18)	0.14(8)
1743.0	I(595)/I(487.0)	0.10(5)	1.9(5)	0.05(3)
	I(1104)/I(487.0)	0.10(5)	1.9(5)	0.05(3)
2108.0	I(365)/I(534.0)	0.10(5)	0.8(2)	0.13(7)
	I(960)/I(534.0)	0.10(5)	0.8(2)	0.13(7)
2274.0	I(536)/I(531.0)	0.10(5)	0.5(1)	0.20(11)
	I(1126)/I(531.0)	0.10(5)	0.5(1)	0.20(11)
2481.5	I(209)/I(743.7)	0.10(5)	12.6(3.0)	0.008(4)
2423.9	I(462)/I(544.9)	0.10(5)	3.4(8)	0.03(2)
2528.4	I(600)/I(477.2)	0.10(5)	1.5(4)	0.07(4)
2789.9	I(516)/I(1052.1)	0.10(5)	0.3(1)	0.33(19)
2879.0	I(398)/I(505.4)	0.10(5)	5.3(13)	0.02(1)
	I(300)/I(505.4)	0.10(5)	5.3(13)	0.02(1)
2899.1	I(179)/I(320)	0.10(5)	0.50(12)	0.20(11)
	I(418)/I(320)	0.10(5)	0.50(12)	0.20(11)
	I(526)/I(320)	0.10(5)	0.50(12)	0.20(11)
	I(371)/I(320)	0.10(5)	0.50(12)	0.20(11)
	I(536)/I(320)	0.10(5)	0.50(12)	0.20(11)
	I(250)/I(320)	0.10(5)	0.50(12)	0.20(11)
3196.6	I(318)/I(431.7)	0.10(5)	10.6(28)	0.01(1)
3330.5	I(451)/I(431.4)	0.10(5)	0.2(1)	0.50(29)
	I(751)/I(431.4)	0.10(5)	0.2(1)	0.50(29)
3423.9	I(659)/I(544.9)	0.10(5)	3.4(8)	0.03(2)
	I(462)/I(544.9)	0.10(5)	3.4(8)	0.03(2)
3758.2	I(334)/I(561.6)	0.10(5)	11.0(2.9)	0.010(5)
3897.5	I(378)/I(567.0)	0.10(5)	2.1(6)	0.05(3)
4029.8	I(833)/I(605.9)	0.10(5)	2.1(5)	0.05(3)
4377.0	I(1011)/I(630.0)	0.10(5)	10.3(24)	0.01(1)

Table 5.1: Measured Branching Ratios for some of the observed transitions for which intensity could be measured. The comparison of the deduced ratios to that from the ENSDF database are also shown (see text).

E_x(keV)	γ_1 & γ_1 (keV)	$I_{\gamma1}$	$I_{\gamma2}$ present work	Ratio	$I_{\gamma1}$	$I_{\gamma2}$ ENSDF	Ratio
2051.2	I(482.7)/I(902.9)	0.7(2)	1.8(4)	0.39(14)	50	100	0.50
2363.0	I(312)/I(435)	2.7(8)	3.0(6)	0.90(32)	62	92	0.67
	I(312)/I(626)	2.7(8)	4.7(12)	0.57(22)	62	100	0.62
2373.6	I(445.6)/I(635.8)	2.9(7)	5.9(15)	0.49(17)	49	100	0.49
2481.5	I(553)/I(744)	2.8(8)	12.6(22)	0.17(7)	23	100	0.23
2579.4	I(205.8)/I(216.4)	1.2(6)	9.2(22)	0.13(7)	14	100	0.14
2764.9	I(389.6)/I(283.4)	2.2(9)	11.8(28)	0.19(9)	28	100	0.28
3747.0	I(608.6)/I(785.1)	14.1(25)	6.8(1)	2.07(37)	100	62	1.61

INGA array, its photopeak detection efficiency can be ∼5% (at 1.3 MeV) with twenty four Clover detectors placed in the array and for the present work this efficiency was ∼4.2% with twenty Clover detectors used in the experiment. Due to the chosen target-to-detector distance (i.e., increasing the single-hit probability through smaller aperture solid angle) and an adequate number of Clover detectors (i.e., increasing both the total photo-peak efficiency and the granularity of the array), the INGA array is very much suitable for detecting the triple gamma coincidences in the case of experiments for which the gamma multiplicity is of the order of 20.

The cross section of ^{160}Yb, populated from the reaction used in the present work, peaked at an angular momentum of 30$\hbar$. It results in the maximum probability for the multiplicity of emitted γ as $\sim$ 15. However, it is worth mentioning that using such HI reaction it is difficult to populate the weak non-yrast levels. This is because of the facts that in such reactions, the low spin non-yrast states are rarely populated and over & above, nearly all of the band feeding comes from the top of the band having almost no side feeding for the low spin states. The alpha induced experiments are suitable for the population of such levels, however, there is no such feasible reaction that populates ^{160}Yb. All the previous experiments on this nucleus were performed using mainly ^{16}O beam which is similar to the present work and in some few cases ^{44}Ca was used [REI05, XUN18]. Hence, the limits on intensities for the γ-rays observed in the present work in comparison to the

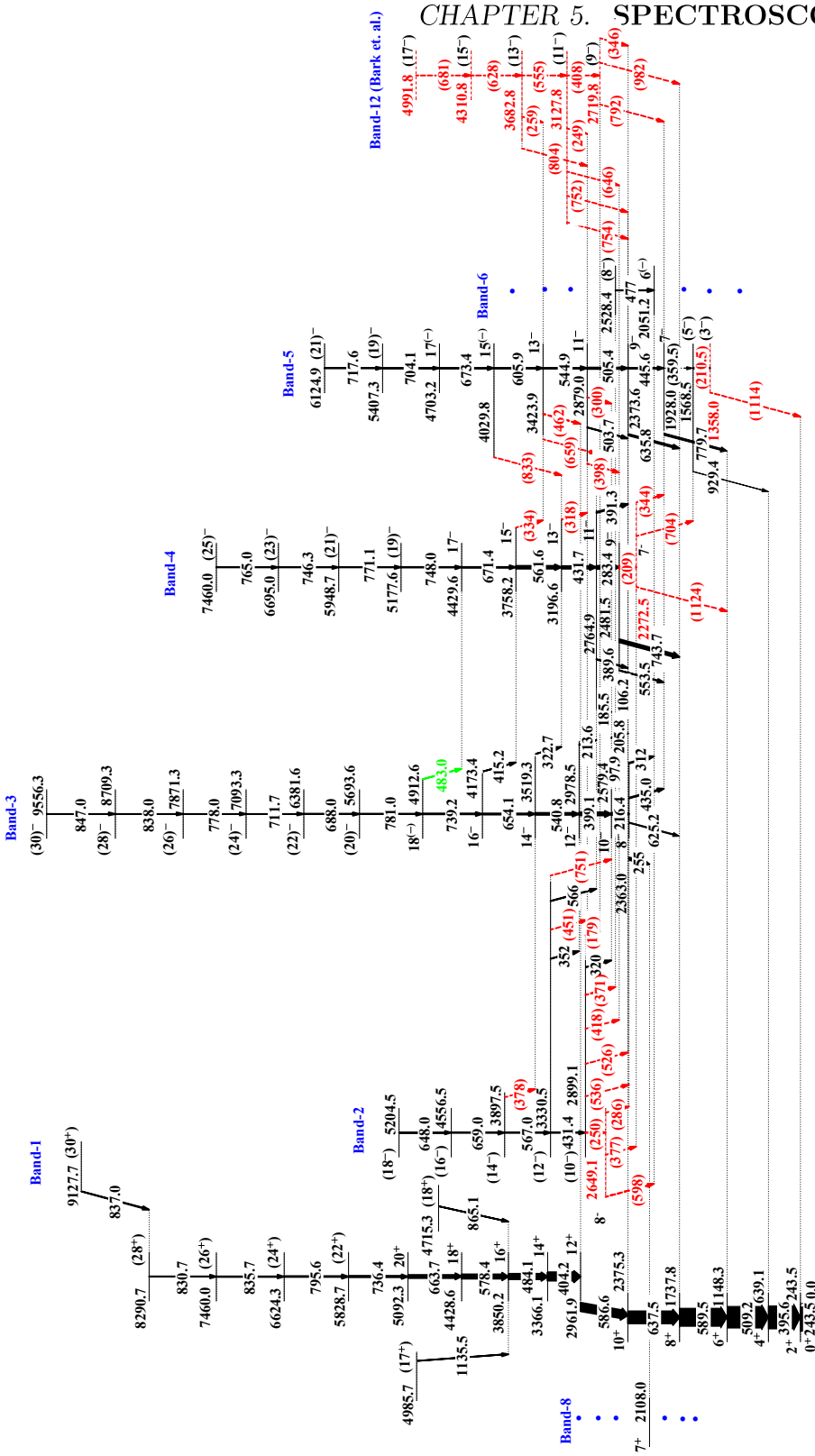

Figure 5.2: The second part of the ^{160}Yb level scheme showing the Yrast band and the negative parity bands (all but Band-6, see figure 5.1). Band-6 and Band-8 are fully displayed in figure 5.1. Transitions reported by other authors [BAR05, BAR10] but unobserved in the present work are shown as red dotted lines and indicated in brackets; the unobserved levels are shown as red dotted (see text). The newly placed transition is shown as green.

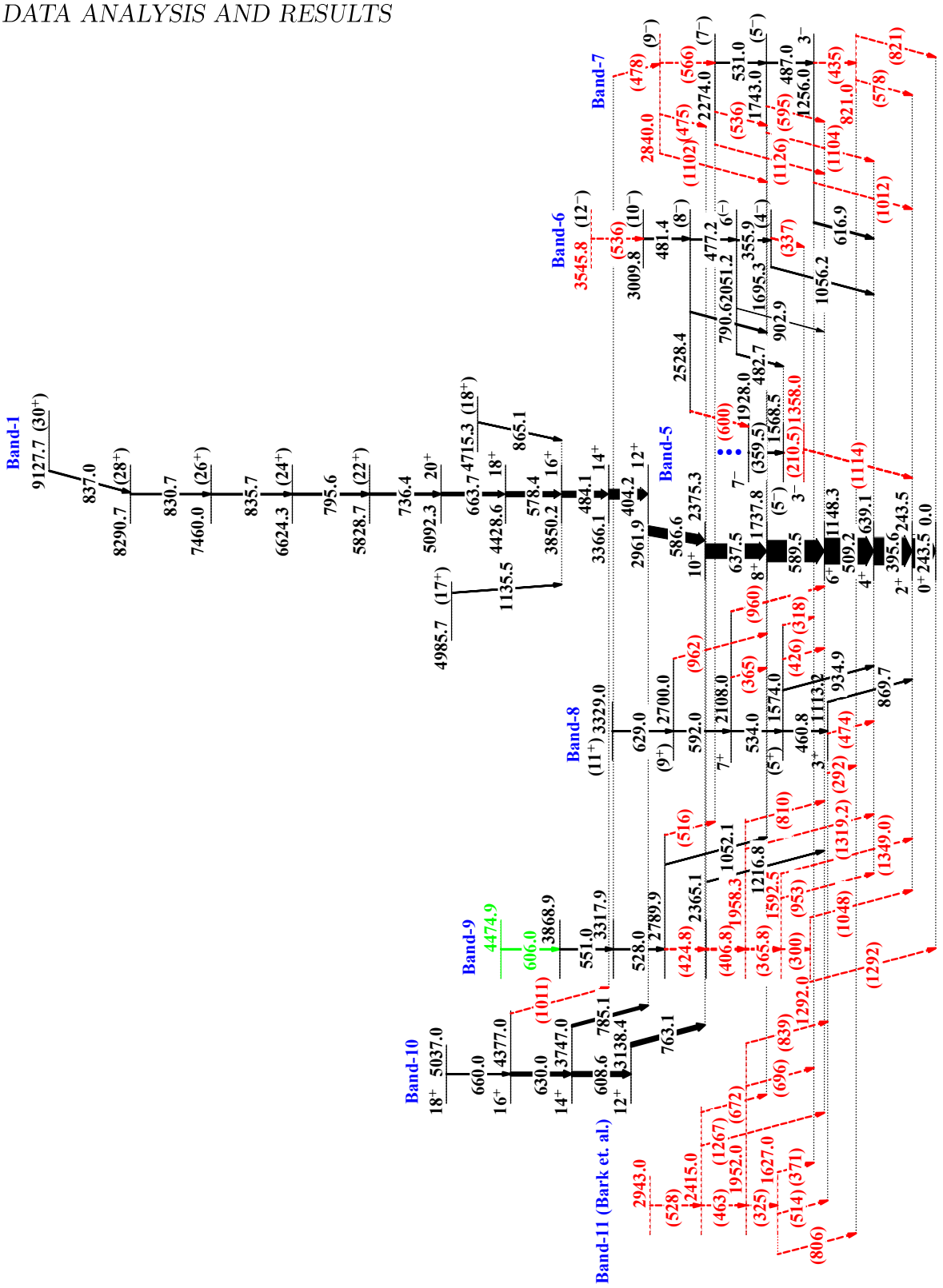

Figure 5.1: The first part of the level scheme of ^{160}Yb showing the Yrast band, the positive parity bands and few of the negative parity bands are shown. The level scheme is divided in two parts for clarity. Band-5 is fully displayed on the second part (figure 5.2). The transitions which could be placed in the level scheme by our analysis including double gating on triple coincidence data have been shown in black arrows. Transitions which are proposed by other authors [BAR05, BAR10] using double-coincidence but could not be confirmed from the triple coincidence analysis of the present work are shown as red dotted lines and indicated in brackets; the unobserved levels are shown as red dotted (see text). The newly placed level and transition are shown as green.

5.3 Data Analysis and Results

The obtained data have been sorted offline using the MARCOS (Multi parameter time stamped based Coincidence Search) program [PAL12] to construct the RADWARE [RAD95] compatible $\gamma-\gamma$ matrix and γ^3 cube for the analysis of coincidence relationships. Some of the gated spectra obtained from the double and triple γ coincidence data are shown in Sect. 5.3.1 and 5.3.2 while discussing the analysis of various band structures in ^{160}Yb. The relative intensities, I_γ, of the transitions of interest were determined mostly from the appropriately gated projections of the $\gamma-\gamma$ matrix as well as from the total projection in some cases. The $\gamma-\gamma$ angle dependent matrices were prepared for the analysis of DCO, R_θ, and IPDCO ratios using the INGASORT analysis package [BHO17].

In the present work, the level scheme of ^{160}Yb has been obtained by using the above information on $\gamma-\gamma$ and $\gamma-\gamma-\gamma$ coincidences, I_γ, DCO, R_θ and IPDCO. The level scheme has been shown in Fig. 5.1 and 5.2 and the new results have been discussed in Section 5.3.2. In addition to the yrast band denoted as Band-1, we have observed six negative-parity bands labelled Band-2, Band-3, ..., Band-7 – and three positive-parity bands labelled Band-8, Band-9 and Band-10, respectively. The numbering of the Bands are as per the level scheme given in Fig. 5.1 and 5.2. In this figure, the transitions, reported by other authors (see Ref. [REI05, XUN18]) which were not observed or could not be confirmed from the present work are shown in parenthesis and similarly, the unobserved levels are indicated with dotted lines. The intensity of the unobserved transitions, if existing, are less than the lowest intensity that could be detected in the present experiment, as discussed in the following Section 5.3.1.

5.3.1 Selective Power of INGA, Reaction used and the limiting intensity branching for unobserved transitions

The Compton suppressed clover detectors of the gamma array used in the present experiment, cf. Ref. [PAL12], consisted of four 50 mm × 70 mm HPGe crystals. The array was designed in a way so as to keep the target to crystal distance at 25 cm. Considering all the design parameters of the

However, the newly placed inter-band transitions, essential for the estimation of the quadrupole moments of the bands of particular interest in the context of the tetrahedral symmetry hypothesis, were reported in Ref. [BAR10] as either uncertain or belonging to the doublets/triplets in the decay scheme of the nucleus in question. In fact, a large number of the other new transitions in the decay scheme of ^{160}Yb of Refs. [BAR10, BAR05] were the elements of at least doublet and/or triplet structures. Recall that the quoted experiment was performed with an array of eight Clover HPGe detectors which enabled only the $\gamma - \gamma$ double-coincidence analysis.

In this context, the only possibility of confirming the presence of these newly placed close lying transitions (hereafter referred to as multiplet transitions) is to study the coincidence relationships by using at least double gating on triple coincidence data that can treat these energy multiplet transitions with a higher selectivity. Similarly, the experimental determination of the intensities and multipolarities is very important for the interpretation and testing the decay and feeding of the bands of interest. The $B(E2)_{in}/B(E1)_{out}$ ratios related to these non-yrast negative-parity bands may provide important information, when comparing to the other similar band structures in this mass region to shed some light on the similarities and possible differences from the patterns(s) observed in the neighbouring nuclei.

In the present work, the main objective was to revisit the spectroscopy of ^{160}Yb in order to study the low and moderate spin structure of this nucleus by using conventional gamma ray spectroscopic technique with the Indian National Gamma Array (INGA).

5.2 Experimental Results

The excited states of the ^{160}Yb nucleus were populated by using the HI fusion evaporation reaction ^{148}Sm(^{16}O, 4n)^{160}Yb with E_{beam} = 90 MeV from the 14UD Pelletron at TIFR, Mumbai. The 900 μg/cm^2 thick Sm_2O_3 target, 97% enriched and electro-deposited on a 3 mg/cm^2 Pb backing foil, was used in the experiment. The Indian National Gamma Array (INGA) (see Section-3.10.4 for details), consisting of twenty Compton suppressed Clover detectors at the time of experiment, was used for the detection of the γ-transitions.

transitions to be able to approach the interpretation of the underlying structures in terms of hypothetical tetrahedral symmetry. Such measurements of the absolute reduced transition probabilities turn out to be very difficult in most of the cases of interest and various authors attempted in the past estimating at least the relative B(E2)/B(E1) probabilities and/or trying to deduce *indirectly* the underlying quadrupole moments using the band-mixing model. In this latter case the difficulty of the problem is transferred into the difficulty of precise measurement of the inter-band transitions and their intensities from and to the right band members.

The absolute transition probabilities or their ratios, measured by using high efficiency γ arrays, may disclose the underlying signature for the associated structure of these negative parity bands. Such efforts have already been initiated and being continued by carrying out several experiments with the Gadolinium isotopes using a variety of detection techniques [JEN10, DOA10, DOA09].

The negative parity bands in ^{160}Yb have been observed in different experiments [DUD02, RIE80-B, RIE80-A, BYR87, BAR05]. The four negative parity non-yrast sequences in ^{160}Yb were first observed in the work of Ref. [RIE80-A] and the bands were assigned to have two quasiparticle (qp) configurations generated out of the $\nu i_{\frac{13}{2}}$ and $\nu h_{\frac{9}{2}}/\nu f_{\frac{7}{2}}$ orbitals. This was confirmed in the later work by Byrski *et al.*, [BYR87], where the alignment of quasiparticles and shape co-existence at high spin of ^{160}Yb were also reported. One of these negative parity bands (Band-5 in fig. 5.2, denoted "3" in Ref. [RIE80-A]) having a very distinct nature of alignment and strong E1 decays to the yrast band, needs probably a special attention in the context of the $\lambda = 3$ deformation in this mass region.

In Ref. [BAR10], a characterisation of the negative parity bands in ^{160}Yb was reported and two more negative-parity bands were reported in addition to the earlier works [RIE80-A, BYR87]. In order to study the characteristics and behaviour of the possible tetrahedral-band candidates, it is necessary to study their connections with the other bands involved in their feeding and decay. Several such connections were proposed in Ref. [BAR10], which were used to perform band mixing calculation to conjucture the transition quadrupole moment of Band-5 using the measured quadrupole moment of Band-4. Moreover, the above authors concluded that Band-5 and Band-6 are signature partners of the Coriolis-mixed rotation-aligned octupole-vibrational band with $K^{\pi} = 1^{-}$.

Chapter 5

Spectroscopy of ^{160}Yb

5.1 Introduction

The N = 90 nuclei around Gadolinium and Ytterbium, having both proton and neutron numbers close to the tetrahedral 'magic' numbers (Z = 64, 70 and N = 90), are predicted to be among the most suitable candidates for the observation of the nuclear tetrahedral symmetry [DUD02]. To the lowest order in terms of spherical harmonics, this symmetry corresponds to the $\lambda = 3$ (octupole) spherical-harmonic component ($Y_{3\pm2}$) in the nuclear surface. The corresponding shapes have been predicted to occur in atomic nuclei by several theory calculations [DUD02, DUD06, SCH05, ZBE09, TAG13, TAG15]. Calculations show that in the exact symmetry limit both the dipole and the quadrupole moments of the nuclei in question vanish and thus such structures are not expected to emit neither E2-, nor E1-type γ-radiation. One can expect that one of the experimental signatures of such structures could take the form of presence of the $E_I \sim I(I+1)$ rotational energy spectra in which the E2-transitions are simply absent.

Since in the discussed case the underlying nuclear shapes are characterised by octupole components [$\lambda = 3$ (odd) multipolarity], it is expected that there will be negative parity rotational sequences involved in the band structures built on top of collective octupole-type vibrations. It is essential to obtain the experimental information about the structure of those bands as precisely as possible, the ultimate goal being to measure the actual quadrupole and dipole strengths of related

absolute CS values directly obtained from the present experiment and the CS values reconstructed from the work by Lebeda *et al.,* show a reasonable similarity to that predicted by the theoretical models. However, the extent of closeness between these two sets of experimental CS values with the theoretical predictions is different. This might be due to the combination of several unknown experimental conditions involved in a multi-step measurement procedure. Again, the theoretical calculations, involving hosts of uncertainties in the large number of input parameters, are necessarily capable of reproducing the overall trend of the excitation function.

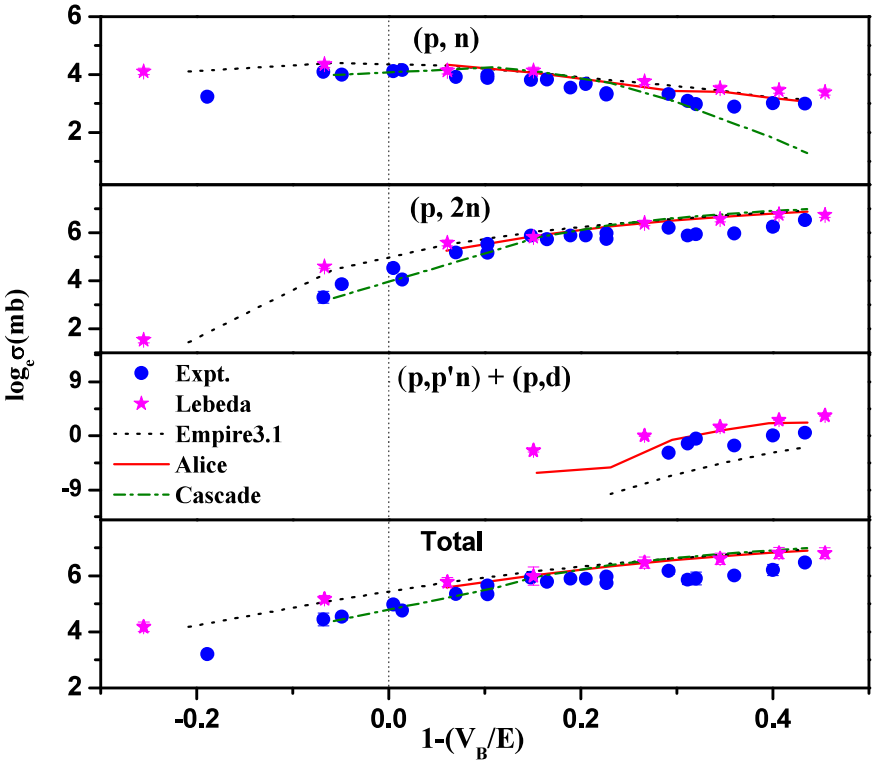

Figure 6.6: Individual CS for different evaporation residues and total CS are plotted in logarithmic scale. Legends used are same as in Fig. 6.5.

The excitation functions for the neutron evaporation residues, obtained from the present work, were found to follow the expected trend in the present range of proton energy. The ^{149}Nd was populated through both (p, p′n) and (p, d) channels whose individual contributions could not be deciphered in the present experiment. Similarly, the production of ^{149}Pm has a contribution from the decay of ^{149}Nd. However, this has been observed to be very negligible compared to the production of ^{149}Pm from the (p, 2n) reaction channel. The above observation is further supported by the low CS values obtained for ^{149}Nd in the present work. The theoretical calculations for the excitation functions have been performed with different statistical model codes, *viz.*, CASCADE, ALICE and EMPIRE3.1. Both the experimental data and theoretical calculations exhibited reasonably similar trend in the entire proton energy range.

The CS values, obtained from the work of Lebeda *et al.*, [LEB12, LEB14], were scaled up to the absolute values by considering the isotopic enrichment ratio of Nd. These reconstructed values are higher compared to the absolute CS measured in the present work. It is obvious that both the

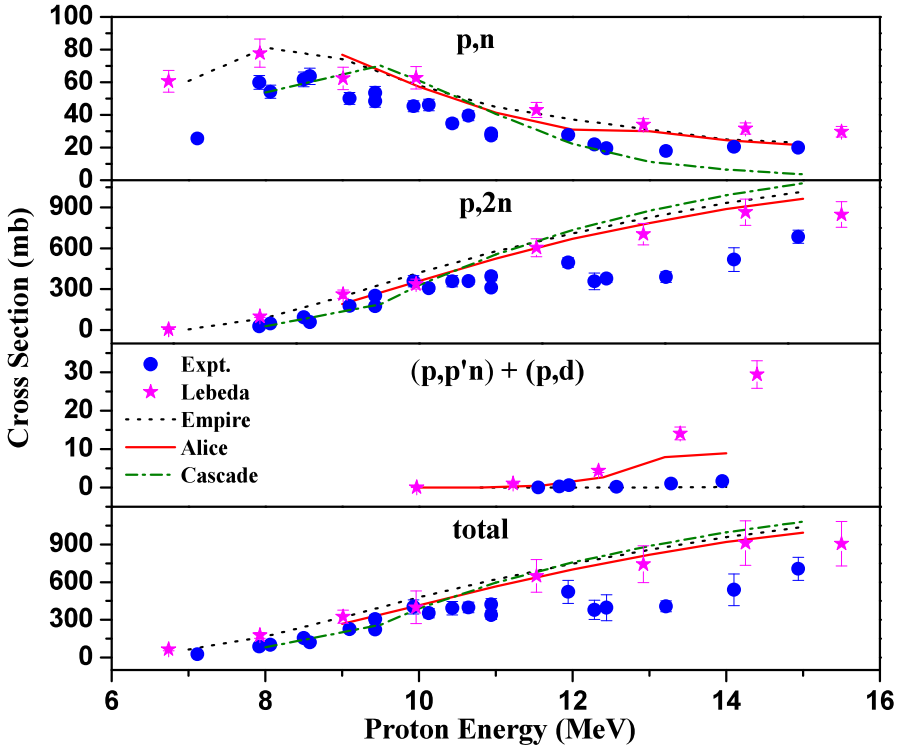

Figure 6.5: Excitation function for ^{150}Nd(p,xnyp) reaction. Experimental data points for (a)^{150}Pm, (b)^{149}Pm, (c) ^{149}Nd and (d) total CS are shown with filled ∘. The calculated values of CS obtained from the work of O. Lebeda *et al.*, are shown with ⋆s. Theoretical CS calculated from Empire3.1, ALICE/91 and CASCADE are shown with dotted, solid and dash dotted lines respectively.

work all sorts of precautions were taken to avoid the over or under estimation of reaction CS. Apart from the use of an enriched target, the target enrichment as well as the Nd:O ratio in the prepared target was considered for the calculation of the number of target Nd atoms. The present work also involved the use of separate Al-catcher foils of appropriate thickness corresponding to each target and monitor in order to ensure the complete collection of the recoiling evaporation residues. Most importantly, the dead time of the detector was kept lower ($\leq$10%) in the present work than that ($\leq$40%) allowed in the work of Lebeda *et al.* [LEB12, LEB14]. The abundances used for the γ transitions were also corrected for the appropriate conversion as per their multipolarity. Wherever possible, the obtained CS values were cross checked by using the activities from two different γ transitions. The CS values at several proton energies were calculated from two different measurements by making appropriate target stacks as explained in section 7.2 in order to ensure the correctness of our experimental data in the present work.

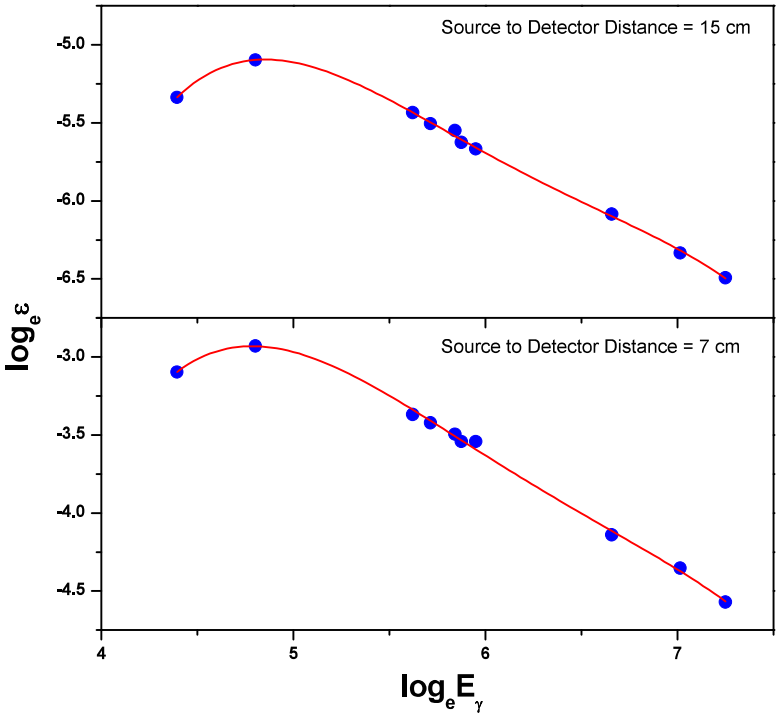

Figure 6.4: The extracted efficiency of the 50% HPGe detector used in the experiment. The efficiency of the detector at a distance of 7 cm and 15 cm from the detector has been shown in the bottom panel and top panel respectively with black square and circles. The solid and dotted lines in the two figures represent the fitted curve.

discussed in details in [BAN15]. A variation between the experimental data and the theoretical prediction was observed for the (p, 2n) channel after E_p = 12 MeV. However, this deviation may be accounted considering the multitude of uncertainties and the limitations embedded in the theoretical codes.

6.4 Discussion

The excitation functions for the p-induced reaction on the 97.65% enriched ^{150}Nd target were measured by γ-decay spectroscopy following the stacked-foil activation technique. In the present work, the absolute CS for the reaction ^{150}Nd(p, xnyp) has been measured for the first time, following the use of the enriched ^{150}Nd target. The present measurement also yields the first set of data points for these reaction CS at several proton energy values covering an energy range of 7 - 15 MeV. In this

Table 6.2: The Reaction CS values obtained in the present work for the reaction ^{150}Nd(p,xnyp).

Proton Energy (MeV)	Reaction CS (σ)[2] mb							
	^{150}Pm (p,n)		^{149}Pm (p,2n)		^{149}Nd (p,p′n) + (p,d)		Total (p,xnyp)	
	Present work	Lit. [LEB12, LEB14]	Present work	Lit. [LEB12, LEB14]	Present work	Lit. [LEB12, LEB14]	Present work	Lit. [LEB12, LEB14]
6.74	-	60.66(6.74)	-	4.63(0.59)	-	-	-	65.29(10.99)
7.12	25.55(1.88)	-	-	-	-	-	25.55(1.88)	64.18(10.8)
7.92	59.95(4.31)	-	27.36(6.66)	-	-	-	87.31(22.17)	-
7.93	-	77.86(8.69)	-	98.26(6.39)	-	-	-	176.13(22.75)
8.06	54.22(4.04)	-	47.23(6.58)	-	-	-	101.45(16.03)	-
8.49	61.81(4.56)	-	92.57(8.99)	-	-	-	154.38(18.82)	-
8.58	63.68(4.94)	-	57.12(4.79)	-	-	-	120.80(13.8)	-
9.01	-	62.43(6.92)	-	262.50(30.15)	-	-	-	324.94(51.86)
9.10	50.15(3.63)	-	176.16(13.61)	-	-	-	226.31(23.97)	-
9.42	53.49(3.97)	-	251.74(19.47)	-	-	-	305.22(32.70)	-
9.43	48.43(3.75)	-	174.56(13.65)	-	-	-	222.98(24.54)	-
9.93	45.36(3.36)	-	358.17(41.79)	-	-	-	392.85(54.14)	-
9.96	-	62.79(6.92)	-	336.99(37.25)	-	0.087(0.025)	-	399.87(130.18)
10.13	46.13(3.56)	-	306.98(22.29)	-	-	-	353.11(37.43)	-
10.43	34.80(2.68)	-	358.05(40.86)	-	-	-	392.85(54.14)	-
10.64	39.58(3.10)	-	358.47(25.57)	-	-	-	398.05(42.19)	-
10.93	27.34(2.09)	-	358.47(25.57)	-	-	-	398.05(42.19)	-
10.94	28.65(2.07)	-	393.89(32.42)	-	-	-	422.54(46.23)	-
11.53	-	43.10(4.61)	-	604.82(65.63)	-	1.04(0.13)	-	648.96(130.05)
11.94	27.76(2.19)	-	495.02(35.47)	-	0.06(0.01)	-	522.85(91.88)	-
12.28	21.98(1.67)	-	357.57(61.25)	-	0.27(0.02)	-	379.83(76.45)	-
12.44	19.62(1.50)	-	377.11(27.77)	-	0.62(0.15)	-	397.35(102.97)	-
12.92	-	34.05(3.72)	-	704.15(78.04)	-	4.43(0.53)	-	742.64(145.99)
13.21	17.95(0.49)	-	389.38(38.42)	-	0.20(0.003)	-	407.54(42.47)	-
14.10	20.46(1.60)	-	517.91(86.87)	-	1.05(0.15)	-	539.42(125.25)	-
14.25	-	31.75(3.37)	-	865.56(95.78)	-	14.08(1.67)	-	911.39(176.55)
14.94	20.01(1.58)	-	685.26(48.72)	-	1.67(0.12)	-	706.95(91.32)	-
15.50	-	29.79(3.19)	-	847.82(94.00)	-	29.44(3.55)	-	907.06(177.49)

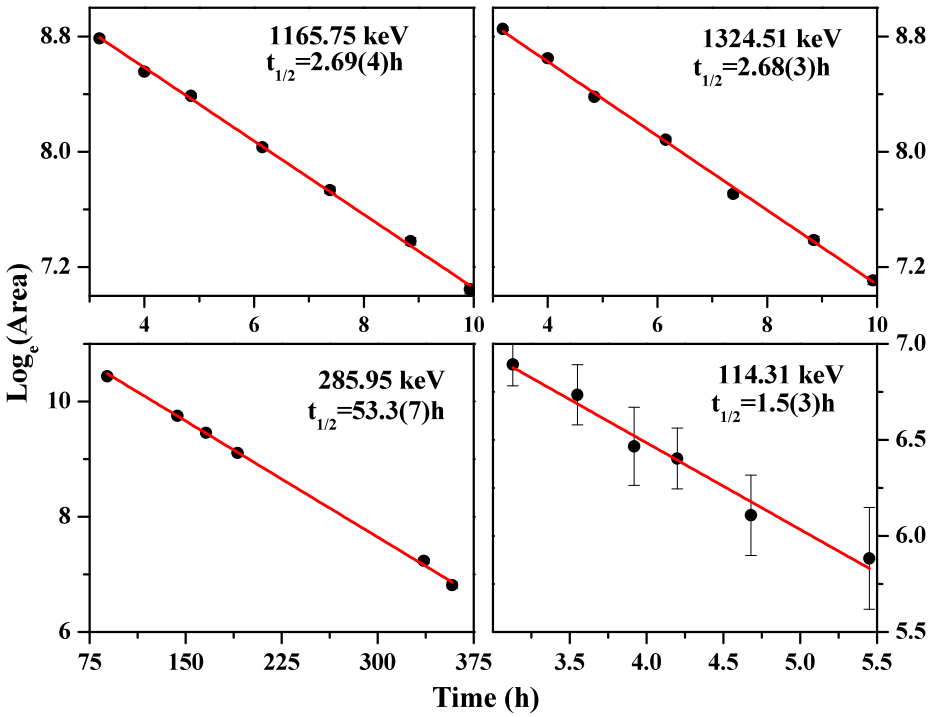

Figure 6.3: The decay plots for the transitions characterising the decay of different evaporation residues formed at a particular beam energy as described in the text.

at the proton energy below the Coulomb barrier by 1.5 MeV. For the ^{150}Nd(p,2n)^{149}Pm reaction, CS values showed a gradual increase in the present energy range of the proton beam. A similar increase was also observed in case of ^{150}Nd(p,p′n)^{149}Nd reaction with a threshold energy of 12 MeV. However, the individual values of CS for (p,p′n) channel are much less than that for (p,xn) channels.

The reaction CS values obtained from the work of Lebeda *et al.,* [LEB12, LEB14] have been scaled up by taking into account the isotopic enrichment of ^{150}Nd [TUL11]. These values have been shown in Fig. 6.5 and Fig. 6.6 in order to compare with the present measurement. These calculated values are higher compared to the data obtained from the present measurement, specially in the higher energy range for the (p, 2n) and (p, p′n) channels and at lower energy for the (p, n) channel. The CS values obtained in the present work have been tabulated in table 6.2 and have been compared with the data obtained by O. Lebeda *et al.* [LEB12, LEB14].

The experimental excitation functions were corroborated using the statistical model codes CASCADE [PUH77], ALICE [ALICE] and EMPIRE3.1 [EMPIRE]. These statistical model codes are

Table 6.1: The details of the measured reactions and the characteristic γ-rays used for the measurements of CS.

Reaction	Q value[1] (MeV)	γ Energy (keV)	Multipolarity	Abundances(γ+CE) %	Conv. Coeff	Abundance(γ) %
^{150}Nd(p,n)^{150}Pm	-0.865	1165.75	E1	15.8	0.000792	14.64
		1324.51	-	17.5	-	17.5
^{150}Nd(p,2n)^{149}Pm	-6.473	285.95	M1(+E2)	3.4	0.079	3.15
^{150}Nd(p,p′n)^{149}Nd	-7.38					
		114.31	M1+E2	40.0	1.24	17.85
		211.31	M1+E2	30.8	0.179	26.12
^{150}Nd(p,d)^{149}Nd	-5.156					
^{65}Cu(p,n)^{65}Zn	-2.134	1115.5	M1+E2	50.04	0.000194	50.03

polynomial function as given below.

$$\log_e \epsilon = a_0 + \sum_{n=1-4} a_n (\log_e E_\gamma)^n \tag{6.2}$$

The efficiency values for the characteristic decay γ-rays were calculated from the interpolation of this fitted curve, while considering E_γ in keV.. The CS values for the individual evaporation residues in the present range of proton energy were calculated using the equation 6.1. The errors associated with $N_0(\leq 2\%)$, $\epsilon(\leq 5\%)$, $N(\leq 1.5\%)$ and $\phi(\leq 5\%)$ contributed towards the error in the CS value. The excitation function for the different evaporation residues are plotted in Fig. 6.5 along with the total fusion CS calculated by adding the above individual evaporation channels. In order to exhibit the pattern of the excitation function below and above the Coulomb barrier (V_B), the $\log_e \sigma$ values were plotted against $(1\text{-}\frac{V_B}{E_p})$ in Fig. 6.6 considering V_B=8.46 MeV. The experimental CS values for ^{150}Nd(p,n)^{150}Pm reaction, obtained in the present work, exhibit a maximum value of 63.7(4.9)mb at around coulomb barrier ($E_p \sim 8.6$ MeV). The CS value for (p,n) channel drops down to $\sim$ 25mb

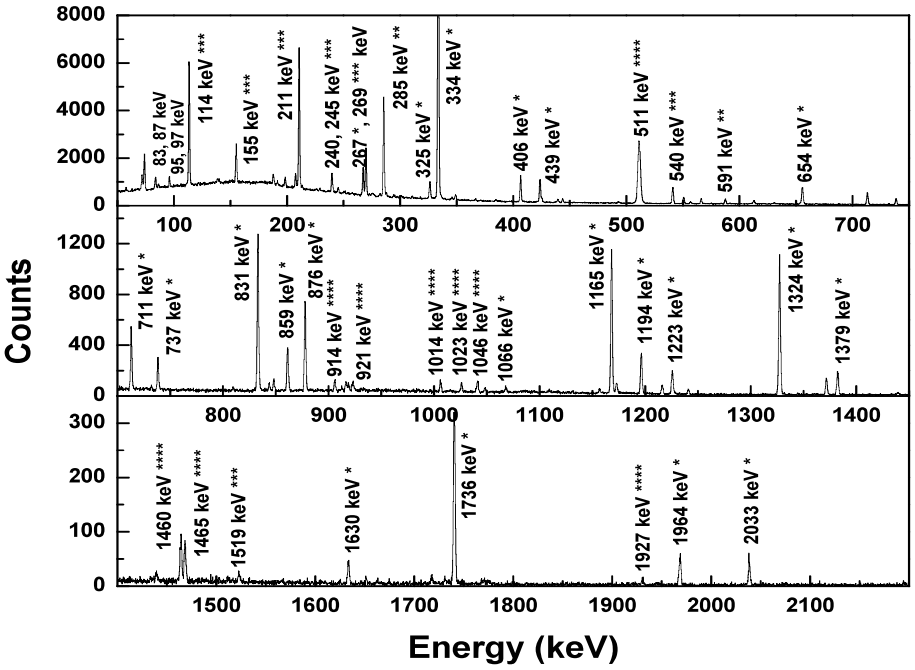

Figure 6.2: The total gamma spectrum taken with the 50% HPGe detector for the irradiated ^{150}Nd target with 15 MeV proton beam. The photopeaks marked with *, **, ***, **** belong to the decay of ^{150}Pm, ^{149}Pm, ^{149}Nd and the Al related or background γ-rays respectively.

been calculated by using the BrIccv2.3S code avaiable in [BRICC], using the multipolarities taken from the ENSDF databases [BAS13, SIN04].

The $\log_e area$ for each of these photopeaks was plotted as a function of time elapsed from the EOB and fitted with a linear function. The said plots obtained for a particular proton energy value is represented in Fig. 6.3. The fitted plot, when extrapolated to t=0 (EOB), yields N_0 for a particular evaporation residue at a particular proton energy. The error in N_0 was considered to be originated from statistical uncertainty($\leq$2%). The absolute efficiency of the detector was calculated from 53 keV to 1408 keV from the area obtained under the known photopeaks and the known values of the absolute intensities of the γ lines of ^{152}Eu and ^{133}Ba decay. The obtained efficiency values were plotted as a function of γ energy in a Log-Log scale as shown in Fig. 6.4. The error in the efficiency was found to be maximum of 5% considering the error in the area of weaker photopeaks as well as activity (dps) of the standard sources. The efficiencies were fitted with a fourth order

number of target atoms (N_0) and proton beam flux (ϕ) by using the following equation:

$$\sigma = \frac{A_0}{N.\phi.[1 - exp(\frac{-0.693 t_{irr}}{\tau_{\frac{1}{2}}})]} \tag{6.1}$$

The term in the parenthesis is known as the saturation factor used for correcting the activity lost during time of irradiation (t_{irr}). A_0 is calculated from the yield(N_0) of the characteristic γ ray at EOB, emitted following the decay of any particular evaporation residue, by using the relation $A_0 = N_0/\epsilon\eta$, where, ϵ is the efficiency of the detector and η is the abundance for that particular γ ray. The beam flux(ϕ) was calculated using the same equation 6.1 and taking the CS values for the reaction ^{nat}Cu(p,xn)^{65}Zn from literature [CUREF]. The errors in N, N_0 and ϵ($\leq$1.5%, $\leq$2% and $\leq$5% respectively as discussed below) were taken in calculating the error in ϕ. The error in N arises from the uncertainty in the thickness measurement of the target foil and has been considered to be $\leq$1.5%.

The γ-rays, used in the CS calculation, were chosen in such a way that they have significant abundance and appear prominently in the spectrum. A representative γ spectrum obtained from the irradiated target along with its catcher foil is shown in Fig. 6.2. Most of the γ-rays were identified to be originated from the decay of ^{150}Pm, ^{149}Pm and ^{149}Nd nuclei. The ^{149}Pm and ^{149}Nd nuclei were found to be produced only above E_p=7 MeV and E_p=11.5 MeV, respectively. The γ lines coming from the target impurities have been observed to be very negligible. Some γ transitions were found to be present due to the activated products of Al-foils used in the experiment. The 1165.75, 285.95 and 114.31 keV transitions were used for calculating the activity of ^{150}Pm, ^{149}Pm and ^{149}Nd nuclei, respectively. The activities of ^{150}Pm and ^{149}Nd were also cross checked by using the 1324.52 keV and 211.31 keV transitions, respectively. Similarly, the Cu-monitor along with its catcher was counted to obtain the yield of the 1115.55 keV transition. This originates from the decay of ^{65}Zn and was used for calculating the beam flux utilizing the reaction ^{nat}Cu(p,xn)^{65}Zn as mentioned above. The relevant details of the above four γ lines are furnished in table 6.1. The abundance values of these γ lines were taken from the ENSDF data base [BAS13, SIN04] and corrected for their respective conversion coefficients while using for the activity calculation. The said conversion coefficients have

The energy of the incident beam was determined from the knowledge of magnetic field, extraction radius and charge state of the accelerated ion. The maximum uncertainty in proton beam energy is known to be ∼100 keV in the present energy range. The degradation of the beam energy as a function of the depth of the stack was calculated with the help of the 'Physical Calculator' available inside the code 'LISE++' [TAR03] giving the beam energy and the target thickness as the input parameters. The beam intensity for each stack was calculated by using the known excitation function for ^{nat} Cu(p,xn) ^{63,65}Zn reactions. The absolute yields of the delayed γ-rays corresponding to the decay of the individual evaporation residues were used to determine the excitation function of the p-induced reaction on ^{150}Nd. Following this method, both the target and the monitor foils were counted along with their respective catcher foils on a 50% HPGe detector after allowing a cooling time of 1-2 h from the end of bombardment (EOB). The irradiated foils were placed at an appropriate distance from the detector to maintain a dead time of $\leq$ 10%. This was further supported by the absence of any sum peak in the γ spectrum. The activities obtained from the stack irradiations were initially counted over a period of ∼10 h, considering three half lives ($\tau_{\frac{1}{2}}$) of the ground state of ^{150}Pm ($\tau_{\frac{1}{2}}$ = 2.68 h). Each counting was performed for 10 min at an interval of ∼ 30 min. The counting for ^{150}Pm could also provide the data for ^{149}Nd ($\tau_{\frac{1}{2}}$ = 1.73 h) because of their similar $\tau_{\frac{1}{2}}$ values. For ^{149}Pm ($\tau_{\frac{1}{2}}$ = 53.08 h), a similar sequence of counting was done over a period of one week where the individual counting had a duration of 30 min to 2 h at an interval of one day. The counting for ^{150}Pm and ^{149}Pm were done keeping the irradiated foils at a distance of 15 cm and 7 cm from the detector respectively. The absolute efficiency of the detector at these two positions was estimated by using the standard ^{152}Eu and ^{133}Ba sources with known activity. The energy calibration of the detector was also performed using the same set of sources. The data were acquired and analysed using a Canberra digital data processing system GENIE 2000.

6.3 Data Analysis and Results

The CS values (σ) of the different evaporation channels produced from the p+^{150}Nd reaction were estimated from the knowledge of the activity (A_0) of the respective evaporation residue at EOB,

neutron beam of flux $\sim$ 1.8 x 10^{14} neutrons /cm^2/sec was available from the research reactor facility 'DHRUVA' at Bhabha Atomic Research Centre, Mumbai. The Nd:O ratio was found to be 1.6:3 in the electro-deposited target compared to 2:3 in the powdered sample. This atom ratio of 1.6:3 was used in the subsequent calculation. The isotopic impurities in the target material consisted of 0.50% ^{142}Nd, 0.31% ^{143}Nd, 0.68% ^{144}Nd, 0.23% ^{145}Nd, 0.47% ^{146}Nd and 0.26% ^{148}Nd, as per the data sheet provided by the supplier. The thickness of the targets used in the experiment was within the range of 650 μg/cm^2 to 900 μg/cm^2 as determined by accurate weight difference method using analytical balance. The CS were measured by using the stacked-foil activation technique where several target stacks were irradiated with the proton beam. Each stack contained Copper (25μm), Al (25μm) and Tantalum (12.5μm) as the beam flux monitor, catcher and degrader respectively. The number of targets in each stack was limited to a maximum value of four. A typical stack with its components has been shown in Fig. 6.1. The target stacks were prepared in such a way that every stack provides one proton energy of irradiation common to that with the previous stack. Single targets along with a monitor foil and the catchers were also irradiated at few proton energies throughout the range of 7 to 15 MeV.

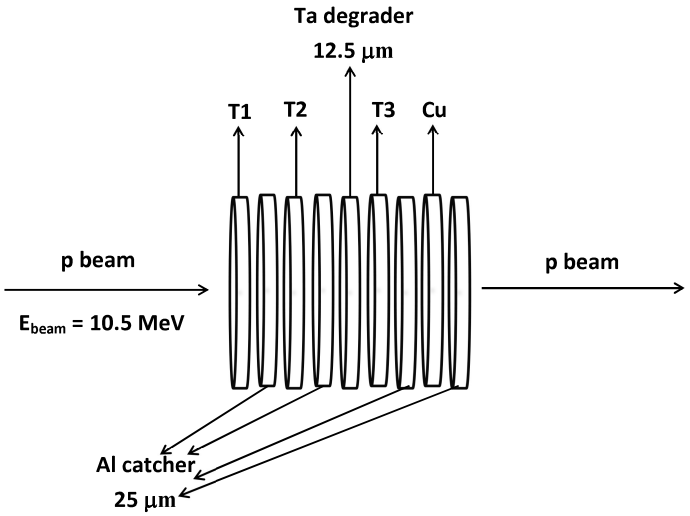

Figure 6.1: The configuration of a typical stack is represented. The number, shape and size of the targets, foils and degraders were different in different stacks as detailed in the text. T1, T2 and T3 are the targets and Cu represents the monitor foil.

The beam spot on the target was confined to 6.0mm by using Al collimator in front of the target.

residual nucleus produced from (p,n) channel, there remains a considerable background from the (p,2n) channel. Hence, it is important to estimate the relative cross-sections of the single neutron and two neutron evaporation channels in order to decide the beam energy for studying the residual nuclei produced from the (p,n) channel. Several such experiments in A $\sim$ 150 region are being explored at VECC, Kolkata [BHA11, SAH14].

In the present work, the excitation functions of the (p, xnyp) reactions have been measured using stacked-foil activation technique [ISM90] with the 97.65% enriched ^{150}Nd target. A similar work was done by O. Lebeda *et al.,* [LEB12] using ^{nat}Nd target. A preliminary result of our measurement with enriched target was reported in Ref. [BAN12]. Following our preliminary report, another set of measurement has been reported by O. Lebeda *et al.,* [LEB14] which also used ^{nat}Nd target. The use of enriched Nd target in our work has facilitated the measurement of absolute CS for the p-induced reaction on ^{150}Nd for the first time. The measurement also provides a completely new set of data on the excitation function for the present reaction with a large number of data points in the proton energy range of 7-15 MeV. Considering the Coulomb barrier for the present system to be $\sim$ 8.5 MeV, the fusion probability below the threshold by 1.5 MeV has been determined in the present work. The measurement of CS for ^{150}Nd(p,n)^{150}Pm, ^{150}Nd(p,2n)^{149}Pm and ^{150}Nd(p,p′n)^{149}Nd / ^{150}Nd(p,d)^{149}Nd reactions have been measured giving rise to a total fusion CS for the p+^{150}Nd reaction. The experimental results have been corroboarated with statistical model calculation using different codes, *viz.,* CASCADE [PUH77], ALICE [ALICE] and EMPIRE3.1 [EMPIRE].

6.2 Experimental Details

The ^{150}Nd (p, xnyp) reaction was carried out using 7 to 15 MeV proton beams provided by K = 130 AVF cyclotron at Variable Energy Cyclotron Centre, Kolkata. The ^{150}Nd target was prepared by electro-deposition technique, starting from commercially available 97.65% enriched powdered oxide sample(Nd_2O_3), on a 0.3 mil thick Aluminium (Al) foil. The Nd:O atom ratio in the deposited target was estimated by neutron activation of both the powdered material and the prepared target. The

Chapter 6

Excitation Function for ^{150}Nd(p,xn) reaction

6.1 Introduction

The light ion induced reactions with neutron-rich targets can be considered as one of the possible avenues to study the nuclei in the neutron rich side of N-Z chart. The population of the neutron-rich nuclei in A $\sim$ 150 region with sizable yield is difficult by either fission reaction, even with trans-uranium elements, or by fusion-evaporation reaction with stable heavy-ion beams [GAG76, NET81]. The information on the light-ion induced reaction cross-section (CS) is required to perform the spectroscopy of the low-lying states of these nuclei which has a lot of current physics interests [JAI98, CEJ10]. The excitation function measurement for this reaction was done prior to the spectroscopic measurements on the low-lying states of ^{150}Sm through decay spectroscopy of ^{150}Pm and as a preparation for the in-beam spectroscopy of ^{150}Pm to be performed in due course.

The proton induced fusion evaporation reactions in this mass region are dominated by few neutron evaporation channels with a small contribution to the single neutron and particle evaporation channels. It is very important to estimate the low CS of the residues produced from the particle evaporation channels, which can be used in meaningful experiments with a suitable tagging device coupled to a high efficiency γ array [ALL10, ELV11]. Also, while performing the spectroscopy of the

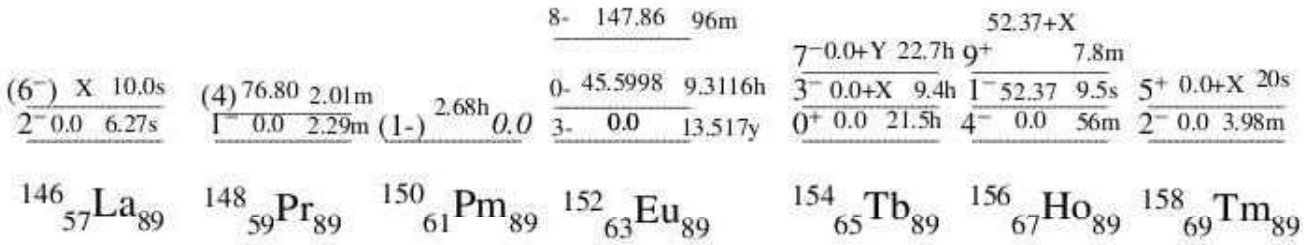

Figure 7.3: The systematics of the isomeric states in neighboring isotones of N=89 ^{150} Pm. The data is taken from ENSDF database [ENSDF].

with a parabolic function as shown in Fig. 7.2 and the minima of the obtained function has been considered as the value of the end-point energy. The end-point energies, thus, obtained have also been tabulated in Table 7.1. The error corresponds to the energy difference required for the change in χ^2 by 1.0.

7.4 Summary

Many of the neighboring nuclei around N=90 ^{150}Pm show the presence of long lived β decaying isomers as shown in the figure below 7.3. The present effort was also aimed at the search for the presence of any such isomer in ^{150}Pm. In the present work, the measurement of β decay endpoint energies have been performed for the first time in the decay of ^{150g}Pm $\rightarrow$ ^{150}Sm corresponding to several excited levels of the daughter nucleus. However, the β decay end point energy measurement could not identify any such isomeric level in ^{150}Pm.

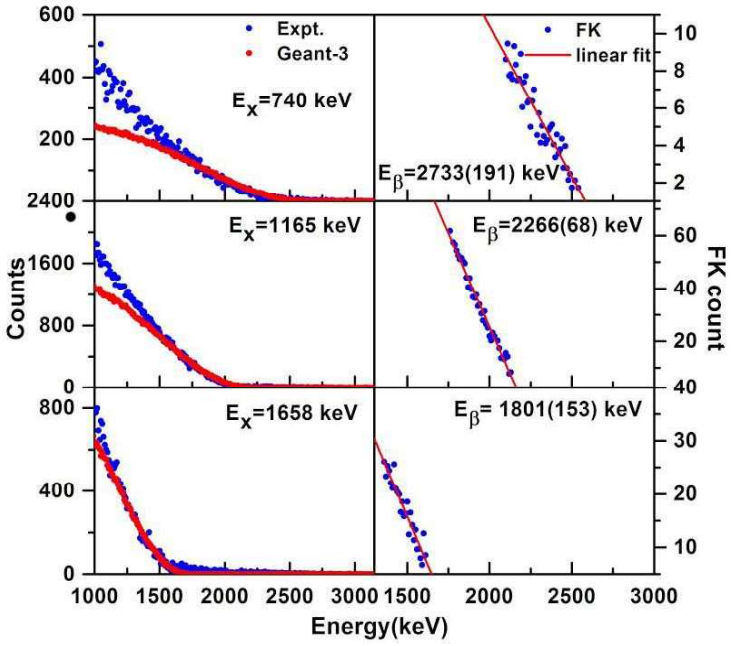

Figure 7.1: The representative β spectra obtained for some of the decay branches of ^{150g}Pm $\rightarrow$ ^{150}Sm. The experimental data points have been shown with blue circles and the Red line shows the results obtained from Geant3 simulation. The FK plots are shown with the obtained end point energies.

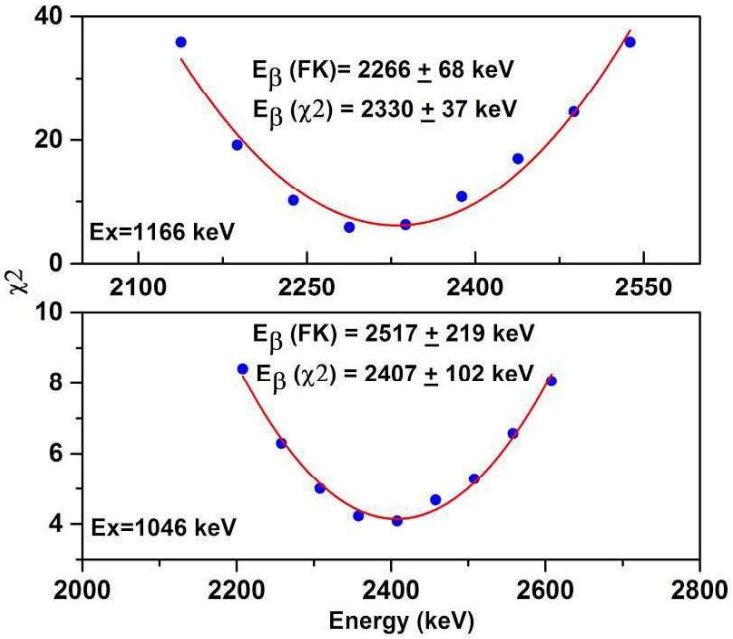

Figure 7.2: The representative χ^2 plot for two of the β decay branches of ^{150g}Pm. The β decay end point energies obtained from χ^2 and FK analyses are indicated.

Table 7.1: The β decay end point energies obtained in the present work with relevant details, as described in text.

Decaying Nucleus (Q_β)	Final Level Energy (E_x) (keV)	J^π	Branching (%)	Gating transition (keV)	β Energy (Q_β - E_x) (keV)	Lit. (keV)	F-K Anal. (uncorr) (keV)	F-K Anal. (corr) (keV)	GEANT3 and χ^2 Anal. (keV)
^{150g}Pm	334.0	2^+	$\leq$10	334	3120.0	-	2957±73	3046±73	3134±34
3454(20) keV	740.4	0^+	1.5	407	2713.6	-	2645±191	2733±191	2673±65
	1046.1	2^+	1.3	712	2407.9	-	2429±219	2517±219	2407±102
	1165.8	1^-	25.9	1165+832	2288.2	-	2179±68	2266±68	2330±37
	1658.4	$2^{(-)}$	19.4	1324	1795.6	-	1715±153	1801±153	1826±28
	1713.5	1	3.5	1379	1740.7	-	1781±105	1868±105	1761±47
	1963.7	1^-	5.5	1223+1964+1630+917	1490.3	-	1529±193	1615±193	1462±40
	2070.3	$2^{(-)}$	17.5	1736+876	1383.7	-	1478±180	1555±180	1424±23
	2259.9	(1^-)	3.26	1214+1004+1066+1926+1519	1194.1	-	1509±115	1594±115	-
	2367.4	(3^+)	1.04	2033	1086.6	-	1331±221	1417±221	1068±67

7.3 Data Analysis and Results

In order to generate the $\gamma-(\beta+\gamma)$ and $\gamma-\gamma$ coincidence information, two RADWARE compatible matrices were made from the coincidence data obtained with two LEPS and four Clover HPGe detectors, in two different configurations (see Section-3.10.6.7 for details of data taking and analysis).

The representative β-spectra obtained in the present work for the decay branches of ^{150}Pm to ^{150}Sm have been shown in Fig. 7.1. The corresponding β-spectra have also been obtained by using Monte Carlo simulation with the Geant3 simulation package [BRU86] with one million events and the exact geometrical configuration. The results from the simulation has been normalized to match the experimental data points based on visual estimation, with an emphasis in the energy range of $0.8E_\beta$ to E_β and is plotted with the corresponding experimental results as shown in Fig. 7.1. The deviation of the experimental results from the simulation at the low energy side corroborates to the effects of background appearing from the β-Compton and Compton-Compton coincidences that could not be subtracted during generation of β spectrum as has been described in Ref. [BHA14]. The Fermi-Kurie (FK) plots were generated from the experimentally obtained β spectrum by using the built in routine *'FK-Energy'* included in the spectrometer code LISE [TAR03, KAN95]. The FK plots corresponding to the different β decay branches have been shown in Fig. 7.1 along with the β spectrum. The β end point energies have been obtained by fitting these plots and the results have been tabulated in Table 7.1 corresponding to different decay branches. The required corrections were made for the attenuation in the Be window of the LEPS detectors and both the corrected and uncorrected energies are mentioned in Table 7.1. The γ energy has also been indicated in the table for each β branch which corresponds to the gating transition that was used for generating the β spectrum.

The endpoint energies have also been derived by performing a chi-square analysis (see 3.10.6.8 for details) following the methodology of Ref. [BHA14] and the representative chi-square plots have been shown in Fig. 7.2. The χ^2 values have been obtained by comparing the experimental data points with the simulation at different end point energies. The obtained values have been fitted

The information on β-decay maximum energy can also be very important for the identification of the nuclear isomeric states when determined in coincidence with the γ-rays de-exciting the excited levels of the daughter nucleus [DIK74]. Such isomers have been identified in many nuclei in A$\sim$150 mass region [JAI98]. Hence, a program has been taken at VECC to identify and characterize such long lived β decaying isomeric states which is important both from nuclear structure and nuclear astrophysics point of view [SOO11, LES89]. As an initiation to this program, the β decay end point energies in the decay of ^{150}Pm$\rightarrow$^{150}Sm have been measured by using planar HPGe detectors which has been found to be quite efficient for this purpose.

Moreover, these detectors provide a very good energy resolution as well as can be calibrated up to very high energy using appropriate gamma ray sources. The coincidence measurement with an appropriate γ detector becomes unique for determining the end-point energies related to even very weakly populated levels of the daughter nuclei.

In this chapter, the beta-decay end point energy corresponding to the ^{150}Pm$\rightarrow$^{150}Sm decay measured for the first time has been discussed.

7.2 Experimental details

The ^{150}Pm was produced by the reaction ^{150}Nd(p,n)^{150}Pm using 8.0 MeV proton beam from K=130 cyclotron at VECC which then, following β-decay produces the excited states of ^{150}Sm. The coincidence setup consisted of four standalone Clover Ge detectors and two LEPS detectors. The Clover Ge detectors were used for the detection of delayed γ transitions and the planer Ge detectors were used to facilitate the detection of the beta decay from ^{150}Pm. Sixteen channel Mesytec amplifier (MSCF-16) was used for the pulse processing of both the clover and planar Ge detectors. For the measurement of $\gamma-\gamma$ coincidence, a MASTER logic of $M_\gamma \geq 2$ was established among the four Clover detectors. The data conversion as well as acquisition was made by using VME standard Mesytec ADC (MADC32) and the Data Acquisition System LAMPS [LAMPS]

Chapter 7

Measurement of β-decay end-point energies for ^{150}Pm$\rightarrow^{150}$Sm decay

7.1 Introduction

The accurate measurement of the end point energies of β-decay branches has long been a standard tool in nuclear spectroscopy. Measurement of β^- end-point energies in decay to known levels in neutron-rich nuclides has provided a convenient method of deriving Q_β values, that is energy (mass) differences between neighboring isobars. Since, nuclide masses close to the line of the beta stability are generally known with good accuracy, such β^- end-point energy measurements allow nuclide masses in isobaric chains to be determined out to the limits of practical neutron-rich nuclide production, e.g., in fission. Extension of the region of known nuclide masses is an essential input to ongoing theoretical efforts to further refine and develop models to predict nuclear masses even further from stability. Mass values of such very neutron-rich nuclides are one necessary input to astrophysical calculations involving the rapid neutron-capture process (r-process) of elemental synthesis in stellar environments [GRE93]. Such measurements represent direct experimental tests of binding energy calculations performed in the framework of microscopic models, collective models and also of the variety of semi-empirical mass formula.

lying structure for ^{150}Pm for understanding octupole correlation in A$\sim$150 region using light ion beams and neutron rich ^{150}Nd target with VENUS or INGA array as it is difficult to produce this nucleus with any other HI beam.

As discussed in the present thesis, it is very much difficult to experimentally identify the weak signature of the existence of tetrahedral symmetry in nuclei. However, it is of extreme importance to enrich the basic understanding of the nuclear many body system. Recently, the possible realization of tetrahedral and octahedral symmetries in ^{152}Sm has been reported in Ref. [DUD18] for the first time. Hence, it will be interesting to look for the characterization of the negative parity band structures in ^{152}Sm by finding the E2 and E1 transitions decaying out from the bands, specifically the three bands, disignated as T, N and O band in ENSDF. These bands are predicted, c.f. Ref. [DUD18], to have signature on the exotic λ=3 symmetry and, thus, have low intensity for the in-band E2 transitions. Hence, it will be worth to look for the decaying transitions by performing an experiment for which alpha beam and INGA/VENUS array can prove to be useful.

band could be its analogue, in that the Y_{30}-vibration is replaced by Y_{32}-vibration. Such bands are said to have the 'pyramid-shape' oscillations. The present work suggests the requirement of future experiment for finding the β and γ bands and to search for stable tetrahedral deformation in this nucleus, which could not be established in the present work.

The measurement of excitation function was done for the ^{150}Nd(p,xnyp) reactions (as discussed in Chapter 6) upto ∼50% above barrier and down to ∼18% below the barrier with proton beam energy of 7-15 MeV from the VECC cyclotron. The (p,n) cross section was found to follow the expected trend with a maximum value of 63.7(4.9) mb at E_p∼8.6 MeV. The (p,2n) cross section gradually increased with E_p and had a maximum contribution to the total reaction cross section after E_p∼9.0 MeV. The (p,2n) residues were not found to be produced below 7.9 MeV. The (p,p'n) reaction channel also showed a reasonable yield with a threshold of E_p∼12.0 MeV. The experimental data were corroborated with statistical model calculations using different codes, viz., CASCADE, ALICE/91 and EMPIRE3.1. All the calculations could reproduce the excitation function fairly well in the present energy range.

Also, the measurement of β-decay end-point energy for the ^{150}Pm→^{150}Sm decay is also accomplished in the present thesis as discussed in Chapter 7.

8.2 Future Outlook

As discussed in the preface of the present thesis, the A∼150 nuclei around N=90 display octupole correlation in their low lying structure due to the presence of λ=3 valence orbitals both for proton and neutron [BUT96, JAI98]. Parity doublet bands connected with strong E1 transitions have been observed in some of the Pm and Eu nuclei [URB90, BAS94], some of which are also studied with light ion beams. No experimental data exists for the study of this experimental phenomenon in N=89 Pm. This is mainly due to the reason that the population of this nucleus is difficult with the use of stable HI beam and available target combinations. In fact, experimental data on level structure on this nuclei are very scanty and the studies are limited to neutron activation and light ion experiments with limited detectors [ENSDF]. Hence, it will be important to explore the low

assignment is done for twenty eight levels of ^{150}Sm with the help of *logft* values for which the assignment were not known or were uncertain. Some of these assignments were also corroborated with the angular correlation measurement which could also confirm the pure E1 nature of five transitions in ^{150}Sm. The intra- and inter-band E2 transitions from 2_2^+ and 2_3^+ levels, observed in the present work, suggest that these levels in ^{150}Sm are the candidates of β and γ vibration bands respectively.

Also, the spectroscopy of ^{160}Yb has been revisited (as discussed in Chapter 5) in order to study the low and moderate spin structure of this N=90 nucleus around A$\sim$160 by using the in-beam gamma ray spectroscopic technique with the Indian National Gamma Array (INGA). The level structure has been deduced from the measurement of double, and triple γ-coincidences, relative intensities, DCO, R(θ) and IPDCO by using conventional techniques. The DCO, R(θ) and IPDCO ratios have been measured for the first time in the present work for some of the transitions. Moreover, relative intensities of certain gamma transitions along with their DCO, R(θ) and IPDCO values have been obtained for the first time in this work. Several fragments of the level scheme obtained in the present work differ considerably from the ones obtained in the earlier measurements. Several inter-band transitions based on which band-mixing calculations were earlier done in the latest experiment by Bark et al. could not be confirmed from the present experiment which makes it necessary to revisit those calculations. Gamma rays which could not be confirmed in the present experiment but were claimed to have been observed ealier is 82 in number. The intensity limits for the unobserved transitions could be estimated following the comparision of the present data with the known branching ratios for the levels where both the transitions are observed. 97 transitions were found to be in confirmation with the earlier work in the present experiment. Two gamma rays (viz., 483 and 606 keV) and a single energy level (viz. 4474.9 keV) have been newly placed in the level scheme of ^{160}Yb. The even and odd-spin negative parity bands in ^{160}Yb have been studied by comparing the reduced transition probability ratios with the similar bands in neighboring even-even rare earth nuclei. The ratios estimated for the even-spin negative-parity band are found to be significantly higher compared to the odd-spin one. This tendency is similar, although not as dramatic as in the results in some of the neighboring nuclei. The behavior of the odd-spin negative-parity band is compatible with that of a pear-shape octupole vibration band whereas the even-spin

Chapter 8

Summary and outlook

8.1 Summary

In the present work, both off-beam and in-beam γ-spectroscopy experiments were carried out in order to study the low lying states of ^{150}Sm populated from β-decay of ^{150}Pm and to populate the low and moderately high spin states of ^{160}Yb. In addition to the $\gamma - \gamma$ spectroscopy experiments, the excitation function of the ^{150}Nd(p,xnyp) reactions have also been measured in order to estimate the relative cross-sections of the single neutron and two neutron evaporation channels in order to decide the beam energy for studying the residual nuclei produced from ^{150}Nd(p,n) channel having very low cross section compared to the other neutron evaporation residues. This is because of the fact that there remains a considerable background from the (p,2n) channel while performing the spectroscopy of the residual nucleus produced from (p,n) channel. The β-decay end-point energy has also been measured for the ^{150}Pm$\rightarrow$^{150}Sm decay in the present thesis.

In the present thesis, the low lying states of ^{150}Sm have been studied (as discussed in Chapter 4) through decay spectroscopy of odd-odd ^{150}Pm populated with ^{150}Nd(p,n)^{150}Pm reaction at E_{beam}=8.0 MeV using 97% enriched ^{150}Nd target. Nineteen new transitions are placed, four tentative γ rays are confirmed and eight transitions are found to have altered placements; resulting in assignment of thirteen new levels to the decay scheme of ^{150}Pm. The β branching and *logft* values have been estimated from the absolute intensities of the γ transitions for all the levels. The J^{π}

[YAM78] Y. Yamazaki, E. B. Shera, M. V. Hoehn and R. M. Steffen, Phys. Rev. C **18** (1978) 1474.

[YXU94] Y. Xu *et al.*, Phys. Rev. Lett. **73** (1994) 2413.

[ZBE09] K. Zberecki *et al.*, Phys. Rev. C **79** (2009) 014319.

[ZIE] J. F. Ziegler *et al.*, "The Stopping and Range of Ions in Solids", *www.SRIM.org.*

[STE72] F. S. Stephens and R. S. Simon, Nucl. Phys. A **183** (1972) 257.

[STE75] F. S. Stephens, Rev. Mod. Phys. **47** (1975) 43.

[SZY83] Z. Szymańsky: **"Fast Nuclear Rotation"** (Clarendon Press. Oxford, 1983).

[TAG13] S. Tagami *et al.*, Phys. Rev. C **87** (2013) 054306.

[TAG15] S. Tagami *et al.*, J. Phys. G **42** (2015) 015106.

[TAR03] O. B. Tarasov, D. Bazin, NIM B **204** (2003) 174.

[TAR08] O .B . Tarasov, D. Bazin NIM B **266** (2008) 4657.

[TAY77] Singh and Taylor, Z. Phys. A **283** (1977) 21.

[TEN88] O. Tengblad, R. V. Dincklage, Nucl. Instr. & Meth. Phys. Res . A **273** (1988) 257.

[TUL11] Jagdish K. Tuli, "Nuclear Wallet Cards", 8^{th} Edition, October (2011).

[UET97] N. Ueta *et al.*, Nucl. Inst. & Meth. A **397** (1997) 163.

[URB87] W. Urban *et al.*, Phys. Lett. B **185** (1987) 331.

[URB90] W.Urban *et al.*, Phys. Lett. B **247** (1990) 238.

[VOI83] M. J. A. de Voigt *et al.*, Rev. Mod. Phys. **55** (1983) 949.

[VOM83] Victor R. Vom, Nucl. Instr. & Meth. Phys. Res. **207** (1983) 395.

[WAP85] A. H. Wapstra and G. Audi, Nucl. Phys. A **432** (1985) 1.

[WER92] T. Werner and J. Dudek, At. Data Nucl. Data Tables **50** (1992) 179.

[WON73] C. Y. Wong, Phys. Rev. Lett. **31** (1973) 766.

[XUN18] "Experimental Unevaluated Nuclear Data List Search and Retrieval (XUNDL)", *http://nndc.bnl.gov/ensdf/ensdf/xundl.jsp*, last updated 02.02.2018.

[PEA94] C.J.Pearson *et al.*, Phys. Rev. C **49** (1994) R1239.

[PII96] M. Piiparinen *et al.*, Nucl. Phys. A **605** (1996) 191.

[PUH77] F. Pühlhofer, Nucl. Phys. A **280** (1977) 267.

[RAD95] D. C. Radford, Nucl. Instr. & Meth. A **361** (1995) 297.

[RAD95A] D. C. Radford, Nucl. Instr. & Meth. A **361** (1995) 306.

[RAM01] S. Raman et al., Atomic and Nuclear Data Tables, Vol. **78** (2001) 1.

[RED69] E. R. Reddingius and H. Postma, Nucl. Phys. A **137** (1969) 389.

[REI05] C. W. Reich, Nucl. Data Sheets **105** (2005) 557.

[RIE80-A] L. L. Riedinger, Nucl. Phys. A **347** (1980) 141.

[RIE80-B] L. L. Riedinger *et al.*, Phys. Rev. Lett. **44** (1980) 568.

[SAH14] A. Saha *et al.*, DAE Symp. Nucl. Phys. **59** (2014) 124.

[SAH18] A. Saha *et al.*, Phys. Scr. **93** (2018) 034001.

[SCH04] N. Schunck and J. Dudek, Int. Jour. of Mod. Phys. E **13** (2004) 213.

[SCH05] N. Schunck *et al.*, Acta Phys. Polon. B **36** (2005) 1071.

[SCH78] O. Scholten *et al.*, Annals Of Phys. **115** (1978) 325.

[SIN04] B. Singh, Nucl. Data Sheets **102** (2004) 1.

[SIN98] B. Singh *et al.*, Nucl. Data Sheets **84** (1998) 487.

[SMI66] R. K. Smither, Phys. Rev. **150** (1966) 964.

[SOO11] P. C. Sood *et al.*, Phys. Rev. C **83** (2011) 027303.

[SOO12] P. C. Sood *et al.*, J.Phys. G **39** (2012) 095107.

[KUM74] Krishna Kumar Nucl. Phys. A **231** (1974) 189.

[LAMPS] *http://www.tifr.res.in/∼pell*

[LEB12] O. Lebeda *et al.*, Phys. Rev. C **85** (2012) 014602.

[LEB14] O. Lebeda *et al.*, Nucl. Phys. A **929** (2014) 129.

[LES89] K. T. Lesko *et al.*, Phys. Rev. C **39** (1989) 619.

[LI94] X. Li and J. Dudek, Phys. Rev. C **49** (1994) R1250.

[LID04] S. N. Liddick *et al.*, Phys. Rev. Lett. **92** (2004) 072502.

[LIN99] A. Lindroth *et al.*, Phys. Rev. Lett.**82** (1999) 4783.

[LOGFT] *http://www.nndc.bnl.gov/logft/*

[MAY49] M. G. Mayer, Phys. Rev. **75** (1949) 1969.

[MOR76] H. Morinaga and T. Yamazaki, "In-beam Gamma-ray Spectroscopy", North-Holand Publishing Company, New York, p.68 (1976).

[MOT55] B. R. Mottelson and S. G. Nilsson, Phys. Rev. **99** (1955) 615.

[NÁC04] E. Nácher *et al.*, Phys. Rev. Lett. **92** (2004) 232501.

[NDS18] *http://www.nndc.bnl.gov/ensdf/xundl/* last updated on 09-03-2018.

[NET81] D. R. Nethaway and A. E. Richardson, J. Inorg, Nucl. Chem. **43** (1981) 889.

[NIL55] S. G. Nilsson, Mat. Fys. Medd. Dan. Vid. Selsk. **29** (1955) 16.

[PAL12] R. Palit *et al.*, Nucl. Instr. and Meth. **680** (2012) 90.

[PAL15] R. Palit and S. Biswas, Pramana-J. Phys. **85** (2015) 395.

[PAS86] A. Passoja *et al.*, J.Phys. G **12** (1986) 1047.

[HIL53] D. L. Hill and J. A. Wheeler, Phys. Rev. **89** (1953) 1102.

[HOR96] Y. S. Horowitza *et al.*, Nucl. Instr. & Meth. Phys. Res. A **371** (1996) 522.

[HOS77] Masaharu Hoshi and Yasukazu Yoshizawa, J. Phys. Soc. Jpn **42** (1977) 1106.

[HUM16] P. Humby *et al.*, Phys. Rev. C **94** (2016) 064314.

[IAC01] F. Iachello, Phys. Rev. Lett. **87** (2001) 052502.

[IAC04] F. Iachello and N. V. Zamfir, Phys. Rev. Lett. **92** (2004) 212501.

[IAC98] F. Iachello *et al.*, Phys. Rev. Lett. **81** (1998) 1191.

[ING54] D. R. Inglis, Phys. Rev. **96** (1954) 1059.

[ING55] D. R. Inglis, Phys. Rev. **97** (1955) 701.

[ISM90] M. Ismail, Phys. Rev. C **41** (1990) 87.

[JAI98] A.K.Jain *et al.*, Rev. of Mod. Phys.**70** (1998) 843.

[JEN10] M. Jentschel *et al.*, Phys. Rev. Lett. **104** (2010) 222502.

[JOH73] A. Johansson *et al.*, Nucl. Instr. & Meth. Phys. Res. **108** (1973) 225.

[JOH96] N.R.Johnson et al., Phys. ReV. C **53** (1996) 671.

[JUN93] A. Jungclaus *et al.*, Phys. Rev. C **48** (1993) 1005.

[KAB93] M. K. Kabadiyski *et al.*, Nucl. Phys. A **563** (1993) 301.

[KAL75] C. A. Kalfas *et al.*, J. Phys. G **1** (1975) 613.

[KAN95] Juhani Kantele: "Handbook of Nuclear spectrometry", Aademic Press Limited (1995).

[KIR63] P. Kirkby and T. M. Kavanagh, Nucl. Phys. **49** (1963) 300.

[KRA89] A. Krämer-Flecken *et al.*, Nucl. Instr. & Meth. A **275** (1989) 333.

[DUD03] J. Dudek, A. Góźdź and N. Schunck, Acta Phys. Pol. B **34** (2003) 2491.

[DUD07] J. Dudek *et al.*, Int. J. Mod. Phys. E **16** (2007) 516.

[DUD09] J. Dudek *et al.*, Acta Phys. Pol. B **40** (2009) 713.

[DUD16] J. Dudek, private communication, 2016.

[DUD18] J. Dudek *et al.*, Phys. Rev. C **97** (2018) 021302(R).

[ELV11] M. Elvers *et al.,* Phys. Rev. C **84** (2011) 054323.

[EMPIRE] M. Herman *et al.*, EMPIRE-3.1 (Rivoli), International Atomic Energy Agency, Vienna (2012): *http://www-nds.iaea.org*

[ENSDF] Evaluated Nuclear Structure Data File (ENSDF) *http://www.nndc.bnl.gov/ensdf/*

[FEW85] M. P. Fewell *et al.*, Phys. ReV. C **31** (1985) 1057.

[FOG92] B.Fogelberg, *et al.*, Phys. Rev. Lett. **68** 3853 (1992).

[GAG76] Gaggler *et al.*, J. Inorg, Nucl. Chem. **38** (1976) 205.

[GAV80] A. Gavron, Phys. Rev. C **21** (1980) 230.

[GRE93] R. C. Greenwood and M. H. Putnam, Nucl. Inst. & Meth. A **337** (1993) 106.

[GRO73] L. Grodzins *et al.*, Phys. Rev. Lett. **30** (1973) 453.

[GRO92] M. Grog *et al.*, Nucl. Instr. & Meth. Phys. Res. A **108** (1992) 512.

[GUP10] J. B. Gupta *et al.*, International Journal of Modern Physics E **19** (2010) 1491.

[GUP13] J. B. Gupta, Phys. Rev. C **87** (2013) 064318.

[GUP81] J. B. Gupta and R. Kumar, J. Phys. G **7** (1981) 673.

[HAX49] O. Haxel, J. H. Jensen and H. E. Suess, Phys. Rev. **75** (1949) 1766.

[BUT96] P. A. Butler *et al.*, Rev. of Mod. Phys. **68** (1996) 349.

[BVU13] S. P. Bvumbi *et al.*, Phys. Rev. C **87** (2013) 044333.

[BYR87] Th. Byrski *et al.*, Nucl. Phys. A **474** (1987) 193.

[CAMXX] D. B. Campbel, PhD thesis, unpublished,
http://diginole.lib.fsu.edu/islandora/object/fsu%3A185022

[CAS98] R. F. Casten *et al.*, Phys. Rev. C **57** (1998) R1553.

[CAS75] C. Castaneda *et al.*, Phys. Lett. **57B** (1975) 335.

[CEJ10] P. Cejnar *et al.*, Rev. Mod. Phys. **82** (2010) 2155.

[CUREF] *http://www-nds.iaea.org/medical/tip48v4.html*

[DIL03] I. Dillman *et al.*, Phys. Rev. Lett. **91** (2003) 162503.

[DDC78] The approach referred to as "Universal Parameterization of the 'deformed' Woods-Saxon Hamiltonian" has been developed in a series of articles:
J. Dudek and T. Werner, J. Phys. G: Nucl. Phys. **4** (1978) 1543,
J. Dudek *et al.*, J. Phys. G: Nucl. Phys. **5** (1979) 1359,
J. Dudek *et al.*, Nucl. Phys. A **341** (1980) 253,
J. Dudek *et al.*, Phys. Rew. C **23** (1981) 920, and has been summarized in
S. Ćwiok *et al.*, Comp. Phys. Comm. **46** (1987) 379.

[DIK74] M. Diksic *et al.*, Phys. Rew. C **10** (1974) 1172.

[DOA09] Q. T. Doan *et al.*, Acta Phys. Pol. B **40** (2009) 725.

[DOA10] Q. T. Doan *et al.*, Phys. Rew. C **82** (2010) 067306.

[DUD02] J. Dudek *et al.*, Phys. Rev. Lett. **88** (2002) 252502.

[DUD06] J. Dudek *et al.*, Phys. Rev. Lett. **97** (2006) 072501.

[BAS94] S. Basu *et al.*, Phys. Rev. C **49** (1994) 650.

[BEN79A] R. Bengtsson and S. Frauendorf, Nucl. Phys. A **314** (1979) 27.

[BEN79B] R. Bengtsson and S. Frauendorf, Nucl. Phys. A **327** (1979) 139.

[BEN84] R. Bengtsson and J. G. Garrett, "Collective phenomena in Atomic Nuclei", page 193, (World Scientific, Singapore, 1984).

[BEN86] R. Bengtsson *et al.*, At. Data Nucl. Data Tables **35** (1986) 15.

[BHA11] T Bhattacharjee *et al.*, DAE Symp. Nucl. Phys. **56** (2011) 358.

[BHA14] T. Bhattacherjee *et al.,* Nucl Instr. Meth. A **767** (2014) 19.

[BHA16] Soumik Bhattacharya *et al.*, Proc. of DAE-BRNS Symposium on Nuclear Physics, **61** (2016) 98.

[BHO17] R. K. Bhowmik, priv. comm. (2017).

[BLA85] M. Blann, ALICE/1991:An Evaporation Code, Lawrence Livermore National Laboratory, University of California, Livermore Report No. UCID-20169, 1985 (unpublished).

[BOH53] A. Bohr and B. R. Mottelson, Kgl. Danske Videnskab. Selskab, Mat. fyz. Medd. **27** (1953) 16.

[BOH75] A. Bohr and B. R. Mottelson: "Nuclear Structure", vol. II (W. A. Benjamin, Inc., New York, 1975)

[BOR06] H. G. Borner *et al.*, Phys. Rev. C **73** (2006) 034314.

[BRICC] *http://bricc.anu.edu.au/index.php* and references therein.

[BRU86] R. Brun, et al., GEANT3, CERN - DD/EE/84-1, 1986.

[BUC12] D. Bucurescu *et al.*, Phys. Rev. C **85** (2012) 017304.

Bibliography

[AFN84] H. Auer *et al.*, Z. Phys. A **318** (1984) 323.

[AHM93] I. Ahmad and P. A. Butler, Annu. Rev. Nucl. Part. Sci. **43** (1993) 71.

[ALICE] M. Blann, ALICE/1991: An Evaporation Code, Lawrence Livermore National Laboratory University of California Livermore

[ALL10] J. M. Allmond *et al.*, Phys. Rev. C **81** (2010) 064316.

[AND76] G. Andersson *et al.*, Nucl. Phys. A **268** (1976) 205.

[AND98] W. Andrejtscheff *et al.*, Phys. Lett. B **437** (1998) 249.

[AUE84] H. Auer *et al.*, Z. Phys. A **318** (1984) 323.

[BAN12] D. Banerjee *et al.*, DAE Symp. Nucl. Phys. **57** (2012) 186.

[BAN15] D. Banerjee *et al.*, Phys. Rev. C **91** (2015) 024617.

[BAR05] R. A. Bark *et al.*, J. Phys. G **31** (2005) S1747.

[BAR10] R. A. Bark *et al.*, Phys. Rev. Lett. **104** (2010) 022501.

[BHA13] T. Bhattacharjee *et al.*, Phys. Rev. C **88** (2013) 014313.

[BAR70] J. Barrette *et al.*, Canadian Journal of Physics **48** (1970) 1161.

[BAS13] S. K. Basu and A. A. Sonzogni, Nuclear Data Sheets **114** (2013) 435.